



The University of
Nottingham

UNITED KINGDOM · CHINA · MALAYSIA

Department of Mechanical, Materials and Manufacturing
Engineering, Faculty of Engineering

Modelling of Abrasive Waterjet Milled Footprints

Saqib Anwar

MSc, BSc (Hons)

Thesis submitted to the University of Nottingham for the degree
of Doctor of Philosophy

October 2013

Abstract

Abrasive waterjet (AWJ) cutting is one of the most promising fast emerging non-traditional cutting technologies. It is highly competitive for machining difficult-to-cut materials like ceramics, composites and titanium alloys as compared to other non-conventional processes (e.g. laser, EDM) which are either technologically inappropriate or fail to be cost-effective. However, at the moment most of the usage of the AWJ machining lies in the area of the through cutting applications and to perform controlled depth cutting (milling) is still at craftsmanship level. This is due to the facts that: (i) AWJ machining is based on employing a jet plume as a “soft body” tool, the footprint of which not only depends on the jet energy parameters (e.g. pressure, abrasive mass flow rate, etc) but also on the jet kinematic parameters (e.g. jet traverse speed) which make controlling of the jet penetration depth very difficult; (ii) there is absence of the appropriate and reliable models that can simulate and predict the AWJ milled footprints and this is one of the major obstructions constraining the use of the AWJ milling applications.

The aim of this thesis is to develop accurate models for predicting the AWJ milled footprints. The workpiece material considered is a titanium based superalloy (Ti-6Al-4V) which is extensively used in the aerospace and medical industry. Two modelling approaches; finite element (FE) modelling and mathematical modelling are presented in this work. Considerable numbers of experiments are conducted to generate the data for validating the results from the models.

The models presented in the current study are closer to the real life conditions occurring during the AWJ machining as compared to the state of the art in modelling

of AWJ machining. Regarding the FE modelling, the abrasive particles (i.e. garnet) are modeled as elastic with a tensile failure criterion with various non-spherical shapes (rhombic, triangular and trapezoidal) and sharp cutting edges in contrast to the usual approach of assuming them as rigid spherical particles. The effects of mass flow rate of the abrasive particles, traverse speed of the AWJ plume across the workpiece and Gaussian spatial distribution of the abrasive particles in the jet plume are also incorporated in the FE model. The FE model is developed to an extent that it can simulate the footprints as a result of overlapping passes of the AWJ. The simulated jet footprints from the FE models are in good agreement (maximum errors $\leq 15\%$) with the experimental results.

From the mathematical modelling point of view, a model is developed that can accurately predict the AWJ milled footprints with root-mean-squared errors less than 9%. The model takes into account the effects of jet incidence angles, traverse speeds and arbitrarily-moving jet-paths within the target surface. The model is computationally inexpensive and can be used for real time predictions of footprints during CNC machining.

The current study provides the reliable models that can be employed for accurate prediction of the abrasive waterjet milled footprints at various process parameters which is a necessary step towards the exploitation of the AWJ machining for controlled depth cutting applications and its automation.

Publications originating from the thesis

S. Anwar, D. a. Axinte, and A. A. Becker, “Finite element modelling of a single-particle impact during abrasive waterjet milling,” *Proceedings of the Institution of Mechanical Engineers, Part J: Journal of Engineering Tribology*, vol. 225, no. 8, pp. 821–832, Aug. 2011.

M. C. Kong, **S. Anwar**, J. Billingham, and D. a. Axinte, “Mathematical modelling of abrasive waterjet footprints for arbitrarily moving jets,” *International Journal of Machine Tools and Manufacture*, vol. 53, no. 1, pp. 58–68, Feb. 2012.

S. Anwar, D. a. Axinte, and A. a. Becker, “Finite element modelling of abrasive waterjet milled footprints,” *Journal of Materials Processing Technology*, vol. 213, no. 2, pp. 180–193, Feb. 2013.

S. Anwar, D. A. Axinte, and A. A. Becker, “Finite element modelling of overlapping abrasive waterjet milled footprints,” *Wear*, vol. 303, pp. 426–436, 2013.

Acknowledgements

At the beginning, I am eternally grateful to God for the gift of life and the blessings which HE has bestowed upon me.

I would sincerely like to thank everyone who has assisted me in carrying out this research project. The most important person I would like to express my sincere thanks is my principal supervisor, Prof. Dragos Axinte. He has given me a great deal of advice and support in the completion of this research project. He was always available to share his time and to discuss any problem. I would also like to express my gratitude to Prof. Adib Becker, my co-supervisor, for sharing his experience and information on Finite Element modelling and to Prof. John Billingham, my co-supervisor, for sharing his experience in mathematical modelling.

Many thanks are given to my colleagues and the staff/technicians (Mr. Barry Holdsworth and Mr. Daine Mark) in the Manufacturing Lab. They gave me a good deal of practical advice and hands-on assistance with my experiments.

I would like to thank the University of Engineering & Technology, Lahore, Pakistan and the University of Nottingham, UK for providing the scholarship assistance.

I would also like to thank to all those people by the efforts of whom the valuable free services like Mendeley and Google Scholar are running and from which I benefitted a lot during my PhD.

In the end, I would like to extend my profound thanks to all my family.

Table of contents

Abstract.....	i
Publications originating from the thesis	iii
Acknowledgements.....	iv
Table of contents.....	v
List of Figures.....	x
List of Tables	xix
Nomenclature.....	xx
Chapter 1 Introduction	1
1.1 Background	1
1.1.1 Process advantages	3
1.1.2 Applications of the AWJ process	5
1.2 Research Problem	7
1.3 Objectives of the Study.....	10
Chapter 2 Literature review	13
2.1 Abrasive Waterjet machining Systems	13
2.1.1 Entrainment system	14
2.1.2 Slurry jet system	19
2.2 Material removal mechanisms during AWJ machining.....	21
2.2.1 Particles erosion mechanisms	21
2.2.2 Kerf generation process	27
2.3 Influence of process parameters on process performance	31
2.3.1 Water pressure (P)	32
2.3.2 Abrasive particles size and shape	33
2.3.3 Abrasive mass flow rate	34

2.3.4	Nozzle and orifice diameter	35
2.3.5	Effect of the jet traverse speed	37
2.3.6	Effect of stand-off distance (SOD)	38
2.4	Modelling of AWJ	40
2.4.1	Finite element (FE) modelling	40
2.4.2	Analytical modelling	48
2.5	Summary of the literature	51
2.6	Main research challenges	53
2.6.1	FE modelling challenges.....	53
2.6.2	Mathematical modelling challenges	54
Chapter 3 Methodology		56
3.1	Abrasive Waterjet Apparatus	56
3.1.1	Fixed machining parameters	57
3.2	Materials used	58
3.2.1	Target material.....	58
3.2.2	Impacting particles.....	58
3.3	Measurement Techniques	60
3.3.1	Equipment: Keyence digital microscope	60
3.3.2	Equipment: Fogale Nanotech 3D profiler.....	62
3.3.3	Equipment: Taylor Hobson Talysurf CLI 1000.....	63
3.3.4	High precision analytical balance	64
3.4	Finite element (FE) modelling	64
3.4.1	Steps involved in FE modelling.....	67
3.4.2	Materials model	72
3.4.3	Generation of validation data.....	76
3.5	Analytical modelling.....	78

3.5.1	Modelling tool	79
3.5.2	Generation of validation data.....	79
Chapter 4 Finite element modelling of a single particle impact		81
4.1	Introduction	81
4.2	Generation of experimental data	85
4.3	Finite Element Modelling	87
4.3.1	Material modelling.....	87
4.3.2	Contact.....	89
4.3.3	Boundary conditions	89
4.3.4	Meshing	92
4.4	Results and discussion	93
4.5	Conclusion	104
Chapter 5 Finite element modelling of a multiple particles impact		107
5.1	Introduction	107
5.2	Selecting the appropriate material properties.....	108
5.2.1	Material properties for the garnet particles.....	108
5.2.2	Material failure model for Ti-6Al-4V.....	112
5.3	Selecting the sizes of the garnet abrasive particles	115
5.4	Selecting the shapes of the garnet abrasive particles	117
5.5	Contact	120
5.6	Results and discussions.....	123
5.7	Conclusions.....	127
Chapter 6 Finite element modelling of a single jet pass		130
6.1	Introduction	130
6.2	Finite element modelling	131
6.2.1	Calculating the required mass of abrasive particles.....	132

6.2.2	Assembling the abrasive particles in the model	133
6.2.3	Boundary conditions	136
6.2.4	Including the process kinematics into the model	138
6.3	Generation of experimental data	142
6.4	Results and discussion	143
6.5	Conclusions	153
Chapter 7 Finite element modelling of overlapping jet passes		155
7.1	Introduction	155
7.2	Finite Element modelling	156
7.2.1	Analysis procedure	158
7.3	Generation of experimental data	159
7.4	Results and discussion	161
7.5	Conclusions	174
Chapter 8 Mathematical modelling of AWJ footprints		177
8.1	Introduction	177
8.2	Footprint prediction model for an arbitrarily moving jet	179
8.2.1	Model Definitions	179
8.3	Generation of experimental data	184
8.4	Results and discussion	186
8.5	Application of the mathematical model	196
8.6	Comparison of the mathematical and FE modelling	197
8.7	Conclusions	200
Chapter 9 Final Conclusions and Future work		202
9.1	Conclusions	202
9.1.1	FE modelling	203
9.1.2	Mathematical modelling	206

9.2 Future work	206
References	209

List of Figures

Figure 1-1: (a) Typical abrasive water-jet cutting head [13] (b) Example of AWJ through cutting [14] (c) Example of AWJ milled part [15].....	3
Figure 1-2: Significant of AWJ modelling for achieving a better process control.....	9
Figure 2-1: Schematic diagram of AWJ cutting system [42]	14
Figure 2-2: Example of AWJ cut and AWJ milled parts at University of Nottingham	17
Figure 2-3: Illustration of difference between plain waterjet (PWJ) and abrasive waterjet (AWJ) machining.....	18
Figure 2-4: Schematic illustration of slurry jet system [41].....	20
Figure 2-5: (a) Impact of a sharp micro particle on a ductile surface at an angle of attack α and velocity v . (b) Contact forces acting on the particle during cutting[60].	23
Figure 2-6: Cutting and ploughing by solid particles at oblique impact angles [64] ..	24
Figure 2-7: Effect of particle rake angle on target deformation [65].....	25
Figure 2-8: Type-I cutting observed in AWJ milling.	26
Figure 2-9: Failure modes in brittle materials; (b) scratching and network cracking [72] (a) schematic view of radial, median and lateral cracks induced by a sliding micro indenter [74].	27
Figure 2-10: Visualization of kef generation process; (a) representation of different regimes of material removal [78], (b) schematic zoomed-in view of individual	

particles impact during kerf generation [76].	28
Figure 2-11: Typical AWJ-machined kerf cutting front wall.	29
Figure 2-12: Illustration of a kerf geometry cut by AWJ [32].	30
Figure 2-13: Deformation and crack produced in γ -TiAl by PWJ impact [29].....	31
Figure 2-14: Variation of material removal rate with different sizes of orifice ((a) 0.25 mm; (b) 0.30 mm; and (c) 0.40 mm) and focusing nozzle at different waterjet pressure and abrasive flow rate (i) P=100 MPa and (ii) P=250 MPa [20].....	36
Figure 2-15: Schematic representation of flow pattern in AWJ milling at 90^0 incidence (a) Jet channeling at low traverse rate (b) No jet channeling at high traverse speed [93].....	38
Figure 2-16: Increasing jet divergence with stand-off distance [18].	39
Figure 3-1: (a) Ormond CNC controlled 5-axis waterjet machine used at the University of Nottingham, (b) KMT ultra-high pressure generation system, (c) cutting head, (d) intensifiers, (e) Fagor CNC control unit.	57
Figure 3-2: Spherical steel shots used as impacting particles.....	59
Figure 3-3: Garnet mesh 80 particles, source Indian garnet.	60
Figure 3-4: Keyence digital microscope operating to analyze an AWJ milled workpiece.....	61
Figure 3-5: Fogale interferometer scanning the steel shot impacts.	62

Figure 3-6: Talysurf CLI 1000 system for 3D scanning.....	63
Figure 3-7: Estimated strain rates associated with the particle sizes and impact velocities. Solid lines represent purely elastic behavior; broken lines, perfect plastic behavior [145].....	74
Figure 4-1: Varying shapes and sizes craters produced by garnets particles at water pressure (P) = 345MPa, impact angle (θ) = 90° , traverse speed (V_f) = 20000 mm/min.....	84
Figure 4-2: Model geometry, a typical mesh and boundary condition used for the workpiece and the ball: (a) a typical configuration used in simulations, and (b) model with infinite elements at boundaries and base.	91
Figure 4-3: Mesh convergence study, P=345MPa, $\theta = 90^\circ$	93
Figure 4-4: Images of steel ball indentations (impact direction is from left to right)..	94
Figure 4-5: Examples of 3D contours of the scanned craters with extracted 2D profiles at P = 276MPa ($V_{imp} = 520\text{m/s}$). Impact direction of steel ball is from left to right.	96
Figure 4-6: Experimental profiles of the craters vs. FE simulation results; P = 345 MPa, $\theta = 90^\circ$ (b) P = 276 MPa, $\theta = 90^\circ$ (c) P = 345 MPa, $\theta = 70^\circ$ (d) P = 276 MPa, $\theta = 70^\circ$ (e) P = 345 MPa, $\theta = 50^\circ$ (f) P = 276 MPa, $\theta = 50^\circ$. Impact direction is from left to right.....	98
Figure 4-7: Stages of contact between ball and the target during the impact. P = 276 MPa, $\theta = 90^\circ$, t = simulation time.	100
Figure 4-8: P = 345MPa, $\theta = 70^\circ$, (a) Cross-section side view: New exposed elements of the ball making contact with the target surface at time = 0.4 μs . (b) Tilted top view	

of the final shape of the crater at time = 2 μ s with some distorted element.	102
Figure 4-9: Generation of ring cracks in FE and experimental craters at P = 345MPa, $\theta = 90^\circ$, (a, c) experimental craters, (b) contour plot of maximum principle plastic strain produced in crater in the model.	103
Figure 4-10: Residual stresses induced in the target at $V_{imp} = 581\text{m/s}$, $\theta = 90^\circ$	104
Figure 5-1: Schematic diagram of a spherical cap [159].	110
Figure 5-2: Variation of maximum tensile stress on the axis and on the surface of the particle during impact [160].	112
Figure 5-3: Results for mesh convergence study at P=138MPa ($V_{imp}=368\text{m/s}$).	113
Figure 5-4: Shapes of the garnet observed under the optical microscope. The colored dots adjacent to the particles represent the category of the shapes they belong to....	118
Figure 5-5: The effect of the particles shape on erosion rate in the target material under the impact of 50 particles [128].	119
Figure 5-6: Free flying nodes from the eroded elements impacting the incoming particles.	121
Figure 5-7: Stress patterns developed after 38 particles impact: (a) with nodal erosion option active and (b) without nodal erosion.	123
Figure 5-8: Multiple particles FE model	124
Figure 5-9: Steady state erosion rates in Ti-6Al-4V determined for various velocities from FE simulations. The particles impact velocities of 367m/s, 450m/s, 520m/s and	

581m/s represent the water pressures of 138MPa, 207MPa, 276MPa and 345MPa respectively.....	125
Figure 5-10: Variation of erosion rate with impact velocity; (a) FE simulation results, (b) experimental results.	127
Figure 6-1: Symmetry of the AWJ milling process at 90° incidence angle.....	131
Figure 6-2: (a) Gaussian spatial distribution [122] and (b) velocity of the abrasive particles after nozzle exit [122].	134
Figure 6-3: Top and sides views of two layers of abrasives illustrating the particles distributed within the jet diameter.	135
Figure 6-4: (a) 3D view of the model. (b) Meshing of the target and the particles. (c) Zoomed-in view of the elements used in the fine mesh area and the particles. (d) Gaps among the layers of the particles; in between these gaps the jet was traversed by fixed percentage of total distance (L_{FE}) to be covered across the target. (e) Tilted top view of the model showing the length of the jet plume.	136
Figure 6-5: Movement of the jet across the target in the model – top view. Points A and B show the initial position of the jet and points C and D show the final position. Hatched area “BCFE” illustrates the region where the jet footprints were measured.	137
Figure 6-6: Negligible erosion produced in Ti6Al4V target after multiple PWJ passes at $P=345\text{MPa}$, $V_f=1000\text{mm/min}$ (a) Zoomed in view of three 100% overlapping passes (b) Single scanned profile across the PWJ surface.....	138
Figure 6-7: CCD camera image showing detected abrasive particles after nozzle exit	

which are widely spaced apart [122].	139
Figure 6-8: Schematic representation of the differences between the particles spatial density in the jet in reality and FE model. (a) Experimental jet with particles far apart from each other (b) Jet in the FE model with closely spaced particles.	140
Figure 6-9: Procedure for extracting 2D profiles from an experimentally generated kerf.....	143
Figure 6-10: (a) A typical scanned 30mm long milled trench with some surface non-uniformities; (b & c) Zoomed in regions within the scanned trench with yellow circles highlighting some relatively deep eroded regions. Process parameters used $P = 207\text{MPa}$, $V_f = 1000\text{mm/min}$	144
Figure 6-11: Stress contour generated in the simulated half kerf; $P = 276\text{Mpa}$, $V_f = 1000\text{mm/min}$	145
Figure 6-12: Stages of erosion of the target during the impact of abrasive particles. *Fifteen different layers of particles were used which were then patterned over each other in the Z-direction to achieve the mass of abrasive particles (mFE) required in each simulation.	147
Figure 6-13: Comparison of FE and Experimental footprints at given parameters...	148
Figure 6-14: (a) Variation in depth of the footprint by changing the water pump pressure. (b) Variation in width of the footprint (w) by changing the water pump pressure.	150
Figure 6-15: Details of piled-up material at the edges of the jet footprint at $P =$	

276MPa, $V_f = 2000\text{mm/min}$: (a) Scanned footprint; (b) Averaged 2D profile of the footprint.	151
Figure 6-16: Erosion rates obtained from FE simulations vs. experimental results. .	152
Figure 7-1: Top and sides views of two layers of abrasives illustrating the particles distributed within the jet diameter.	156
Figure 7-2: (a) 3D view of the FE model explaining the SO distance between adjacent overlapping jet passes. (b) Meshing of the target and the particles.	157
Figure 7-3: Movement of the jet across the target in the model – top view.	158
Figure 7-4: Procedure for extracting 2D profiles from an experimentally generated kerf. Kerf milled at $P=345\text{MPa}$, $V_f = 2000\text{mm/min}$, $SO=0.5\text{mm}$, number of jet passes, $n = 3$	161
Figure 7-5: Explanation of the simulation process for three jet passes at $P = 207\text{MPa}$, $V_f = 1000\text{mm/min}$, $SO=0.5\text{mm}$. (a) First jet pass simulation; (b) second jet pass simulation; (c) third jet pass simulation; (d) cross-sectioned view of final target surface after three jet passes.	163
Figure 7-6: Preliminary comparison of FE and experimental (Exp) footprints at $P=276\text{MPa}$, $V_f = 2000\text{mm/min}$, $SO = 0.5\text{mm}$, $n = 2$	166
Figure 7-7: Comparison of mass distribution of particles in the jet plume. * As-is distribution is calculated when particles are arranged based on ref [122] number based spatial distribution.	167
Figure 7-8: Comparison of simulated and experimental footprints at $V_f =$	

2000mm/min (a) SO=0 (b) SO=0.3mm (c) SO=0.5mm.....	171
Figure 7-9: Effect of secondary (reflected) jet on the footprints; $P = 345\text{MPa}$, $V_f = 2000\text{mm/min}$, $SO = 0.5\text{mm}$	172
Figure 7-10: Comparison of FE simulated and experimental erosion rates at $V_f = 1000\text{mm/min}$, $SO = 0.3\text{mm}$, $n = 3$	174
Figure 8-1: Variable and fixed parameters used in the footprint models for AWJ machining.	179
Figure 8-2: Schematic diagram of the jet footprint: (a) cross-sectional view and (b) top view.	180
Figure 8-3: Test specimen designed for the model validation: (a) schematic illustration of the jet paths on the testpiece; (b) a testpiece after machining.....	185
Figure 8-4: Examples of the model predicted footprint profiles (blue solid lines) against the experimental ones (red dotted lines) at indicated parameters:(a) $V_f=2000\text{mm/min}$ and $\theta=90^\circ$; (b) $V_f=2000\text{mm/min}$ and $\theta=70^\circ$; (c) $V_f=1000\text{mm/min}$ and $\theta=90^\circ$; (d) $V_f=1000\text{mm/min}$ and $\theta=70^\circ$. Jet impact direction is from right to left. (Note: the units for both the abscissa and the ordinate are “mm”)......	188
Figure 8-5: Mean of residuals, R_M at jet impingement angle $\theta = 70^\circ, 90^\circ$ when: (a) $V_f = 2000 \text{ mm/min}$ and (b) $V_f = 1000 \text{ mm/min}$; root-mean-square error of residuals, R_{RMS} at $\theta = 70^\circ, 90^\circ$ when: (c) $V_f = 2000 \text{ mm/min}$ and (d) $V_f = 1000 \text{ mm/min}$. [Note: the unit is in “mm”]	193
Figure 8-6: Illustration of different depth of cut and surface roughness in backward	

and forward milling resulting from different jet traverse directions.	195
Figure 8-7: ConforM ² -Jet logo milled in Ti-6Al-4V based on the traverse speeds computed by the developed mathematical model [40].	197
Figure 8-8: Comparison of footprint prediction from FE and mathematical models at $P=138\text{MPa}$, $ma=0.04\text{kg/min}$: (a) $V_f=2000\text{mm/min}$; (b) $V_f=1000\text{mm/min}$	198
Figure 8-9: Footprints predicted by the mathematical model after being calibrated from the data generated by the FE model at $P=207\text{MPa}$, $ma=0.02\text{kg/min}$: (a) $V_f=2000\text{mm/min}$; (b) $V_f=1000\text{mm/min}$	199

List of Tables

Table 2-1: Differences between AWJ cutting and AWJ milling	17
Table 2-2: Typical applications for PWJ and AWJ technology [38].....	19
Table 2-3: Summary of FE modelling parameters used in different studies	47
Table 3-1: Fixed AWJ milling parameters in the current study.	57
Table 3-2: Process parameters used for single particles impact trials.	77
Table 3-3: Process parameters used during multiple garnet particles impact.....	77
Table 3-4: Process parameters used for single AWJ pass trials.	77
Table 3-5: Process parameters used for overlapping AWJ pass trials.....	78
Table 3-6: Process parameters used in trials for analytical model.	80
Table 4-1: Material constants for Ti-6Al-4V [143].....	88
Table 4-2: Comparison of steel and Ti-6Al-4V strength properties [94], [148–150].	88
Table 4-3: Material constants used for the steel shots.....	89
Table 4-4: Parameters used in the FE model.	93
Table 5-1: Fracture velocities and associated failure stresses for some irregular shaped brittle particles [158].....	109
Table 5-2: Material constants for garnet.....	112
Table 5-3: Details of the abrasive particles mix used in the FE model	117
Table 5-4: Sizes and number of particles assigned to different shapes. (Note: particles shown in the table are not to scale).....	120
Table 6-1: Process parameters used in the FE model.	138
Table 7-1: Process parameters used in the FE model.	159

Nomenclature

ASJ	Abrasive slurry jet
AWJ	Abrasive waterjet
d	Nozzle exit diameter (mm)
EDM	Electric discharge machining
ER	Erosion rate (mg/mg)
L_{FE}	Length to be traversed in the FE model (mm)
L_j	Length of the jet in real life for m_{FE} (Kg) mass of particles (mm)
L'_j	Length of the jet in FE model for m_{FE} (Kg) mass of particles (mm)
l_p	Length of the pile-up material (mm)
\dot{m}_a	Abrasive mass flow rate (Kg/min)
m_{FE}	Mass of one jet pass in the FE model (mg)
m_L	Mass of particles impinged per unit length (Kg/mm)
m_{PM}	Mass of one particles mix (mg)
n	Number of jet passes
n_P	Number of particles required in the FE model
n_{PM}	number of particles mix's required in the FE model
θ_R	Resultant angle of particles impact in the model ($^{\circ}$)
P	Water pump pressure (Pa)
PWJ	Plain waterjet
ρ	Density of water (Kg/m ³)
SO	Step-over distance (mm)
SOD	Standoff distance (mm)
V_f	Traverse speed of the jet across the workpiece during experiments (m/s)
V_{imp}	Impacting velocity of the abrasive particles (m/s)
V_w	Waterjet velocity (m/s)
w	Width of the footprint (mm)

Chapter 1 Introduction

This chapter presents the introduction to the abrasive waterjet (AWJ) technology, the background for undertaking the current project and the objectives of the current study.

1.1 Background

The development of the capabilities of niche non-conventional processing techniques is of critical importance in widening the expertise for the manufacture of high value added parts/products (e.g. jet engine components, medical implants, optical components and smart actuators) made of advanced engineered materials. This is of the critical importance in today's scenario with increasing emphasis being placed on the use of green and environmentally-friendly technologies for the generation of these components. This means that it is inevitable that the research topics related to the development of these eco-friendly technologies (e.g. AWJ machining, dry EDM, ultrasonic machining) are in demand by the manufacturing industry. For example, in the Air Force ManTech Sustainable Aerospace Manufacturing Initiative in the USA [1] and in the EU Sky Clean Joint Technology Initiative in 2008-2014 [2], one of the key objectives is to make the manufacturing practices and the resultant parts/products more environmental friendly. To achieve this goal, the selection of the materials and methods of manufacturing play a significant role.

Titanium (Ti) and Nickel (Ni) based superalloys have been materials of choice for many years for various high value added applications such as jet engine parts, power plant components and medical implants. This is due to the properties which they possess such as high strength-to-weight ratio, high stiffness, high temperature strength

and good oxidation and corrosion resistance [3, 4]. These properties will help to ensure efficient fuel consumption, which is an economic and environmental consideration, and longer operational service life. However, Ti alloys are classified as extremely difficult to cut materials; this is owing to several inherent properties of these material [5], [6]. Generating complex shape parts from these ever developing/improving superalloys present significant challenges from a machinability point of view. The conventional operations (e.g. milling, grinding, drilling) are difficult to employ as they lead to extensive tool wear and to the generation of surface malfunctions (e.g. deformed layers and cracks) [7], [8], [9]. On the other hand, the existing non-conventional machining processes, known by their low material rates, either leave undesired surface damages (e.g. recast layer – laser /EDM) or require special materials properties (e.g. electrical conductivity - EDM) [10]. Moreover, most of these conventional/non-conventional machining processes make use of cutting fluids which results in increased process cost and environmental contamination [11].

Abrasive water jet (AWJ) machining is one of the most promising environmental friendly non-conventional machining processes that has the capability to machine difficult-to-cut materials (e.g. Ti-6Al-4V) at high geometrical accuracies with damage-free surfaces owing to its unique advantages. In the AWJ machining process, high pressure water is supplied by a pump at the orifice inside the cutting head from where it is converted into a high velocity jet. While passing through a mixing chamber, water creates a vacuum which draws the abrasive particles into a focusing tube where the abrasive waterjet (AWJ) mixture is formed (see Figure 1-1(a)). When the jet plume (mixture of abrasives and water droplets) impacts the target surface, it results in the generation of a unique footprint (kerf). As a result of this, the workpiece material removal is mainly caused by the impact of a multitude of high velocities

abrasive particles [12]. Since material is removed by the erosion phenomenon in AWJ machining, the process is able of machining any material independent of its properties. Figure 1-1(b) and Figure 1-1(c) show an example of AWJ through cutting and an AWJ milled part respectively.

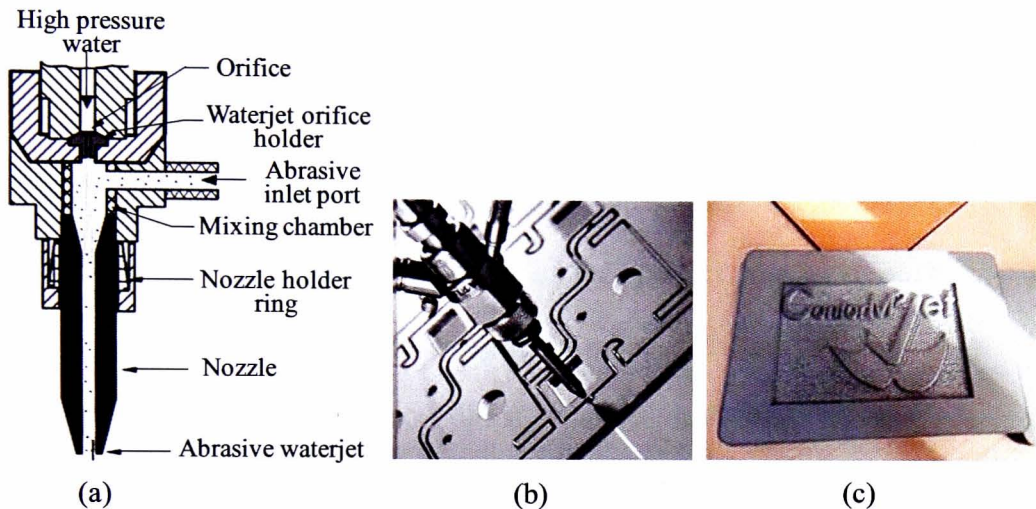


Figure 1-1: (a) Typical abrasive water-jet cutting head [13] (b) Example of AWJ through cutting [14] (c) Example of AWJ milled part [15].

1.1.1 Process advantages and disadvantages

AWJ machining offers a set of paramount advantages over other competitive machining methods, some of which are detailed below:

- AWJ machining is a highly environment friendly process, water and abrasive used during machining can be recycled [16] as compared with conventional chip removal processes (milling, turning) which also make use of cutting fluids (toxics).
- AWJ enables the machining of difficult-to-cut materials (e.g. Ti/Ni alloys, ceramics) [17], [18]. In contrast with the conventional (e.g. milling) /non-

conventional (e.g. EDM) cutting techniques, AWJ processing is practically capable of cutting any material regardless of its properties.

- AWJ machining involves very low specific cutting forces at acceptable material removal rates [19], [20], [21]. With these unique attributes, AWJ processing has the capability to shape low rigidity components (e.g. thin walls) where other conventional processes would struggle with.
- AWJ processing results in overall low cutting temperatures typically less than 60°C [19], [22], [23]. Compared with conventional/non-conventional (EDM, Laser) machining, AWJ processing offers the “perfect” method to generate parts made of heat sensitive materials (Ni/Ti aerospace and shape memory alloys) that are used in aerospace (e.g. disks, casings) and medical (e.g. implants) applications.
- The AWJ machining uses a “universal cutting tool”, i.e. abrasive waterjet plume, of which the characteristics can be adjusted (e.g. pressure, grit specification, stand-off distance, jet tilt angle relative to target surface) to enable integrated manufacturing solutions (i.e. roughing & finishing & ultra polishing) in a single manufacturing cell to address the machining of a wide range of advanced engineered materials.

Despite all these advantages, there are several disadvantages of the AWJ machining process which are mentioned below.

- Abrasive embedment in the target surface is one of the most prominent drawbacks of the AWJ machining process [24], [25]. The embedded abrasive particles and associated cracks results in reducing the strength of the target surface and can act as crack propagation points during the loading of the target. However, methods

such as plain waterjet passes over the target surface following the AWJ passes have been reported to overcome this issue [26].

- It is very difficult to control the geometry (e.g. kerf taper) [27] of the part being machined and the process heavily relies on human intervention and skill.
- The quality of the surface finish is low as compared to the conventional machining processes e.g. the development of striation marks on the cut face [28].

More research work is required to overcome the disadvantages of the AWJ machining process to fully exploit its unique advantages.

1.1.2 Applications of the AWJ process

In the following some of the niche applications of AWJ machining are mentioned; however, most of these have been done only at the test level with little attempt to generate complex surfaces/parts. AWJ machining is employed for the processing of the following:

- Ti/Ni alloys for aerospace applications (e.g. casings) [29].
- Biologic (bones) compatible materials (NiTi) for medical applications (e.g. implants) [17].
- Engineered ceramics (SiC, Al₂O₃) for parts with chemical inertness and/or high wear resistance [18], [30].
- Ultra-hard materials (e.g. diamond) for tooling fabrication [31].
- Engineering composites for aerospace, automotive applications [32], [33].
- Turning and dressing of grinding wheels [34].
- Coating removal in aerospace and nuclear industries [35].
- Machining of large and/or complex shape parts by mounting the cutting head on a

robotic arm [36], [37].

With these unique capabilities, AWJ machining is regarded as a key enabling technology for the manufacture of complex geometry components made of notoriously difficult-to-cut materials. A global market research on abrasive waterjet machines estimate that their use will reach almost US\$854 million by 2015; Europe and Asia-Pacific alone account for more than 55% of the global waterjet cutting machine market [38]. Taking also into consideration that more advanced (but difficult-to-cut) materials are being developed, it seems that in medium/long term, AWJ machining will be a key manufacturing technology enabling the production of high value added products [39].

However, at the moment, most of the AWJ usage lies in the area of through cutting [25] and milling of freeforms is still at the infancy stage. Moreover, in its current status, AWJ machining process is heavily relying on human intervention. In such scenarios, it is no wonder that AWJ technology needs a technological breakthrough to enable efficient and knowledge intensive exploitation (i.e. freeforms generation) of these unique capabilities of AWJ process.

This problem has brought about a strong collaboration between academic and commercial partners in form of a European FP7 research project (Conform²Jet 2009-2013 [40]) led by Professor Dragos Axinte at The University of Nottingham, UK . The project aims to investigate and enhance the capabilities of the AWJ technology to such an extent that it can be used for the freeform milling of the difficult to cut materials with minimum levels of human intervention. The project aims to deliver the first self-learning control system for abrasive water jet milling to enable the generation of freeform surfaces. In order to enable this, there is a principal need for

the development of abrasion models either in analytical and/or numerical forms. This PhD study is undertaken as part of Conform²Jet project and the focus will be on the development of the accurate and reliable models of AWJ impingement on the target.

1.2 Research Problem

AWJ machining is technologically appropriate for machining difficult-to-cut materials in a cost effective way owing to its unique advantages. Despite all these advantages, there are some significant scientific and technological challenges regarding employing the AWJ process for the controlled depth machining, and there is a certain need for the development of abrasion models that will assist in understanding and controlling the AWJ process for milling difficult-to-cut materials (e.g. Ti-6Al-4V). The complexity of the AWJ process is due to the following main challenges:

- The AWJ process uses a jet plume as a “soft body” tool and the effective diameter of the jet that impinges the target surface changes by varying the standoff distance and jet tilt angle. This means that different widths of the kerfs will be generated in the target at different standoff distances and jet tilt angles. This phenomenon makes the modelling of the AWJ very complicated and hinders the development of better process understanding.
- The effect of the jet impingement upon the target surface, i.e. jet footprint/kerf, is dependent not only on the energy-dependent parameters (e.g. water pressure, abrasives mass flow rate) but also on the kinematic parameters (i.e. traverse speed). Hence above all, AWJ milling is a dwell time dependent process and this characteristic has a critical influence on the cut quality especially when the jet path changes direction (i.e. accelerates/decelerates), and starts and stops. Such events are quite frequent since for covering large surfaces, AWJ milling strategies

need to adopt raster jet paths. In this scenario it becomes obvious that it is difficult to control AWJ milling without specialist abrasion models that take into consideration dwell time as a process variable and then output the necessary information regarding the jet traverse speed to the CAM software to control the jet (tool) path.

- On-line control of the AWJ milling process parameters is still at an infancy level. This is again because of the lack of the jet plume – workpiece interaction models with which the sensorial systems can interact to control the process output i.e. the magnitude and the shape of abraded footprint.

Figure 1-2 summarizes the challenges of the AWJ process and emphasizes that one of the critical steps to overcome the challenges and enhancing the capabilities of the AWJ milling process is to develop suitable abrasion models for AWJ milling. These models can be used to provide the key inputs to the CAM softwares and process monitoring systems such as the inputs of the traverse speed required for achieving a specific depth of the cut to the CAM softwares and calculated jet energy to cross check the energy output of the sensorial systems. In addition, these models can also be used for further understanding of the process and thus resulting in better control of the process.

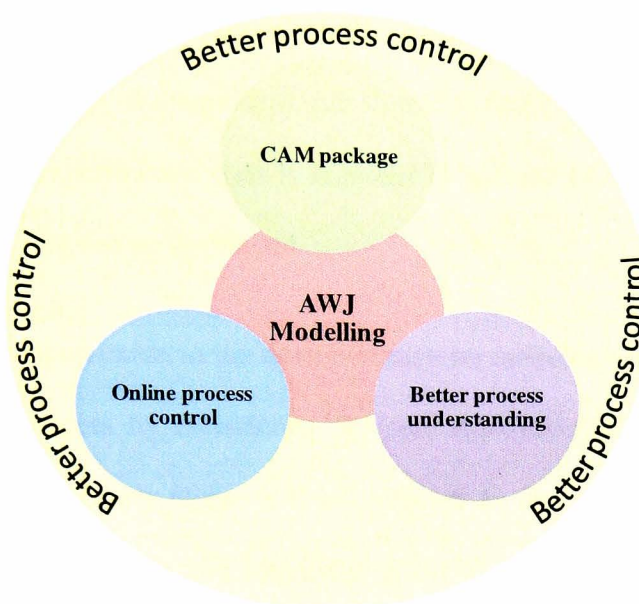


Figure 1-2: Significant of AWJ modelling for achieving a better process control.

The AWJ technology has enormous potential for machining difficult-to-cut materials as compared to other non-conventional processes but not enough research has been carried out regarding using this process for milling high value-added components. The current project aims to overcome the challenges mentioned above by developing suitable models that can reliably predict the complete (depth and profile) eroded footprints in the target at given process parameters. The prediction of footprints is necessary because various footprints overlap to generate the freeforms. The information generated from these models can then be fed into the CAM systems (machine controls) to control the shape/geometry of the milled surface. In order to bridge these gaps, the current study focuses on developing the models to accurately simulate the AWJ milled footprints. Two separate approaches will be used for devising these models in order to utilize the advantages of both techniques; one by exploiting the finite element (FE) method and the other by using a mathematical/analytical modelling approach. The benefit of analytical models is that they are fast and they can be used for real time predictions; however, experimentally

generated data is required to run these models. FE models, on the other hand, being based on the real physics of the process, run slower to make real time predictions, but once validated no experimental data is required to run the FE models and a better process understanding can be developed .

To date, no information exists in the open literature on modelling the controlled depth AWJ machining process by considering the real experimental conditions. For the analytical modelling, the jet plume will be modeled as free moving and for the FE modelling, a non-rigid target and impacting particles (abrasive particles) and non-spherical shapes of abrasive particles with Gaussian spatial distribution in the jet plume will be considered. Therefore, there is a need to develop and investigate these models to enhance the capability of AWJ technology to manufacture advanced engineering materials and to optimize the process parameters (e.g. traverse speeds, water pressure) and to explore/expand AWJ niche applications for its strategic developments. This research study not only benefits academic research but also results in industrial benefits.

1.3 Objectives of the Study

The overall aims of the study are to build up and validate the FE and analytical models for AWJ milling in order to enable an accurate prediction of the kerf profile (footprint), perform in-depth analysis of simulated footprints and enhance the overall understanding of the AWJ process to enable the generation of freeform surfaces on difficult-to-cut materials. Specific objectives of the study are as follows:

- Analysis and validation of a 3D FE model of a single particle impact with ultra high velocity from the real AWJ process. This is because of the fact that single

particle impact is the key task in the erosion process during AWJ milling and it is very difficult to study and understand it experimentally. The single particle model will provide an insight into the process at its basic level.

- Extension of the single particle FE model to multiple particles overlapping impacts i.e. towards simulating more realistic experimental conditions. Only few particles (up to 50) will be included at this stage to check the response of the target material during these impacts. This will help in understanding how particles of different shapes and sizes influence the erosion process during AWJ milling.
- Extension of the FE model to simulate the complete AWJ milled footprint. At this stage the model will incorporate the effects of mass flow rate of the abrasive particles and the dwell time, i.e. jet traverse speed across the target. The simulated footprint will be compared and validated against the corresponding experimental data. This will provide an opportunity for studying the footprint generation process in a controlled manner and will assist in enhancing the understanding of the process. This will also facilitate the prediction of jet footprints and erosion rates at any given milling parameters without the need for recalibration.
- Extension of the FE model to simulate the overlapping trenches which is a crucial step for understanding the development of the freeform surfaces which contain several such passes of the AWJ. The effect of various step-over distances and multiple passes on the generation of overlapping footprints will be studied at this stage.
- Development of a mathematical model to predict the jet footprints generated by a freemoving jet at any nozzle tilt angle. The proposed model will be generic in its

approach such that it can be readily applicable to other machining setups.

Chapter 2 Literature review

Due to the increasing use and high demand of AWJ technology in industry, significant research and development activities are underway to understand and further improve the existing AWJ technology. In this chapter, a comprehensive literature review is presented on the developments of this technology. A detailed description is first provided on how the AWJ system works. This is followed by a detailed discussion on the principles of material removal in AWJ machining and the influence of process parameters on process performance. Finally, a detailed review of existing FE and analytical modelling approaches for AWJ machining are presented. The present research gaps, upon which the current research work is based, will be summarized and concluded at the end.

2.1 Abrasive Waterjet machining Systems

Abrasive waterjet machining is a non-conventional machining method that can cut virtually any kind of material into two or three-dimensional shapes provided that the machine has the flexibility of positional movement. With abrasives added and proper process parameters selected, an abrasive waterjet machine can cut through metallic materials, exotic materials such as graphite, ceramic, composites and architectural materials including marble, granite, wood, rubber, etc. Based on the formation and the treatment of the abrasive particles, the AWJ systems are further categorized into two types; entrainment system and slurry jet system.

2.1.1 Entrainment system

The commercial market for AWJ systems is mainly dominated by entrainment type abrasive waterjet [41]. Figure 2-1 shows a schematic diagram of this machining system that includes various units such as a water preparation unit, a high pressure generation system, a cutting head and a catcher tank. The high pressure generating system is basically an intensifier that contains two fluid circuits, namely hydraulic circuit (oil circuit) and working fluid circuit (water circuit).

The hydraulic circuit includes an electric motor, hydraulic pump, oil reservoir and piston / plunger. The motor powers the pump to supply oil from the reservoir into the cylinder of an intensifier. The working fluid circuit consists of inlet water filters, intensifier and attenuator.

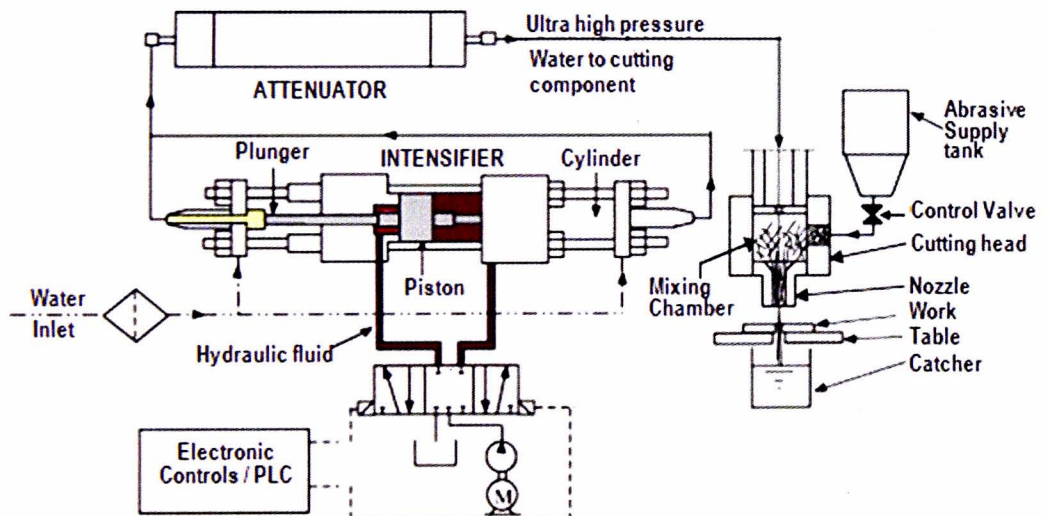


Figure 2-1: Schematic diagram of AWJ cutting system [42]

The intensifier is a reciprocating pump with plunger assembly reciprocating back and forth to deliver high pressure water out of the intensifier. The filtered water is pumped to the intensifier to intensify the pressure of water up to 400MPa. High pressure water

is delivered into an attenuator so as to avoid any pressure fluctuations caused due to the reciprocating action of the plunger in the intensifier.

The abrasive delivery system consists of an abrasive supply tank which stores the abrasive particles. An abrasive metering system equipped with a control valve which is used to generate user specified abrasive flow rate. The delivery pipe transports the abrasive particles under gravity from the metering valve to the abrasive inlet in the cutting head. Among the various types of abrasive materials such as garnet, silicon carbide, alumina and glass, garnet is the most widely used abrasive material for processing of different types of materials [43].

Both the high pressure water and the abrasives particles are fed into the cutting head where the entrainment of the particles takes place. The major components of the cutting head are orifice, mixing chamber and focusing nozzle. The high pressure water is converted into a high velocity waterjet after passing through the orifice, and while passing through the mixing chamber it evacuates the air inside this chamber and creates partial vacuum due to venturi effect or jet-pump action [44], [45]. The suction created in the mixing chamber also aids in the suction of abrasives into the mixing chamber along with the gravity action. The abrasive particles partly enter the waterjet and are accelerated by the jet gradually. The coherency of water jet is lost due to its spreading and mixing with air and abrasives. In order to generate a coherent AWJ, the partial mixture of abrasives and waterjet is directed through the focusing nozzle where the complete mixing takes place and the abrasives are accelerated to a high velocity resulting in the generation of a high energy abrasive waterjet. The abrasive waterjet is moved over the work material by maneuvering either the cutting head or the work table with CNC controls. The jet possessing energy exits through the work material.

Hence, the jet is directed into a catcher tank filled with water to absorb the remaining energy in the jet.

On the basis of the applications, the entrainment system can further be classified as follows:

- (a) AWJ Cutting
- (b) AWJ Milling
- (c) Plain waterjet (PWJ) processing

At the moment most of the usage of the AWJ machining lies in the area of cutting applications where the jet penetrates through the thickness of the material [24]. However, AWJ technology can also be employed for milling where the penetration of the jet in the target material is controlled and the jet does not pass through the thickness of the workpiece [46]. However, it is very difficult to perform AWJ milling due to the complexity of the process as the jet is not a geometrically stiff tool; therefore, the material removal becomes dependent on the dwell time and the local material geometry and response [47]. This is particularly true when compared with conventional milling where the final geometry of the workpiece can be decided on the basis of the tool path of the solid cutter. Table 2-1 presents some of the major differences between AWJ cutting and AWJ milling. There is still a lot of room for improvement in AWJ milling. Only few studies have been reported so far focusing on exploiting the AWJ milling process [25], [46], [48], [49], [50], [51], [52]. The focus of the current research will be on the modelling of the AWJ milling process. Figure 2-2 shows examples of some parts generated by AWJ cutting and AWJ milling.

Table 2-1: Differences between AWJ cutting and AWJ milling

AWJ Cutting	AWJ Milling
1 The depth of cut is not controlled. The jet passes through the workpiece thickness.	The depth of cut is controlled for every pass of the jet.
2 Lower traverse speeds of jet are employed.	Higher traverse speed of jet are used.
3 Higher abrasive mass flow rate are used.	Lower abrasive mass flow rates are used.
4 Higher water pressure is applied to increase the erosion rate.	Selection of water pressure depends on the target material being machined.

Sometimes the abrasive inlet is kept closed and no abrasive particles are added into the waterjet, to achieve a high energy plain waterjet (PWJ). Figure 2-3 schematically shows the difference between the PWJ and AWJ. PWJ is generally employed for cutting soft/light materials (e.g. plastics, paper, food) while AWJ is usually employed for cutting glass (e.g. stained/laminated glass), metallic sheets (e.g. Ti, Al, stainless steel) and advanced materials (e.g. composites, ceramics) [42].

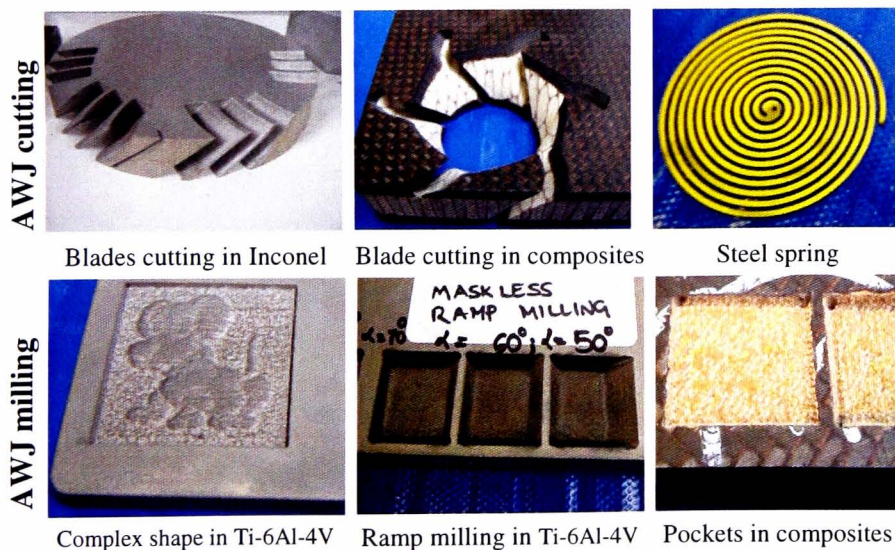


Figure 2-2: Example of AWJ cut and AWJ milled parts at University of Nottingham

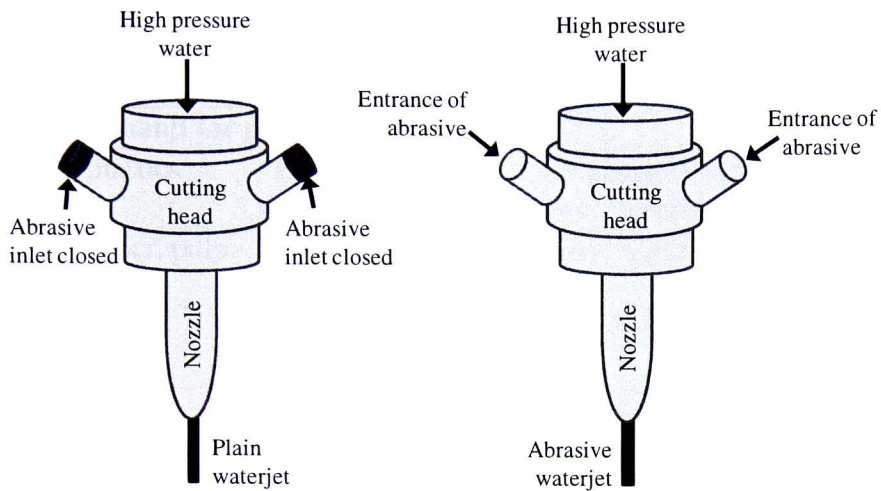


Figure 2-3: Illustration of difference between plain waterjet (PWJ) and abrasive waterjet (AWJ) machining.

In addition, sometimes PWJ is also employed for coating removal applications [53], [54], and to remove the embedded grit from the target surface following the AWJ machining [55]. More recently it has been used to mill pockets in gamma titanium aluminide superalloy by Kong et al., [29]. Table 2-2 highlights some of the areas where PWJ and AWJ technology are employed.

Table 2-2: Typical applications for PWJ and AWJ technology [42].

A. Fields of demand for plain waterjet (PWJ)	
1. Cutting of plastics	Engineering plastics moulding industry; parts industry for domestic use; film industry
2. Cutting of paper, pulp	Corrugated board industry; waste recovery; paper diaper industry
3. Cutting of fiber, fabrics	Fiber industry; sporting goods industry; apparel industry
4. Cutting of rubber, leather	Rubber industry; leather industry; synthetic leather processing; shoe industry
5. Cutting of food	Food industry; frozen food industry; confectionery manufacture
6. Cutting of timber, plywood	Forestry; housing industry; interior decoration industry
7. Others	Explosive industry (cutting of solid fuel); icebreaker (cutting floe)
B. Fields of demand for abrasive waterjet (AWJ)	
1. Cutting metallic sheet: titanium, aluminium, stainless steel, high tensile strength steel, super alloy	Aircraft industry; rolling stock industry; automobile industry; ship building industry; mechanical engineering industry; steel frame products; bridge manufacturing; ferrous industry; non-ferrous industry; manufacture of metallic products, etc.
2. Cutting of glass: wire glass, stained glass, laminated glass, etc.	Glass industry; housing industry; interior decoration; advertising; medical appliances manufacture
3. Cutting advanced materials: composite materials, ceramics, other (magnetic materials, etc.)	Aircraft industry; rolling stock industry; automobile industry; sporting goods industry; fine ceramic industry; ceramic industry; electronic parts industry; optical fiber industry
4. Cutting of building material: board, light weight concrete, etc.	Construction industry; housing industry; tile industry
5. Others	Atomic power industry (cutting of spent nuclear fuel pipe); manufacture and processing of graphite (various kinds of graphite)

2.1.2 Slurry jet system

In this system, abrasive particles are pre-mixed with water to form slurry that is then pumped and forced through a nozzle to form an abrasive slurry jet (ASJ). The main components of this system are shown in Figure 2-4. High pressure water from the

pump is stored in the accumulator (attenuator) for some time to stabilize the water pressure and then fed into the pressure tank which contains the pre-mixed slurry inside a rubber bladder. The bladder keeps the slurry isolated from the incoming pressurized water. The pressure tank is equipped with a shaker (vibrator) which ensures the uniform presence of the abrasive particles throughout the slurry. When the pressurized water squeezes the rubber bladder containing the pre-mixed slurry, a high energy ASJ is formed after passing through the nozzle.

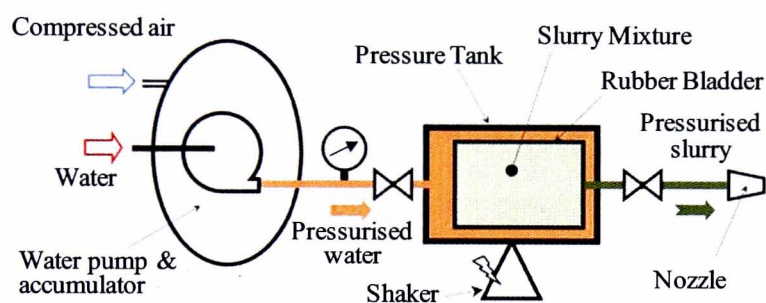


Figure 2-4: Schematic illustration of slurry jet system [41]

Since in the slurry jet systems, the particles are already mixed with the water, they achieve a higher velocity at the same water pressure compared to an entrainment system due to their better mixing with the water. More fluid energy is transferred to the particles and a higher energy density for the impacting particles is achieved. This results in generating higher material removal rates compared to those achieved by the jets produced by the entrainment system [56], [57].

ASJ systems only require a single feed connection to a cutting head, i.e. no separate grit supply is required, and they operate with reasonable effectiveness at water pressures that can be contained by flexible hoses. This has allowed portable slurry systems to be developed for on-site demolition and the cutting open of munitions in remote locations [58]. Rapid starting and stopping of cutting is not required in these

applications. ASJ has also been reported to be utilized for the coating removal applications [59]. The main disadvantage of the ASJ system is the severe wear in the pipes and nozzles; this limits the use of ASJ system for few applications only.

2.2 Material removal mechanisms during AWJ machining

Various studies have been reported to understand the physics of the AWJ machining process. Based on the reviewed literature, the material removal mechanisms in AWJ machining can be generally classified into two types. The first can be termed as micro-mechanism which describes the underlying phenomenon related to material removal by individual abrasive particles. The second type can be termed as macro-mechanism which refers to the kerf formation process. In this section, a brief explanation of these material removal mechanisms is provided.

2.2.1 Particles erosion mechanisms

In AWJ machining, abrasive particles impact the target surface at high velocity and the material removal takes place due to the micro-machining action of these particles. This means that the impact of a single solid abrasive particle is the basic event accountable for the material removal during AWJ machining. Therefore it is important to understand the effect of the single particle impact on the target before moving to the simultaneous multiple particles impact. Based on the target material properties, the micro erosion mechanisms can further be categorized into ductile and brittle erosion mechanisms.

2.2.1.1 Ductile material erosion mechanism

With regards to material erosion by micro particles impact, pioneering research was

conducted by Finnie [60]. Figure 2-5 gives the geometrical and kinematic parameters for Finnie's model. He derived the equations that calculate the volume removed (V_M) in the material in relation with the kinetic energy of the impacting particle and the flow stress generated in the material. V_M is defined as the volume swept out by the tip of the particle as a result of the plastic deformation. The mathematical equations for the volume removed by a single particle for shallow (Eq. 2.1) and large angle (Eq. 2.2) of attacks are as follows:

$$V_M = \frac{m_p v^2}{\Psi \sigma_f k} \left(\sin 2\alpha - \frac{6}{k} \sin^2 \alpha \right) \quad \tan \alpha \leq k/6 \quad \text{Eq. 2.1}$$

$$V_M = \frac{m_p v^2}{\Psi \sigma_f k} \left(\frac{k \cos^2 \alpha}{6} \right) \quad \tan \alpha \geq k/6 \quad \text{Eq. 2.2}$$

where m_p is particle mass, v is particle velocity, α is attack angle (as shown in Figure 2-5), σ_f is target material flow stress, k is the ratio of vertical to horizontal force, and Ψ is the ratio of the depth of contact " L " to the depth of the cut Z_t . However, Finnie's model exhibits a large divergence from the experimentally generated data especially at higher impact angles due to the simplicity of the model. Later, this model was refined [61] by making more realistic assumptions about the interaction forces between the particle and material surface.

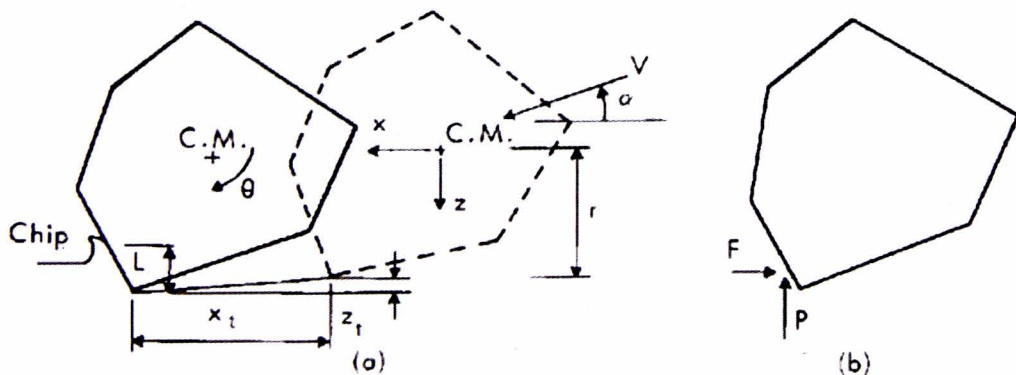


Figure 2-5: (a) Impact of a sharp micro particle on a ductile surface at an angle of attack α and velocity v . (b) Contact forces acting on the particle during cutting[60].

Bitter [62], [63] presented material removal models based on the energies involved in the erosion process and divided the entire process into two modes; (i) cutting wear that happens at low impact angles and (ii) deformation wear that occurs at high impact angles. Deformation wear is in fact related to the component of particle velocity in the direction perpendicular to the material surface, while the component of particle velocity in the direction parallel to the material surface is accountable for cutting wear. Bitter introduced the concept of threshold velocity i.e. a particle cannot erode the workpiece if its velocity is less than a critical velocity V_{cr} . Bitter derived separate expressions for volumes removed by deformation wear, (V_D) (Eq. 2.3) and cutting wear, (V_C) (Eq. 2.4) mechanisms and the total volume removed at any time is the sum of both volumes ($V_D + V_C$).

$$V_D = \begin{cases} \frac{m_p (v \sin \alpha - V_{cr})^2}{2\varepsilon_d}, & v \sin \alpha > V_{cr} \\ 0, & v \sin \alpha < V_{cr} \end{cases} \quad \text{Eq. 2.3}$$

$$V_C = \begin{cases} \frac{2m_p C (v \sin \alpha - V_{cr})^2}{\sqrt{v \sin \alpha}} \times \left(v \cos \alpha - \frac{C (v \sin \alpha - V_{cr})^2}{\sqrt{v \sin \alpha}} \times \varepsilon_c \right), & \alpha \leq \alpha_o \\ \frac{m_p \left(v^2 \cos^2 \alpha - K (v \sin \alpha - V_{cr})^{\frac{3}{2}} \right)}{2\varepsilon_c}, & \alpha \geq \alpha_o \end{cases} \quad \text{Eq. 2.4}$$

where m_p is the mass of the abrasive particle, v is the particle velocity, α is the attack angle, α_o is the impact angle at which the horizontal velocity component has just become

zero when the particle leaves the target, V_{cr} is the critical particle velocity, ϵ_d and ϵ_c are the deformation wear factor and the cutting wear factor respectively determined experimentally, and C and K are an empirical parameter. The disadvantage of this model is that it relies on experimentally determined parameters for a complete application.

Later, Hutchings [64] introduced an alternative discussion based on high speed photographs and SEM observations. He defined two modes of material removal due to micro cutting; (i) cutting deformation and (ii) ploughing deformation and related them to impact angle, shape and rotation of the abrasive particles (see Figure 2-6). He found out that the ploughing deformation mode is prevailing for spherical particles while the cutting deformation is dominant for sharp edged angular particles.

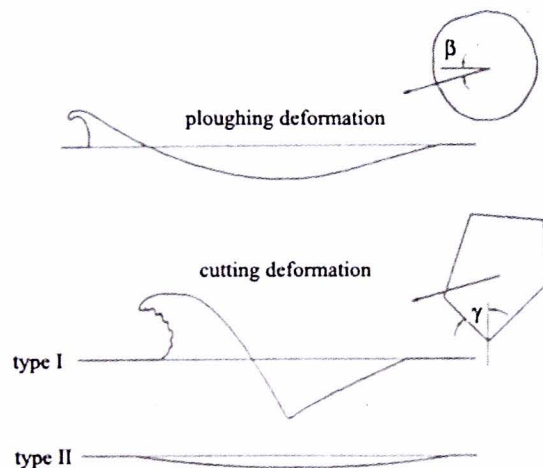


Figure 2-6: Cutting and ploughing by solid particles at oblique impact angles [64]

Hutchings [64] further sub-divided the cutting deformation into Type-I and Type-II cutting deformations based on the direction of the particles rotation. For forward rotating particles, Type-I is dominant whereas Type-II is applicable for backward rotating particles, as shown in Figure 2-6. Hutchings and Winter [65] also classified

the impact of the particles according to the particles rake angles i.e. the angle between the leading face of the particle and the normal to the target surface as shown in Figure 2-7(a). At rake angles greater than a material dependent critical rake angle, deformation is dominated by the cutting mode i.e. the target material will flow along the particle inclined face and a piled up lip is formed above the surface (Figure 2-7(b)). Alternatively, if the rake angle is more negative than this critical angle, the ploughing deformation dominates, and the particle slides over the surface of the target causing shear in it along the direction of the travel. In this case, lip formation occurs both on the sides and front (towards the direction of impact) of the formed crater (Figure 2-7(c)).

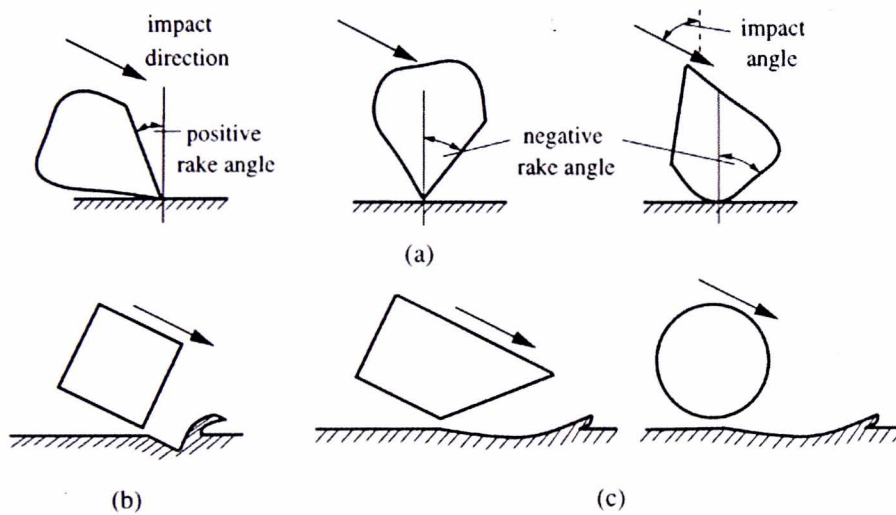


Figure 2-7: Effect of particle rake angle on target deformation [65]

Several researchers [29, 30] have observed the SEM images of AWJ machined ductile materials and detected the separated wear tracks generated by single abrasive grains.

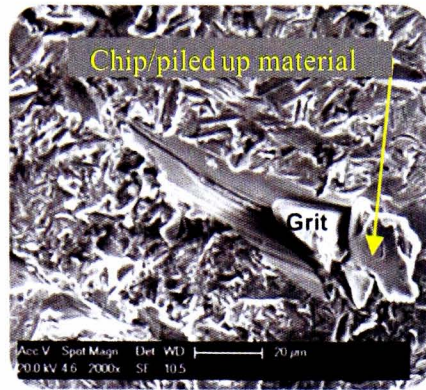


Figure 2-8: Type-I cutting observed in AWJ milling.

The eroded tracks fall under the categories of Type-I and Type-II cutting. The widths of these tracks/paths vary due to the particle size distribution of the abrasives used. Figure 2-8 shows an example of Type-1 cut observed during AWJ milling of a shape memory alloy observed in a SEM.

2.2.1.2 Brittle material erosion mechanism

A number of studies have been reported on the failure of brittle materials, and most of them agree that the erosion in these materials occurs by a cracking process [68], [69], [70], [71]. Zeng and Kim [72] classified the erosion mechanisms for brittle materials found in the literature into six categories; (1) conical, radial and lateral crack systems; (2) intergranular cracking; (3) ring fracture; (4) micro-chipping; (5) plastic deformation and melting; and (6) mixed damage. They claimed that among these mechanisms, the conical, radial and lateral crack systems are the most commonly observed impact damage mechanisms in brittle materials. Plastic deformation has also been observed during the impact of angular and spherical particles on brittle materials and contributes to the process of crack formation and surface chipping [73]. Figure 2-9(a) shows the general appearance of failure in brittle materials where a central

plastic impression zone is surrounded by a combination of median, radial and lateral cracks. Figure 2-9(b) shows how small cracks interact to form a network which grows further as the stress waves propagate through the material and eventually erosion fragments are created [71].

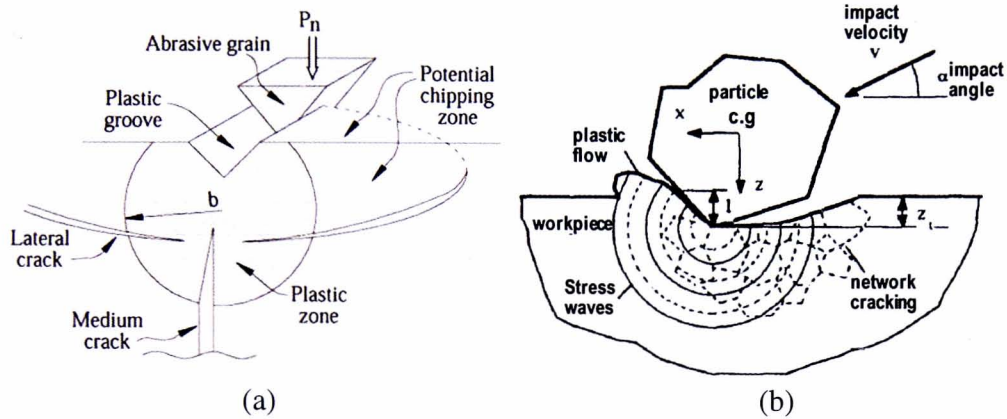


Figure 2-9: Failure modes in brittle materials; (b) scratching and network cracking [72] (a) schematic view of radial, median and lateral cracks induced by a sliding micro indenter [74].

In the case of single/multiple particles impact situations such as in AWJ machining, the suggested major cause of material removal in brittle materials is the lateral crack mechanism [70].

2.2.2 Kerf generation process

In early investigations, Hashish [75], [76] commented that the surface of the cutting front generated by the jet has two distinct zones – the upper smooth zone which is at the entry of the jet flow and the lower striation zone which is at the exit of the jet flow as shown in Figure 2-10(a). The material at the upper smooth zone is actively removed by the cutting wear mechanism due to the shallow impact angle of the abrasive particles while that at the lower part striation zone is dominantly removed by

the deformation wear mechanism due to the high impact angle. This is schematically expressed in Figure 2-10(b) and it is also in accordance with the Bitter's theory [62], [63]. Along the depth of cut, the jet loses energy owing to the jet-material interaction and mutual particle impacts [77]. This is the reason that the surface quality of the upper region is always better than that of the lower region. The degree of striation can be controlled by a reduction of the jet traverse speed across the target but it would cause a change in the cutting width and kerf taper angle.

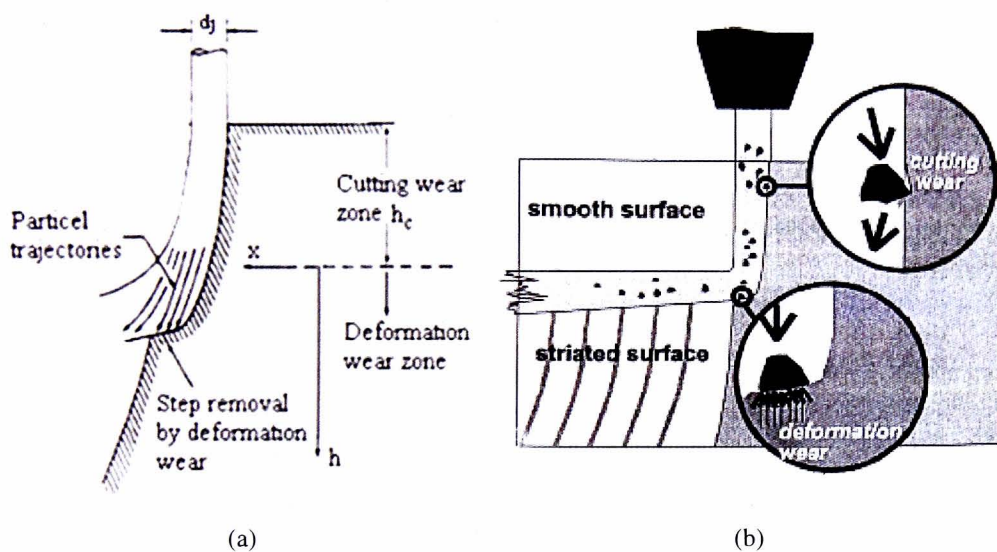


Figure 2-10: Visualization of kerf generation process; (a) representation of different regimes of material removal [78], (b) schematic zoomed-in view of individual particles impact during kerf generation [76].

Arola and Ramulu [32] presented an alternative three zone model for the kerf generation based on an experimental study of a Graphite/Epoxy composite. The surface being cut is divided to three zones along the jet penetration direction; an initial damage region (IDR) at the jet entrance, a smooth cutting region (SCR), and a rough cutting region (RCR) near the jet exit. A SEM photograph of these three regions on an AWJ machined Ti-6Al-4V alloy is shown Figure 2-11.

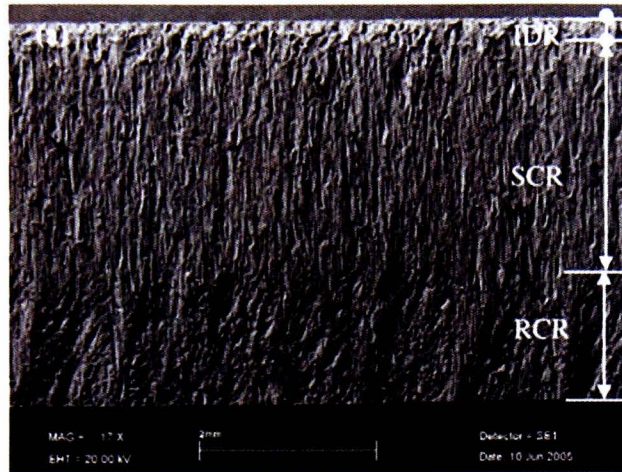


Figure 2-11: Typical AWJ-machined kerf cutting front wall.

The IDR is generated at the top of the kerf as a result of the impact of the abrasive particles at much higher attack angles and higher energy compared to the remaining of the cutting depth [79]. The cutting mechanism of material removal is a plastic deformation due to the almost perpendicular impacting particles [80]. It was pointed out that the depth and width of the IDR mainly depend on the standoff distance [32]. The surface waviness patterns differentiate between the SCR and RCR. SCR is characterized by very low waviness, minimal surface roughness and limited damage phenomena. Jet pressure, particle size and traverse speed are the dominant parameters that affect the depth of SCR. The beginning of the waviness patterns often termed as striation marks indicates the start of the RCR on the kerf surface. As the jet penetrates into the surface, the length of the path of the single abrasive particles in the workpiece decreases and the randomness of the path orientation of particles increases [68]. This is due to the fact that when the jet moves across the workpiece, the kinetic energy of the particles decreases as the depth of the cut increases. As a result, the RCR with high waviness and striation marks is generated and the exit point of the jet plume lags behind the entrance point and the top kerf width is more than the bottom

kerf width [81]. This lag affects the level of contour accuracy and causes waviness (striations) on the cutting front wall. A typical kerf geometry is schematically expressed in Figure 2-12. Usually, a large scale of waviness can be observed when cutting with low pressures, small particles and high traverse speeds [82].

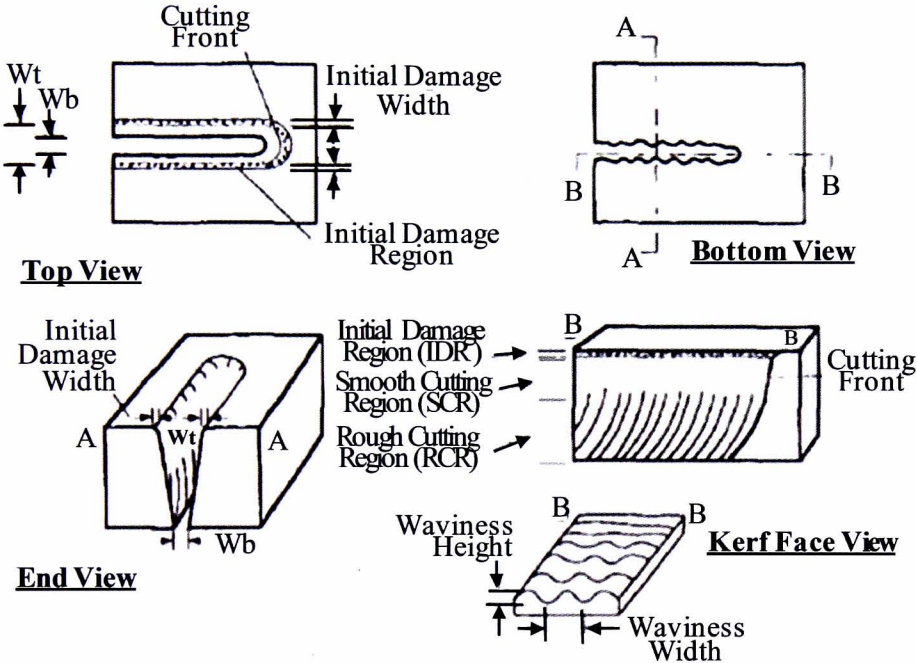


Figure 2-12: Illustration of a kerf geometry cut by AWJ [32].

In AWJ milling, material is always removed with smaller depth of the cuts in order to control the geometry of the workpiece, and the cutting front is expected to remain within IDR to SCR.

Besides the abrasive particles, the water droplets have also been reported to assist the erosion during AWJ machining at certain process parameters, primarily at very low traverse speeds where the target exposure time to jet is very high. The high Reynolds numbers reported by Wu and Kim [83] at the nozzle exit indicated the occurrence of jet turbulence and the total atomization of the jet into water droplets. When these

water droplets continuously hit the surface, they produce plastic deformation and cracks in the workpiece surface as shown in Figure 2-13 [29].

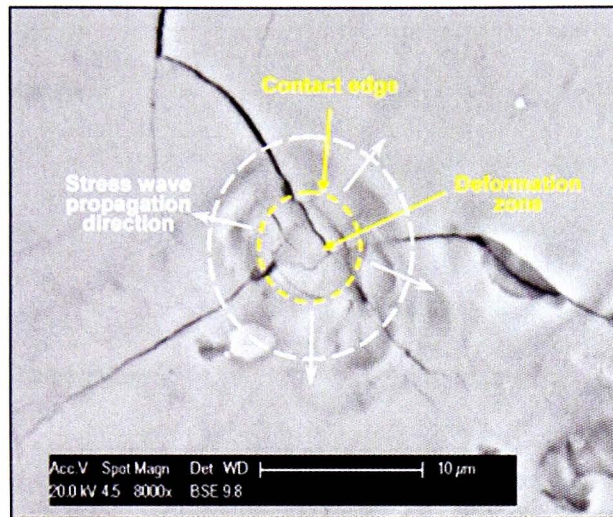


Figure 2-13: Deformation and crack produced in γ -TiAl by PWJ impact [29]

Moreover, when the water droplets enter into the cracks and pits generated by abrasive particles impacts, high stresses are exerted on the crack walls. When the intensity of these stresses exceeds the material fracture toughness, the crack grows. Subsequently the intersection of several such cracks leads to microscopic material removal [84], [85], [86]. However the capability of the water to erode the target material is far less than the abrasive particles. Furthermore, at the milling parameters i.e. at high traverse speeds used in the current study, water will not be able to erode the target material.

2.3 Influence of process parameters on process performance

In order to build models for AWJ milling, the effects of process parameters on the target surface need to be understood. Many studies have been reported to explore the influence of process parameters on the output parameters such as depth of cut, surface

roughness and waviness, material erosion rate, and kerf width and taper. According to Momber and Kovacevic [12], the process parameters affecting the AWJ performance include the following:

- | | |
|--|--|
| <p>1 <i>Hydraulic parameters</i></p> <p>Water pressure</p> <p>Orifice diameter</p> | <p>4 <i>Abrasive parameters</i></p> <p>Abrasive mass flow rate</p> <p>Abrasive particle size distribution</p> <p>Abrasive particles shape</p> <p>Abrasive particle hardness</p> |
| <p>2 <i>Mixing and acceleration parameters</i></p> <p>Focusing Nozzle diameter</p> <p>Nozzle length</p> | <p>5 <i>Target material properties</i></p> <p>Flow strength</p> <p>Elastics Modulus</p> <p>Hardness</p> |
| <p>3 <i>Cutting parameters</i></p> <p>Traverse speed</p> <p>Stand-off distance</p> <p>Impact angle</p> | |

Although the AWJ process is influenced by several process parameters as listed above, a detailed discussion on some the crucial parameters is given below.

2.3.1 Water pressure (P)

Several research studies show that the depth of cut generally increases linearly with an increase in the water pressure for a certain range [87], [88], [89]. It has been reported that there exists a critical pressure below which no material removal takes place, and this critical pressure depends only on the material properties [89], [90]. Kovacevic [91] claimed that increasing the water pressure is one of the most effective

ways of increasing the cutting ability of the jet. It is known from Bernoulli's equation (see Eq. 2.5) that increasing the water pressure will result in an increase in the velocity of the waterjet (V_w) passing through the orifice. This in turn increases the velocity of the abrasive particles when they are mixed with the waterjet in the mixing chamber, i.e. higher water pressure results in higher energy particles to generate a deeper cut.

$$V_w = \sqrt{(2P/\rho)} \quad \text{Eq. 2.5}$$

An approximately linear relationship between the depth of cut and water pressure exists until a certain water pressure value is reached [92]. This is because of the increased fragmentation of the particles as the water pressure increases. The consequent decrease in the size of the abrasive particles and increased particles collisions adversely affect the particles acceleration process, and hence reducing the depth of the cut in the target. During AWJ milling, the water pressure needs to be selected in combination with other factors such as abrasive mass flow rate, traverse speed of the jet, etc.

2.3.2 Abrasive particles size and shape

The particle size is directly related to the material removal rate and depth of cut. The larger the size of the particle, the more the depth of cut and erosion rate will be, and this effect is more pronounced at lower traverse speeds [25], [93]. This is attributed to the fact that bigger particles have more inertia and at lower traverse speed they will have more time to interact and erode the surface. However, it should be noted that for a given focusing nozzle size, the larger the abrasive particles size, the smaller the number of particles that will pass in a given time, hence reducing the particles impact

density/frequency which will result in reducing the depth of cut and increased surface roughness and waviness [50], [93]. Moreover, with an increase in abrasive particles size, the particles acceleration process becomes less efficient for the same length of focusing nozzle, resulting in reduced kinetic energy of the abrasive particles [94]. Therefore, a balance between the abrasive particles kinetic energy and the impact frequency is required [12]. The shape of the abrasive particle also has a significant influence on the erosion rate. The sharp edged angular particles (e.g. garnet) produces higher erosion rate in ductile materials (e.g. Ti-6Al-4V), as compared to rounded and spherical particles for the same velocity of impact [95]. This is due to the fact that sharp edge particles make point contacts with the target surface upon impact which results in generating much higher stresses as compared to the impact by rounded particles. Also, sharp particles support the micro cutting material removal mechanism in ductile materials which results in higher erosion rates as compared to ploughing mechanism from spherical particles, as discussed in refs. [64], [96] and [97].

In the current study, an angular shape abrasive garnet mesh 80 (average particle size 0.18mm) will be used based on the fact that it has been reported to give high material removal rate in most ductile materials with relatively less wear in the focusing nozzle [31], [98].

2.3.3 Abrasive mass flow rate (\dot{m}_a)

It has been reported that the depth of the cut and material removal rate increase significantly by increasing the abrasive flow rate, and at the same time and enhanced surface finish is obtained [50]. This is attributed to the fact that increasing the abrasive mass flow rate increases the number of particles striking the target per unit area. However, this is only true up to a critical mass flow rate of abrasives at a given

water pressure because increasing the abrasive mass flow rate further will increase the particles collision and turbulence in the AWJ, thus leading to a lower material removal rate [99], [100], [101]. Furthermore, limited kinetic energy from the water will be available to accelerate more particles, leading to a decrease in the kinetic energy acquired by single particles [12]. This is the reason why the cutting performance, e.g. material removal rate or depth of cut, does not increase linearly with the abrasive mass flow rate.

In the current study, since AWJ milling is under focus, a low abrasive mass flow rate will be used in order to achieve a smaller depth of cut. A low depth of cut can also be achieved by using a higher traverse speed of the jet, but it will result in surface irregularities. Therefore, a suitable combination of both will be selected.

2.3.4 Nozzle and orifice diameter

The material removal rate is found to increase with an increase in water pressure for different combinations of orifices and focusing nozzles. This trend was found to be predominant with smaller orifice diameters (0.25 mm and 0.30 mm) and less prominent with larger orifices (0.40 mm) due to the reduction of jet velocity with an increase in the orifice diameter [20], [102]. Slight variations in the orifice diameter reduce the depth of cut drastically at higher water pressures due to reduction in the velocity of the jet [101], [103]. For a given orifice size and water pressure, the depth of cut and material removal rate are increased up to a certain value of the focusing nozzle diameter and then decrease with further increase in the nozzle diameter; this is more prominent at higher water pressures (see Figure 2-14) [20].

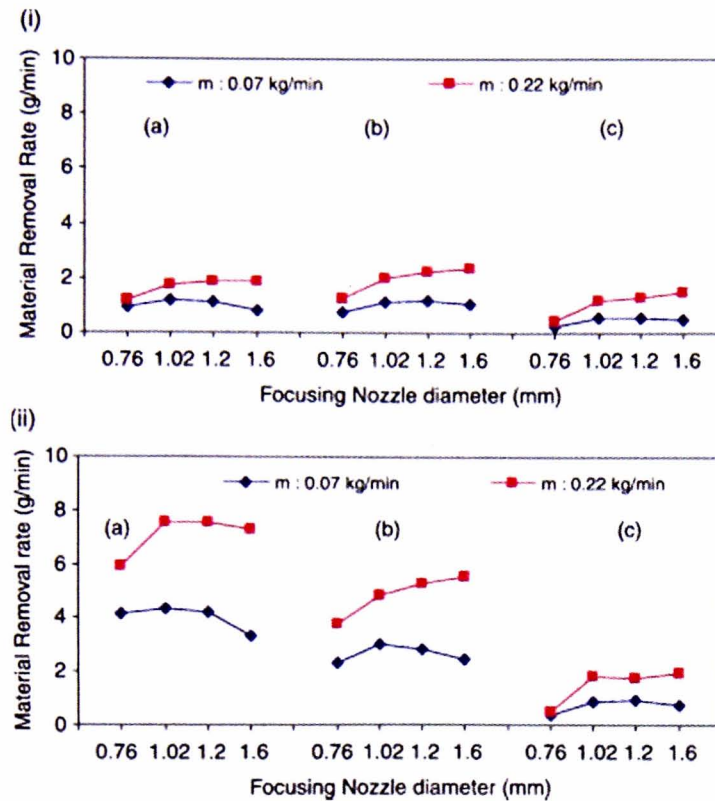


Figure 2-14: Variation of material removal rate with different sizes of orifice ((a) 0.25 mm; (b) 0.30 mm; and (c) 0.40 mm) and focusing nozzle at different waterjet pressure and abrasive flow rate (i) $P=100$ MPa and (ii) $P=250$ MPa [20]

It is due to the fact that focusing nozzle size influences the jet coherence thus affecting the hydraulic power density on the work material [102]. A certain optimum size of the focusing nozzle is required to maximize the velocity of the abrasive particles during the mixing and momentum transfer process with water along the length of the nozzle. However, a smaller nozzle diameter will produce more collision (abrasive fragmentation) and friction that will cause an ineffective mixing and acceleration process [12]. The ratio of the focusing nozzle diameter to the orifice diameter of 3 to 4.5, results in maximum material removal rate [20].

In the current study, the diameters of the orifice and the nozzle will be kept at 0.28mm

and 1.02mm respectively i.e. maintaining a ratio of 3.6 throughout this study. It has also been reported that the focusing nozzle undergoes wear during AWJ machining due to the high flow of water and abrasive through it [31]. This means that the depth of cut will be affected during the course of the process due to nozzle wear especially for jobs with longer machining time. However, this factor will not affect the experiments in the current study because of their shorter duration.

2.3.5 Effect of the jet traverse speed (V_f)

Traverse speed (V_f) is the traveling speed of the jet above the target. Traverse speed is one of the most crucial process variables that controls the exposure time of the target material to the AWJ plume. The exposure time is the period over which the cross sectional area of the jet acts on the workpiece. For a given water pressure and abrasive mass flow rate, the depth of cut and material removal rate decrease by increasing the traverse rate of the jet. This is due to the fact that the number of the particles impacting on the target per unit area reduces by increasing the traverse speed, yielding a reduction in the kinetic energy transferred to the workpiece [12]. Traverse speed also influences the quality of the milled surface by affecting the surface roughness and waviness [17]. At higher jet traverse speeds, a kerf with a high surface roughness is generated due to less overlapping impacts of the abrasive particles. Surface waviness increases with decrease in traverse rate due to the reason that a higher depth of cut is generated at lower traverse speed and the jet is channeled along the already cut slot which produces directional morphology and increased surface waviness. In the case of high traverse speed, since the depth of cut is much smaller, the jet channeling is not produced, as explained in Figure 2-15 [93].

During AWJ milling, high traverse speeds are employed to obtain shallow depth of

cuts, in order to control the geometry of the workpiece [25], [46], [90], [95]. However, no general value can be given because of the fact that different penetration depths could be reached in different materials for the same traverse speed.

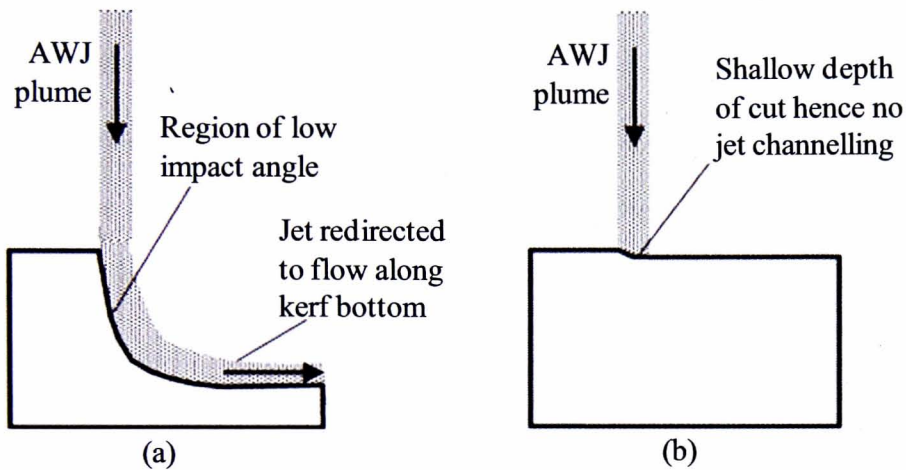


Figure 2-15: Schematic representation of flow pattern in AWJ milling at 90° incidence (a) Jet channelling at low traverse rate (b) No jet channelling at high traverse speed [93].

2.3.6 Effect of stand-off distance (SOD)

The SOD is the normal distance between the workpiece and the nozzle exit. It has been reported that the velocity of the abrasive particles is not significantly influenced by changing the SOD [104]. This means that the energy of the jet remains almost unchanged by changing the SOD. The variation in the depth and width of the eroded footprint by changing the SOD is attributable to the widening and divergence in the diameter of the AWJ plume and subsequent change in the exposed area on the target. When the SOD is increased, the width of the jet footprint increases while the depth of cut decreases because the density of the energy transmitted to the target surface decreases [18], [48], [105]. This process of jet widening and resulting lower impact

density of the particles is shown in Figure 2-16. It should be noted that when the divergence in AWJ plume increases, more loose abrasive particles are present at the boundary of the jet which will result in difficulty in controlling the width of the cut. This is undesirable for AWJ milling applications where controlling the geometry of the workpiece is of primary importance. It has been reported that varying the SOD between 2 mm to 5 mm does have a significant effect on the process outcomes and the width of the cut also remains under control [106]. The standoff distance used in the current study is 3 mm for all the tests.

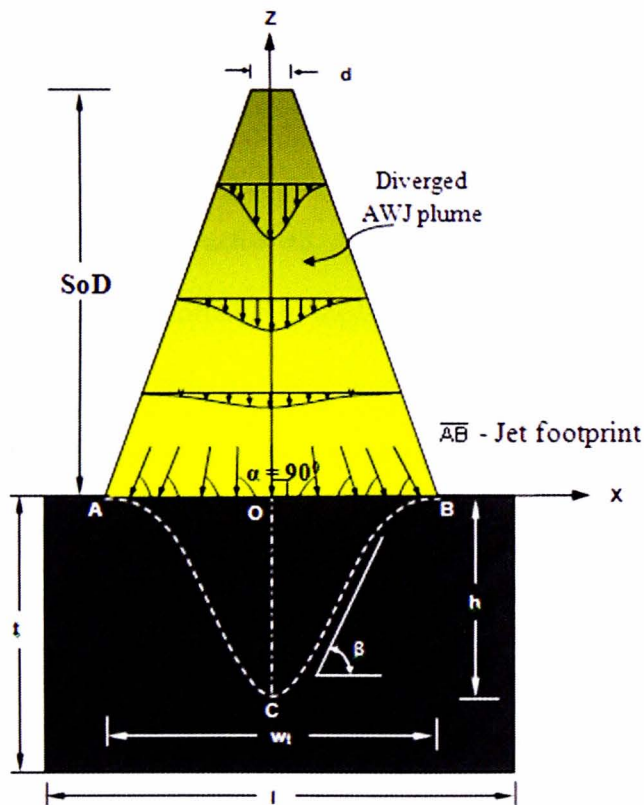


Figure 2-16: Increasing jet divergence with stand-off distance [18].

It can be seen from the above discussion that AWJ milling is quite complex in view of several process parameters, such as hydraulic, abrasive, mixing and cutting parameters, influencing the performance of the process. Therefore, the development of appropriate models for studying the effects of the desired variables on the process

outcomes is important.

2.4 Modelling of AWJ

Unlike conventional machining where a hard cutting tool is used, a soft tool, i.e. an abrasive waterjet plume, is employed in the AWJ machining, whose ability to machine depends on various process parameters (e.g. water pressure and mass flow of the abrasives) [12]. A unique kerf (footprint) is generated when the jet plume impacts the target surface that not only depends on the jet plume energy but also on the kinematic parameters (e.g. jet traverse speed and tilt angle) and the properties of the target material (e.g. hardness) [18], [50]. The profile of a single jet footprint represents the actual cutting edge of the jet plume at any given process parameters. As the required geometry can be achieved by successive positioning of this profile (footprint), it is of crucial importance to model the cross sectional profile (footprint) against the target workpiece material. This is of critical importance when employing AWJ milling for the generation of complex geometry surfaces [107]. To address this requirement, various modelling approaches of the jet footprint have been considered. Models of jet footprint/particles impact have been developed by using both the finite element (FE) and analytical techniques. In the following sections, reviews of the state of the art of FE and analytical modelling of AWJ footprints are presented.

2.4.1 Finite element (FE) modelling

Finite element modelling has been successfully applied in numerous fields. FE models allow studying the physical process in a more controlled manner and the effects of desired variables (e.g. particles size, shape, impact velocity) on the erosion can be determined. Since in AWJ milling, the material removal is mainly caused by the

impact of a multitude of abrasive particles at ultra-high velocities, the FE models reported for the erosion from single/multiple particles impact are also reviewed.

Shimizu et al. [108], [109] studied the erosion of structural mild steel (SS400) and ferritic spherical-graphite cast iron (FDI) due to the blasting of steel shot both experimentally and through FE simulation. A 2D formulation was used in the FE model with no failure criterion defined and the dynamics inertial forces and friction were neglected. The experimental craters that were generated by impact of spherical steel shots were generated in the FE simulation by assigning displacement forces on static particles. This approach leads to increased deviations between the experimental and simulation conditions in which the indentation is produced.

Takaffoli and Papini [110] presented a rhombic shape rigid single particle erosion model in oxygen-free high-conductivity copper (OHFC C10100). For plasticity, the Johnson and Cook [111] material model was used, and to simulate the failure in the target material a failure plastic strain was defined. However, they simplified the erosion problem by using a 2D configuration in the FE model. This results in neglecting the effect of the third component of strain on the strain hardening and fracture strain and also the multi-particles' erosion effect is difficult to model by this approach.

Eltobgy et al. [112] developed a 3D FE model of erosion for multiple rigid spherical particles impact at a single location and incorporated Johnson-Cook (JC) plasticity [111] and JC failure [113] criteria to simulate material removal during the erosion process. The results for the erosion rate were compared only with previously existing analytical models and no comparisons were made against experimental results. Comparing the results with the analytical models can have some drawbacks because

analytical models have their own limitations as well.

Griffin et al. [114] built a 3D FE model of five rigid particle impact on an alumina scale formed on MA956 substrate; a tensile failure criterion was used for simulating the failure of brittle alumina coating. When the pressure stress reaches the tensile strength of the alumina material, the corresponding elements were removed from the model.

Wang and Yang [115] developed FE erosion models for both ductile and brittle materials by using multiple (100) rigid particles impact in groups of 10, each group impacting at the target center area at random locations. JC plasticity and failure criteria were employed along with Gruneisen equation of state for modelling ductile material response during high velocity impact.

Some FE models of single/multiple particles workpiece interaction during AWJ machining have been reported (discussed below). However, up to now, no evidence exists in open literature regarding capturing the profile of a single particle impact during AWJ machining for validating the FE models, and also no attempt has been recorded for FE modelling of the AWJ milling process.

Hassan and Kosmol [116] presented a dynamic elastic-plastic FE analysis of an abrasive particle impact during AWJ machining with garnet for analyzing the particle and the workpiece interaction during the impact. The experimental data used for validating the FE results were the depths of the craters which were extracted from the AWJ machined surface by scanning them with a stylus. However, this approach could be quite misleading due to the fact that during AWJ machining several particles make overlapping impacts on the target surface. It is difficult to tell whether the extracted

depth is a result of a single or multiple particles impacts. This effect will become more pronounced at lower jet traverse speed and higher mass flow rates, which were not discussed by the authors. Furthermore, the velocity of the impacting particle used in the FE model for simulating the effect of the pressure during AWJ machining was not revealed.

Another single rigid spherical particle impact model on alumina ceramic during AWJ machining was reported by Gudimetla and Yarlagadda [117]. This model uses the fixed mass scaling technique for reducing the computational time by assigning fixed masses to more deformed or distorted elements. However, in the case of highly dynamic impact events, it is recommended not to use mass scaling to avoid changes in the natural inertia of the system [118].

Junkar et al. [119] also developed a FE model of a single rigid particle impact in AWJ machining to study the influences of the particle impact angle and velocity. For validating the FE model, the study focuses only on the top view (sphericity) of the craters i.e. the roundness of the simulated craters was compared to the corresponding experimental ones. However, the top view alone is not sufficient to validate the FE simulation results because it does not provide enough information about the depth of the crater produced which is a very important parameter in controlled-depth AWJ cutting (i.e. milling) to supply crucial information for understanding the effect of the particle impact upon the target surface. Furthermore, the theoretically estimated velocities (180m/s-220m/s) of the impacting particles used in the FE model [119] are quite low when compared to the reported experimental values (400m/s-700m/s) in the literature [120], [121], [122]. This will result in differences in the kinetic energy of the impacting particles between the FE model and experimental results.

Maniadaki et al. [123] and Kumar et al. [124] extended the work of Junkar et al [119] from a single particle impact model to 20 particles impact. Once again, all the particles were considered rigid with spherical shapes and the impacting velocities were in the range 180m/s-220m/s. Conclusions were drawn based on the fact that all the impacting particles of same size impinged the target surface on the same spot. However, this does not match the real-life AWJ conditions where the impacting particles have different sizes and they are impacted on random locations on the target. Moreover, no comparisons were made with the experimental data apart from the crater sphericity results adopted from Junkar et al. [119]. Only one size (100 μm) was assigned to the particles, whereas in reality garnet particles consist of a size distribution.

One of the common shortcomings in most of the FE models [108], [110], [112], [114], [115], [117], [119], [123], [124] discussed above is that they have used a rigid particle approach for modelling the impacting particles. However, in real-life impact, a significant amount of energy is absorbed by the impacting particles through their own deformation and fracture even at lower impacting velocities, as demonstrated by [125], [126]. It is therefore not accurate to use a rigid particle approach at ultra-high velocity impact, because the particles in the model will transfer significantly more energy to the target than in reality, resulting in over-erosion of the target.

In relation to the approaches in which the FE models are validated [117], [119], [123], [124] using real abrasive particles (e.g. garnet) during experiments, it has been demonstrated [16] that significant abrasive particles fragmentation takes place during their entrainment in the cutting head. This phenomenon is more prominent in the case of abrasives (of a ceramic nature, e.g. garnet) which display brittle behaviour and are

irregularly shaped. When such abrasives (garnet) particles strike the surface of the workpiece during AWJ machining, it is not possible to tell (while performing surface examinations) which crater is produced by which size (fragmented) particle. Consequently, it will become difficult to correctly select indentation marks (i.e. craters) of the impacting particles to enable the validation of the FE model. The size of the impacting spherical particle use in FE models [117] was assumed to be the average particle size (180 μm) of the fresh garnet abrasive (mesh 80) used during the experiments. However, it is also reported that the average particle size for garnet (mesh 80) is reduced by 35% after passing through the nozzle [16]. This difference in size will have a huge influence (2 to 3 times) on the mass and hence the kinetic energy of the impacting particles, given that during high velocity impact, the deformations of the projectile and the target are dominated by inertia [127].

In previous studies [117], [119], garnet particles (mesh no. 80, average particle size 180 μm) have been used during the experimentations, which are known to have irregular shapes and sharp cutting edges while the shape of the particles used in the FE models was spherical. This difference significantly increases the deviation between the experimental and simulation conditions of impact. For example, the deformation mechanism will change from cutting (experimental) from sharp particle impact to ploughing (simulation) from spherical particle impact as explained by Hutchings [64], i.e. important tearing phenomena will be suppressed. Furthermore, it has been explained in ref. [128] that there is a difference of more than 2 times in the erosion rate or the depth of cut for a single particle impact from a sharp particle and a spherical particle at same velocity of impact. All these factors magnify the differences between the experimental and simulated conditions of impact and adversely affect the accuracy of the FE models.

Apart from single/multiple particles impact models of AWJ, some efforts have been recorded for modelling the complete AWJ machining process. Wenjun et al. [129] presented a FE model for AWJ penetration in the workpiece by modelling abrasive particles and water as a pre-defined mixture in an Eulerian FE mesh, i.e. each element in the mesh is assigned two materials (water and abrasives). However, this approach completely neglects the particles shape effect which is crucial in problems where erosion is a result of multiple particles impact [130]. In addition, by considering the abrasive particles as a portion of individual elements in the mesh, the authors have also ignored the size effect of the abrasive particles. Furthermore, the abrasive particles are assigned an equation of state (EOS) material properties without failure which assumes that they will undergo deformation indefinitely as the impact load will increase. In contrast, brittle materials like garnet fracture upon impact with little or no plastic deformation. No information has been provided regarding the impact velocity of the water and abrasive particles.

Another AWJ machining FE model is presented by Jianming, et al. [131]. This model uses a smoothed particles hydrodynamics (SPH) approach to model the abrasive particles as spherical balls equivalent to the average diameter of the fresh abrasive, i.e. before fragmentation. Only one size is used for the abrasive particles, whereas in reality they have a size distribution which also influences the depth of the cut [16], [95]. This approach also models the garnet abrasive particles as spherical balls which will suppress the cutting action of the garnet particles which they possess in reality and will change the resulting erosion rate [130].

The key modelling parameters in the above discussed FE models are summarized in Table 2-3. The red colored text shows the discrepancies in the each model.

Table 2-3: Summary of FE modelling parameters used in different studies

Research studies	Modelling parameters							
	Application area	FEM package used	Formulation used	Geometry of impacting particle	Number of particles	Particle size (μm)	Particle material model	Velocity of impact (m/s)
Shimizu [108], [109]	Shot peening	MARC	2D, static	Spherical	1	660	Rigid	145
Takaffoli [110]	Impact erosion	LS-DYNA	2D, dynamic lagrangian	Rhombic	1	-	Rigid	46-81
Eltobgy et al. [112]	Impact erosion	ABAQUS	3D, dynamic lagrangian	Spherical	4	300-600	Rigid	40-100
Griffin et al. [114]	Scale removal	ABAQUS	3D, dynamic lagrangian	Spherical	5	10	Rigid	100
Gudimetla [117]	AWJ machining	ABAQUS	3D, dynamic lagrangian	Spherical	1	180	Rigid	500-700
Junkar et al., [119]	AWJ machining	LS-DYNA	3D, dynamic lagrangian	Spherical	1	100	Rigid	180-220
Ref. [123] [124]	AWJ machining	LS-DYNA	3D, dynamic lagrangian	Spherical	20	100	Rigid	180-220
Wenjun et al. [129]	AWJ machining	LS-DYNA	3D, dynamic eulerian	No shapes assigned	-	-	EOS	-
Jianming, et al., [131]	AWJ machining	LS-DYNA	3D, dynamic SPH	Spherical	-	180	Rigid	-

2.4.2 Analytical modelling

In terms of analytical modelling of the erosion from impacting particles, pioneering research was conducted by Finnie [60] where models of single particle impact in ductile materials were presented. Later, Bitter [62] developed an erosion model which simultaneously included both deformation and cutting actions of the impacting particles. Momber and Kovacevic [132] proposed a model that enables the estimation of the energy absorption from AWJ impingement on a target as a function of the erosion depth. Zeng and Kim [72] presented a model for calculating the volume removed in polycrystalline ceramics in abrasive waterjet cutting. The major drawback in the analytical models is that they require experimentally determined constants which in turn depend on target material properties and the equipment (e.g. cutting head geometry) being used. Hashish [133] presented an erosion model which did not require any experimental constants; the model only worked for shallow cutting angles. Moreover, these models are aimed at calculating the volume removed, erosion rate or depth of cut in the target material and are unable to predict the jet footprint which is the key parameter for controlling the AWJ milling.

Although some methods of predicting machined surfaces/profiles in abrasive waterjet technology have been proposed, they are limited to: (i) statistical approaches such as interpolation, regression analysis (e.g. [52]) with their inherent disadvantages of being valid only within the intervals where the operating parameters have been varied; (ii) artificial intelligence approaches such as genetic algorithms, genetic programming (e.g. [134], [135]) that require a great deal of raw data for model construction; (iii) computationally expensive graphical models to simulate the kerf surface [136]; (iv) model to simulate the jet cutting front by using cellular automata approach which is

based on defining a special set of rules which depends on the target material strength and AWJ intensity [137]. Moreover, most of these models are actually related to a larger jet penetration i.e. not a shallow milled surface.

However, there is another set of approaches for predicting footprint profiles; those based on geometric modelling. Since these approaches are closer to the analytical modelling work in the current research, they are discussed in more detail. The advantage of such models is their relationship to the physical process of material removal and their ability to predict the jet footprint whenever the initial conditions are known. Some attempts at theoretical modelling of footprints of air powder-blasted jets have been reported, but they were limited to either stationary jets [138], [139], [140] or moving above a mask at a constant distance between the work surface and the jet [141]. In the latter approach, a mask of harder material is positioned between the jet and the component and the jet is directed to machine the surface of the component through the openings in the mask. A mask is provided to define the area to be worked whilst covering and protecting the adjacent areas of the component. However, the use of masks incurs extra resources (e.g. manufacture of the mask and setup time) and other problems such as secondary strike and limitation on the ability of the jet to generate 3D or freeform surfaces by using tilted jets in the vicinity of the masks. Furthermore, the solutions of these models cannot be directly adapted to AWJ machining due to the difference in fluid mechanics of the jet as well as the jet energy (governed by the pressure of the accelerating fluid).

More recent work by Burzynski and Papini [142] using the level set method was able to predict the surface profile of poly-methyl-methacrylate (PMMA) channels machined by a microblaster at incidence angles of 90° , 60° and 30° with several

passes. However, in this model the projection of the tilting angles are parallel to the trajectory of the travelling paths. The predicted surface profiles were closer to the measured ones than those predicted by traditional analytical and computer models. However, the execution times (about 16–150 min on a 2.6 GHz Intel CPU with 4MB of RAM) were considered not to be fast enough to enable efficient control of the jet paths on CNC machines. In addition, the reported model cannot provide information on the trajectory of the travelling path with an angle to the projection of the tilting jet. In fact, a report [18] has showed that the shapes of the surface profiles are changed with the projection of the tilting angles perpendicular to the trajectory of the paths. Despite a later work of Burzynski and Papini [14] which considered tilting angles and travelling straight, blastering is still a two-phase flow process that cannot be compared with the three-phase flow AWJ process. Furthermore, for milling complex features, different strategies of straight paths against angles may be required to optimise the geometrical accuracy of the final AWJ milled surfaces.

2.5 Summary of the literature

In this chapter, a comprehensive literature review of the relevant research and development in AWJ technology is presented. It can be observed that there is a wide range of research within this area, including fundamental studies on the AWJ machining process to improve process understanding, parametric studies to optimize the process performance and development of predictive models for erosion rate, depth of cut and kerf profiles.

In the beginning of the chapter, a brief overview is provided on how the AWJ technology works and on its major types (entrainment and slurry jets). This is followed by the principle of material removal in AWJ machining which further divided into micro mechanisms, i.e. single particle erosion, and macro mechanism, i.e. kerf generation.

A detailed review is presented on the effect of process variables on the AWJ performance. It is highlighted that there are a number of process parameters (e.g. water pressure, jet traverse speed, abrasive mass flow rate, etc) that affect the performance of the AWJ process, which makes it difficult to control the amount of material to be removed. The review indicates that a complex relationship exists among the process parameters, for example the erosion rate increases by increasing the abrasive mass flow rate up to a certain limit, but it starts declining with further increase. Moreover, this limiting abrasive flow rate is also dependent on the other process variables such as the focusing nozzle diameter and water pressure. This also indicates the necessity of appropriate AWJ model that can study the exclusive effect of the desired variable on the process outcome. Another main difficulty of the AWJ process in terms of machined parts is that the process relies on a soft tool, i.e. the jet

plume, which does not possess a fixed geometry, unlike conventional machining where the cutter is a hard tool. In particular, when employing the jet plume as a milling “tool”, the capability of the AWJ technology for accurate controlled-depth cutting and the development of freeform surfaces are still the main challenges that this technology is facing today.

In addition, the process itself is subject to some degree of fluctuation/variation in characteristics such as pressure and abrasive mass flow over the machining time. This is a particular issue for controlled-depth AWJ cutting (milling), since a small variation in the footprint per unit time leads to different cut penetrations along the travelling path or an unevenly milled surface. Therefore, controlling the geometry of the footprint is of paramount importance in generating desirable geometries, particularly for freeform surfaces. In other words, predictive models for surface profiles are of critical importance in overcoming these challenges.

Several modelling approaches for simulating the surface profiles in AWJ machining have been reviewed and their limitations are discussed. From the FE modelling point of view, the existing models are mostly limited to single or few multiple particles impact and are unable to predict the complete jet footprints in AWJ milling applications. Moreover, there are various drawbacks in the modelling and validation approaches of these models such as usage of a rigid particle approach, wrong particle size and shape estimations. There is still a need for a FE model that can incorporate more realistic experimental conditions and be able to simulate the complete the AWJ milled footprints.

Regarding the analytical modelling of AWJ machining, several models have been reported, which are usually related to cutting applications, i.e. deeper penetrations of

jet. Although some geometrical nature models exist that can be used for predicting shallow footprints in a masked target only, they have been developed for blastering processes and the solutions cannot be adapted for predicting AWJ footprints. Furthermore, these models cannot be used for real time prediction of jet footprints due to their higher computational times. There is still a requirement to develop a fast running geometrical model that can predict the footprints for abrasive waterjetting conditions.

2.6 Main research challenges

From the extensive literature review, it is possible to see that there is a requirement for developing appropriate models to predict the footprints generated during AWJ milling. Although some models exist for simulating eroded footprints, they are limited either in terms of their relevance to AWJ machining conditions or the modelling approaches selected. In order to bridge these gaps, the following research challenges are addressed in the current study.

2.6.1 FE modelling challenges

- The impacting particles will be modeled as elastic-plastic along with the failure properties included in the material definition to consider the damage response of the particles as it exist in reality. This aspect is rarely addressed in the literature while modelling the impact of the particles against a target.
- Abrasive particles will be modeled with various sharp shapes rather than considering them as spherical. This takes into account the significant effect of the shape of the particle during the impact and realizes the substantial differences between the deformation phenomenon active in the target material for the

spherical and sharp shaped particles.

- Considering the critical importance of the inertial affects during the impact problem, it will be attempted to consider the sizes of the impacting particles as close to the reality as possible. This will be accomplished by selecting the sizes of the garnet particles after the fragmentation process from the focussing nozzle, instead of assuming a single size for all the particles as normally observed in the literature review.
- After considering the above listed challenges, methods will be devised for the followings: (i) taking into account the effect of mass flow rate of the particles; (ii) considering the effect of the traverse speed of the jet; (iii) using a Gaussian distribution of the particles in the jet plume; (iv) including multiple passes of the jet, i.e. thousands of impacting particles in the FE model to simulate the overlapping trenches without becoming extremely computationally expensive. It should be noted that the points (i) to (iv) have not been addressed before in the reported FE models.

2.6.2 Mathematical modelling challenges

A generic mathematical model will be developed with the benefit of simplicity of having fewer variables for predicting maskless waterjetted footprints for arbitrarily moving jet-paths, i.e. going one step further compared to existing models which consider either stationary or up to straight moving jets only. The model will take into account the effects of the nozzle tilt angle and arbitrarily moving jet paths as well.

As mentioned earlier, the AWJ process is a highly capable technology, but most of its current usage is limited in the area of through cutting applications. This is due to the lack of accurate and reliable models for AWJ milling applications. This research

addresses the scientific challenges to develop FE and geometrical models such that the AWJ milled footprints can be simulated with good accuracy and reliability. The current study attempts to model the AWJ milling process by considering most of the real life conditions.

Chapter 3 Methodology

This chapter describes the experimental equipment, materials, measurement techniques and procedures used in the current study. The procedures for the finite element (FE) modelling and the analytical modelling are also described. The experimental parameters used for generating the model validation data are also discussed.

3.1 Abrasive Waterjet Apparatus

All the machining work for the current research was conducted on an Ormond five-axis entrainment type abrasive waterjet system at the University of Nottingham. Figure 3-1 shows the images of the Ormond CNC controlled five-axis waterjet machine which consists of the following main sub-systems: (i) CNC controlled (Fagor 8055) five-axis manipulator; (ii) KMT streamline SL-V100D ultra-high pressure pump; (iii) an analogue controlled abrasive flow metering system (FeedLine IV); (iv) catcher tank filled with water to absorb the jet energy and muffle the sound of the jet; (v) cutting head. The cutting head can be programmed to move on five-axes (linear X-Y-Z, and rotary B and C axis). However, due to the focus of the modelling work, only four axes X-Y-Z and B were used in the current study. The pump pressure can be adjusted manually from 10,000psi to 60,000psi (69 – 413.7 MPa). The maximum traverse rate that can be reached is 20000 mm/min; however, due to the machine dynamics this velocity might reach the programmed values only after particular time intervals. This situation has been taken into consideration in this research. The machine is capable of accommodating orifices with diameter of 0.05 – 0.4mm while the range of nozzle diameters depends on the tool supplier. However, a rule of thumb for the ratio of orifice diameter to nozzle diameter is 1:3 (e.g. a Ø0.3mm orifice and a

Ø1mm nozzle) [20]. The abrasive feeder is appropriate for grits of mesh size between #60 (200 – 400µm) and #220 (70 – 100 µm) depending on the application.

In order to generate the paths of the jet, the G-Codes containing the information on traverse speeds and jet movement directions were manually written and transferred to the machine controller. The nozzle tilt angle (θ) with respect to the target and the standoff distance (SOD) were set by using the jog control unit before starting the trials.

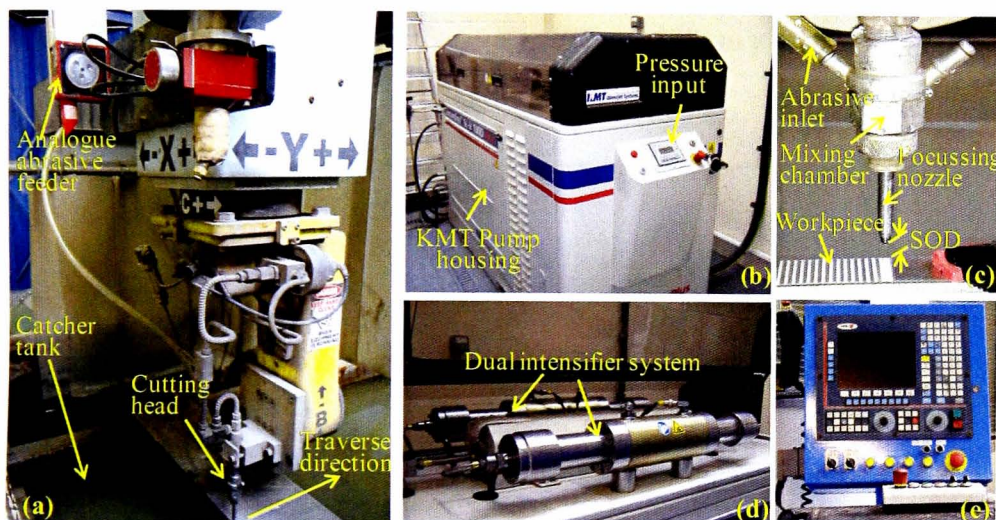


Figure 3-1: (a) Ormond CNC controlled 5-axis waterjet machine used at the University of Nottingham, (b) KMT ultra-high pressure generation system, (c) cutting head, (d) intensifiers, (e) Fagor CNC control unit.

3.1.1 Fixed machining parameters

The parameters detailed in Table 3-1 remained fixed throughout the current research based on the fact that these are static parameters and either these cannot be changed during the AWJ milling process (e.g. orifice and nozzle diameters) or changing these parameters (e.g. standoff distance) does not provide better control of the milling in

terms of depth and width of the footprints.

Table 3-1: Fixed AWJ milling parameters in the current study.

Fixed parameters	Values employed
Orifice diameter	0.3mm
Nozzle diameter	1.02mm (for garnet abrasives)
Nozzle diameter	0.75mm (for steel shots)
Nozzle length	76mm
Abrasive mesh size	80 (100 μ m -300 μ m particles size)
Standoff distance	3mm

3.2 Materials used

3.2.1 Target material

The target/workpiece material used throughout the current study was Ti-6Al-4V, a superalloy widely utilized for both aerospace and medical applications, with the following mechanical properties: average hardness 35 HRC, density 4430 kg/m³, modulus of elasticity 113.8 GPa and Poisson ratio 0.342. In order to remove any scratches or micropits from the surface of the test specimens before generating the jet footprints or single particles impacts, they were hand polished ($R_a=0.07 \mu\text{m}$) by sand papers starting with the grit number 400 then 800 and finally 1200.

3.2.2 Impacting particles

Two different types of impacting particles were used in this research; (i) steel shots and (ii) garnet abrasives. The steel shots were only used during the initial validation stage of the FE modelling while the garnet abrasives were used for the rest of the

tests.

Steel shots used (see Figure 3-2) were spherical grade S110 with density 7000-7500Kg/m³. These steel shots were made of hypereutectoid steel with carbon percentage varying from 0.77-1.20% and their microstructure consisting of uniformly tempered martensite. The steel shots in S110 grade vary in size (diameter) from 0.18 mm to 0.60 mm. In order to obtain a consistent size, the steel shots were sieved and the average size selected for the trials was 0.53 mm diameter with a standard deviation of ± 0.0214 mm.

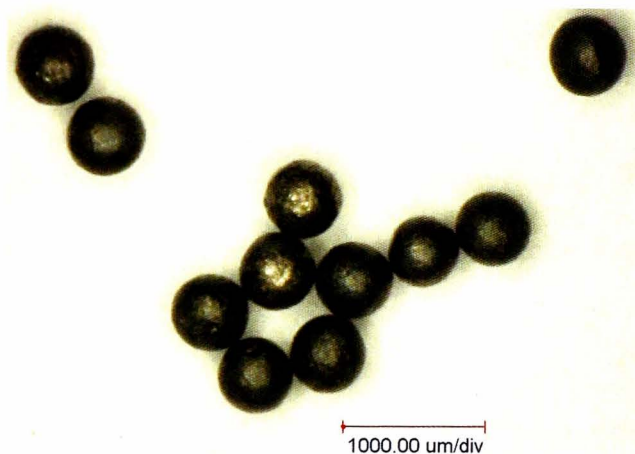


Figure 3-2: Spherical steel shots used as impacting particles.

Garnet mesh 80, shown in Figure 3-3 with an average particle size of 0.180 μ m, was used as an abrasive material during the trials, which is the most common type of abrasive used in AWJ machining due to the facts; (i) it provides better cutting efficiency and nozzle wear performance for a wide range of operating parameters as compared to even more harder abrasives such as alumina (Al₂O₃) and silicon carbide (SiC) [97], [101], (ii) it is relatively cheaper and environmental friendly compared to Al₂O₃ and SiC.



Figure 3-3: Garnet mesh 80 particles, source Indian garnet.

3.3 Measurement Techniques

In order to understand and visualize the results of the steel shot impacts and AWJ impingement trials on the workpiece material, various equipments were used. The equipments used and the procedures followed are detailed below.

3.3.1 Equipment: Keyence digital microscope, 25x-175x magnification

3.3.1.1 Procedure

The target surfaces were analyzed using a laboratory optical digital microscope (see Figure 3-4) between magnifications of x50 and x175. First, the specimen was brought in focus by manually adjusting the distance of the lens from the workpiece. Afterwards, an appropriate lens (magnification) was selected to capture sufficiently zoomed-in images of the specimens. The computer interface linked with the microscope was used to make the scale settings and various linear measurements (lengths and diameters).

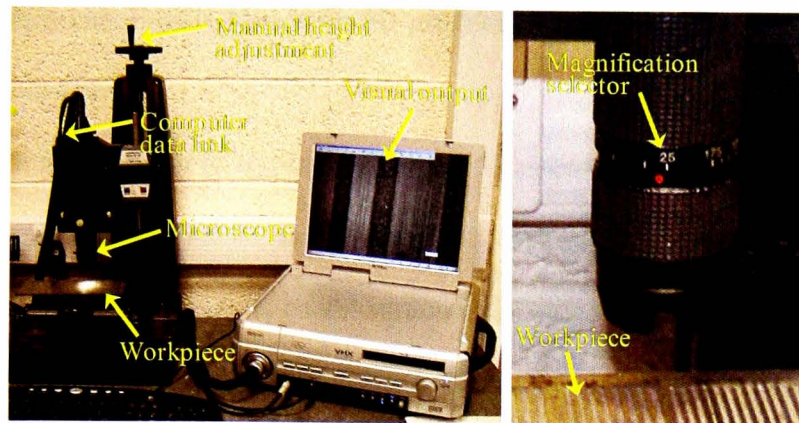


Figure 3-4: Keyence digital microscope operating to analyze an AWJ milled workpiece.

3.3.1.2 Purpose:

The digital microscope was used for the following main purposes:

- To measure the sizes of the steel shots before the trials to make sure that they had almost the same size. This allowed the correct selection of the size of the steel shot in the FE model.
- To observe and capture the shapes of the indentations/craters generated on the target at various impingement angles to visualize the effect of the impact angle on craters' shapes.
- To observe any material removal or fracture caused by the steel shots impacts in the target. This allowed the correct selection of the material models for the target material, based on whether the material had been removed or only plastic deformation had occurred.
- To detect if any significant material is removed by the water droplets during the AWJ trials.

3.3.2 Equipment: Fogale Nanotech 3D profiler (interferometer)

3.3.2.1 Procedure

The Fogale interferometer as shown in Figure 3-5 can easily and instantly captures the 3D images of extremely small sizes (fraction of microns to $100\mu\text{m}$) by using fringe patterns. The sample was placed on the stationary working table and the scanning area was set over the workpiece (usually $0.5 \times 0.5\text{mm}^2$) by using the computer interface. Afterwards, the position of the scanning head was adjusted above the workpiece by moving it up and down in such a way that the fringe patterns were able to detect the lowest and highest point in the scanning area. Once the 3D images of the scanned areas were generated after scanning, the Mountain software (provided by Fogale) was used for further analysis such as 2D profile extraction from 3D images.

3.3.2.2 Purpose

Owing to the very small dimensions of the indentations produced by the steel shots impact, the Fogale interferometer was employed to scan the craters. 2D profiles across the central lines of the indentations were extracted by using the Mountain software. These profiles were later used to validate the FE simulation results.

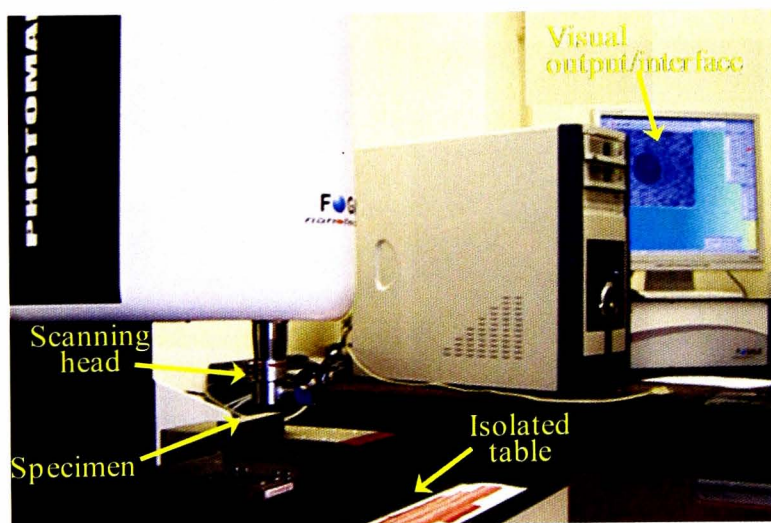


Figure 3-5: Fogale interferometer scanning the steel shot impacts.

3.3.3 Equipment: Taylor Hobson Talysurf CLI 1000

3.3.3.1 Procedure

The channels produced after AWJ milling trials were scanned using a Talysurf CLI 1000 laser scanner as shown in Figure 3-6. The samples were placed on a XY moving table and by using the computer graphic interface, the scanning area was set depending on the length and width of the milled trench to be scanned. The scanning length (Y-direction) of the of the milled trenches were either 30mm or 60mm long, both revealing the same level of accuracy. However, the scanning width (X-direction) of the trenches varied depending on whether scanning a single trench or overlapping trenches with various step-over distances. Once the focus of the laser head was set on the target by moving it up or down (Z-direction), it remained stationary afterwards and the workpiece (and table) moved in XY-directions under the laser head. The scanning resolution of X-5 μ m, Y-100 μ m and gauge resolution Z-0.168 μ m was used throughout the current research. Once the scanned images were generated, the Mountain software provided by Taylor Hobson was used to extract the averaged 2D footprints of the milled trenches i.e. an average of all the single footprints scanned in the Y-directions at a distance of 100 μ m.

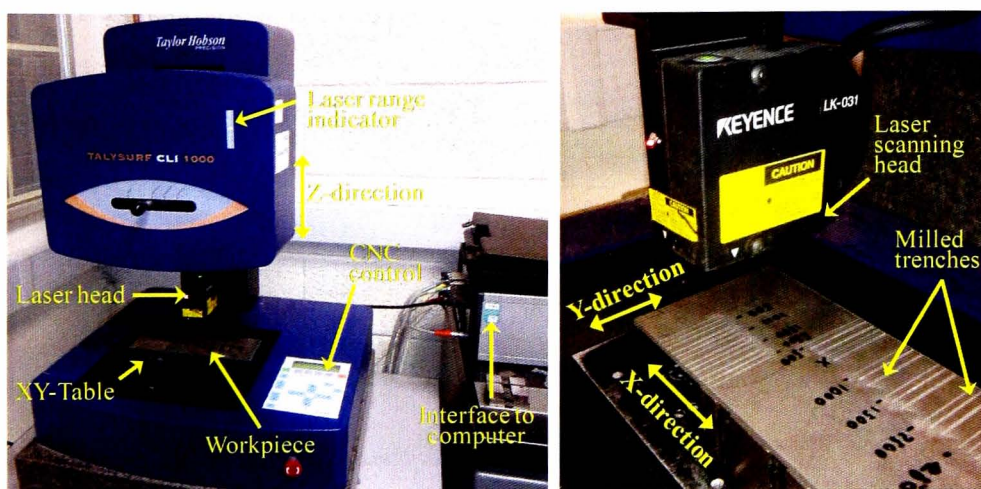


Figure 3-6: Talysurf CLI 1000 system for 3D scanning.

3.3.3.2 Purpose

The averaged 2D footprints generated by Talysurf CLI 1000 were compared with the predicted footprints to validate the simulation results. In addition, the scaled 2D and 3D images generated from the scanned trenches were also used to understand the behavior of the AWJ and target interaction.

3.3.4 High precision analytical balance

3.3.4.1 Procedure

A high precision analytical balance with 0.1mg accuracy was used to measure the weight of the workpiece. Before the sample was put over the weighing pan, the balance was calibrated and set to zero every time in order to account for the surrounding disturbances. The weight of the target was measured before and after each AWJ pass.

3.3.4.2 Purpose

The balance was employed in order to measure the erosion rate (mg/mg) in the target by using the following Eq. 3.1.

$$\text{Erosion rate (ER)} = \frac{\text{Total mass removed in the target}}{\text{Total mass of the impacting particles}} \quad \text{Eq. 3.1}$$

Mass removed in the target was determined by the difference in the mass of the workpiece before and after the AWJ pass, and the mass of the impacting particles for one AWJ pass was known from the mass flow rate (\dot{m}_a) of the abrasives used.

3.4 Finite element (FE) modelling

The FE method is a numerical technique that involves subdividing a large problem

into many smaller segments (elements) and finding the solution for the equations of each element. The behavior of each element is determined by its displacements and the material law described for it. The equations for the whole model are solved for the known initial and boundary conditions from the original problem to provide a numerical solution for the overall problem. The FE model in the current research is developed and validated in four stages which are briefly discussed below.

Stage 1: Single particle model

In AWJ milling, the material removal is mainly caused by the impact of a multitude of abrasive particles at ultra-high velocities. This means that it was of critical importance to first generate and validate the models on single-particle impact to gain the confidence that the model was working in an accurate manner for this basic event. Only then the model was extended for the more real situation involving multiple particles impacts. Moreover, single particle modelling was also necessary due to the fact that it was observed in the literature review that no attempt has been made for capturing the profile of a single particle impact during AWJ machining for validating the FE models. At this stage, the spherical steel shots were used as the impacting particles rather than the normal garnet abrasives due to the fact that it was easier to make clear judgments on the indentations produced by the known size and shape steel shots as compared with the varying shapes and sizes garnet abrasive particles. Furthermore, the impacting steel shots were modeled in a more realistic way by considering them with a deformable elastic-plastic response with a failure criterion, contrasting to the usually selected rigid particle approach as observed in the literature survey in section 2.4.1.

Stage 2: Multiple particles impact model

After gaining confidence that the model works correctly at the single particle level, the model was extended to multiple garnet abrasive particles to reflect the conditions occurring in real abrasive waterjet milling. The failure stresses for the garnet abrasives were calculated. The abrasive particles were modeled with various non-spherical shapes (rhombic, triangular and trapezoidal) and sharp cutting edges as opposed to the usual approach of considering them as spherical shape only, as mentioned in section 2.4.1. The particles were also assigned a size distribution after the fragmentation from the nozzle which is essential to be able to compare the simulated and experimental results. A method was devised to calculate the number of particles required in the model corresponding to the total mass of the garnet used in the experimentation. The results from the multiple particles simulation were validated by using the experimentally determined erosion rates and the velocity exponent for the target material.

Stage 3: Single AWJ pass model

In this stage the FE model was extended to a single jet pass containing hundreds of garnet abrasive particles over the target material. Due to the symmetry of the problem and to save computational time, only a half 3D model was developed and evaluated at this stage. The effects of mass flow rate of garnet abrasives and traverse speed of the jet were also included in the model. A unique method based on the experimental results of [121], [122] was devised to control the shape of the footprints in the FE model by assigning a Gaussian spatial distribution to the abrasive particles in the jet plume.

Stage 4: Overlapping AWJ passes model

In the real life AWJ milling, 3D surfaces are generated when several single footprints overlap. This implies that in order to simulate the overlapping footprints, a full scale FE model was required. At this stage, the FE model was extended to full scale, i.e. a complete jet plume was modeled because a half jet model cannot predict the overlapping AWJ footprints. The size of the problem (total number of elements needed for the multiple jet passes and the target), was too large to be able to run by including them in one model. A methodology was set up to make the simulations possible, which is discussed in detail in Chapter 7.

3.4.1 Steps involved in FE modelling

The FE package used in the current research was ABAQUS version 6.9-1. The steps involved while using the ABAQUS for developing the model and achieving a solution are as follows:

Step 1: Generation of CAD parts

The part module within the ABAQUS was used to create the required geometry and shapes of the impacting particles and the targets. The type selected for all the parts which were used to obtain the solution is classed as 3D deformable. No rigid parts were used in the model.

Step 2: Assignment of material properties

Material properties such as elastic modulus, density, Poisson ratio were allocated to the parts. In addition to these simple material constants, material models were also used to simulate the behavior of the materials at high strain rates. The Johnson-Cook material model and tensile failure models were used in this study, which are discussed

later. Accuracy of the simulation results is significantly affected by the material models used.

Step 3: Assembly of parts

When the parts are created in the part module, they exist in their own coordinate systems, independent from other parts. On the contrary, in the assembly module they were positioned relative to each other in the global coordinate system by applying various positional constraints, translations and rotations, e.g. the impacting angle of particle with respect to target. Also, at this stage the abrasive particles were arranged/assembled in the jet plume to form a Gaussian spatial distribution.

Step 4: Meshing of parts

An FE mesh was generated on all the parts in the model which consists of elements connected at discrete points called nodes. The regions in the model where high stress concentrations are expected, such as particles impact zone on the target, are assigned relatively more refined meshes. The type of the elements used for modelling target and the particles throughout this research is linear eight-noded brick (hexahedral) elements (C3D8R) due to the reason that linear brick elements are accurate and efficient for problems involving erosion, which is the case in this study. In addition, meshes comprised of hexahedral elements are easier to visualize and measure footprints and erosion rates than meshes comprised of tetrahedral elements. It should be noted that the final mesh refinement was reached after several runs such that the mesh refinement was neither too coarse that it could not smoothly capture the profile of the footprint nor too fine that it would consume unnecessary computational time.

Step 5: Defining contact between parts

When the abrasive particles and the target were assembled, surfaces were also defined

on them in order to allow the interaction between them. One surface was comprised of all the elements of all the particles, and the second surface consisted of the elements in the fine mesh region in the target. The “general contact” algorithm in ABAQUS was used to define the contact between the particles and target surfaces. When one layer of elements fails during the impact either on the impacting particles or on the target, the general-contact algorithm automatically defines the new contact surfaces between the newly exposed elements. The value of the coefficient of friction between the garnet particles and the workpiece surface is assumed to be 0.1 based on the work of [143] which states that the variation of the residual stresses and plastic strains is negligible for coefficients of friction between 0.1 to 0.5.

Step 6: Assigning loads and boundary conditions

A single constant impact velocity was assigned to a set of nodes which comprises of all the nodes in the abrasive particles. The traverse velocity was also assigned to the same nodal set. The target was fully constrained at the bottom in all directions in the case of single particle impact and one jet pass simulations, whereas in the case of multiple/overlapping jet passes simulations, the target was allowed to move in the step-over direction only. In order to incorporate the effect of large amount of material present around the impact site in the target in reality, the target boundaries were always extended beyond the impact site 3 to 4.5 times the width of biggest particle in the model. This also ensured that the stresses and strains were mostly limited only in the fine mesh region, away from the free boundaries of the target.

Step 7: Selecting the analysis/solver types

The choice of the solver solely depends on the nature of the process being modeled. In the current study the basic event modeled was the impact of single or multiple

particles which is a highly non-linear dynamic and transient process. This was due to the high speed and small dimensions of the impacting particles used. Furthermore, the impact time of an abrasive particle against the target (i.e. the loading time) was in the range of fractions of a micro second. Hence, the stable time increment in the FE simulations should be much less than this loading time in order to adequately capture the impact event. Based on this, an “explicit dynamic solver” in ABAQUS was selected in the current research which is highly recommended for solving problems involving highly dynamic short term responses (e.g. high speed impact) [118], [119]. During an explicit analysis, the equations of motion for the entities in the model are integrated by using the explicit central-difference integration rule as detailed in Eq. 3.2 and Eq. 3.3.

$$\dot{u}_{(i+1/2)} = \dot{u}_{(i-1/2)} + \left(\frac{\Delta t_{(i+1)} + \Delta t_{(i)}}{2} \ddot{u}_{(i)} \right) \quad \text{Eq. 3.2}$$

$$u_{(i+1)} = u_{(i)} + \Delta t_{(i+1)} \dot{u}_{(i+1/2)} \quad \text{Eq. 3.3}$$

where $\Delta t_{(i)}$ is the increment time, u is a degree of freedom (a displacement or rotation component) and the subscript i refers to the increment number in an explicit dynamics step. The central-difference integration operator is explicit in the sense that the kinematic state is advanced using known values of $\dot{u}_{(i-1/2)}$ and $\ddot{u}_{(i)}$ from the previous increment. The accelerations $\ddot{u}_{(i)}$ are computed at all the nodes at the beginning of every increment by using the diagonal element mass matrices along with the externally and internally applied loads as given in Eq. 3.4.

$$\ddot{u}_{(i)} = (M)^{-1} (F_i^{ext} - F_i^{int}) \quad \text{Eq. 3.4}$$

where M is the mass matrix, F_i^{ext} is the applied load vector, and F_i^{int} is the internal

force vector. A diagonal mass matrix is used because its inverse is simple to compute and this provides the computational efficiency.

It should be noted that if the increment time step $\Delta t_{(i)}$ is too large, the explicit procedure may not be stable, may give unreasonable results and/or it may abort. The stable increment time in explicit procedure is calculated as given in Eq. 3.5.

$$\Delta t_{(i)} \leq \frac{L_e}{c_d} \quad \text{Eq. 3.5}$$

where L_e is the characteristic length of the smallest element in the model and is determined from the ratio of the volume of element (V_e) to the maximum area of largest side of the element (A_{max}) and c_d is known as dilatational wave speed i.e. the speed of the sound in material [144] and is given by Eq. 3.6

$$c_d = \sqrt{\frac{E(1-\nu)}{\rho(1+\nu)(1-2\nu)}} \quad \text{Eq. 3.6}$$

where E , ν and ρ are the elastic modulus, Poisson ratio and the density of the material respectively. It can be noted in Eq. 3.5 that the increment time is significantly affected by the selected mesh size. If the elements are very small, very small time increments will be used which will considerably increase the computational time. On the other hand, large sizes of elements could result in an inaccurate analysis. Therefore, an appropriate mesh size was selected with a great deal of caution.

An explicit analysis also offered the benefits of handling a large size problem more efficiently and allowed the modelling of wear/erosion on both the impacting bodies, which was a necessity in the current study.

Step 8: Visualization of the results

This was the last step in the FE analysis. The visualization module within the ABAQUS was utilized to manipulate the data and results obtained in step 7 for generating deformed shapes of the target and particles, creating stress plots, animations, etc. A graphical representation of the results was very useful in understanding the interaction of the abrasive particles and the target during AWJ milling. Erosion rates and footprints were also measured at this stage by using various graphical tools within the visualization module and then comparing them with the experimental data.

In classical terms of FE analysis, steps 1-6 are known as *pre-processing*, step 7 where the equations are resolved is termed as *analysis/solver* and step 8 where the results are reviewed and desired variables are extracted is called *post-processing*.

3.4.2 Materials model

The material models used to define the behavior of the materials during the simulations were one of the most important parameters that govern the accuracy of the predicted results. While selecting the material model, consideration was given to the fact that the model must be valid for the loading regimes where it was employed. Various fracture and damage material models are available in ABAQUS material library, and the chosen models were deemed appropriate for the conditions arising in AWJ milling.

3.4.2.1 Models for ductile materials

For modelling the plastic and failure responses of the ductile materials, i.e. for Ti-6Al-4V and steel, the Johnson and Cook (JC) models [111], [113] were employed in the

current study. Johnson and Cook proposed two models: (i) JC plasticity model also known as JC strength model and (ii) JC failure model also known as JC fracture model or JC shear failure model. Both these plastic and failure JC material models are suitable for cases which involve high strain rates [112], [115], [118]. Hutchings [145] reported that in case of a particle impacting upon a target, the strain rate increases by the increase in the impact velocity and the reduction in the size of the particle as shown in Figure 3-7. In the case of AWJ machining, particle velocities are in range of 400-600 m/s [120], [121] and the abrasive particles sizes are in the range of 100-300 μ m (for mesh size 80). Therefore, high strain rates in the range of 10^5 s^{-1} were expected when the particle hits the target surface. Many researchers [110], [112] have employed JC strength and fracture models to simulate the flow stress and failure respectively in the target material while studying the erosion phenomena due to particle impact by FE modelling.

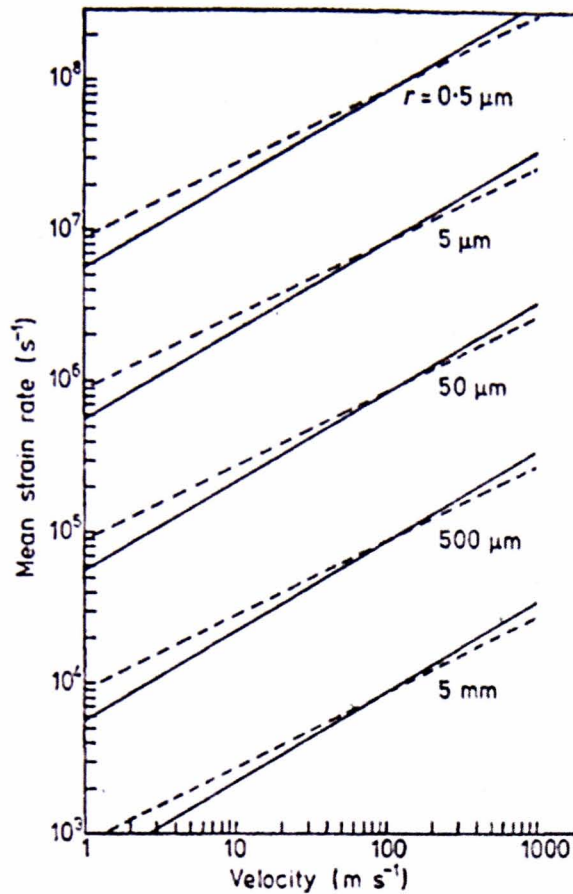


Figure 3-7: Estimated strain rates associated with the particle sizes and impact velocities. Solid lines represent purely elastic behavior; broken lines, perfect plastic behavior [145].

The *Johnson-Cook plasticity (strength) model* is a particular type of isotropic hardening where the yield stress, σ_Y is assumed to be of the following form:

$$\sigma_Y = [A + B\varepsilon^n] \left[1 + C \ln \frac{\dot{\varepsilon}}{\dot{\varepsilon}_0} \right] \left[1 - \left(\frac{T - T_r}{T_m - T_r} \right)^m \right] \quad \text{Eq. 3.7}$$

where ε is the strain in the material, $\dot{\varepsilon}$ is the strain rate, $\dot{\varepsilon}_0$ is the reference strain rate at which material constants (A and B) are determined [146], T is the workpiece temperature, T_r is the room temperature and T_m is the melting temperature of the simulated material. A , B , n , C and m are material constants determined experimentally

from a compressive split Hopkinson bar test [147]. The expression in the first set of bracket represents the yield stress as a function of strain; the second set of brackets shows the increase in the yield stress at elevated strain rates and the third expression represents the reduction in the yield stress due to the thermal effects.

The *Johnson-Cook failure model* can be expressed as follows:

$$\varepsilon_f = [d_1 + d_2 e^{d_3 \sigma^*}] \left[1 + d_4 \ln \left(\frac{\dot{\varepsilon}}{\dot{\varepsilon}_0} \right) \right] \left[1 - d_5 \left(\frac{T - T_r}{T_m - T_r} \right)^m \right] \quad \text{Eq. 3.8}$$

where, ε_f is the plastic strain at failure, σ^* is a dimensionless hydrostatic stress to von Mises stress ratio, and d_1 , d_2 , d_3 , d_4 and d_5 are the material constants determined from compressive split Hopkinson bar tests. The failure/damage of an element in the FE model occurs when the damage parameter D reaches the value of 1 as follows:

$$D = \frac{\sum (\Delta \varepsilon)}{\varepsilon_f} \quad \text{Eq. 3.9}$$

where $\Delta \varepsilon$ is an increment of the equivalent plastic strain while the summation is done to add the plastic strain produced in all the increments during the analysis. Each element is accessed for damage by monitoring the value of D over all the increments, and as the damage parameter reaches 1 for any element, it is removed from the mesh.

3.4.2.2 Model for brittle material

Garnet, which was used as an abrasive in the current study, is classified as a brittle material. The material model adopted for the damage of the garnet was a *tensile failure criterion*, which is often used and recommended for high strain rate damage of brittle materials in which inertia effects are important [118]. The tensile failure model uses the hydrostatic pressure stress as a failure measure to model a pressure cutoff for

the material. The tensile failure criterion considers the failure to occur when the stress in an element becomes more than the user defined hydrostatic cut-off stress (σ_{cutoff}), i.e. the element is assumed to have achieved the required amount of energy to fracture and subsequently it is removed from the mesh.

3.4.3 Generation of validation data

In order to validate the FE simulation results, the trials were conducted on the Ormond AWJ machine. Table 3-2 to Table 3-5 list the summaries of the experimental parameters at which the trials were conducted for generating the validation data for the results of single particle (steel shot) FE model, multiple garnet particles FE model, single AWJ pass FE model and overlapping AWJ passes FE model respectively. It should be noted that the experimental AWJ milling parameters employed in the current study were selected from the work of ref. [24], [26], [93] where thorough investigations on AWJ milling of titanium alloys were presented and the process parameters were optimized for the milling applications, i.e. for controlled depth of cuts.

Table 3-2: Process parameters used for single particles impact trials.

Trial	P (MPa)	V_f (mm/min)	Particle diameter (μm)	θ (°)
1	276, 345	20000	500	90
2	276, 345	20000	500	70
3	276, 345	20000	500	50

Table 3-3: Process parameters used during multiple garnet particles impact.

Trial	P (MPa)	V_f (mm/min)	\dot{m}_a (Kg/min)	θ (°)
1	138	1000	0.02	90
2	207	1000	0.02	90
3	276	1000	0.02	90
4	345	1000	0.02	90

Table 3-4: Process parameters used for single AWJ pass trials.

Trial	P (MPa)	V_f (mm/min)	\dot{m}_a (Kg/min)	θ (°)
1	138	2000	0.02	90
2	138	1000	0.02	90
3	207	2000	0.02	90
4	207	1000	0.02	90
5	276	2000	0.02	90
6	276	1000	0.02	90

Table 3-5: Process parameters used for overlapping AWJ pass trials.

Trial	Jet passes (n)	SO (mm)	V_f (mm/min)	P (MPa)	θ (°)
1	1,2,3	0	1000, 2000	207, 275, 345	90
2	1,2,3	0.3	1000, 2000	207, 275, 345	90
3	1,2,3	0.5	1000, 2000	207, 275, 345	90

3.5 Analytical modelling

From the analytical (mathematical) modelling point of view, an AWJ and target interaction model was developed in the form of partial differential equations. The model was based on the physics and geometry of the footprint generation process. The scope of this model was to develop a mathematical model with the benefits of: (i) simplicity of having fewer variables for predicting maskless AWJ milled footprints for arbitrarily moving jet-paths, (ii) very small computational time. The presented analytical model was based on the work of Axinte et al. [107] where the model was only able to predict the trenches at normal jet impingement for a straight path. The current mathematical model was extended to take into account the effects of normal to tilted jet impingement angles (θ) on the target surface and the trajectories/paths of the jet in any direction (β). Since the mathematical model of the jet footprint resulted in nonlinear partial differential equations, a method of evaluating the material specific erosion/etching rate was proposed by using a high jet traverse speed to generate a shallow kerf. This allowed the governing equation to be linearised, and then solved analytically to find the specific erosion rate of the target material. Once this was

found, the jet footprints were predicted accurately for any jet feed speed and milling direction (i.e. jet path).

3.5.1 Modelling tool

MATLAB[®] programming was used as a tool to generate the code for the mathematical equations in order to run the model and predict the AWJ milled footprints. MATLAB (matrix laboratory) is a numerical computing environment and it can create and manipulate arrays of vectors and matrices. MATLAB consists of various built in functions (e.g. integration, sine, cosine, etc) that make the code generation process more quick and easy. Two separate codes, linked to each other, were developed in order to run the model. The first code was used to determine the etching rate function by using a shallow AWJ milled footprint, and in the second code the calibrated etching rate function was used to generate the predicted footprints at the user defined parameters e.g. traverse speed and nozzle angle.

3.5.2 Generation of validation data

In order to validate the results predicted by the analytical model, several trials were conducted. Table 3-6 lists the summary of the experimental parameters at which the trials were conducted for generating the validation data for the results of the mathematical model.

Table 3-6: Process parameters used in trials for analytical model.

Trial	P (MPa)	\dot{m}_a (kg/min)	SOD (mm)	V_f (mm/min)	θ (°)	β (°)
1	138	0.04	3	2000	70	-90, -45, 0, 45, 90, 135, 180, -135
2	138	0.04	3	1000	70	-90, -45, 0, 45, 90, 135, 180, -135
3	138	0.04	3	2000	80	-90, -45, 0, 45, 90, 135, 180, -135
4	138	0.04	3	1000	80	-90, -45, 0, 45, 90, 135, 180, -135
5	138	0.04	3	2000	90	-90, -45, 0, 45, 90, 135, 180, -135
6	138	0.04	3	1000	90	-90, -45, 0, 45, 90, 135, 180, -135

After defining the procedures for the modelling, experimentation and target surface examinations, the models were developed and the experiments were conducted, surfaces were investigated and the validation data was generated. First of all, the FE modelling work for a single particle impact was carried out and the trials were performed for providing the validation data. The results for the single particle FE modelling are presented in the next chapter.

Chapter 4 Finite element modelling of a single particle impact

This chapter provides the detailed description of the first stage of the FE modelling procedure, i.e. for single particle impact modelling. The grounds for which the FE modelling process started from the single particle modelling are discussed in detail. The methodology for achieving the single particles impacts from the abrasive waterjet machining is elaborated. A detailed description of the FE model development is provided together with the experimental validation of the FE model. Conclusions are drawn to enable the development of the full models of the abrasive waterjet eroded footprint.

4.1 Introduction

The use of the AWJ machining for through cutting is well developed, but its use for the controlled-depth milling is still a subject for further investigations to enable better understanding of its particularities and material removal mechanisms [24]. The main challenges for performing controlled-depth AWJ cutting (i.e. milling) are: (i) difficulty of predicting the jet footprint that is not only dependent on the jet plume characteristics (e.g. energy, mass flow of abrasives) but also on the kinematic parameters of the process (e.g. jet transverse speed of jet, vector position of the jet plume) as well as on the characteristics of the workpiece material (e.g. hardness, toughness) [2, 3]; (ii) key characteristics of the waterjet system (e.g. acceleration/deceleration) that can influence the dwell (surface exposure) time as well as the jet tool path strategy; (iii) interaction between the secondary (reflected) jet and the surface to be milled.

However, to enable the generation of complex surfaces using AWJ milling, a critical

step is to develop methods to predict the jet footprint. In AWJ milling, the material removal is mainly caused by the impact of a multitude of abrasive particles at ultra-high velocities. Nevertheless, before conducting simulations on the jet footprint as a whole (i.e. multi-particles impact), it is of critical importance to firstly generate and validate models on single particle impact. Although the real AWJ consists of a large number of irregular particles, the investigation on impact of a single particle of known shape onto a target will provide an insight into further FE modelling to predict complete jet footprint.

Various FE models of single particle–workpiece impact during the general erosion process have been reported e.g. [110], [112], which have been discussed in detail in section 2.4.1 (Literature review). However, these models are only tested for a low regime of velocities (40m/s to 100m/s) compared to those resulting in the AWJ machining and all these models use a rigid particle approach which cannot be applied for high speed impact situations. Up to now, only scarce evidence exists in the literature regarding FE modelling of a single particle impact during AWJ milling and no attempt has been recorded for capturing the profile of a single particle impact during AWJ machining for validating the FE models. Moreover, there are several weaknesses in the FE models reported for modelling the single particle impact in AWJ milling both in terms of the modelling approach adopted and the method selected for the validation of the simulation results. Regarding the modelling approaches, the main flaws observed are: (i) using the rigid particle approach at ultra-high velocity impact situation [117], [119]; (ii) selecting the velocity and size of impacting particle contrary to the experimental data [116], [117]; (iii) selecting a shape of the impacting particle which is non-representative of the particle shapes used in the experiments [117], [119]. Concerning the validation methods selected, the main

issues are: (i) using only the top view of crater to confirm the FE simulation results without focussing on the depth of the crater [119]; (ii) comparing the erosion rate resulting from a single particle with that of the multiple particles [117] knowing that the erosion rate becomes stable only after several particle impacts [112]; (iii) comparing the depth produced by a single size spherical particle from the simulation with the average depth of the craters generated by varying sizes and irregular sharp shapes particles from experiments [116], [119].

After realizing the shortcomings of the reported models, the focus of this preliminary step of the research was devoted to develop a methodology that can generate reliable data for validating the FE model results. It has been demonstrated [16] that when the abrasive particles pass through the mixing chamber and the focussing tube they undergo significant fragmentation; this phenomenon is more prominent in the case of abrasives (of ceramic nature – e.g. garnet) which display brittle behaviour and irregularly shaped particles. When such abrasive (garnet) particles strike the surface of the workpiece during AWJ machining, it is not possible to tell while performing the target surface examinations, which crater is produced by which size (fragmented) particle. Consequently, it will become difficult to correctly select the size of the indentation marks (i.e. craters) of the impacting particles to enable an accurate validation of the FE model. Moreover, a wrong size selection in the FE model will result in significantly large deviations in the inertial effects in the model and those in the experiments. In order to avoid these complexities, it should be therefore more appropriate to use known shapes of impacting particles (e.g. spherical steel balls) in the initial phase of validating the FE model. Furthermore, it has been highlighted [29] that at high water pressure (typically more than 276MPa), water droplets in the jet could contain enough energy (at particular process parameters) to create micropits on

the workpiece surface. As a result when the AWJ plume, with fragmented garnet particles of small sizes, impacts the target surface at high water pressure, it becomes more difficult to differentiate between the craters produced by the abrasive particles and the water droplets. This means that the problem of identifying single particle indentations becomes more pronounced with the decrease in the size of the abrasives. Figure 4-1 show an example of the target surface after an AWJ pass at very high traverse speed (V_f) to minimize the overlap among the particles, but even then no judgment can be made on the indentations produced due to varying sizes and overlapping of the craters produced.

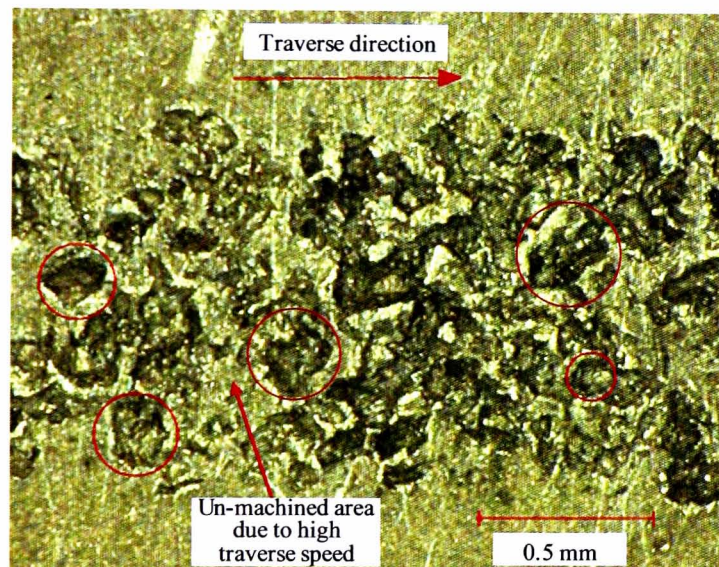


Figure 4-1: Varying shapes and sizes craters produced by garnets particles at water pressure (P) = 345MPa, impact angle (θ) = 90° , traverse speed (V_f) = 20000 mm/min.

It can be seen in Figure 4-1 that the majority of the machined region consists of overlapped craters and those that appear to be single craters are of varying shapes and sizes. This proves that no conclusion can be drawn relating to selecting the size and shape of the impacting particles in the FE model while using garnet as abrasives.

In order to avoid this situation, a methodology was defined to achieve and easily identify the craters produced by the impacting particles. Once a validated FE model is developed, it is believed that only then it will be appropriate to take into account the effect of shape and size of the abrasive particles commonly used in AWJ machining. Therefore, a cornerstone of this stage of research was the development of suitable model for a single impact of an ultra-high velocity particle against a target surface. To address this, this chapter reports on a method to employ 3D FE modelling of an ultra-high velocity particle impact on a target surface. The proposed methods take care of accurate validation of the model by employing known shape and size of “abrasives” upon which clear judgements on the real indentations caused by particles (not water droplets) on the surface can be reached. Of course, once the model is fine-tuned in this way, further research can be directed towards modelling the erosion generated by sharp shape varying-size multiple particle impacts.

4.2 Generation of experimental data

The trials, aimed at generating experimental data for validating the FE model results, were conducted on a 5-axis waterjet machine (Ormond) with an orifice diameter of 0.28 mm and nozzle diameter of 0.75 mm. Experiments were performed on a rectangular (140mm x 70mm x 3mm) plate of an aerospace Titanium based superalloy (Ti-6Al-4V). Prior to the experiments, the surface of the workpiece was hand polished so that no scratches or micropits would remain on the surface and clear judgements would be made after the trials in distinguishing the craters produced from the water-droplets and the impacting particles. To enable the generation of the well-defined indentations on the workpiece surface, in order to allow the validation of the model, spherical steel shots (grade S110) instead of commonly employed abrasives, i.e.

garnet, were used as the impacting particles. The steel shots in S110 grade vary in size (diameter) from 0.18 mm to 0.60 mm. In order to obtain a consistent size, the steel shots were sieved and the average size selected for the trials was a 0.53 mm diameter with a standard deviation of ± 0.0214 mm.

To increase the chance that single particles would produce indentations on the workpiece (Ti-6Al-4V) surface, high water pump pressures (P) of 345 MPa (50000 psi) and 276 MPa (40000 psi) were used in the trials. High water pressure results in high energy (velocity) of the particles that increases the probability that each single particle would significantly deform the workpiece surface. All the trials consisted of only a single pass of AWJ across the target surface. Since the trials were directed to enable the visualisation of indentations/craters generated by single particles, high jet traverse speed (V_f) of 20000 mm/min was used to lessen the likelihood of overlapping between the impacting particles. In addition, only a small number of steel balls (5 to 10) were manually fed into one of the abrasive inlets (while the other was blocked) before each pass rather than using a continuous mass flow rate of steel balls.

In real AWJ milling, when the footprint is generated by multiple particles impact, sloped/tilted surfaces are developed along the side of the milled kerf. This means that the further incoming particles will impact at inclined surfaces as well. Therefore, to address the long term goal of modelling the complete AWJ footprints, experimental trials for single particle impacts were conducted at 90° , 70° and 50° jet impingement angles from the workpiece surface. For each impact angle and pressure, ten repeated jet passes were generated, out of which craters were examined for further study.

Once the singular particle indentations were generated, their analysis was carried out by using a VHX digital microscope (Keyence) to obtain a magnified top view of the

craters. For 3D scanning of the craters, a Fogale Photomap 3D (interferometer) was used. From the scanned 3D craters, the 2D profiles were extracted and averaged for comparison with the FE simulation results.

4.3 Finite Element Modelling

For modelling the single particle impact, the ABAQUS FE package (version 6.9-1) was used in an explicit formulation to enable more efficient solving of the problem involving a short term response i.e. high speed impact. The modelling procedure is discussed below.

4.3.1 Material modelling

4.3.1.1 Target material model

In order to replicate the response of the target material (Ti-6Al-4V) under loading in the FE model, correct material models are required. As explained in section 3.2.1, high strain rates are expected during the particle impacts due to the small size and the high velocity of the impacting particles. The Johnson and Cook [111] plasticity model was selected to calculate the flow stress in a target metal. The material constants required in Eq. 3.7 for the Ti-6Al-4V have been taken from the experimental work of Lesuer [147]. After the experimentation, the craters were analysed under an optical microscope and it was found that plastic deformations were generated on the Ti-6Al-4V surface along with some cracks, but no clear evidence of detached/eroded material was found on the crater area. Hence, no failure criterion was included in the target material definition at this stage.

No thermal effect such as adiabatic heating is included in the model due to the fact that any heat generated on the target surface during the particle impact will be

instantly absorbed by the enormous cooling effect of the water. The material constants used for Ti-6Al-4V are listed in Table 4-1.

Table 4-1: Material constants for Ti-6Al-4V [147].

Density	4428 (Kg/m ³)
Elastic modulus	113.8 (GPa)
Poisson ratio	0.34
A	1098 (MPa)
B	1092 (MPa)
n	0.93
C	0.014
m	1.1
$\dot{\epsilon}_0$	5000 s ⁻¹

4.3.1.2 Impacting particle material model

It can be observed from Table 4-2 that Ti-6Al-4V is much stronger than steel, and the steel ball material was modelled as elastic-plastic with a failure criterion. The Johnson and Cook (JC) plasticity and failure models, as detailed in Eq. 3.7 and Eq. 3.8, were used to model the plastic and failure response of the steel shots respectively. The material constants for the steel ball are listed in

Table 4-3 and have been extracted from refs. [149], [150].

Table 4-2: Comparison of steel and Ti-6Al-4V strength properties [97], [151], [152], [153]

Properties	Tensile strength (MPa)	Yield strength (MPa)	Fracture toughness (MPa√m)
Steel	615.4	375.8	50
Ti-6Al-4V	993	924	80

Table 4-3: Material constants used for the steel shots.

Density	7250 (Kg/m ³)
Elastic Modulus	205 (GPa)
Poisson ratio	0.27
A	525 (MPa)
B	3.54 (GPa)
n	0.63
C	0.029
m	0.75
$\dot{\epsilon}_o$	2500 s ⁻¹
d1	0.05
d2	3.44
d3	-2.12
d4	0.002
d5	0.61

4.3.2 Contact

The general-contact algorithm in ABAQUS was used to define the contact between the impacting ball and the flat workpiece surface because it facilitates the removal of the elements from the mesh. When the elements on the exterior of the steel ball fail during the impact, the general-contact algorithm automatically defines the contact between the newly exposed elements and the target surfaces.

4.3.3 Boundary conditions

In order to restrain the motion of the workpiece, its bottom plane was constrained in the X, Y and Z directions (see Figure 4-2(a)). According to the experimental work of

refs. [121], [122], the maximum number of the particles in the AWJ travel at 70% of the pure waterjet velocity (V_w). Therefore, in the FE model the velocity of the impacting particle (V_{imp}) was set at $0.7 \times V_w$. The waterjet velocity behind the orifice (V_w) was calculated by Bernoulli's law, as presented in Eq. 3.7:

$$V_w = \sqrt{(2P/\rho)} \quad \text{Eq. 4.1}$$

$$V_{imp} = 0.7 \times V_w \quad \text{Eq. 4.2}$$

In order to keep consistency with the experimental conditions in refs. [121], [122], similar diameters of the orifice (0.28 mm) and the focussing nozzle 0.75mm were used in during the experiments.

In order to minimize the boundary effect and to allow enough distance for the propagations of stress waves during the impact, a relatively large size of the target surface was used almost 3 times the particle diameter (0.53 mm) on either side of the impact as shown in Figure 4-2(a).

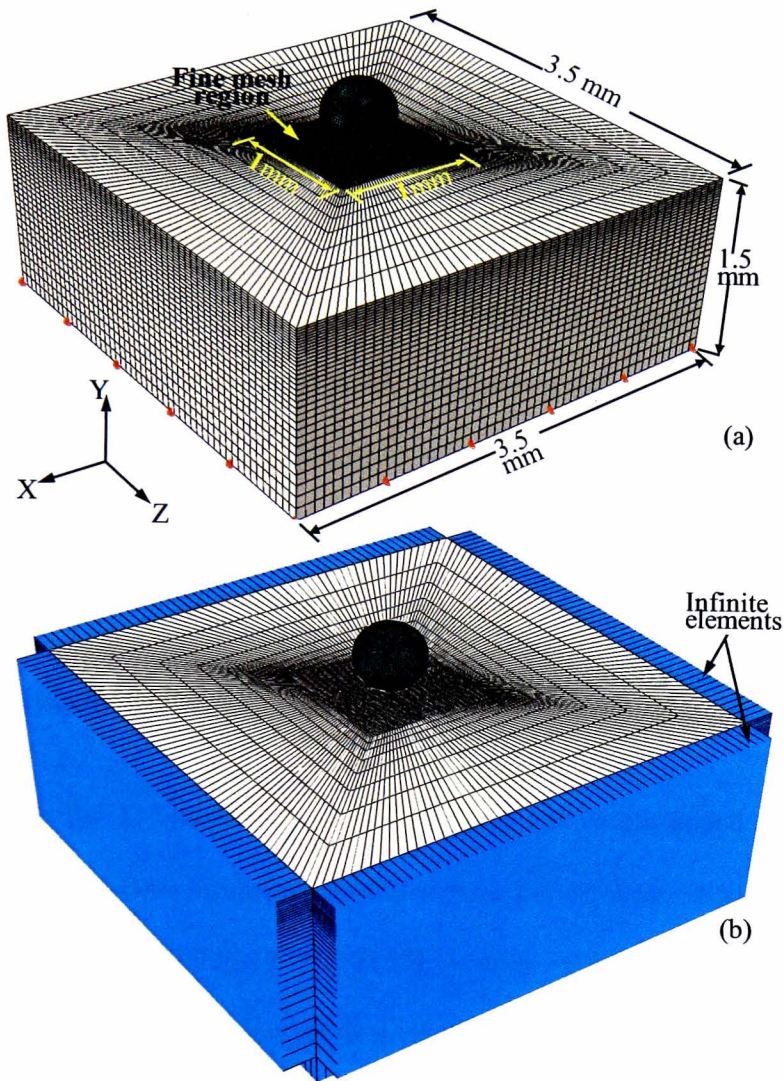


Figure 4-2: Model geometry, a typical mesh and boundary condition used for the workpiece and the ball: (a) a typical configuration used in simulations, and (b) model with infinite elements at boundaries and base.

Although in real life the boundaries of the target are much farther from the impact site, it was found that reducing the target dimensions to even $2 \times 2 \times 1 \text{ mm}^3$ only had a negligible influence on the crater geometry, stress/strain distribution, etc. This implies that the effects of the high speed impact event are contained in a small zone.

Infinite elements (CIN3D8) are often used, see for example [117], [154], [155], [156],

to provide non-reflecting boundary conditions i.e. to prevent the reflection of the shock waves. In order to further verify that no boundary effects are present in the model, a separate model with same dimensions was developed with infinite elements at the boundary and the base of the Ti-6Al-4V target as shown in Figure 4-2(b). Negligible differences in stress/strain values were observed after running the model with infinite elements compared to when these were not used. However, the computational time was increased by ~30%, when infinite elements were incorporated in the model. Therefore, it was decided not to use infinite elements since no noticeable difference was observed.

4.3.4 Meshing

For both the Ti-6Al-4V target and the steel ball, eight-noded linear brick elements along with viscous hourglass control were used; the latter is particularly designed for high strain rate problems [118], [157]. A more refined mesh was used in the vicinity of the impact on the target while a relatively coarse mesh was employed away from the impact area as shown in Figure 4-2. The element size used in the target fine mesh area was $20 \times 20 \times 10 \mu\text{m}^3$ (i.e. X x Z x Y directions) which is $\sim 1/27$ of the average indentation size and is usually more refined or either equal to most of the published FE models for particle impact cases, e.g. refs. [112], [117], [119], [158]. The global element size used in the particle mesh was $20 \mu\text{m}$. Mesh sensitivity analysis was carried out for the target mesh to assure that the used mesh (element) size was neither time-consuming nor leading to discretization errors. Figure 4-3 shows the results of the mesh sensitivity analysis for three different elements sizes. The values of both the depth of the craters and the height of the piled-up material at the boundaries of the craters are almost the same for all the mesh sizes, which represents a good

convergence of the numerical solutions.

Table 4-4 summarizes the parameters used in the FE model

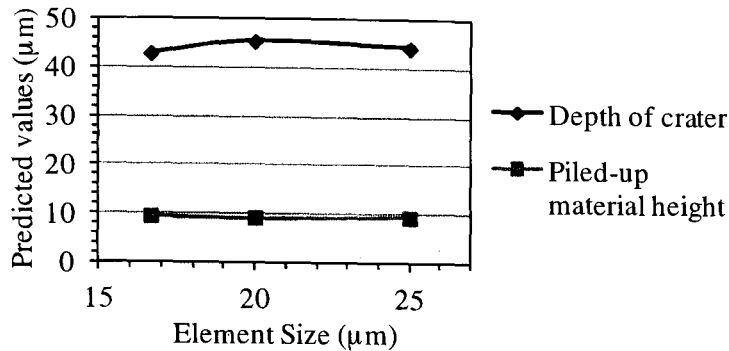


Figure 4-3: Mesh convergence study, $P=345\text{MPa}$, $\theta = 90^\circ$.

Table 4-4: Parameters used in the FE model.

Water pressure, P (MPa)	Corresponding velocity of particle, V_{imp} (m/s)	Impact angle with target, θ ($^\circ$)
345	581	90
276	520	90
345	581	70
276	520	70
345	581	50
276	520	50

4.4 Results and discussion

Figure 4-4 shows examples of typical indentations produced by the steel shot impacts by AWJ impingement on Ti-6Al-4V targets at various incidence angles and pressures. It can be clearly seen that well defined single particle indentations have been achieved and these indentations can be easily distinguished from the craters/pits generated by water droplets (see Figure 4-4(b, f)).

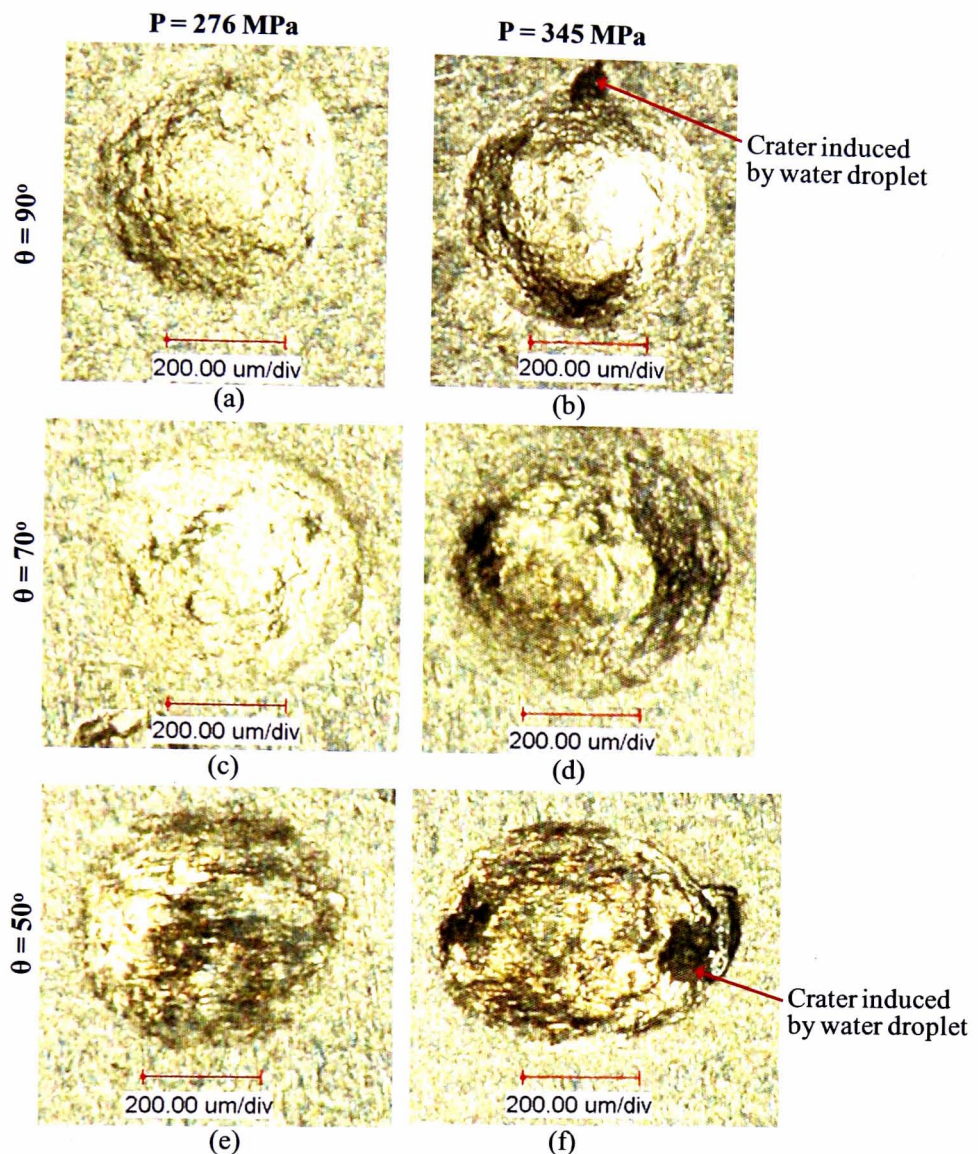


Figure 4-4: Images of steel ball indentations (impact direction is from left to right)

This is because of the fact that unlike garnet particles, no fragmentation has occurred in the steel balls while passing through the focussing tube and relatively larger size steel balls were used. In other words, it can be concluded that because of using the high traverse speed of the jet and regular shape and size of the impacting particles, clear and well defined indentations have been generated by the AWJ impingement. Furthermore, as mentioned in section 4.3.1.1 that craters are formed mainly due to the plastic deformation only while some cracks lines can be observed within the craters.

Figure 4-5 shows examples of the 3D contour of the scanned craters at various impingement angles and out of these, 2D cross-sections i.e. profiles of the craters were extracted as schematically shown by yellow highlighted lines. It can be seen in Figure 4-5(a) that in case of 90° impingement the material has piled up uniformly around the boundary of the crater, while in cases of angled incidences (70° and 50°), the material has been displaced more along the direction of the impact of the particle. Similar ploughing deformation behaviour was also reported by Hutchings [64]. These shape trends of the experimentally generated craters were used as the qualitative parameter for comparing the shapes of the FE simulated craters. For each impingement angle and pressure ten 2D profiles were averaged and then compared with the FE simulation results.

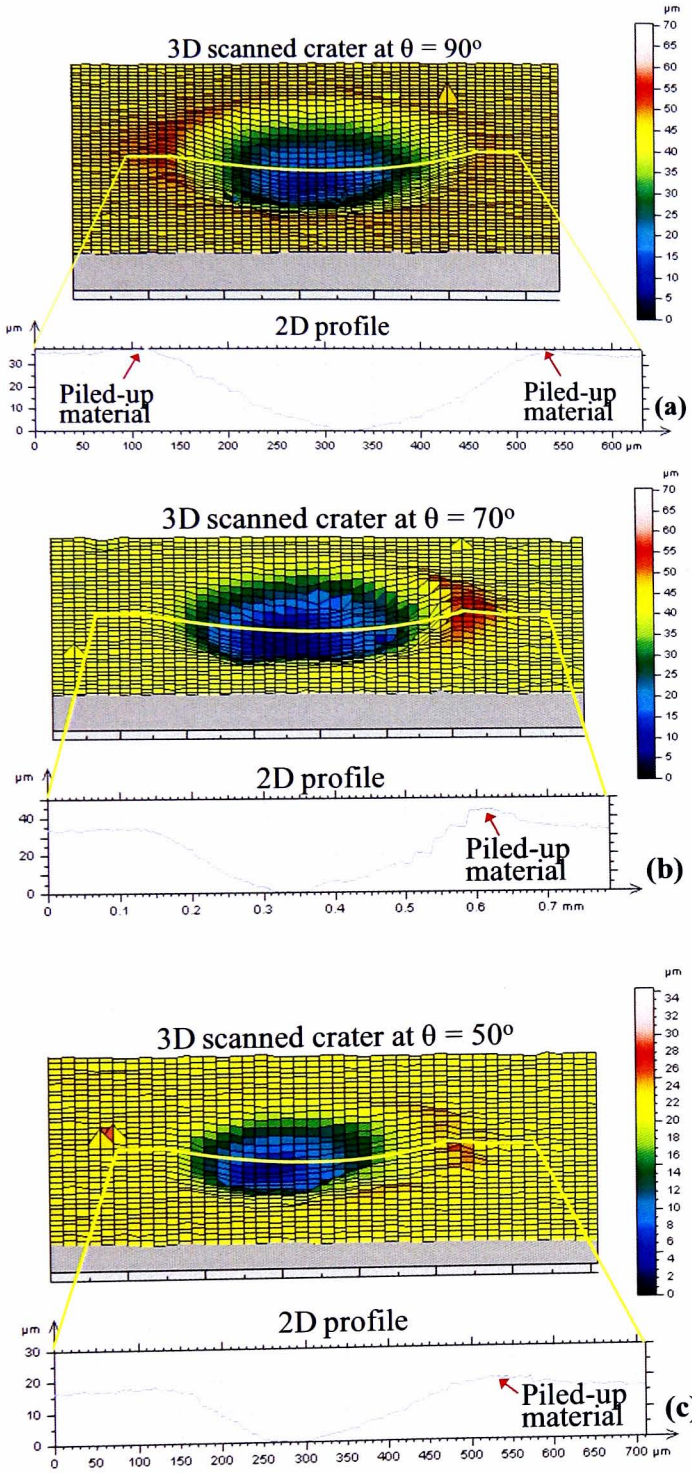


Figure 4-5: Examples of 3D contours of the scanned craters with extracted 2D profiles at $P = 276\text{MPa}$ ($V_{\text{imp}} = 520\text{m/s}$). Impact direction of steel ball is from left to right.

Figure 4-6 illustrates both the qualitative (shape of the crater and material piling up

tendency) and quantitative (dimensions of the craters) comparison of the FE model results with the experimental data. For 90° impacts the FE simulated profile of the crater is similar in shape to that obtained experimentally; the material is piled up at the boundaries of the craters after the impact as the stress waves flow through the material representing the ploughing phenomenon [64]. For the angled impingements, the simulated profiles are steeper towards the trailing edge of the craters as generated in the experiments and more material has piled up along the direction of the impact. This is attributed to the fact that in angled impact, the particle transfers more energy and hence, more plastic deformation to the trailing end of the crater. Afterwards, under the effect of decreasing energy of the particle and reaction forces from the target material, it slides and leaves through the other end of the crater generating relatively less deformation and stresses there.

The depth of the craters from the FE simulations is within the same range (average error $\leq 8.5\%$) as that of the experimental results for all the cases. These differences can be explained by: (i) even after sieving there was still a distribution of sizes of the steel shots used during the experimentation which resulted in different depth of the crater corresponding to different sizes at same impact angle and water pressure, whereas in the FE model only one consistent size of the impacting particle was employed; (ii) steel shots are not always perfectly spherical, this variation affects the shape and the dimensions of the indentations generated in the experiments; (iii) the velocities of the particles leaving the nozzle are not always at the value considered in the FE model (i.e. $0.7 \times V_w$), rather it could be slightly different due to the minor fluctuations in water pressure. This implies that there were craters produced by the particles which had the velocities both lower and higher than the velocity of the particle (V_{imp}) in the FE model; so their depth will definitely vary; (iv) the impact

angle of the steel ball in the model was assumed to be equal to the angle of the jet (nozzle tilt angle), although in real life the particles hit the surface at slightly different local impact angles as explained in ref. [18].

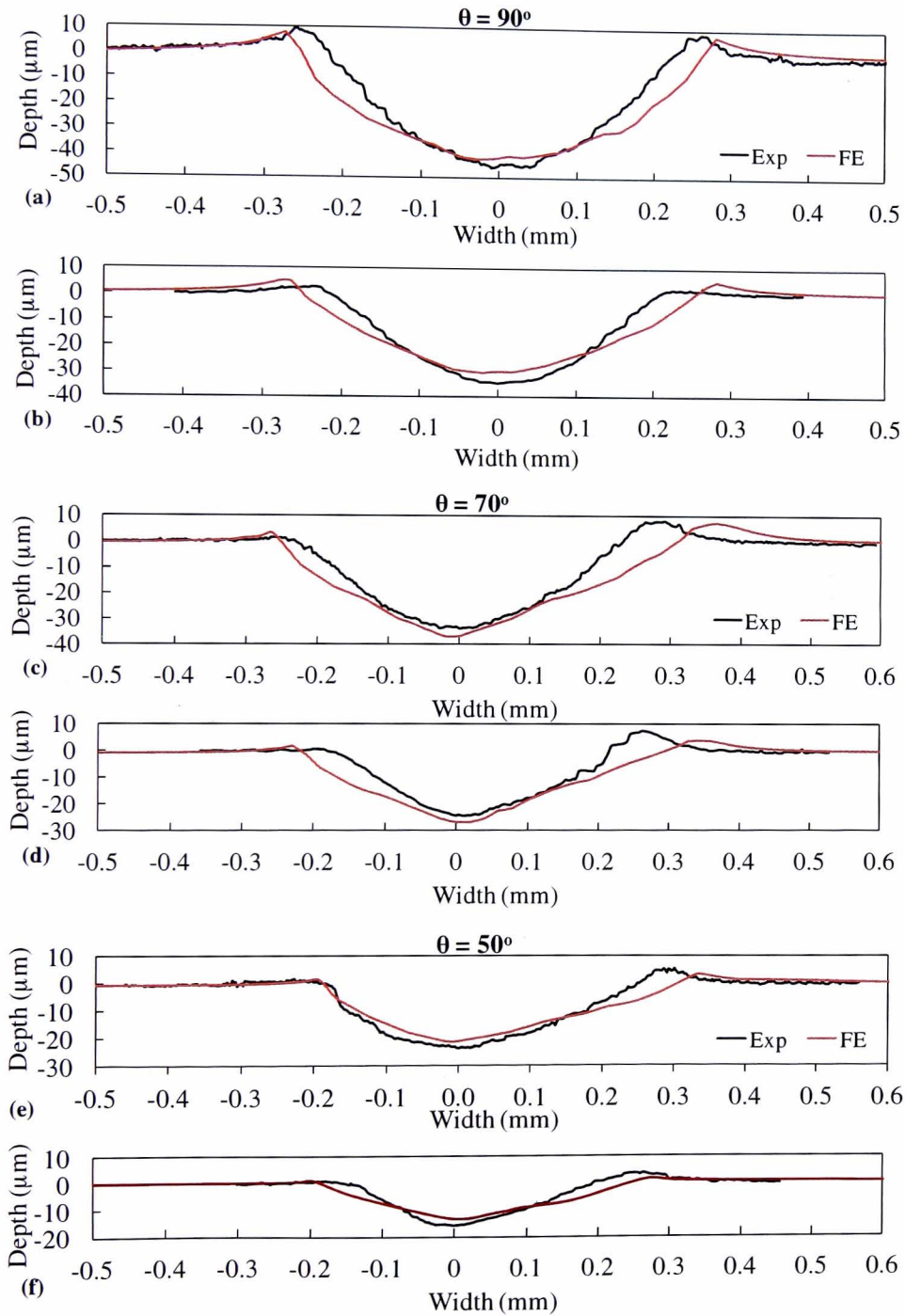


Figure 4-6: Experimental profiles of the craters vs. FE simulation results; P = 345

MPa, $\theta = 90^\circ$ (b) $P = 276$ MPa, $\theta = 90^\circ$ (c) $P = 345$ MPa, $\theta = 70^\circ$ (d) $P = 276$ MPa, $\theta = 70^\circ$ (e) $P = 345$ MPa, $\theta = 50^\circ$ (f) $P = 276$ MPa, $\theta = 50^\circ$. Impact direction is from left to right.

Despite the good agreement in the depth of the craters, there are relatively larger differences in the width of the simulated craters at all impact angles (average error $\leq 13\%$ and maximum error $\leq 21\%$); the reason for this is explained as follows. When the particle impacts the target, initially the contact is established uniformly at the periphery of the ball and the target surface and a smooth initial profile of the crater can be seen in Figure 4-7(a). When these initial contacting elements at the center of the ball fail, a temporary void of elements is created in this region above the target surface and the contact is shifted to relatively less number of nodes of newly exposed elements away from the center. This condition results in more load per node than in real life and hence, more material is displaced towards the edges of the crater than it would have been in reality as shown in Figure 4-7(b, c). After the elements at the periphery of the ball fail, the contact is dominantly shifted back to the center of the ball as shown in Figure 4-7(d). It should be noted that the stages shown in Figure 4-7, i.e. the contact shifting away from the centre of the ball to its edges and then moving back to its centre, are repeated multiple times until the ball finally starts to bounce back, as presented in Figure 4-7(e). It is worth mentioning that the problem remains even if the mesh size is further reduced due to the fact that load per node increases instantly when the elements at the center of the ball are removed. The only difference noted was that the stages presented in Figure 4-7 are repeated more frequently for a finer mesh.

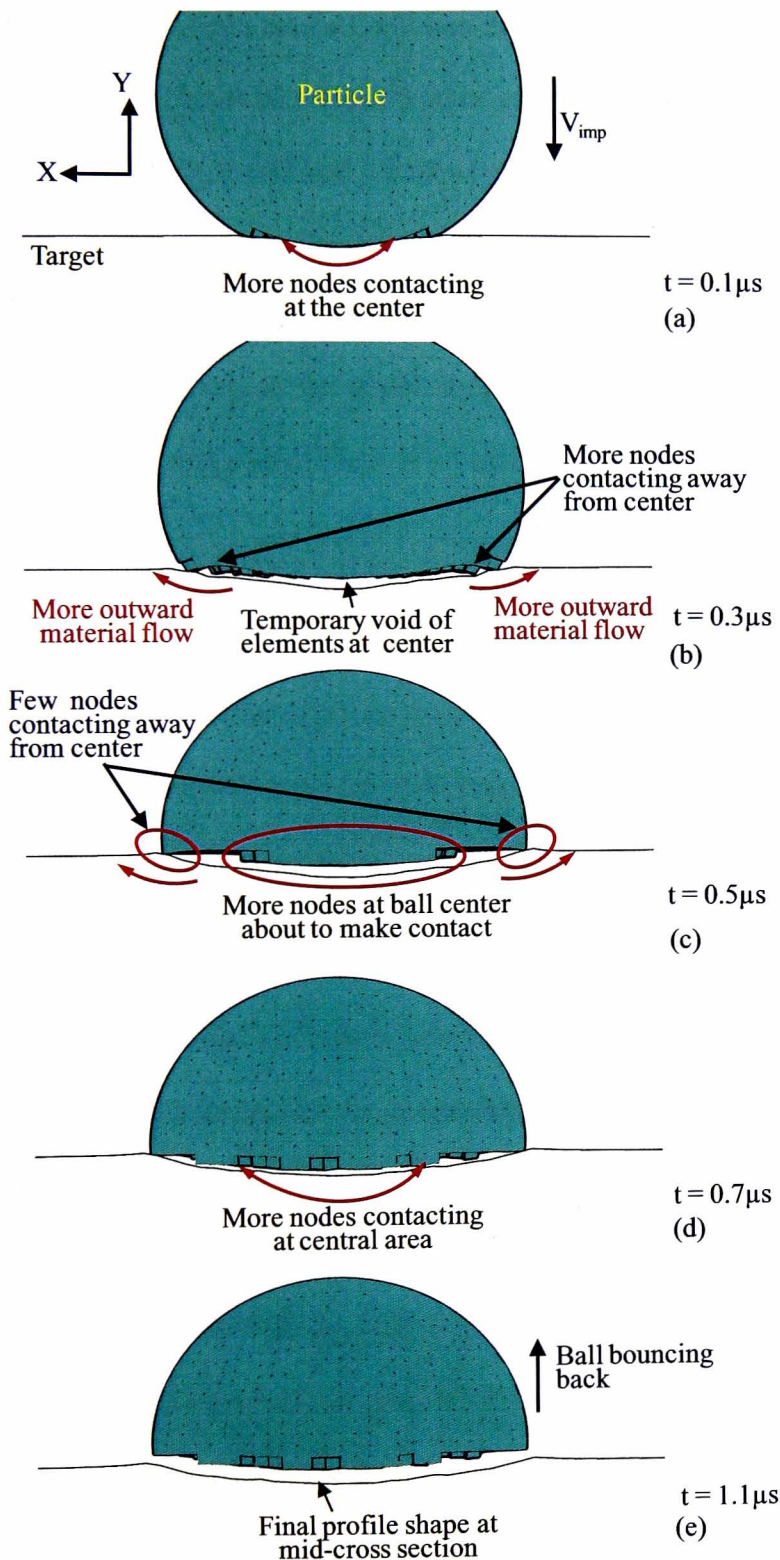


Figure 4-7: Stages of contact between ball and the target during the impact. $P = 276$ MPa, $\theta = 90^\circ$, $t =$ simulation time.

This phenomenon of more displacement of material in the width direction due to the

shifting of contact from the ball centre to the peripheral nodes can also be observed in Figure 4-6 (c, d). It can be noticed that the profiles of the craters for the range -0.12 to +0.12 mm in Figure 4-6(c) and for the range -0.05 to +0.13 mm in Figure 4-6(d), i.e. in the central region where the ball makes the initial uniform contacts, are almost the same as the experimental ones. However, when the contact is shifted to the peripheral nodes, a sudden change in the slopes of the craters can be observed in Figure 4-6(c & d) beyond ± 0.12 mm and -0.05 to +0.13 mm respectively.

Another issue encountered during the impact is that mesh distortion on the target surface is produced because of the tangling/dragging of the exposed internal elements of the steel ball with the elements on the target surface. When the steel ball hits the Ti-6Al-4V surface, the external elements of the ball start failing and new internal elements with a sharp geometry are uncovered and make contact with the target surface and cause distortion on it.

This problem becomes more prominent in the case of angled impingements where the particle also has a horizontal component of the velocity that causes dragging over the target surface as shown in Figure 4-8(a). Figure 4-8(b) shows the final shape of the crater where some relatively more distorted elements exist. This problem is a result of the physics of the problem (i.e. ball with failed toothed elements exerting pressure and sliding over the target surface) and should not be thought of as a result of numerical instabilities. This problem will be minimized when the current model will be extended to simulate the erosion in the Ti-6Al-4V target from multiple particles impingement. In this case, a failure criterion will be incorporated in the target material definition as well, and this will remove the elements before they become excessively distorted. The simulated profiles presented in Figure 4-6 have been extracted in such a way that the

nodes of the excessively distorted elements were not selected in the path of the profile.

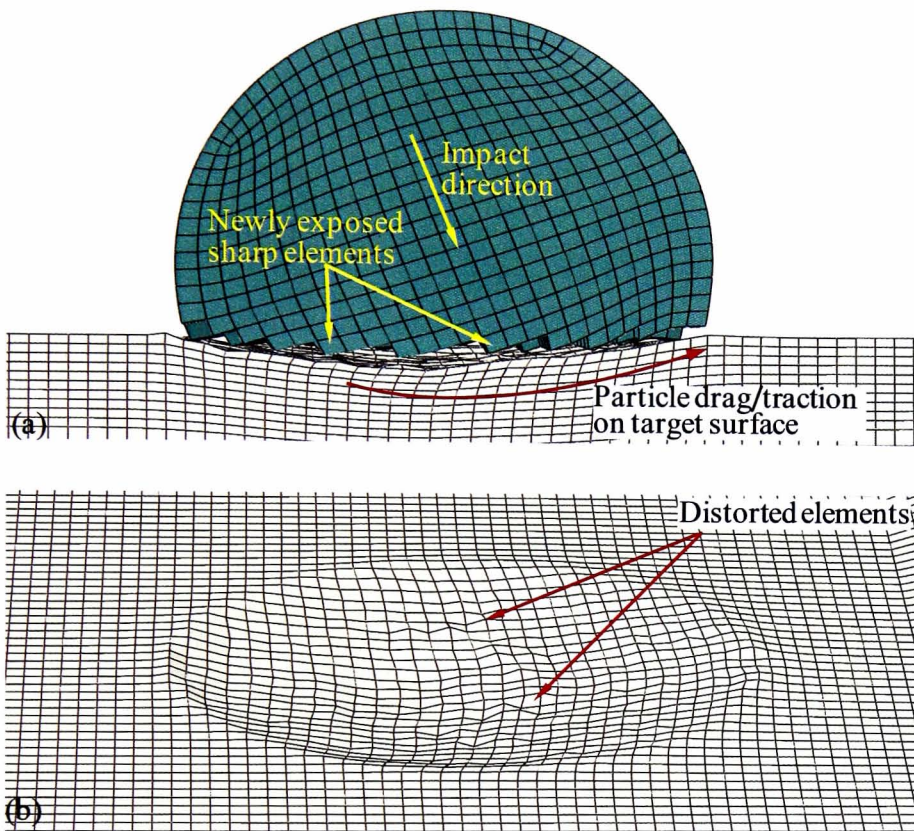


Figure 4-8: $P = 345\text{MPa}$, $\theta = 70^\circ$, (a) Cross-section side view: New exposed elements of the ball making contact with the target surface at time = $0.4\ \mu\text{s}$. (b) Tilted top view of the final shape of the crater at time = $2\ \mu\text{s}$ with some distorted element.

The results of the model were further analysed by qualitative means as follows. It was observed during the optical microscopy of the craters that ring like cracks are formed within the crater formed at 90° impacts. In some cases, such as in Figure 4-4(a, b), a series of circular cracks are present throughout the indented area, and in some cases a dominant ring crack can be observed either near the edge or near the centre of the crater as highlighted by red arrows in Figure 4-9(a) and Figure 4-9(c) respectively. These cracks are formed in the regions that experience the maximum loading during

the impact and hence the maximum plastic deformation. The FE model also successfully captured this effect, as shown in the Figure 4-9(b) where the accumulation of maximum plastic deformation has occurred in the form of rings.

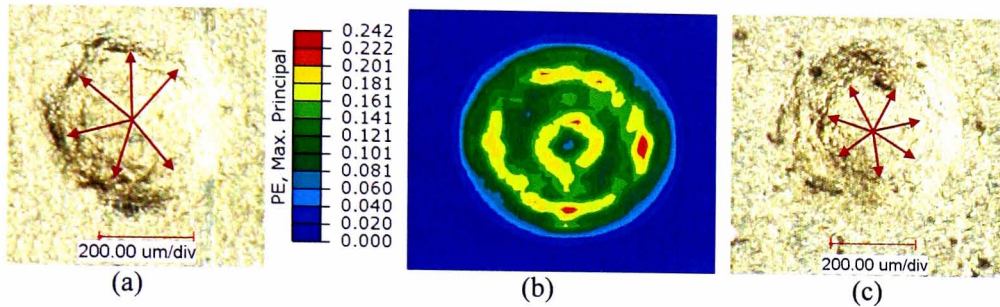


Figure 4-9: Generation of ring cracks in FE and experimental craters at $P = 345\text{MPa}$, $\theta = 90^\circ$, (a, c) experimental craters, (b) contour plot of maximum principle plastic strain produced in crater in the model.

Due to the high speed impingement of the steel ball on the target, residual stresses are induced in the target material. As part of further qualitative validation of the model, Figure 4-10 presents the pattern of the residual stresses induced in the target in the X (S_{xx}) and Z (S_{zz}) directions after the impact of the particle at 90° angle. The plot shows that compressive residual stresses are induced in the target material. The magnitudes of these stresses increase below the target surface and after reaching a maximum at a certain depth, the stresses decrease as the depth increases further and gradually transform into tensile stresses of lower magnitude which then reduce to zero as the depth further increases. Similar patterns were reported for the residual stresses induced in Ti-6Al-4V after multiple particles impact in [112],

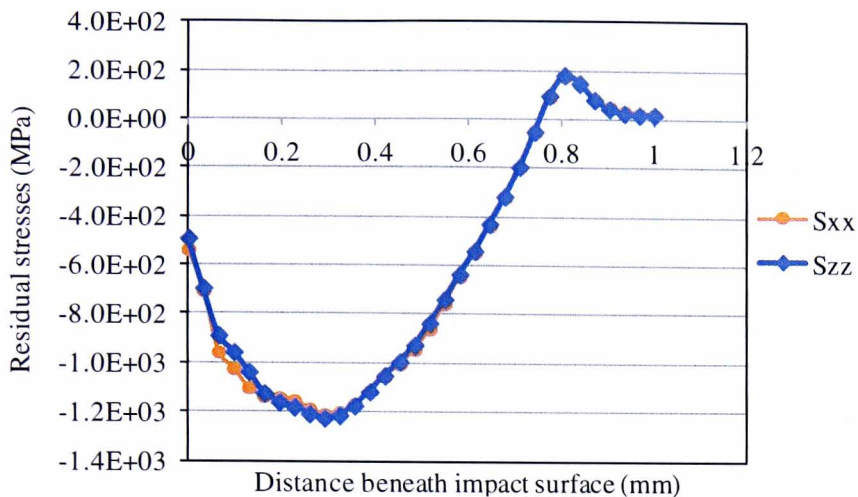


Figure 4-10: Residual stresses induced in the target at $V_{imp} = 581\text{m/s}$, $\theta = 90^\circ$.

The agreement of the simulated results for all the impact velocities and impact angles with the experimental data and the published literature is very encouraging, with an average agreement of $\geq 91.5\%$ in the depth of the simulated craters. This result suggests that the developed FE model is capable of simulating the ultra-high velocity particle impact scenario. Therefore, the model can be extended to multiple particles impact situations.

4.5 Conclusions

This chapter presents an approach for modelling the indentation produced by a single particle impact with an ultra-high velocity, a situation that occurs during abrasive waterjet machining. Of critical importance for the acceptance of the FE model was the development of a carefully designed experimental procedure to provide data on singular particle indentations on the target, which enabled the validation of the proposed model. From the presented work following main conclusions can be drawn:

- The strategy employed for generating the experimental data successfully

provided clear and well defined singular particle indentations from the AWJ impingement over the Ti-6Al-4V target surface at various AWJ pressures and incidence angles. These indentations could easily be distinguished from the craters produced by the water droplets, unlike the case when garnet particles are employed as abrasives.

- In contrast to the previous studies reported for FE modelling of AWJ machining, the present study takes into account more real life conditions of the AWJ such as the high velocity of the impacting particle (up to 581m/s), and its elastic-plastic and failure behavior was also considered rather than considering it as rigid during the impact. The present study has also presented the full in-depth analysis of the simulated craters involving 2D/3D contours of craters at various impingement angles (90° , 70° & 50°).
- The FE simulated profiles of the craters were found to be in good agreement with the experimentally generated data. The maximum depth of the predicted craters was the same as the experimental ones with an average error of less than 8% at any pressure and incidence angles used. The width of the indentations were found to within an average agreement of $\geq 87\%$ when compared with the experimental ones. The proposed model correctly captured the material piling up and ploughing phenomenon during the particle impact. The pattern of the residual stresses predicted by the model was also in line with work reported by other researchers.
- At a 90° impact angle, the FE model has predicted the maximum plastic deformation zones in form of the circular rings which is in agreement with the ring like cracks generated in the experimental craters.

The work presented in this chapter with its carefully considered approaches for model

validation, provides the basis for further more realistic work involving multiple particles impact with the effect of sharp shaped garnet particles to simulate the complete AWJ footprint.

Chapter 5 Finite element modelling of a multiple particles impact

This chapter provides a detailed description of the second stage of the FE modelling where the single steel ball is replaced with multiple garnet abrasive particles; this is to reflect the conditions occurring in real abrasive waterjet milling. A procedure has been devised to select the damage material properties of the garnet abrasives and the Ti-6Al-4V workpiece target material. A method is discussed for selecting the size distribution of the garnet particles after fragmentation and for calculating the number of particles required in the model corresponding to the total mass of the garnet used in the experiments. The results from the multiple particles simulation at various impact velocities are presented, respective erosion rates are calculated and the velocity exponent for target material is determined followed by the conclusions.

5.1 Introduction

As mentioned earlier in section 2.4.1, little evidence exists in the literature for modelling multiple particles impact scenarios for conditions that fulfil the requirements of AWJ machining. The approaches [123], [124] that have been reported for multiple particles impact for AWJ machining are limited to employing only rigid spherical abrasive particles which results in a totally different response as compared to the real deforming sharp shaped particles [65]. Furthermore, the impact velocities utilized in these models (e.g. 220 m/s [119]) are almost half of the experimentally reported values. Knowing the deficiencies of the reported models and following the validation of the FE model for the single particle impact situation, the next step considered was to extend the FE model to a more real situation of multiple particles impact while taking into account the effects of particles shapes and sizes.

It should be noted that in the first stage of FE modelling (Chapter 4), as a starting point to validate the FE model, a relatively simple situation was selected, i.e. steel shots of known shape and size were used as the abrasives (impacting particles). After gaining the confidence that the model was working correctly at this stage, the steel shots were replaced with the garnet particles which are commonly employed abrasives during the AWJ machining [43]. The challenges that were addressed for developing the multiple particles impact model are detailed below.

5.2 Selecting the appropriate material properties

5.2.1 Material properties for the garnet particles

Garnet is classed as a brittle material and is known to fracture during impact loading [159]. As mentioned in section 3.4.2.2 a tensile failure criterion is recommended for modelling brittle materials during the impact. In order to utilize this criterion, the value of the failure stress for the garnet is required. Various experimental studies have been reported that demonstrate the fact that brittle particles such as silicon carbide (SiC) and alumina (Al_2O_3), silica (SiO_2) fracture completely upon impact at much lower velocities (≤ 100 m/s) compared to the range of velocities (368 m/s – 581 m/s) used in the current study [126], [160], [161], [162]. This is true for both macro [126] and micro [161] sized brittle particles.

It is also reported that the highest tensile stress occurs internally in the impacting particle; however, the failure is caused by the lower tensile stresses developed on the surface of the particle due to the flaws present on the surface of the particle [125]. This is the reason that the reported fracture velocities and the failure tensile stresses of the brittle particles were found to be quite low as highlighted in Table 5-1.

Table 5-1: Fracture velocities and associated failure stresses for some irregular shaped brittle particles [161]

Material	Fracture velocity, U (m/s)	Failure stress, σ_{θ} (MPa)
SiO ₂	62-83	70-99
Al ₂ O ₃	68-81	131-159
SiC	90-100	160-180

Furthermore, it was demonstrated that the value of the failure tensile stress in the abraded brittle particles of different materials was reduced by a factor of ~2.4 compared to when there are no scratches or abrasion marks (surface flaws) on the surface of the particles [162]. Therefore, a relatively lower value of the failure stress could be expected for garnet particles due to the fact that they underwent an abrasion phenomenon during their delivery through the abrasive hopper and developed surface flaws while passing through the focusing nozzle due to the collisions among the particles themselves and with the nozzle walls. The procedure, acquired from refs. [159], [161], to calculate the failure stress for the garnet is detailed as follows.

The average failure load for garnet (mesh 80) during a uniaxial compression test is reported as 5.66 N [159], which is similar to that reported for silica [161]. Silica particles of size ~ 700 μm are reported to fracture at an impact velocity of ~ 70 m/s [161]. Since it is known that the fracture velocity of the particles increases as the particles size decreases [126], in order to compensate for the size difference, fracture velocity (U) for garnet (average diameter after fragmentation 190 μm [16]) was doubled, i.e. 140 m/s. Assuming that the entire kinetic energy (K.E) of the impacting particle is converted into plastic work in the target to create the indentation and the

contact pressure remains constant during the impact, the K.E and the plastic work can be related as follows:

$$\mu V = \frac{1}{2} m U^2 \quad \text{Eq. 5.1}$$

where μ is the contact pressure, m is the mass of the impacting particle and V is the volume of the indentation given by:

$$V = \frac{\pi h^2 (3R - h)}{3} \quad \text{Eq. 5.2}$$

where R is the radius of the impacting particle and h is the depth of the indentation known from the experiments. It should be noticed that to make these calculations possible, the impacting particle was assumed to have a spherical shape with a radius R and the indentation was assumed as a spherical cap as shown in Figure 5-1 [161].

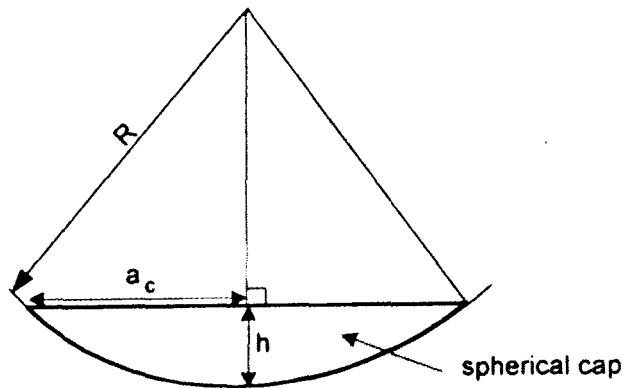


Figure 5-1: Schematic diagram of a spherical cap [159].

The contact radius (a_c) can be calculated as follows:

$$a_c = \sqrt{R^2 - (R - h)^2} \quad \text{Eq. 5.3}$$

Knowing a_c , the force (F_o) acting on the impacting particle can be calculated as

$$F_o = \mu \pi a_c^2 \quad \text{Eq. 5.4}$$

In order to determine the value of F_o , the parameters required were; (i) U i.e. impact velocity at which the particle fractures which was assumed to be 140 m/s, (ii) R i.e. radius of the impacting particle 95 μm , (iii) m i.e. the mass of the impacting particle which was calculated as 0.0148 mg based on assuming the particle to be equivalent in mass of a sphere of radius R and (iv) h i.e. the value of the depth of the craters produced in the target when the particle hit the target at the velocity $U = 140\text{m/s}$. The value of h was determined as $\sim 14\mu\text{m}$ from the experiments. This was done by inserting a few (10 – 20) garnet particle in the abrasive inlet and setting the water pressure at 20MPa which resulted in accelerating the particles to the velocity of $\sim 140\text{m/s}$. Using the values, $U = 140\text{ m/s}$, $m = 0.0148\text{ mg}$, $R = 95\ \mu\text{m}$ and $h = 14\ \mu\text{m}$ in Eq. 5.1 to Eq. 5.4 gives $a_c/R = 0.53$ and $F_o = 20\text{ N}$. Using the value of a_c/R in Figure 5-2 gives $\sigma_\theta \pi R^2 / F_o = 0.22$ from the curve of surface stress, and hence the value of σ_θ is determined as $\sim 150\text{ MPa}$. The material properties used for the garnet are listed in Table 5-2.

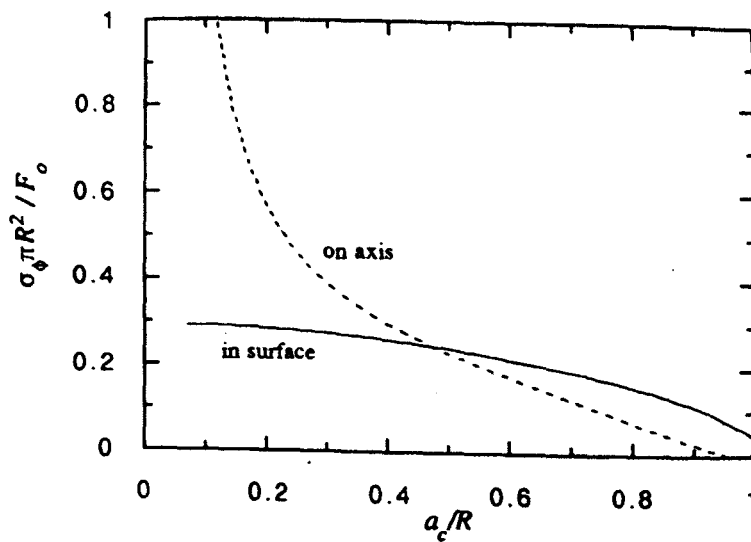


Figure 5-2: Variation of maximum tensile stress on the axis and on the surface of the particle during impact [160].

Table 5-2: Material constants for garnet

Density	4120 (Kg/m ³)
Young's Modulus	248 (GPa)
Poisson ratio	0.3
Tensile failure stress (σ_{cutoff})	150 (MPa)

5.2.2 Material failure model for Ti-6Al-4V

In Chapter 4, while modelling a single particle impact, the Ti-6Al-4V target was modeled only with the Johnson and Cook (JC) plasticity model based on the fact that no significant material removal was observed in the experiments. However, for multiple particles impact, a failure material model is required in the target material definition to simulate the material removal. As mentioned in section 3.4.2, the JC failure criterion was used to simulate the erosion in the target material. It was found in the preliminary research that the material constants adapted for the JC damage model from the work of Lesuer [147] produced excessive erosion in the target even for few

particles impact. A similar problem was also observed in previous work [163], [164], [165], [166], [167], where the as-is material constants adapted for the damage model resulted in over-erosion in the target. This happened due to the difference between the conditions (e.g. size, shape and velocity of impacting projectiles and resulting strain rates) at which the simulations were run and the conditions when these material constants were determined. It is further highlighted in these studies that due to unavailability of experimental data at higher strain rates, it is necessary to calibrate the damage parameters for a specific mesh size to attain a better agreement with the experimental data. The reported research also demonstrated that in the erosive impact simulations, simply refining the mesh size does not improve the simulation results. A preliminary study carried within this research also showed that as the mesh was refined in the fine mesh region, a continuous increase in the erosion rate (ER) occurred, as shown in Figure 5-3. The mesh size shown in the Figure 2 refers to the element size in the X direction in the fine mesh region, while the size of the element in Y and Z-directions were changed accordingly keeping the element aspect ratio the same in all the cases.

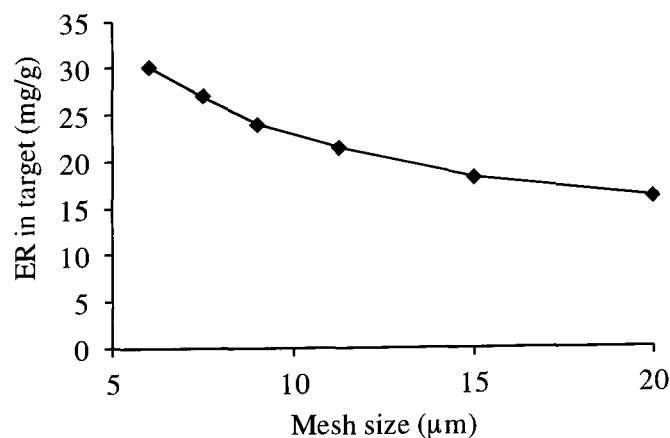


Figure 5-3: Results for mesh convergence study at $P=138\text{MPa}$ ($V_{\text{imp}}=368\text{m/s}$).

Billon et al. [166] also found a similar behavior in their FE model, i.e. the ballistic limit of their target decreased by refining the mesh i.e. the impacting projectiles penetrated through the same thickness of the target at lower impact velocities when the smaller mesh size was used in the target. This means that the target became more erodible by reducing the element size in it. Therefore, in the current study an optimum mesh size of $X \times Y \times Z = 20 \times 7 \times 22.5 \mu\text{m}^3$ was selected after several trials. The selected mesh size is considered small enough to capture the fine details of footprint generated without consuming unnecessary computing resources. A relatively smaller element size was selected along the direction of the impact aiming to ensure that a sufficient number of elements were used to capture a smooth profile of the single footprints where the maximum depth is in the range of 75 – 200 μm .

Since no experimental data could be found in the open literature on the damage constants for Ti-6Al-4V at strain rates above $10^4/\text{s}$, and based on the highlighted necessity of re-calibrating the damage constants in the FE model for a specific mesh size for obtaining a good consistency with the experimental results [110], [164], [165], the value of the JC damage parameter d_1 was increased from -0.09 as in ref. [147] to 0.28 in the current study, i.e. it was assumed that no failure in the target will occur for $\varepsilon_f \leq 0.28$. The damage constants used for the Ti-6Al-4V were $d_1 = 0.28$, $d_2 = 0.25$, $d_3 = -0.5$, $d_4 = 0.014$, $d_5 = 3.87$.

Since the value of the tensile failure stress ($\sigma_{\text{cutoff}} = 150\text{MPa}$) for the impacting particles and the damage parameter d_1 for the JC failure model for Ti-6Al-4V were determined in the current research, it was attempted to analyze how much the erosion rate in the target material is sensitive to these values. This was done by running the FE model at 10% higher and 10% lower values of both σ_{cutoff} and d_1 and comparing

the erosion rate among the different cases. No significant differences were observed in the erosion rates in the target at any combination of the values of σ_{cutoff} and d_1 . This is due to the fact that in the high velocity impact situation the deformations are mainly governed by the K.E and momentum of the impacting particles [127] which remained unchanged.

Furthermore, it should also be noticed that the values of the tensile failure stress (σ_{cutoff}) for the garnets particles and the damage parameter d_1 for Ti-6Al-4V were kept constant for all the simulations in the current research.

5.3 Selecting the sizes of the garnet abrasive particles

In the AWJ milling process, the jet footprint is mainly generated as a result of cumulative erosion caused by the impact of the high velocity abrasive particles of different sizes upon the target surface. It has been reported that during high velocity ($\geq 500\text{m/s}$) impact conditions, the response of the material (deformation/erosion) is mainly dominated by inertia [127] which is the property of the mass (size) of the impinging particles. Since the abrasive particles undergo fragmentation while passing through the nozzle (focussing nozzle) [12], it is very important to carefully consider in the model the real sizes of the abrasive particles that impact the surface. This aspect was addressed by selecting the size distribution (SD) of the mesh 80 garnet particles after enduring a fragmentation process as reported from the experimental work of Babu and Chetty [16] (see Table 5-3). In this way, the particle sizes closer to the reality were utilized in the FE model rather than just employing one single size for all the particles [123], [124]. It should be noted that the SD acquired in the model (column A in Table 5-3) did not consider the garnet particles in the range of 355-400 μm , 315-355 μm , 63-90 μm and the pan (dust < 63 μm) which comprise ~18% of

the total mass of the garnet after the nozzle exit. The first two sizes were ignored because they only add up to 1.8% of total mass and the last two were discounted as a preliminary FE investigation indicated that the impact of the particles within these size ranges had negligible contribution in the overall erosion process compared to the larger sizes particles. This implies that whichever garnet mass is used in the experiments, 82% of it will be used in the FE simulation.

Babu and Chetty [16] also reported the percentages of mass as mentioned in column C in Table 5-3 for each size (column A) of the fragmented garnet abrasives. It was required to convert these percentages of mass into the number of particles to be used for each size in the FE model. To fulfill this task, a term “*particles mix*” was defined which referred to a group of 19 garnet particles in the model which contains approximately the same proportion of mass for each size of the particles as in real life after fragmentation through the nozzle. The group of these 19 particles (*particles mix*) was used repeatedly to attain the required total mass of the abrasives in the model. While calculating the number of particles for each size in one *particles mix*, it was aimed to match the corresponding values in column D (relative percentage of each size among selected sizes in real life) and column G (relative percentage of each size by mass in model) of Table 5-3. This was done by developing an excel file and changing the value of Column E until the value of columns D and G closely matched. This ensured that the amount of mass used in the FE model for a particular abrasive size was as close to the AWJ experiments as possible.

Table 5-3: Details of the abrasive particles mix used in the FE model

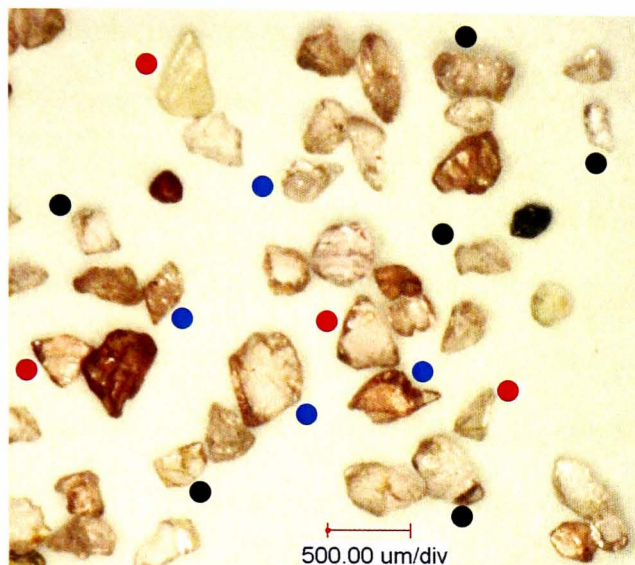
A (mm)	B (mg)	C (%)	D (%)	E	F (mg)	G (%)
0.275	0.041	0.14	0.17	1	0.041	0.19
0.225	0.029	0.24	0.29	2	0.057	0.27
0.190	0.014	0.10	0.13	2	0.028	0.13
0.170	0.010	0.13	0.16	3	0.031	0.15
0.140	0.006	0.12	0.14	5	0.029	0.14
0.125	0.004	0.09	0.11	6	0.025	0.12
Total		0.82	1.00	19	0.211	1.00

Legend for Table 5-3

- A Approximated particle size used in model adapted from Babu and Chetty [16] (mm)
- B Mass of each particle based on a sphere of same diameter (mg)
- C Percentage by mass of each size in the collected fragmented garnet abrasives from experiments [16] (%)
- D Relative percentage of each size by mass among selected sizes in real life (%)
- E Total number of particles used of this size in one particle mix
- F Total mass of each size in one “particles mix” (mg)
- G Relative percentage of each size by mass in model (%)

5.4 Selecting the shapes of the garnet abrasive particles

In the majority of the studies reported for the FE modelling of the AWJ machining process (discussed in section 2.4.1), only a spherical shape of the garnet particle was used, whereas in reality the garnet particles are of irregular shapes with sharp cutting edges as shown in Figure 5-4. This difference significantly affects the accuracy of the model by changing the erosion mechanism in the model since the spherical particles create a ploughing deformation with lower erosion rates compared to sharp shaped particles which are well-known for their cutting deformation behavior with higher erosion rates [64], [168].



● Triangular shaped ● Rhombic shaped ● Trapezium shaped

Figure 5-4: Shapes of the garnet observed under the optical microscope. The colored dots adjacent to the particles represent the category of the shapes they belong to.

In order to further elaborate the significance of the influence of the shape of the impacting particle,

Figure 5-5 shows the comparison of the material removal in a ductile target after multiple (50) impacts for each particle shape shown in the figure [128].

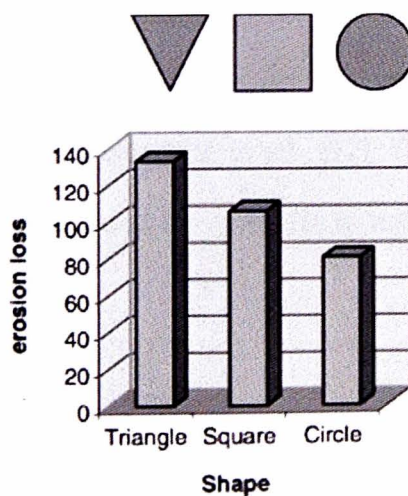
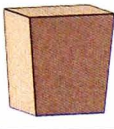
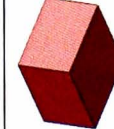
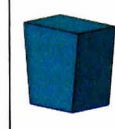
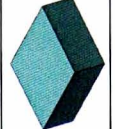


Figure 5-5: The effect of the particles shape on erosion rate in the target material under the impact of 50 particles [128].

The mass of the impacting particles for each of the shapes was the same. It can be seen that each shape resulted in different amounts of material eroded from the target with the highest erosion rate occurring in the case of sharp shaped (triangular) particles and the lowest for the spherical particles. This is due to the facts that: (i) sharp edges contact during the impact created very high shear stresses resulting in more target surface damage and (ii) different amounts of energy were transferred to the target surface per unit area due to the differences in the contact area in each case. Due to the sharp edged contact in case of triangular particles, more kinetic energy is transferred to a relatively smaller area which resulted in higher erosion rate as compared to the rounded particles. This emphasized the importance of correctly selecting the shape of the impacting particles during the model development.

To address this issue, three different shapes of the abrasive particles (triangular, rhombic and trapezoidal) were employed in the current model. These shapes were selected from the usually occurring shapes of the garnet particles as observed under an optical microscope as depicted in Figure 5-4 and were in line with the generic shapes of the garnet particles as presented in ref. [12]. The sizes allotted to various shapes and numbers of particles used for each size in one particles mix are listed in Table 5-4.

Table 5-4: Sizes and number of particles assigned to different shapes. (Note: particles shown in the table are not to scale)

Shapes used						
Assigned Sizes (μm)	275	225	190	170	140	125
No. of particles of this shape in one particles mix	1	2	2	3	5	6

5.5 Contact

When an element is removed from the mesh, its nodes act as free-floating point masses that are capable of transferring momentum either to the incoming particles by striking them or to the target surface by bouncing back from the following impacting particles. In order to avoid this situation, the “nodal erosion” capability of ABAQUS was incorporated in the contact definition to eliminate the masses of these free flying nodes from the simulation and thus making them ineffective. Figure 5-6 represents a situation when the nodal erosion option was not included in the contact definition.

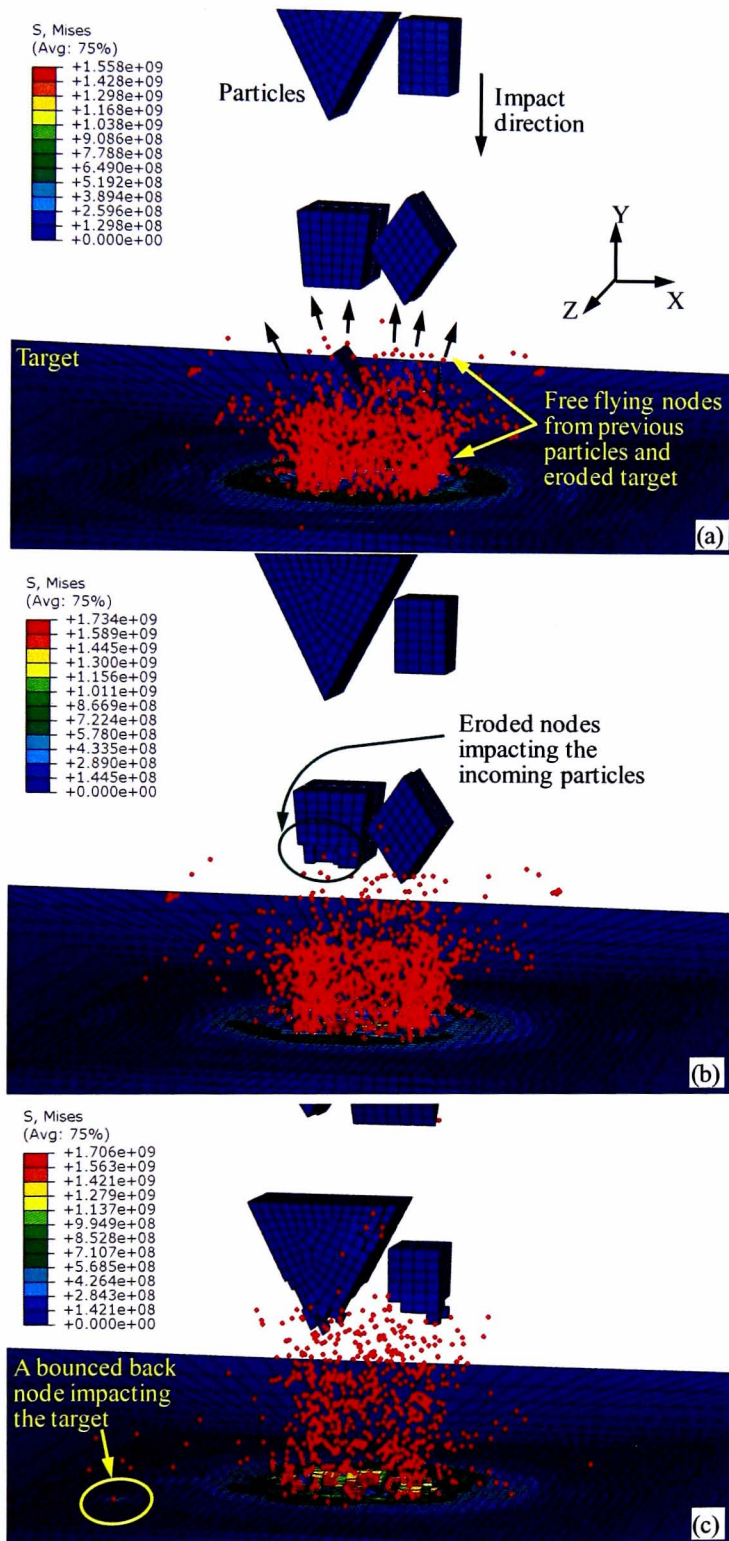


Figure 5-6: Free flying nodes from the eroded elements impacting the incoming particles.

It can be observed in Figure 5-6(a) how the nodes from the previous impacted particles and the eroded target were dispersed in various directions under the corresponding reaction forces, as highlighted by the black arrows. When these eroded nodes collided with the new incoming particles, stresses were generated in the particles prior to impact and their elements were removed as shown in Figure 5-6(b). Furthermore, after hitting the incoming particles, these nodes were bounced back towards the target and caused the stresses to be developed in the target away from the particles impact site as depicted in Figure 5-6(c). Figure 5-7 shows the difference in the stress pattern after the impact of 38 particles (i.e. 2 particles mix) when the nodal erosion was included (Figure 5-7(a)) in the contact and when it was not active (Figure 5-7(b)). It can be seen in Figure 5-7(a) that the stresses were uniformly distributed around the vicinity of the particles impact whereas the stress pattern is quite distorted when the nodal erosion option is inactive, as shown in Figure 5-7(b). This is due to the fact that in the latter case the eroded nodes were continuously hitting the impacting particles and reflecting back to strike the target on random locations around the main impact site and caused disturbances in the normal stress pattern. Therefore, in order to correctly simulate the multiple particles impact situation, it is important to remove the masses of the eroded nodes before these could affect the following impacting particles or the target surface.

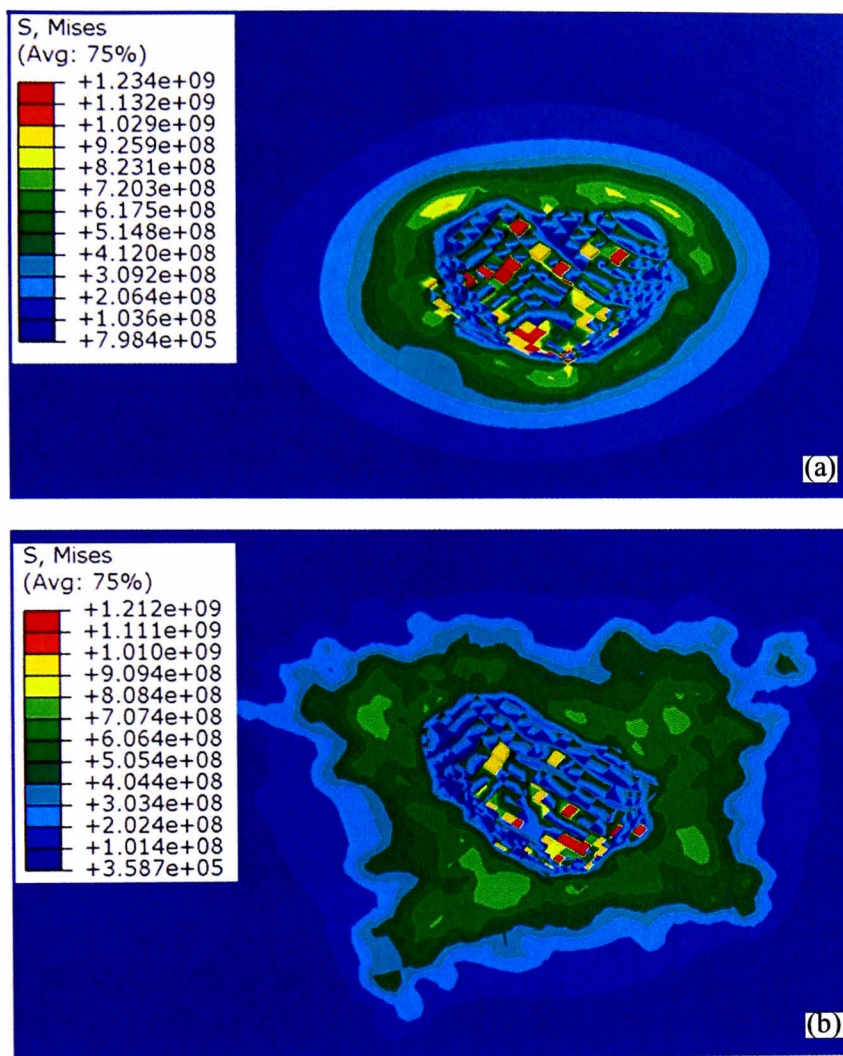


Figure 5-7: Stress patterns developed after 38 particles impact: (a) with nodal erosion option active and (b) without nodal erosion.

5.6 Results and discussions

Figure 5-8 shows the upgraded FE model after including the garnet particles of various shapes and sizes and incorporating the damage material properties of Ti-6Al-4V. The colour scheme used for the garnet particles is the same as presented in Table 5-4.

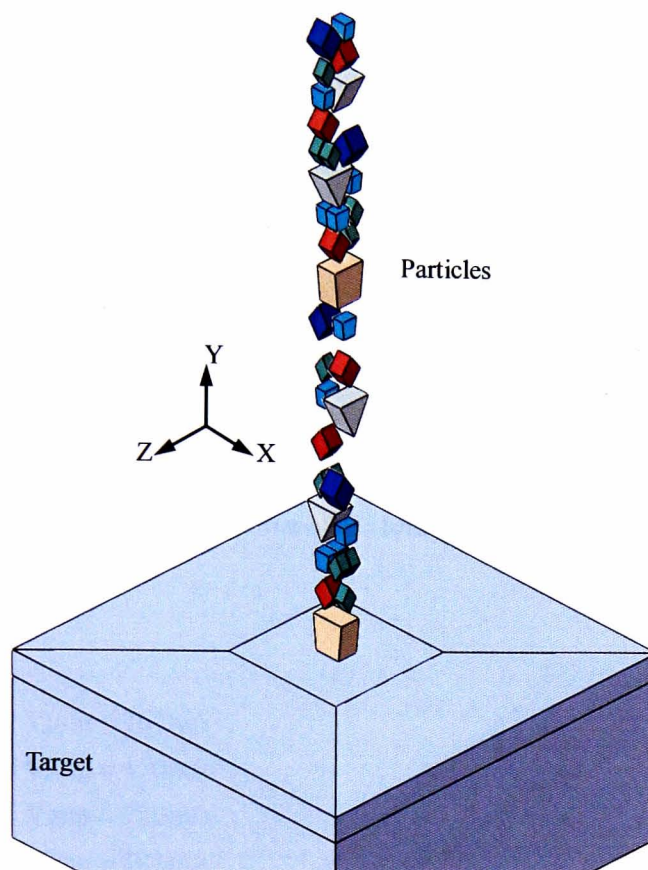


Figure 5-8: Multiple particles FE model

It has been reported by a number of researchers [97], [138], [169] that the erosion rate (ER) in a material is directly proportional to the exponent (n) of the impacting velocity (V_{imp}) of the particles as mentioned in Eq. 5.5. A value of $n = 2$ was reported by Finnie [60] for ductile materials and a value of 2.5 was suggested by Hashish [133]. An experimental value of 2.35 was found for the velocity exponent for Ti-6Al-4V by Yerramareddy [170].

$$ER \propto V_{imp}^n \quad \text{Eq. 5.5}$$

In order to calculate the exponent “ n ” from the model and check its validity, the subsequent procedure was followed. Particles impacting the workpiece at different

impact velocities at 90° incidence angle were simulated using the FE model. A plot of the mass lost (mg) in the target vs. the cumulative mass of the particles was constructed. The steady state erosion rate (ER) for each impact velocity (V_{imp}) was determined from the slope of the fitted straight line through the data points, given as mass loss in target per gram of erodent (mg/g) as shown in Figure 5-9. The erosion rate increased with the increase of the impact velocity due to the fact that the increase in velocity resulted in an increase of the kinetic energy of the particles. This led to more erosion in the target material at the same total mass of the impacting particles.

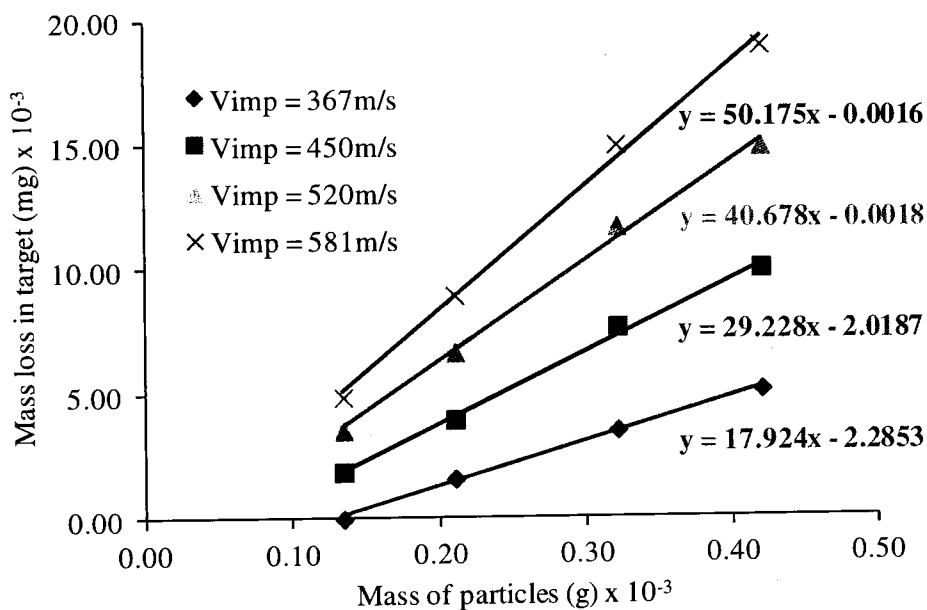


Figure 5-9: Steady state erosion rates in Ti-6Al-4V determined for various velocities from FE simulations. The particles impact velocities of 367m/s, 450m/s, 520m/s and 581m/s represent the water pressures of 138MPa, 207MPa, 276MPa and 345MPa respectively.

Eq. 5.5 can also be written in the following form:

$$\log(\text{ER}) \propto n \log(V_{imp}) \quad \text{Eq. 5.6}$$

This means that the exponent “n” can be determined from the slope of the line by plotting $\log(\text{ER})$ vs. $\log(V_{\text{imp}})$. Using the values of the erosion rates (slopes) from Figure 5-9, the data points in Figure 5-10(a) were obtained. The slope of the straight line fitted through these data points provided the exponent “n” equal to 2.25 for Ti-6Al-4V. The above procedure was repeated to calculate the experimental value of the velocity exponent as shown in Figure 5-10(b). This value of “n” determined from FE simulations falls within the ranges of the experimentally calculated value 2.55 and the reported experimental value (2.35) for Ti-6Al-4V [133]. This is one of the advantages of the FE modelling where, without doing experimentation, important material constants could be determined. The good agreement between the simulated and experimental data indicates the good reliability of the model.

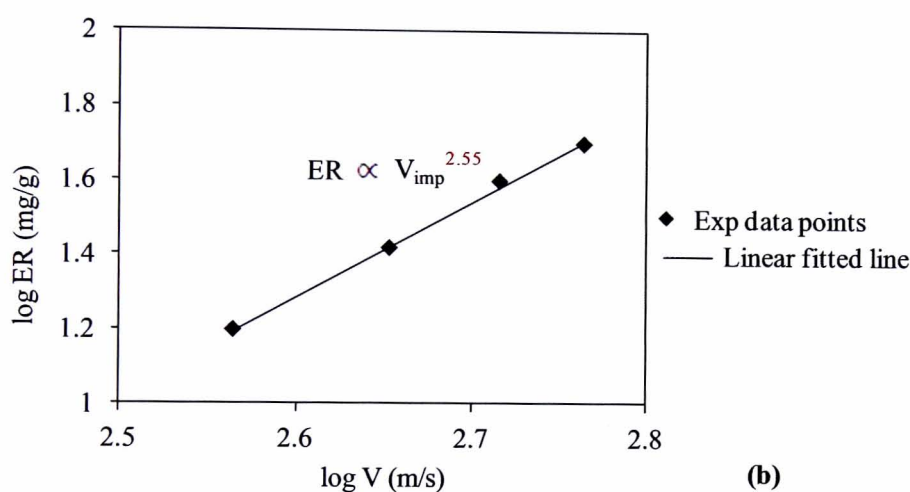
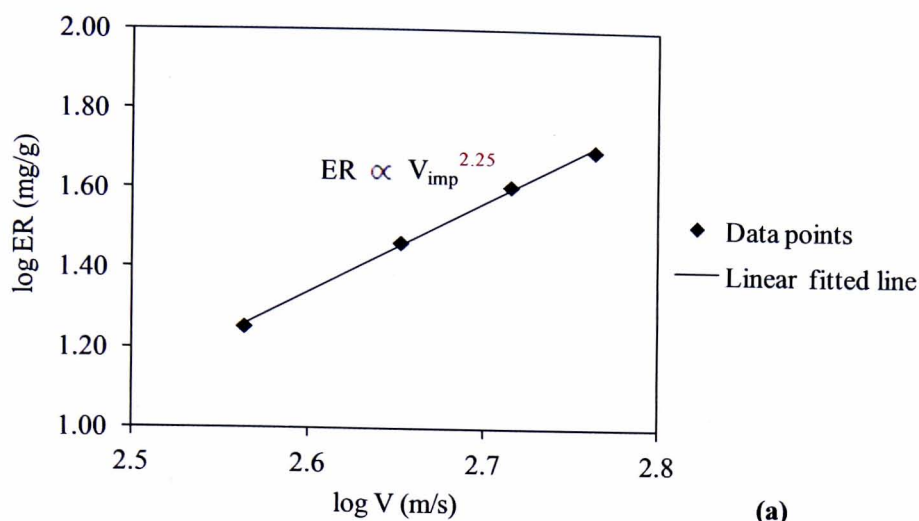


Figure 5-10: Variation of erosion rate with impact velocity; (a) FE simulation results, (b) experimental results.

5.7 Conclusions

This chapter presents an approach for modelling of impact of the multiple garnet abrasives with ultra-high velocity; a situation that occurs during abrasive waterjet machining. It was of much importance to carefully check the validity of the FE model for a relatively few multiple particles impact before proceeding to the simulation of a more complex situation, i.e. a complete jet pass containing hundreds of particles. The following main conclusions can be drawn from the presented work:

- A large majority of published literature proves the fact that the brittle particles fractures upon impact at relatively much lower impact velocities than those expected in AWJ machining. Therefore, unlike the previous AWJ FE modelling approaches, the garnet particles were modelled as elastic with a tensile failure criterion rather than considering them as rigid.
- The damage properties were incorporated in the Ti-6Al-4V material definition to simulate the erosion in the target and the Johnson-Cook damage constant “ d_1 ” was recalibrated for the mesh size that was used in this study.
- Due to the critical importance of inertial affects during the impact problem, the FE model takes into account the size distribution of the garnet particles after the fragmentation from the focussing nozzle rather than assuming a single size for all the particles. Thus, the FE model attempts to consider the sizes of the impacting particles which is as close to reality as possible.
- Considering the significant effect of the shape of the particle during the impact, the garnet particles were modelled in three different shapes with sharp edges, contrary to the usual approach of considering them as spherical shapes. The selected shapes were in line with the shapes of garnet particles observed under an optical microscope.
- It was demonstrated that the free flying nodes left from the eroded elements in the model collided with the following impacting particles and the target as well after reflecting back from the particles and caused damage in them. It is therefore necessary to remove the masses of these eroded nodes during the multiple particle impact situations.
- The model was run with 38 particles at four different impact velocities. By using the calculated erosion rate in the target material at each impact velocity, the

velocity exponent “n” was determined as 2.25 which is within the same range as the calculated experimental value (2.55) for Ti-6Al-4V.

The agreement of the simulated results with the published literature is very encouraging. This result suggests that the extended FE model is capable of simulating the more real situation of multiple garnet particles impact. The model will now be extended to simulate the single jet footprints at various pressures and traverse speeds.

Chapter 6 Finite element modelling of a single jet pass

This chapter provides detailed description of the third stage of the FE modelling where a single pass of the abrasive waterjet plume was considered in the model. The model includes the effects of the mass flow rate of the abrasives and the traverse speed, which are very important parameters while modelling the AWJ milled footprints. In the model, it is necessary to “assemble” the particles close to each other in the form of layers to run the simulation efficiently. A procedure is devised to arrange the garnet abrasive particles in the jet plume in such a way that they form a Gaussian spatial distribution around the jet central axis. Results from the FE simulations and the experiments are presented, compared and discussed, and conclusions are drawn.

6.1 Introduction

It has been detailed in section 2.4.1 that very limited research has been reported in the literature regarding the FE modelling of AWJ machining where the effects of traverse speed and mass flow rate have been considered. Two studies [129], [131] were reported for AWJ cutting; however, both these studies ignore the effects of the shapes and sizes of the impacting garnet particles. The fracturing phenomenon of the abrasive (garnet) particles was also neglected, leading to abrasion levels that cannot be matched to the reality. Moreover, in these approaches, it was not highlighted how the velocities of the impacting particles were assumed corresponding to the working water pressures.

Realizing the deficiencies of the reported models and following the extension and validation of the proposed FE model for multiple garnet particles impact, the model

was further developed to simulate the single jet footprint while taking into account the effects of traverse speed, mass flow rate and Gaussian distribution of the particles in the jet plume. This chapter addresses the scientific challenges such that the AWJ milled footprints can be predicted with good accuracy for a wide range of operating parameters. The challenges that were addressed for developing the single AWJ pass model are detailed below.

6.2 Finite element modelling

Owing to the symmetry of the AWJ milling at a 90° incidence angle, as illustrated in Figure 6-1, and to save computational time, only a half model was developed and evaluated at this stage. After completing the simulation, the half footprints were mirrored and then compared with the experimental footprints. The modelling procedure is discussed below.

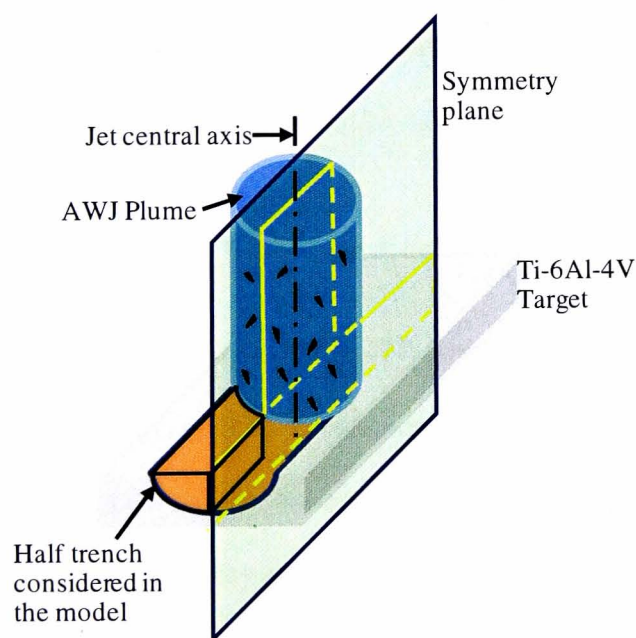


Figure 6-1: Symmetry of the AWJ milling process at 90° incidence angle.

6.2.1 Calculating the required mass of abrasive particles

Since the model was now required to incorporate the effect of the mass flow rate of the garnet particles, it was important to run the model with the same amount of mass of abrasives impacting per unit length as in the experiments. The calculations for obtaining the mass and number of the abrasive particles for a given length (L_{FE}) in the FE model are presented as follows.

Let V_f (mm/min) be the jet traverse speed and \dot{m}_a (kg/min) be the abrasive mass flow rate used in the experiments. The mass of particles impinged per unit length in the experiments, m_L (kg/mm) is therefore given by:

$$m_L = \dot{m}_a / V_f \quad \text{Eq. 6.1}$$

Since only a symmetrical half model was employed in the FE model and 82% of the total mass was used in the experiments (as explained in section 5.3), the mass of the particles required in the FE model (m_{FE}) can be calculated as follows:

$$m_{FE} = 0.5 \times 0.82 \times m_L \times L_{FE} \quad \text{Eq. 6.2}$$

where L_{FE} is the length to be traversed in the FE model, 0.5 comes from the fact that only half model was used and 0.82 compensates the neglected particles sizes as explained in Table 5-3. Let m_{PM} be the mass of one particles mix, i.e. 19 particles (0.211mg) from Table 5-3. The number of particles mixes required in the FE model (n_{PM}) is therefore given by:

$$n_{PM} = m_{FE} / m_{PM} \quad \text{Eq. 6.3}$$

Hence, the total number of particles required in the FE model (n_P) can be obtained as:

$$n_P = 19 \cdot n_{PM} \quad \text{Eq. 6.4}$$

For example, for $V_f = 2000$ mm/min and $\dot{m}_a = 0.02$ kg/min, the mass of the abrasive particles impinged per unit length, $m_L = 10$ mg/mm. If $L_{FE} = 1.5$ mm then $m_{FE} = 6.15$ mg. This means 29 (n_{PM}) particles mix will be required in the model i.e. 551 particles (n_P) of various selected shapes and sizes will need to be simulated.

6.2.2 Assembling the abrasive particles in the model

After knowing the total number of particles to be used in the model for a set of process parameters (e.g. V_f , \dot{m}_a), the next task was to “assemble” the particles in the model. It was reported that the abrasive particles form a Gaussian spatial distribution around the jet central axis and possess almost a constant velocity at the nozzle exit throughout the jet diameter [121], [122] as shown in Figure 6-2. The vertical red lines in Figure 6-2(a) represent the nozzle diameter on a dimensionless scale, and in Figure 6-2(b) the axial velocity of the abrasive particles is expressed as the ratio of the particles velocity to the pure water jet velocity (Bernoulli’s Equation Eq. 4.1). This means that the shape of the eroded footprint is controlled by the distribution of the particles in the AWJ plume. In the current study, the experimental parameters used such as water pressure, mass flow rate and orifice diameter are similar to the one used in ref. [122], the Gaussian spatial distribution of particles reported in this reference was adopted for assembling the garnet particles in layers above the target. This was done by dividing the jet diameter into smaller sub-circles and the number of particles to be placed in each sub-circle were derived proportionally from the spatial distribution of particles given in ref.[122].

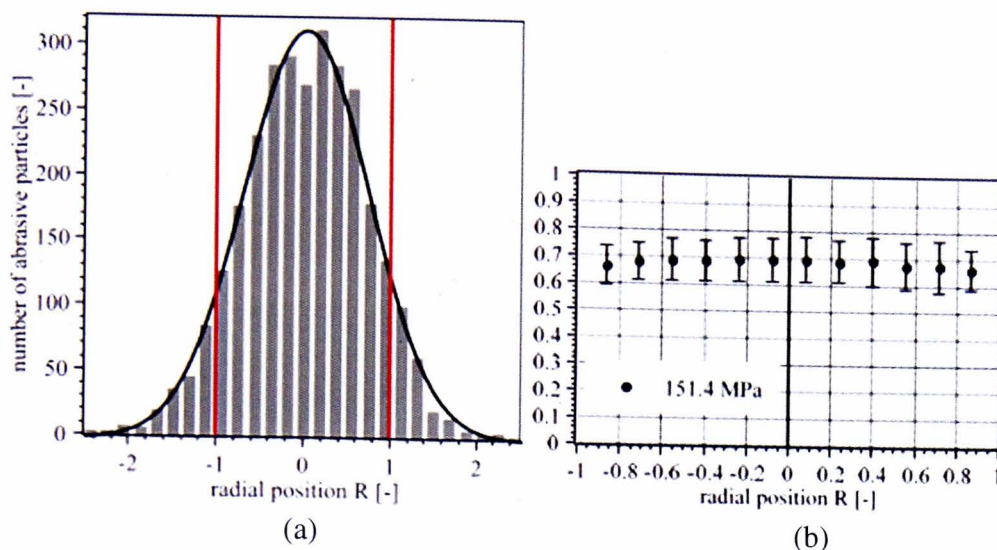


Figure 6-2: (a) Gaussian spatial distribution [122] and (b) velocity of the abrasive particles after nozzle exit [122].

Figure 6-3 shows examples of two layers containing abrasive particles distributed within a jet diameter (d). It can be seen that the particles were arranged in various orientations along the Y-direction to cover the maximum area within the jet diameter and to keep the particles within the jet boundary. However, no particular initial orientations were set for particles along X or Z-directions because of their negligible effects on the results. This was also demonstrated by Chen and Li [128] who stated that in the case of multiple impacts of sharp edged particles, setting the initial orientations of the particles only had a negligible effect on the erosion rate. This is due to the fact that after the target surface was eroded and it formed a slope, some particles (e.g. quadrilateral) which were initially oriented with flat faces towards the target surface might be impacting at their corners (sharp edges) on the eroded surface, and those particles (e.g. triangular) which were initially facing with their sharp edges towards the target surface, might land with their flat faces on the eroded surface. Since in the current study hundreds of particles impacted the target surface, setting particular orientations for particles along the X and Z-directions were not considered.

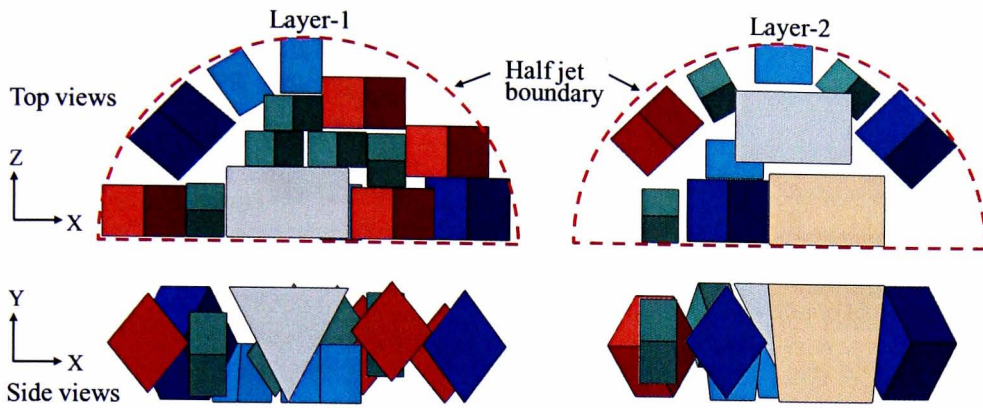


Figure 6-3: Top and sides views of two layers of abrasives illustrating the particles distributed within the jet diameter.

Fifteen different layers of abrasive particles comprising of particles mixes (n_{PM}) were utilized in the FE model which were randomly patterned over each other in the Y-direction to achieve the required total mass of the abrasive particles (m_{FE}) for one jet pass. While assembling the first 15 layers of the particles, particles of different sizes and shapes were arranged such that they occur all around the half jet area. Care was also taken to ensure that there was no concentration of any size or shape at one location in the jet (e.g. periphery or centre). In order to visualize the FE model, Figure 6-4 shows various views of the model with and without the mesh after the particles were assembled in layers above the target. It can be noticed in Figure 6-4(e) that the mesh size along the Z-direction in the target fine region was increased from $20\mu\text{m}$ (in Chapter 4) to $22.5\mu\text{m}$. It was found that this difference had a negligible effect on the erosion rate; however it resulted in reducing ~ 17000 elements in the target which helped in reducing the computational time further.

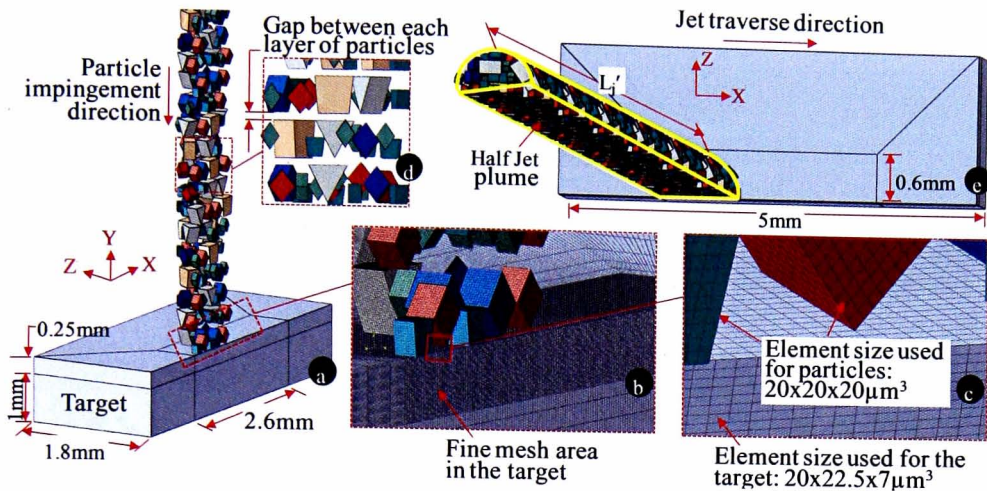


Figure 6-4: (a) 3D view of the model. (b) Meshing of the target and the particles. (c) Zoomed-in view of the elements used in the fine mesh area and the particles. (d) Gaps among the layers of the particles; in between these gaps the jet was traversed by fixed percentage of total distance (L_{FE}) to be covered across the target. (e) Tilted top view of the model showing the length of the jet plume.

6.2.3 Boundary conditions

The motion of the workpiece was constrained at the bottom plane in the X, Y and Z directions and at the symmetry plane in the Z-direction. The diameter of the half-jet in the model was the same as the focusing nozzle diameter (d) used in the experiments. The jet was traversed $1.5 \times d$ mm in the X-direction in all the simulations to generate an area marked as BCFE (see Figure 6-5) which received the complete impact of the jet diameter. In the following, all the results related to the jet footprint will be referred to the eroded profile of this region. All the garnet particles were assigned the same velocity ($V_{imp} = 0.7 \times V_w$ (see Eq. 4.2)) corresponding to the selected water pump pressure. The process parameters used in the FE model are summarized in Table 3.

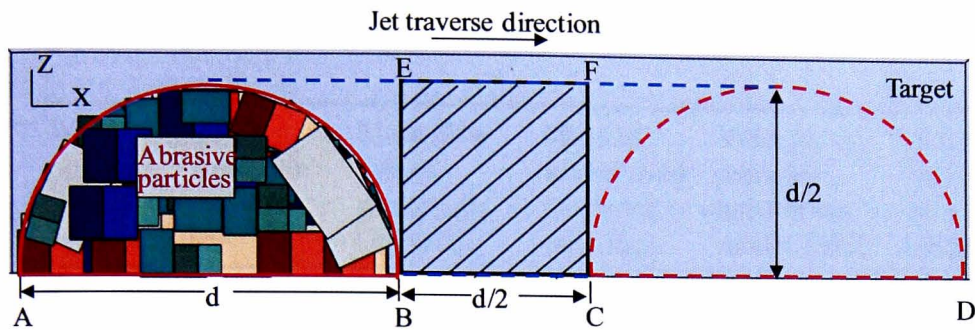


Figure 6-5: Movement of the jet across the target in the model – top view. Points A and B show the initial position of the jet and points C and D show the final position. Hatched area “BCFE” illustrates the region where the jet footprints were measured.

It should be noted that water was not included in the FE model due to the fact that within the selected range of traverse speeds and pressures, water does not have the capability to erode Ti-6Al-4V. Figure 6-6(a) shows a photograph of the target after three 100% overlapping passes of a plain waterjet (PWJ) i.e. a mixture of water droplets and air at 345MPa (the highest pressure used in current study) and 1000mm/min (lowest TRS used in the current study), the most aggressive parameters employed in the current research. It can be seen that no considerable erosion was produced in the Ti-6Al-4V target and most of the surface was left un-eroded. Figure 6-6(b) shows an example of a single scanned profile across the surface of the target after three PWJ passes to show the magnitude of the micropits produced. It can be seen that the maximum depth produced in some local micropits after three PWJ passes was only a few microns compared to the footprint depth of $430\mu\text{m}$ for three jet passes at the same parameters when the garnets particles were included.

The parameters at which the FE simulations were run are listed in Table 4-4.

Table 6-1: Process parameters used in the FE model.

Water pressure (MPa)	TRS (mm/min)	Mass flow rate of garnet, \dot{m}_a (Kg/min)	Mass of garnet used in model, m_{FE} (mg)	Velocity of particles used in the model (m/s)	Angle of incidence of AWJ (degrees)
138	2000	0.02	6.15	368	90
138	1000	0.02	12.3	368	90
207	2000	0.02	6.15	450	90
207	1000	0.02	12.3	450	90
276	2000	0.02	6.15	520	90
276	1000	0.02	12.3	520	90

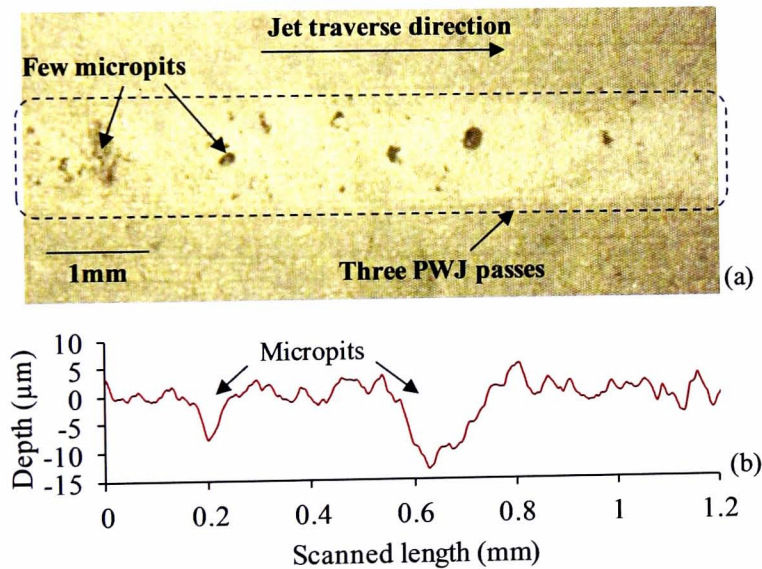


Figure 6-6: Negligible erosion produced in Ti6Al4V target after multiple PWJ passes at $P=345\text{MPa}$, $V_f = 1000\text{mm/min}$ (a) Zoomed in view of three 100% overlapping passes (b) Single scanned profile across the PWJ surface.

6.2.4 Including the process kinematics into the model

It was quite challenging to incorporate the exposure time of the target to the jet into the FE model which is controlled by the jet traverse speed across the target. In real

life, the abrasive particles are spaced quite apart from each other particularly along the direction of the impact (Y-direction in the model). This can be observed in Figure 6-7 which shows a CCD camera snap shot of the laser reflecting fluorescent dyed garnet particles travelling at random and relatively larger distances from each other along the direction of impact velocity [122].

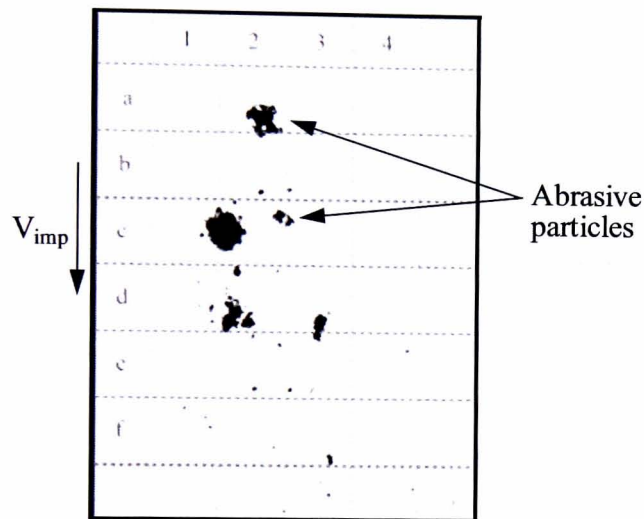


Figure 6-7: CCD camera image showing detected abrasive particles after nozzle exit which are widely spaced apart [122].

Furthermore, the impacting velocity of the particles is very high as compared to the jet traverse velocity across the target ($V_{imp} \gg V_t$). This means that the experimental values of the traverse speeds could not be used in the model because these would result in prohibitively long simulation times. In order to save computational time, the particles in the FE model were arranged in layers and these layers are spaced close to each other ($50\mu\text{m}$) as shown in Figure 6-4(a & d), hence significantly reducing the length of the jet plume for the same amount of mass of impacting particles as used in the experiments. Figure 6-8 shows the schematic illustration of the difference in how the abrasive particles are spaced in the real jet and in the FE model.

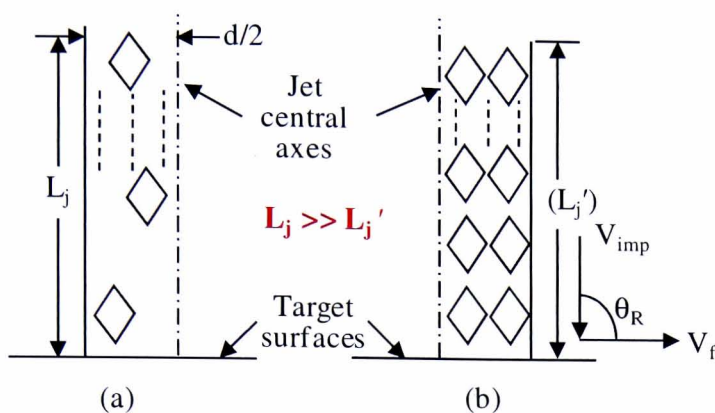


Figure 6-8: Schematic representation of the differences between the particles spatial density in the jet in reality and FE model. (a) Experimental jet with particles far apart from each other (b) Jet in the FE model with closely spaced particles.

In order to have the same number of particles impacting per unit area in the FE model and the real AWJ process after arranging the particles in closely spaced layers, the jet was required to be traversed much faster in the model compared to the experiments. However, if a higher traverse velocity was applied to the jet, the resultant angle of impact will deviate from 90° , whereas it is well-known that for ductile materials, the erosion rate changes considerably due to a change in the angle of impact [60]. This is explained as follows.

Let L'_j be the length of the jet plume in the FE model. The total time (t) required by all the particles to hit the target surface is given by:

$$t = \frac{L'_j}{V_{\text{imp}}} \quad \text{Eq. 6.5}$$

Let V'_f be the traverse velocity that could be used in the FE model such that all the particles in the jet plume will make impact upon a target length " L_{FE} " over the span of simulation time (t). V'_f can be determined as follows:

$$V_f' = L_{FE}/t \quad \text{Eq. 6.6}$$

The resultant angle of impact (θ_R) can be obtained as:

$$\theta_R = 90 - \tan^{-1} \left(\frac{V_f'}{V_{imp}} \right) \quad \text{Eq. 6.7}$$

As an example, the calculations for θ_R at $V_f = 2000\text{mm/min}$ and $V_{imp} = 368\text{m/s}$ (i.e. $P=138\text{MPa}$) are presented as follows. From the FE model $L_j = 13.7\text{mm}$. Therefore, from Eq. 6.5 and Eq. 6.6, $t = 37.6 \mu\text{s}$ and $V_f' = 40 \text{ m/s}$. Substituting the values of V_f' and V_{imp} in Eq. 6.7, θ_R is obtained as 83.7° . This means that the footprint obtained from the FE simulation at this traverse speed ($V_f' = 40 \text{ m/s}$) will be equivalent to that obtained at 83.7° in the experiments. To overcome this issue, i.e. keeping the normal angle of impact between the particles and the target, an alternative way of modelling the traverse speed was suggested. Rather than employing a continuously moving jet, the jet was moved across the target in small equal increments along the X-direction and it was only moved in between the gaps (see Figure 6-4(d)) between two adjacent layers of the abrasive particles. Each increment was a fixed proportion of the total length (L_{FE}) to be traversed in the model. This was accomplished in the FE model by applying a displacement boundary condition to the jet in the X-direction with an amplitude which divides the total displacement (L_{FE}) over the time (t) into a number of equal smaller segments. Hence, it was avoided to generate a second component of velocity of the particles along the X-direction which can affect the erosion rate because in reality the particles only have one component of velocity along Y-direction.

6.3 Generation of experimental data

AWJ milling trials for validating the FE model results were conducted by using the process parameters mentioned in Table 3-4. The mass flow rate (\dot{m}_a) of the garnet abrasive was kept constant at 0.02kg/min. To ensure repeatability and accuracy of the abrasive mass flow rate during the whole experiment, the abrasive was delivered by an analogue controlled mechanical abrasive metering system (FEEDLINE IV) which was calibrated before each start of the test. All the trials consisted of a single pass of AWJ over the target surface at 90° incidence angle. In order to measure the mass removed per AWJ pass, the weight of the workpiece was measured before and after each AWJ pass. This measurement was used to calculate the erosion rate (ER) in the target material, which was defined in Eq. 3.1. Once the AWJ milled trenches were generated, 3D surface scanning of the footprints was performed using a Talysurf laser scanner. In each scan, an area of 1.8 x 30 mm² (width x length) was evaluated along the jet traverse direction. Then, a mean surface profile line was extracted out of each 3D scanned surface to enable the validation of the FE model results. A brief illustration of the scanning process is presented in Figure 6-9.

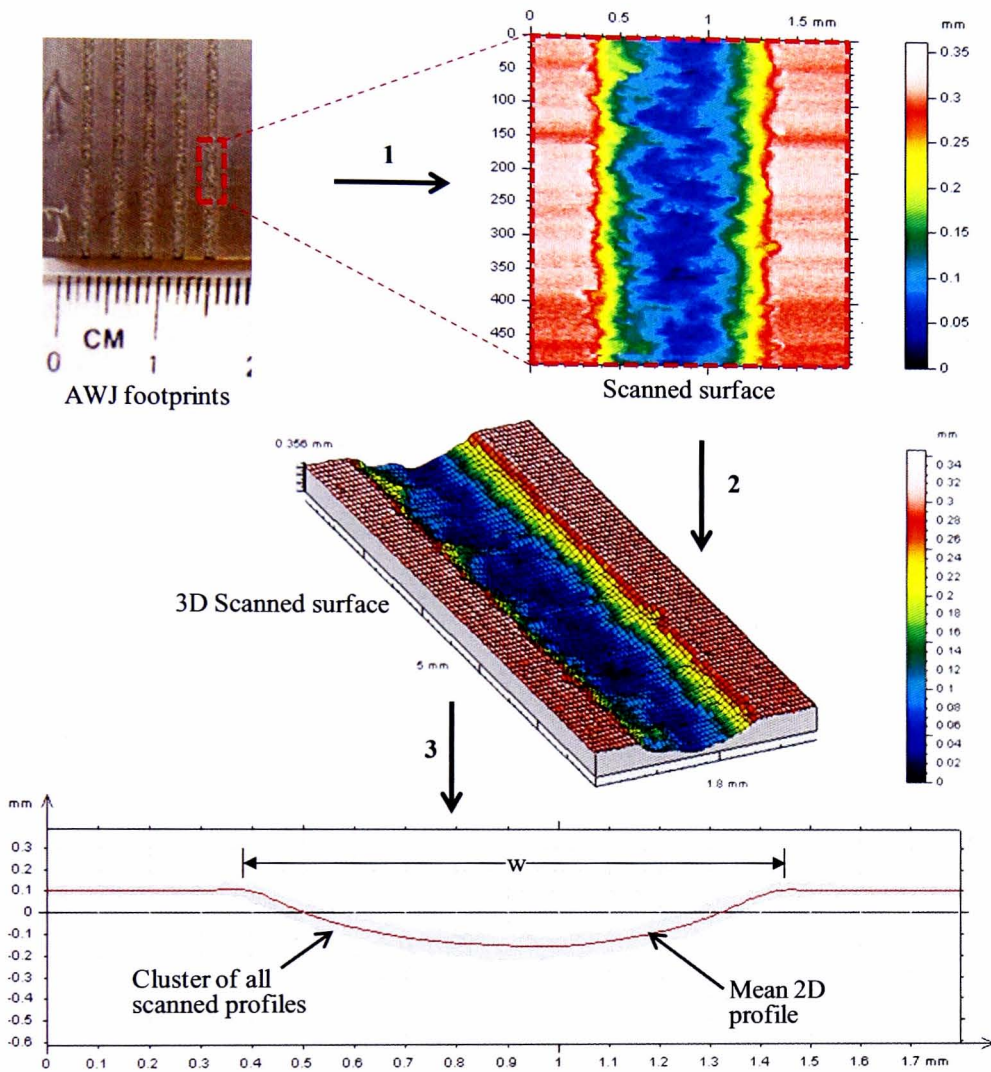


Figure 6-9: Procedure for extracting 2D profiles from an experimentally generated kerf

6.4 Results and discussion

It is evident from the images of the 3D scanned surfaces in Figure 6-9 and Figure 6-10 that the surfaces of the milled footprints are not very uniform; rather they are uneven and have some pits. This is attributed to the facts that: (i) erosion was mainly caused in the target by the impact of a number of particles which differ in their masses (kinetic energy), i.e. their capability to erode, hence causing a non-uniform erosion at micro levels; (ii) although the abrasive particles were supplied by an analogue feeder

which can accurately control the amount of abrasive supplied to the cutting head, there was a degree of variation of this parameter as the particles were entrained into the cutting head and streamed in the focusing tube. That is the reason that the individually scanned 2D profiles differ from each other, as shown by the cluster of the 2D profiles around the mean 2D red profile in Figure 6-9. This is due to the variation of the milled surface along the jet traverse direction. In order to overcome these issues, a longer length of footprint (30mm) was scanned along the jet traverse direction, so that a better overall picture of the eroded footprint could be captured by averaging all the individually scanned profiles. In the following the jet footprints will be referred to their mean surface profiles.

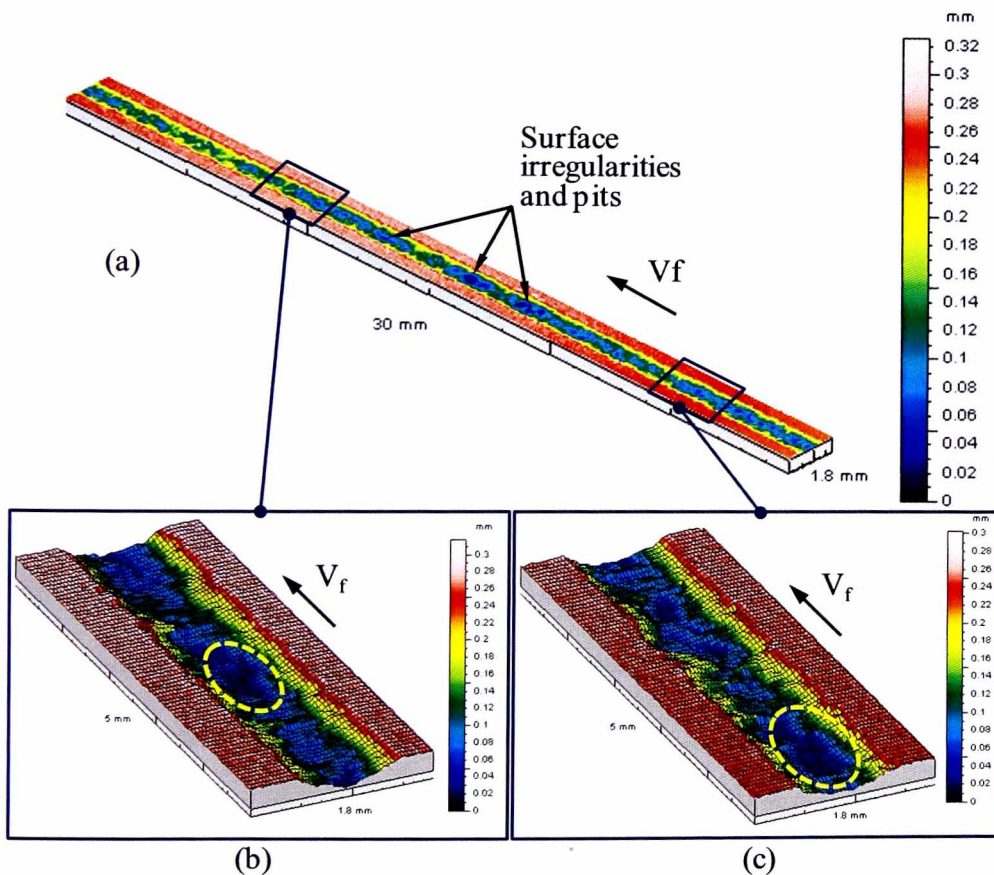


Figure 6-10: (a) A typical scanned 30mm long milled trench with some surface non-uniformities; (b & c) Zoomed in regions within the scanned trench with yellow circles highlighting some relatively deep eroded regions. Process parameters used $P =$

207MPa, $V_f = 1000\text{mm/min}$.

Figure 6-11 presents a typical eroded surface from the FE simulations. Points A and B show the initial position of the jet while points C and D correspond to the jet final positions.

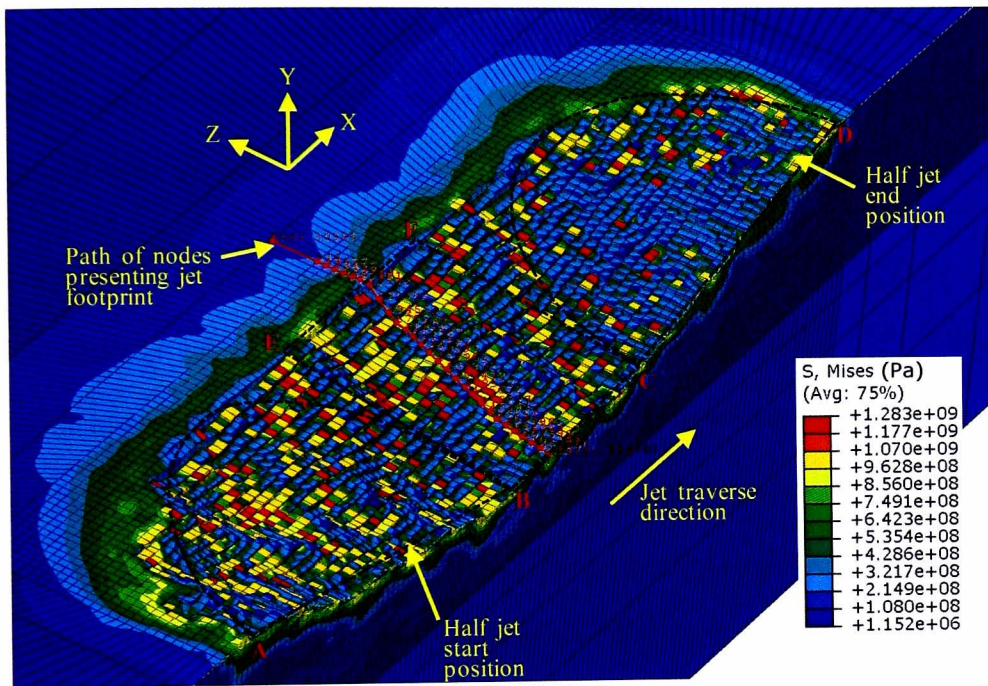


Figure 6-11: Stress contour generated in the simulated half kerf; $P = 276\text{MPa}$, $V_f = 1000\text{mm/min}$.

The dotted rectangle BCFE represents the same area BCFE as shown in the Figure 6-5 which received one complete pass of the jet diameter in the X-direction. All the half 2D FE footprints were measured within this area by selecting a path of the nodes in the Z-direction and then the Y-coordinates of these nodes were recorded across the path. An average of the Y-coordinates for 10 such nodal paths (half footprints) was taken for each of the eroded trench from the FE model and then mirrored (by using Matlab) as complete 2D footprints to be compared with the corresponding scanned

experimental footprints. The simulation time varies from 40 – 50 min for 2000mm/min traverse speed (i.e. for 551 particles) and 1.16 – 1.5 hours for 1000mm/min traverse speed (i.e. for 1102 particles) on a cluster of eight nodes (3GHz Intel quad-core each node) with 16GB total RAM depending on the pressure (velocity of the impacting particles) used in the FE model. It was noticed that keeping the same number of elements in the target and doubling the number of particles in the FE model, the simulation time was increased by more than ~2 times, hence a considerable amount of computational time was saved by using the half model.

In Figure 6-12(a) to Figure 6-12(e), the evolutions of the erosion due to the impact of the abrasive particles on the Ti-6Al-V4 target and the formation of the eroded footprint are illustrated. The different stages in Figure 6-12 are expressed in terms of the percentage of the total mass of the abrasive particles in the FE model (m_{FE}) that has impinged the target surface. Figure 6-12(a) represents the initial stage before the particles started impinging the target surface. In Figure 6-12(b) to (d), the particles impacted the target at various locations and both the target and the particles undergo erosion. Figure 6-12(e) corresponds to the final eroded kerf after all the particles have impacted and the jet has traversed the total distance L_{FE} . It can be seen that the depth of cut increases with time as more and more particles impact the surface, and stabilizes only in the red highlighted region which has received one complete pass of the jet diameter i.e. the region BCFE in Figure 6-5 and Figure 6-11. This means that it is necessary to traverse the jet by a distance larger than the jet diameter, because only after one full jet pass the eroded kerf depth gets stable.

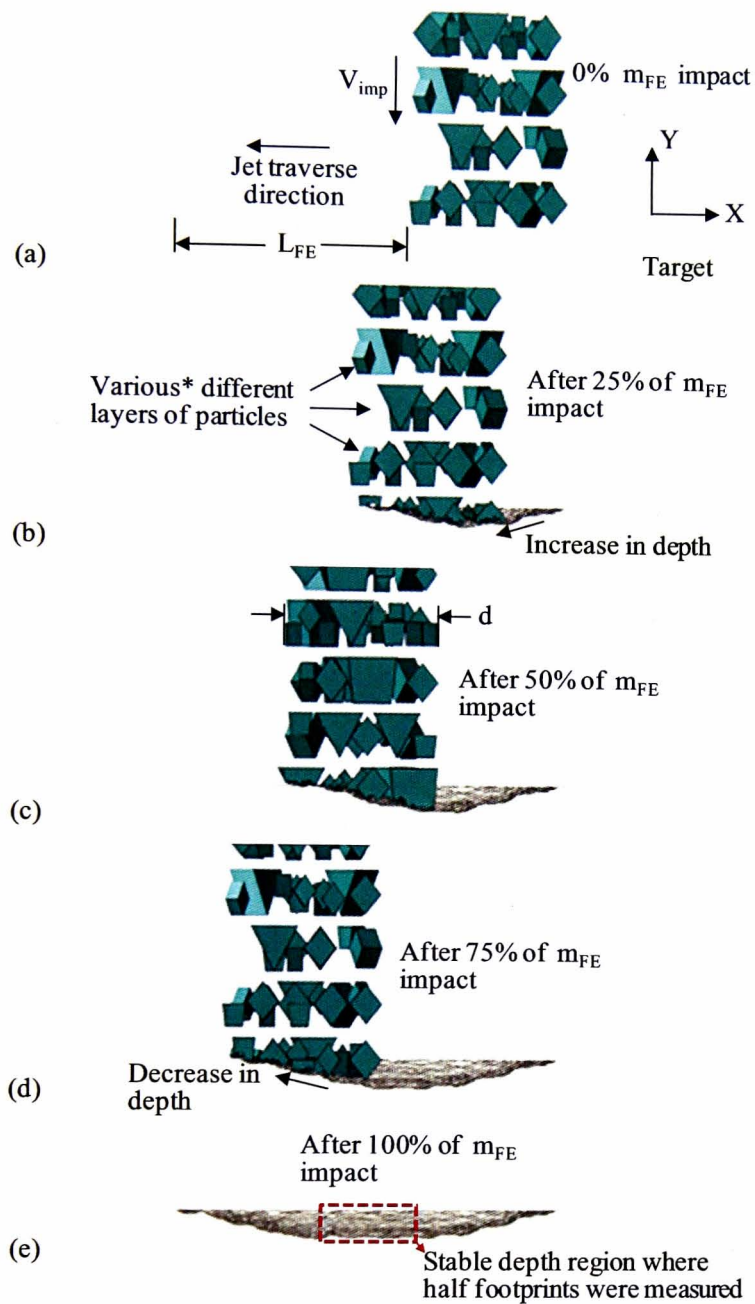


Figure 6-12: Stages of erosion of the target during the impact of abrasive particles.

*Fifteen different layers of particles were used which were then patterned over each other in the Z-direction to achieve the mass of abrasive particles (m_{FE}) required in each simulation.

Figure 6-13 shows the simulated averaged jet footprints compared with the corresponding experimental footprints.

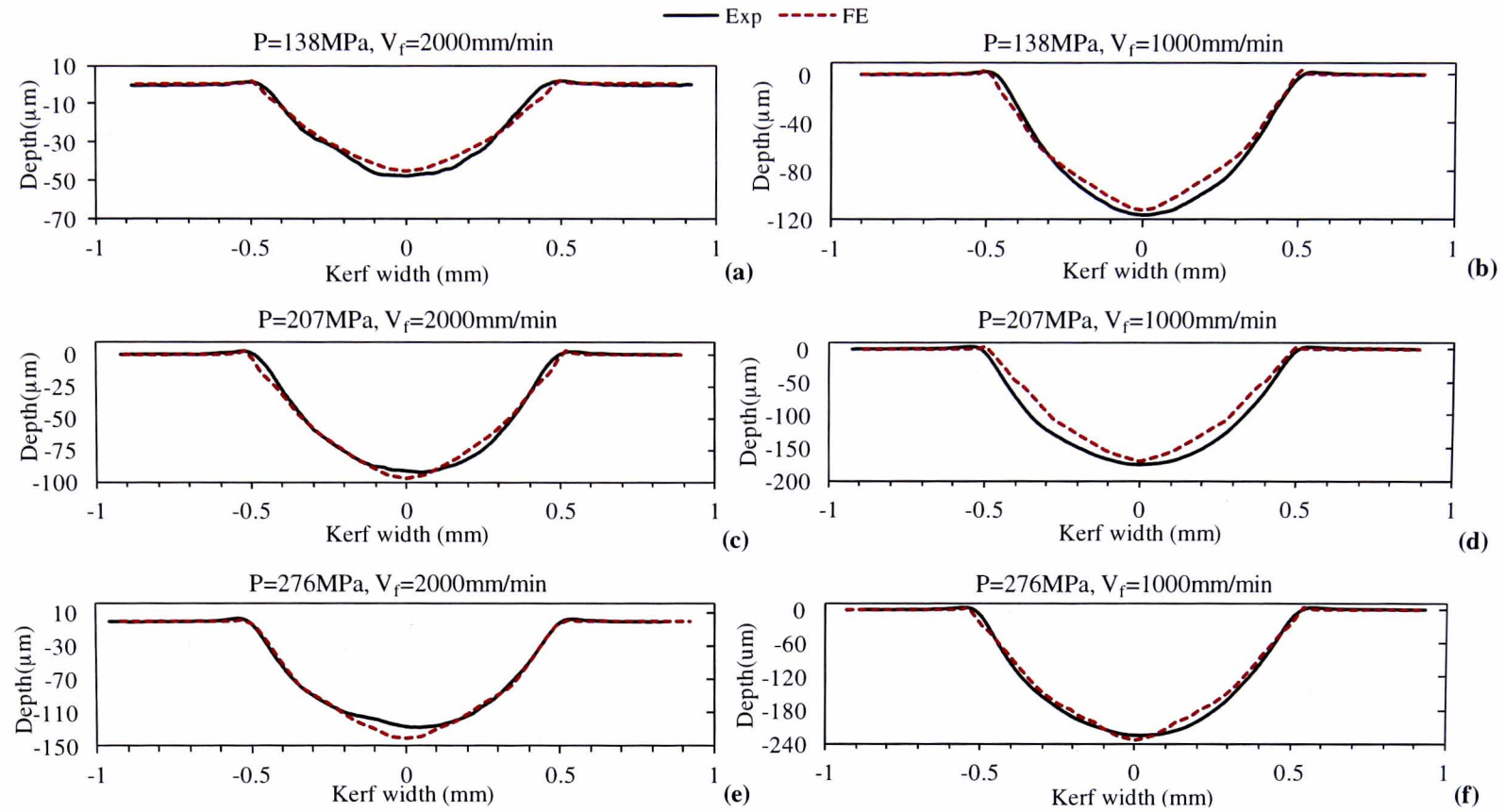


Figure 6-13: Comparison of FE and Experimental footprints at given parameters.

The results of the FE model are quite encouraging both qualitatively (shape of footprints) and quantitatively (depth and width of footprints). The shape of the footprint was controlled by the distribution of the particles in the jet while the depth and the width were controlled by both the impacting velocity of the abrasive particles and traverse speed of the target across the jet. The shapes of the simulated kerfs at different pressures and traverse speeds are similar to the corresponding experimental ones, confirming that the particles were correctly distributed while assembling them into layers over the target surface.

The depth and the width of the simulated kerfs are also in good agreement (maximum error < 10%) with the experimental ones. Like the experiments, the FE model also predicted different depths of penetrations when the traverse speed was changed keeping the same water pressure. The depth reduced when the traverse speed was increased. This is due to the fact that when the traverse speed is increased, less particles impact per unit area on the target surface, thus reducing the exposure time of the target to the impacting particles leading to less erosion in the target. Figure 6-14(a) shows that a linear relationship exists between the pressure (in the used range 138MPa-276MPa) and the depth of the footprint at both traverse speeds used. Moreover, it can be observed that the depth of the footprint is more sensitive to the change in pressure compared to the width of the footprint. Similar experimental results were also found by Srinivasu et al. [18]. The width of the footprint (w) was increased only by 1.04% when the water pump pressure (P) was doubled (see Figure 6-14(b)). This implies that most of the particles in the AWJ plume travel close to the central axis of the jet and only fewer particles are travelling near the jet periphery. Furthermore, keeping the same mass flow rate (\dot{m}_a), the spatial distribution of the abrasive particles in AWJ column is not affected by changing the water pressure,

based on the fact that a single spatial distribution of the particles in the FE model predicted the correct shapes of the footprints for all the cases.

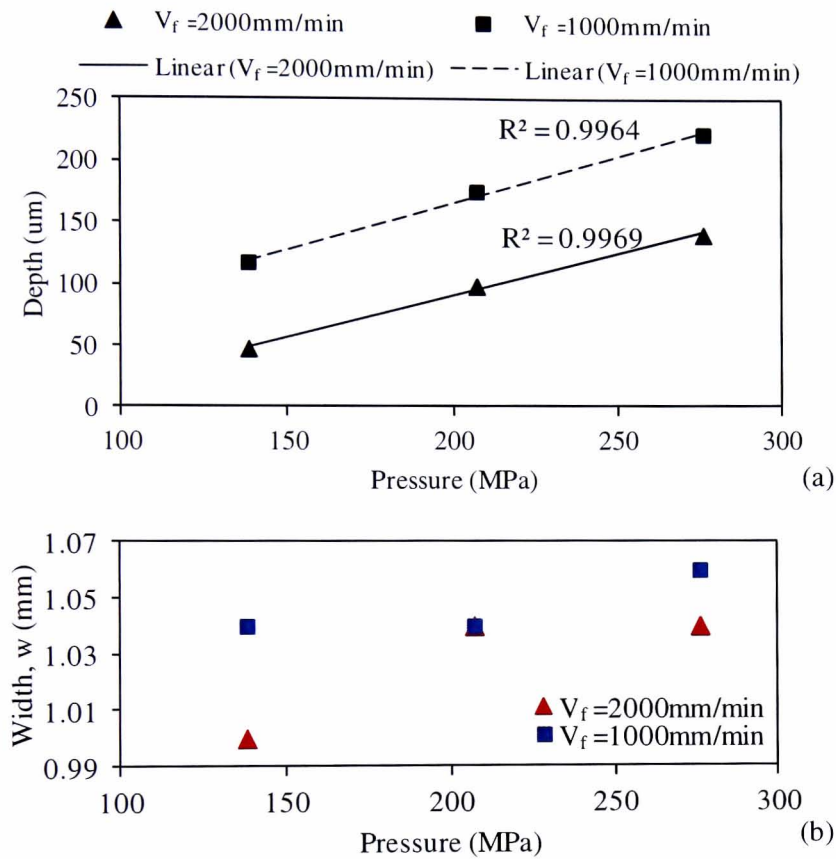


Figure 6-14: (a) Variation in depth of the footprint by changing the water pump pressure. (b) Variation in width of the footprint (w) by changing the water pump pressure.

It can be observed in Figure 6-13 that the height of the piled-up material at the boundaries of the simulated footprints is the same as the corresponding experimental ones, whereas there are differences in the length (l_p) of the piled up material in the Z-direction. In the simulated footprint, the target material was piled-up over a smaller length compared to the experiment footprints. The reason for this difference can be explained by closely observing the boundaries (edges) of the scanned footprint within

the dotted rectangles as shown in Figure 6-15(a). During the experiments, the abrasive particles on the boundaries of the jet plume were not always impacting the target surface at the jet diameter (d); rather they hit the surface both inside and outside of the jet boundary as well. This means that the width of the experimental footprint was varying across the jet traverse direction. Therefore, when the average of all the scanned footprints was calculated over the entire trench length, the length of the piled up region (l_p) also increased (see Figure 13(b)). However, in the FE model all the particles impact at a constant diameter (d). On the other hand, the height of the lip remains the same in both the simulated and experimental footprints due to fact that the numbers of particles impacting per unit area are identical in both cases.

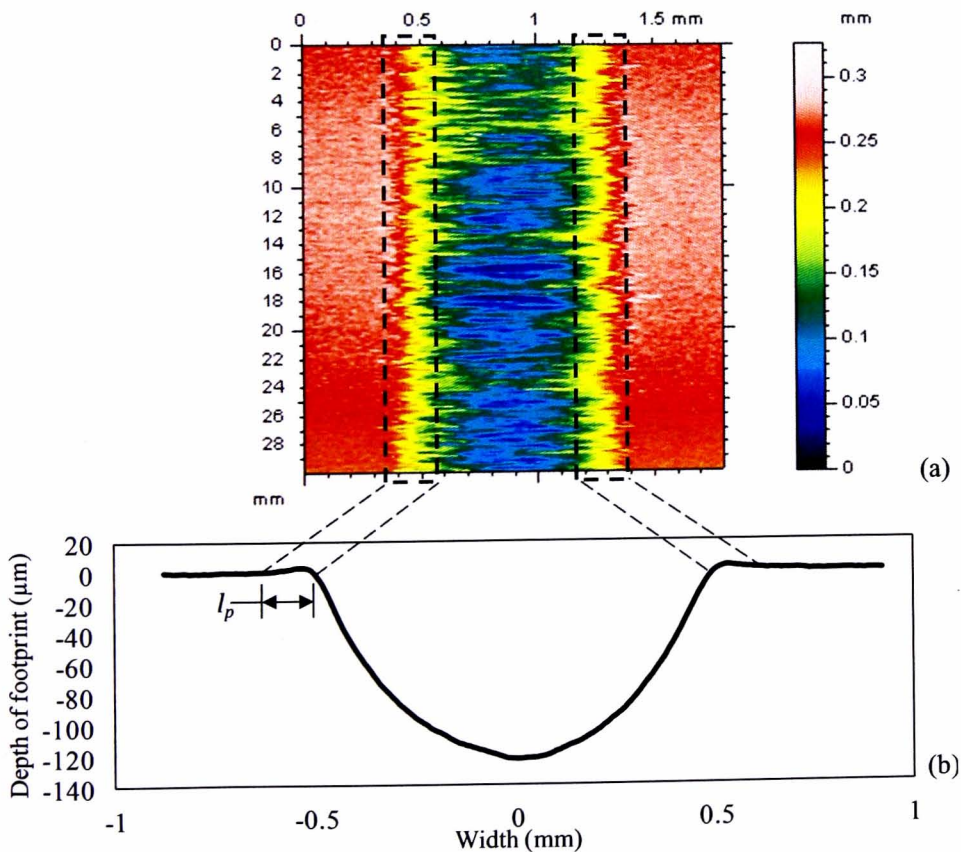


Figure 6-15: Details of piled-up material at the edges of the jet footprint at $P = 276\text{MPa}$, $V_f = 2000\text{mm/min}$: (a) Scanned footprint; (b) Averaged 2D profile of the

footprint.

In order to further validate the model, the erosion rates (ER) were calculated from the FE model and compared with the corresponding experimental values, as shown in Figure 6-16. It should be noticed that only the abrasive particles impacted the target in the FE model, whereas in the experiments both water and the abrasive particles impacted the target. The good agreement between the experimental and the simulated ER shows that the erosion produced in the Ti-6Al-4V target by the water droplets present in the AWJ plume is negligible at the pressures and traverse speeds used in the current study. Thus, the current model can be used to reliably predict the single AWJ milled footprints up to an operating pressure of 276MPa.

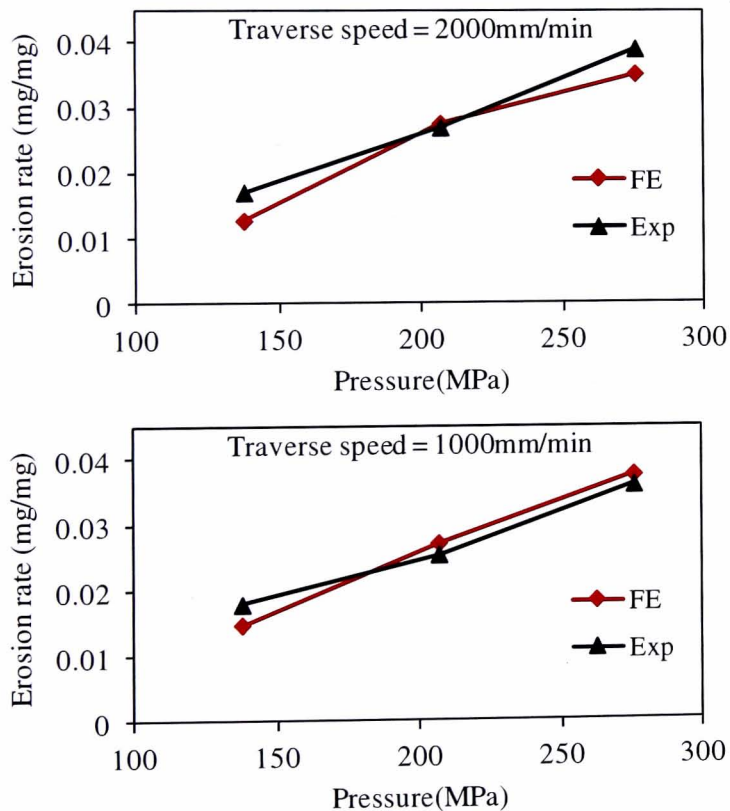


Figure 6-16: Erosion rates obtained from FE simulations vs. experimental results.

6.5 Conclusions

In this chapter, a new FE model is developed to predict the abrasive waterjet milled footprints. In comparison with the previously reported AWJ FE models, this model is much closer to the experimental conditions by considering more real life challenges such as the effects of mass flow rate, particles spatial distribution, water pump pressures and traverse speeds along with the correctly selected shapes and sizes of the abrasive particles. A method has been identified that facilitate including the mass flow rate of the abrasive particles in the FE model such that the model can be run for the same amount of the mass of abrasive particles as in the experiments. Abrasive particles were arranged in layers in the jet plume to form a Gaussian spatial distribution which was essential for controlling the shape of the footprints. The layers of the particles were placed very close to each other as compared to the distances among the particles in the real jet; thus saving a considerable amount of the computational time. The effect of exposure time, i.e. the traverse speed, was also included in the model by moving the target in an incremental fashion in such a manner that it resulted in the same particles impact density as in the experiments without disturbing the erosion rate in the target.

The simulated jet footprints and the erosion rates generated by the presented FE model were consistent (maximum errors $\leq 10\%$) with the experimental results. The good agreement confirms the validity of the model. In addition, the model provides further understanding of the AWJ process by revealing the fact that the spatial distribution of the abrasive particles in the jet plume is not affected by the changing the water pump pressure. This is demonstrated by the fact that a good agreement with the experimental data is exhibited at various pressures by employing only a single particles spatial distribution.

Due to the stochastic nature of the AWJ milling process, a model is required that can reliably predict the depth of the cut and the profile of the footprints at a given pressure and traverse speeds. The presented FE modelling approach, by closely simulating the AWJ milling process, enables the prediction of accurate jet footprints, and this leads to the possibility for further developments of the model to simulate the generation of 3D surfaces as a result of overlapping passes of the abrasive waterjet.

Chapter 7 Finite element modelling of overlapping jet passes

This chapter provides the detailed description of the final stage of the FE modelling where the footprints generated as a result of overlapping abrasive waterjet pass were considered. A method has been proposed by which multiple overlapped AWJ milling passes can be simulated without being computationally extremely expensive. The importance of the mass distribution of the abrasive particles around the jet central axis is explained and the mechanism of the overlapping of the footprints is discussed. Results from the FE simulations and the experiments at various process parameters are presented, compared and discussed. Finally, conclusions are drawn.

7.1 Introduction

The development of models to reliably predict the jet footprints is of principal importance in AWJ milling for the generation of desirable geometries, because several single footprints overlap to produce the end shape. After developing and validating the half jet model, it was decided to extend the model to predict the footprints generated as a result of several overlapping jet passes. Up to this stage, being a half model based on the symmetry of the process, the model can only predict the jet footprints for a single pass of the AWJ. However, in real life milled 3D surfaces are generated as a result of an overlap of several single footprints. This implies that in order to simulate the overlapping footprints, the existing model will need to be upgraded to a full scale model, i.e. including the complete jet diameter, because without having the full jet, overlapping footprints cannot be simulated.

In this chapter a new FE model for AWJ milling of overlapping jet footprints is presented. A new approach is discussed which makes it possible to predict the

footprints for different numbers of jet passes (n). The aim of this chapter is to build and validate an FE model that will simulate the overlapping AWJ milled footprints after multiple passes of the jet. The modelling procedure is explained below.

7.2 Finite Element modelling

The key modelling challenge for simulating the overlapping AWJ footprints is that by including the multiple jet passes and the target in the simulation, the size of the problem (total number of nodes and elements) becomes prohibitively large. To provide an estimation of problem size, the total number of nodes in a three jet pass to be traversed over a length of 1.5mm at a traverse speed of 2000mm/min is 1,683,000 and an additional 674,966 nodes in the target. Consequently, a methodology was required to make the simulation runs possible which is discussed later in this section.

Figure 7-1 represents the examples of the top and side views of the individual layers of the garnet abrasive particles after they were arranged in the full jet diameter (d).

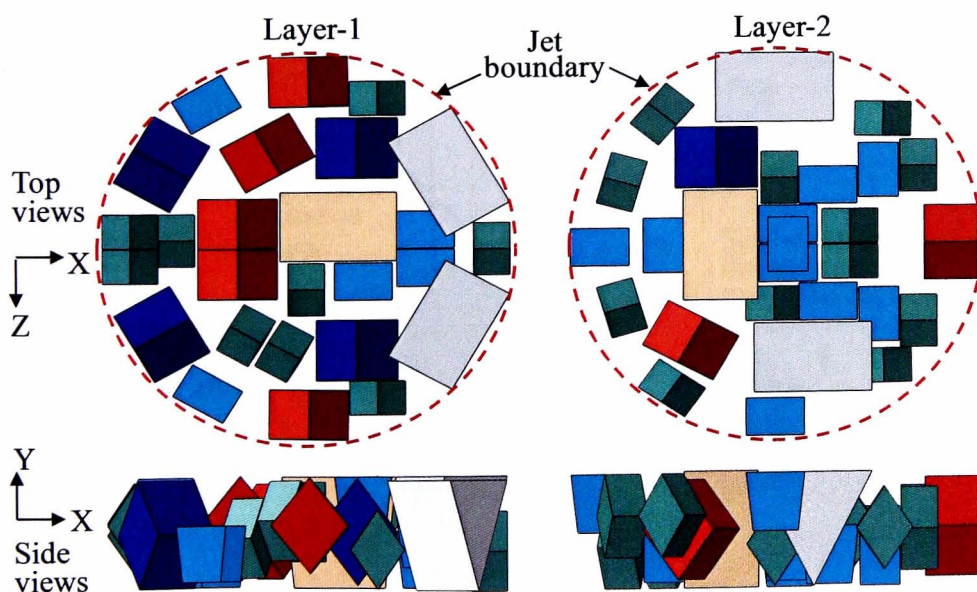


Figure 7-1: Top and sides views of two layers of abrasives illustrating the particles

distributed within the jet diameter.

Figure 7-2 depicts typical views of the FE model for overlapping footprints after the abrasive particles were assembled in the form of a complete jet above the target. The positions for the three jet passes and the step-over distance (SO) between the adjacent passes are shown in Figure 7-2(a) and a meshed view of the target and the particles is shown in Figure 7-2(b). In the current work, only three jet passes were simulated, firstly because three passes were enough to obtain a good picture of the overlapping behavior of the footprints, and secondly to save computational time.

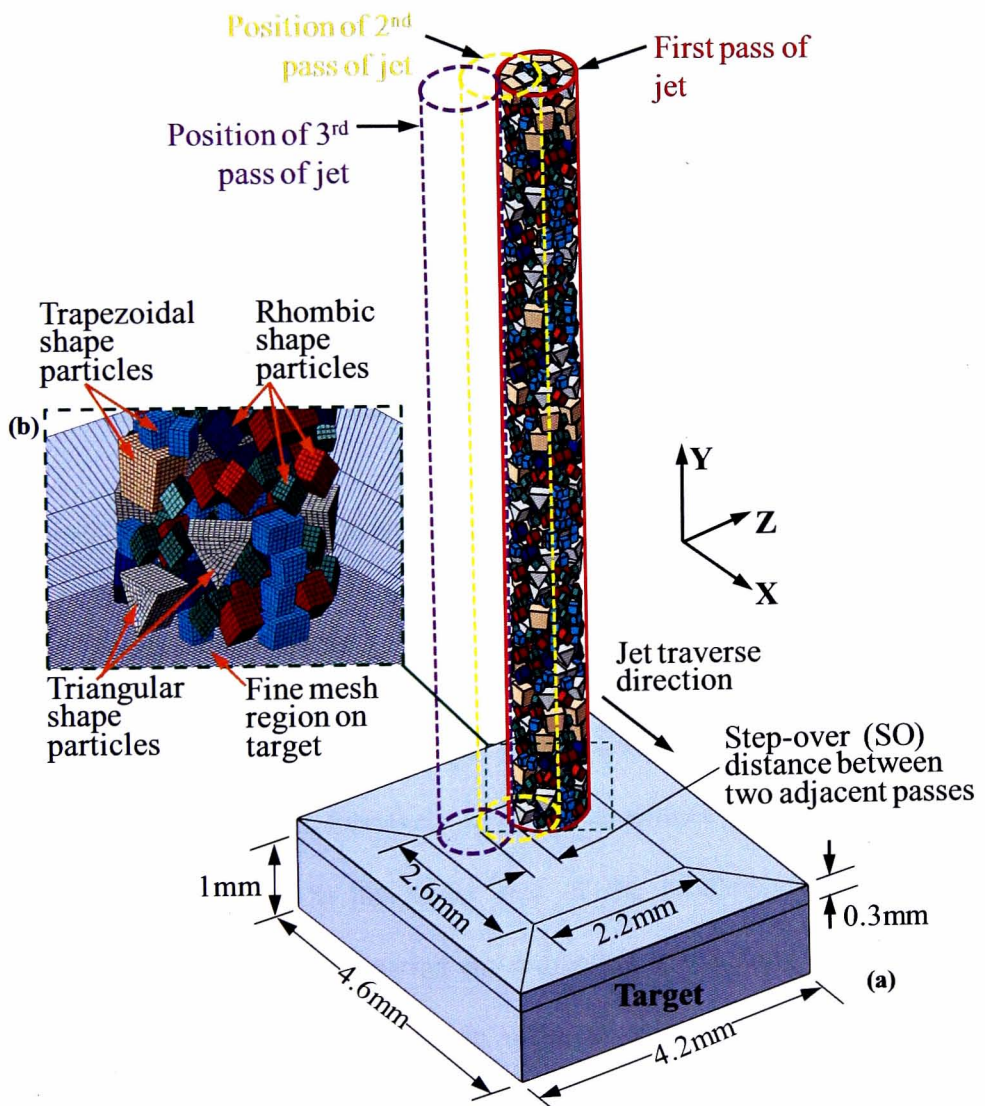


Figure 7-2: (a) 3D view of the FE model explaining the SO distance between adjacent

overlapping jet passes. (b) Meshing of the target and the particles.

The jet was traversed $1.5 \times d$ mm in the X-direction in all the simulations to generate an area marked as BCFG (see Figure 6-5) which received the complete impact of the jet diameter where later the simulated footprints were measured. It should be noted the width of the area BCFG varied in the Z-direction depending on the step-over distance used in between the successive jet passes.

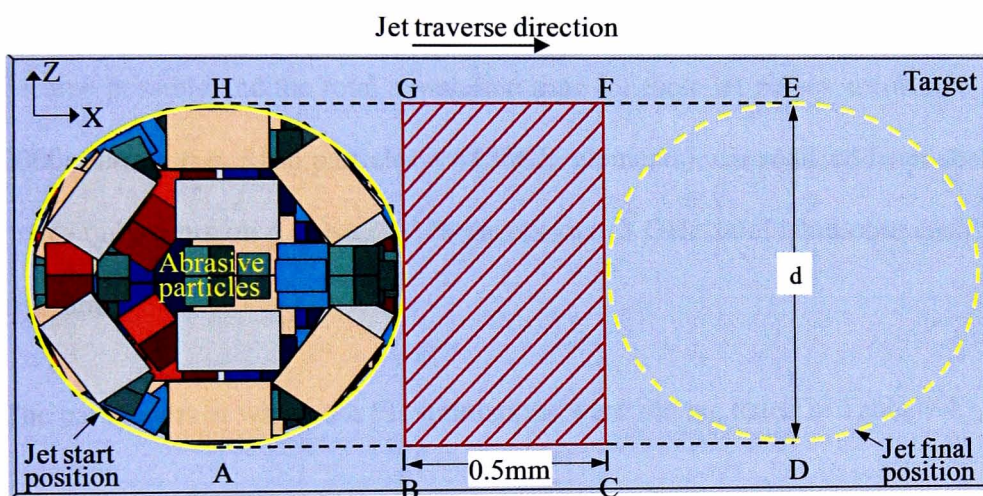


Figure 7-3: Movement of the jet across the target in the model – top view.

7.2.1 Analysis procedure

When all the jet passes and the target were included in one single simulation, either the run time became prohibitively large or sometimes the FE solver failed due to memory errors owing to the larger size of the problem. Moreover, even if the simulation was completed, viewing and extracting results from such large output files would be cumbersome processes. In order to make the simulations possible and efficient, the analysis was run in stages. Each stage contained only one jet pass and the target. This was the reason that the second and the third jet passes were presented

hypothetically by dotted cylinders in the Figure 7-2(a). When the first pass simulation was completed on the target, the stresses and deformations from it were mapped at the beginning of the second pass simulation on a new (non-eroded) target containing the same dimensions and geometric features as the previous one. Once the initial state was mapped on the new target, i.e. it acquired the same eroded shape as after the first jet pass, the second jet pass was then traversed over the target at the selected step-over distance (SO). The same process was repeated for the next stage, i.e. the third pass simulation. By using this procedure, the simulation for the overlapping footprints became possible and the total simulation time for three jet passes at traverse speed of 2000mm/min (i.e. 3106 particles = 1156626 elements) was reduced from about 36-40 hrs to only 6 hrs on a cluster of 16 processors (3 GHz Intel quad-core each) with 16 GB ram.

The parameters at which the FE simulations were run are listed in Table 4-4.

Table 7-1: Process parameters used in the FE model.

Water pressure, P (MPa)	Corresponding velocity of particles, V_{imp} (m/s)	Traverse speed, V_f (mm/min)	Mass of one jet pass, m_{FE} (mg)
207	450	2000	12.3
207	450	1000	24.6
276	520	2000	12.3
276	520	1000	24.6
345	581	2000	12.3
345	581	1000	24.6

7.3 Generation of experimental data

AWJ milling trials for validating the FE model results were conducted by using the process parameters mentioned in Table 3-5. All the trials consisted of two and three

overlapping passes of the AWJ over the target surface at a 90° impact angle. The weight of the target sample was measured before and after each AWJ pass to determine the erosion rate (ER) in the target material, which was defined in Eq. 3.1. After the AWJ milled trenches were generated, 3D surface scanning of the footprints was accomplished by using a Talysurf laser scanner. In each scan, a 60mm length was scanned along the jet traverse direction while the scanned width of the footprint varied between 1.5 to 3mm depending on the step-over distance (SO) at which the trench was milled. Then, a mean surface profile of the footprint was determined by averaging all the scanned single profiles which together form the 3D scanned surface. Figure 6-9 illustrates the experimental setup and the scanning process.

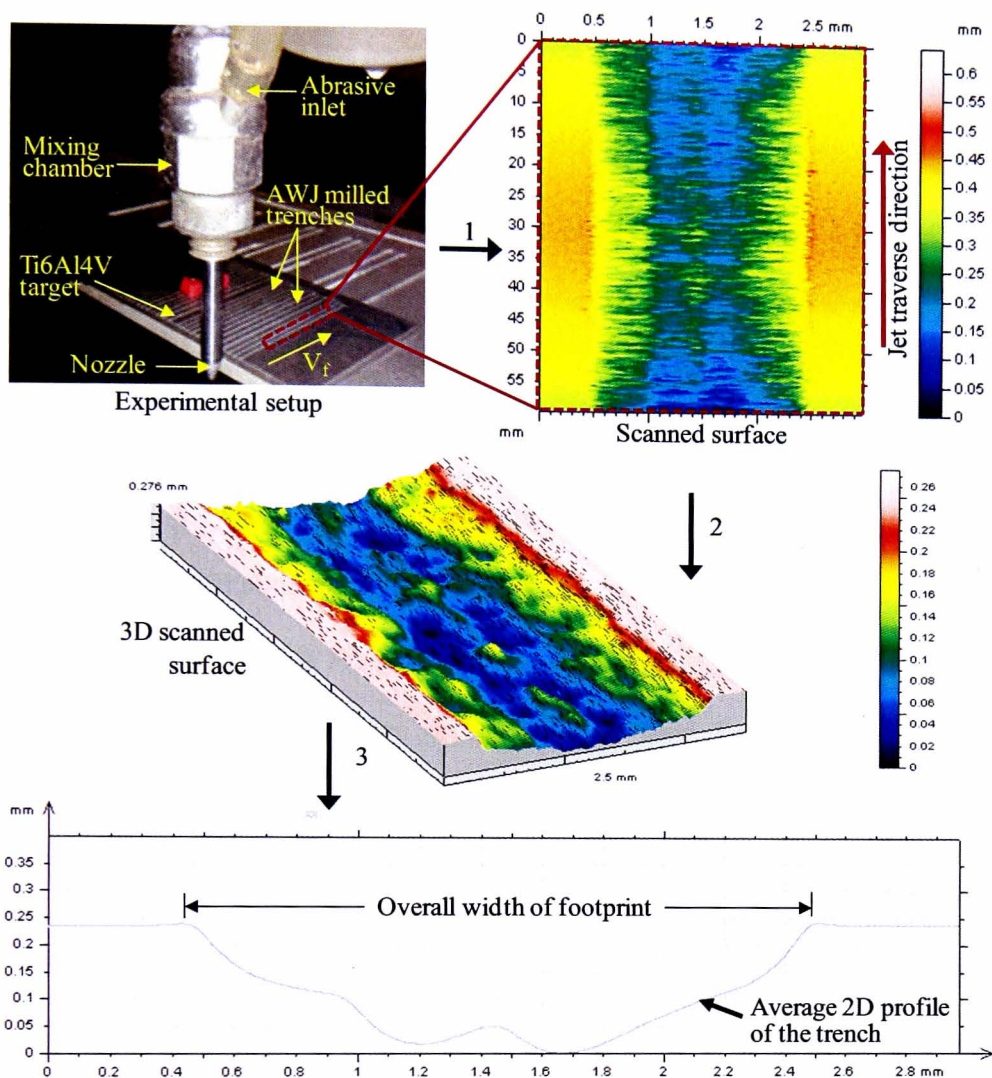


Figure 7-4: Procedure for extracting 2D profiles from an experimentally generated kerf. Kerf milled at $P=345\text{MPa}$, $V_f=2000\text{mm/min}$, $SO=0.5\text{mm}$, number of jet passes, $n=3$.

7.4 Results and discussion

Figure 7-5 explains the simulation process for one set of parameters ($SO=0.5\text{mm}$, $P=207\text{MPa}$, $V_f=1000\text{mm/min}$). Figure 7-5(a) illustrates the starting state of the first pass simulation and no erosion is produced in the target. Figure 7-5(b) represents the beginning stage of second pass simulation and it can be seen that at simulation time of

0sec, the deformed state of the target from the first pass simulation has been mapped on a new target and the jet has been displaced along the Z-axis by the required step-over distance which in the presented case is 0.5mm. The dotted rectangle BCFG in Figure 7-5(b) shows the same area BCFG as in Figure 7-3 which has received one complete pass of the jet. Figure 7-5(c) represents the starting position for the third pass simulation with the initial state mapped on the target from the second pass simulation. Figure 7-5(d) shows the sectioned view of the final state of the target after three jet passes. In Figure 7-5(b-d), the red highlighted nodal paths show the examples of single footprints in the target after each pass. It can be seen that after every jet pass, the shape of the footprint changes. Later, the average of 10 such nodal paths (footprints) from the target after each pass was used for comparison with the experimental data.

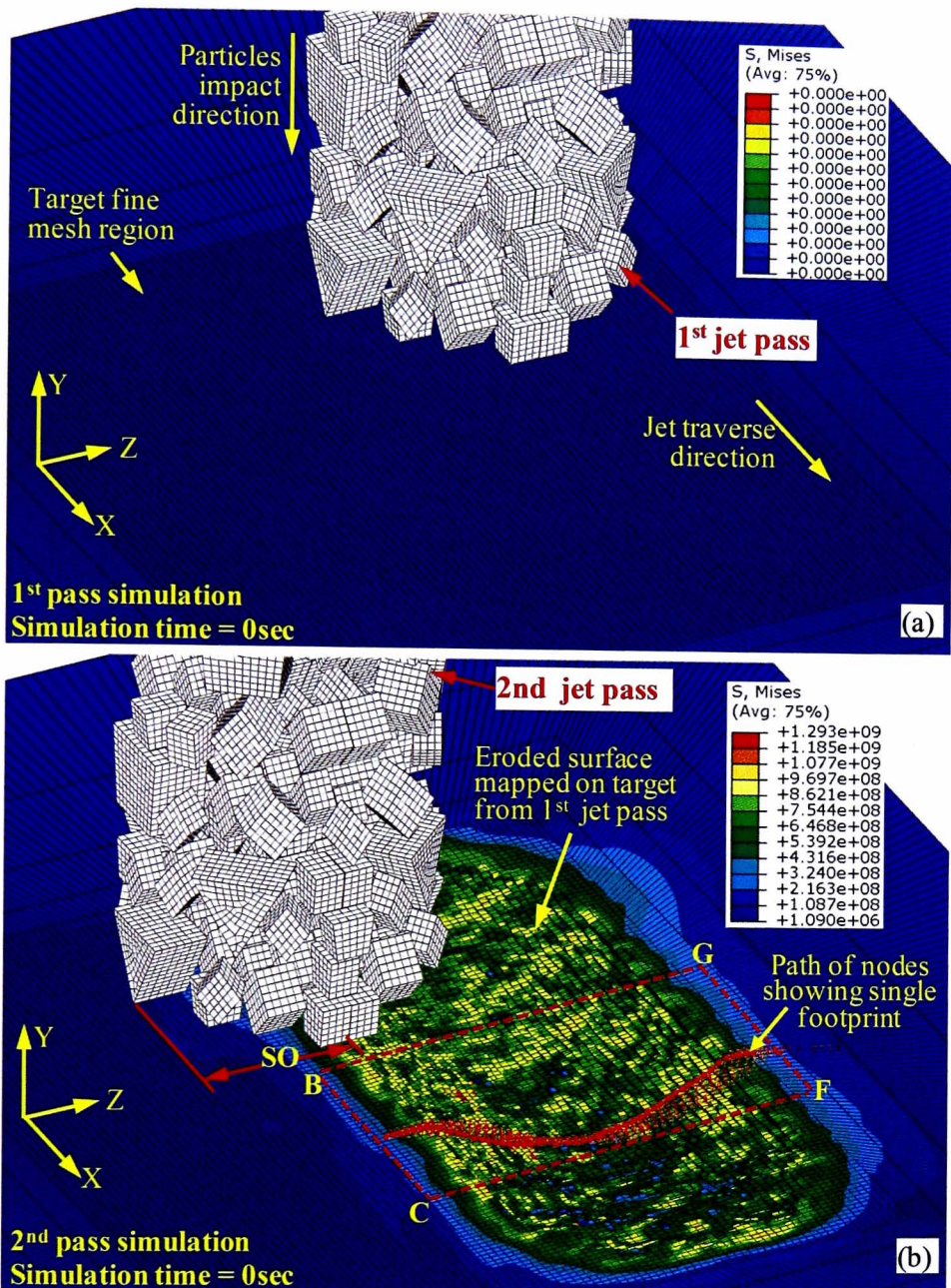
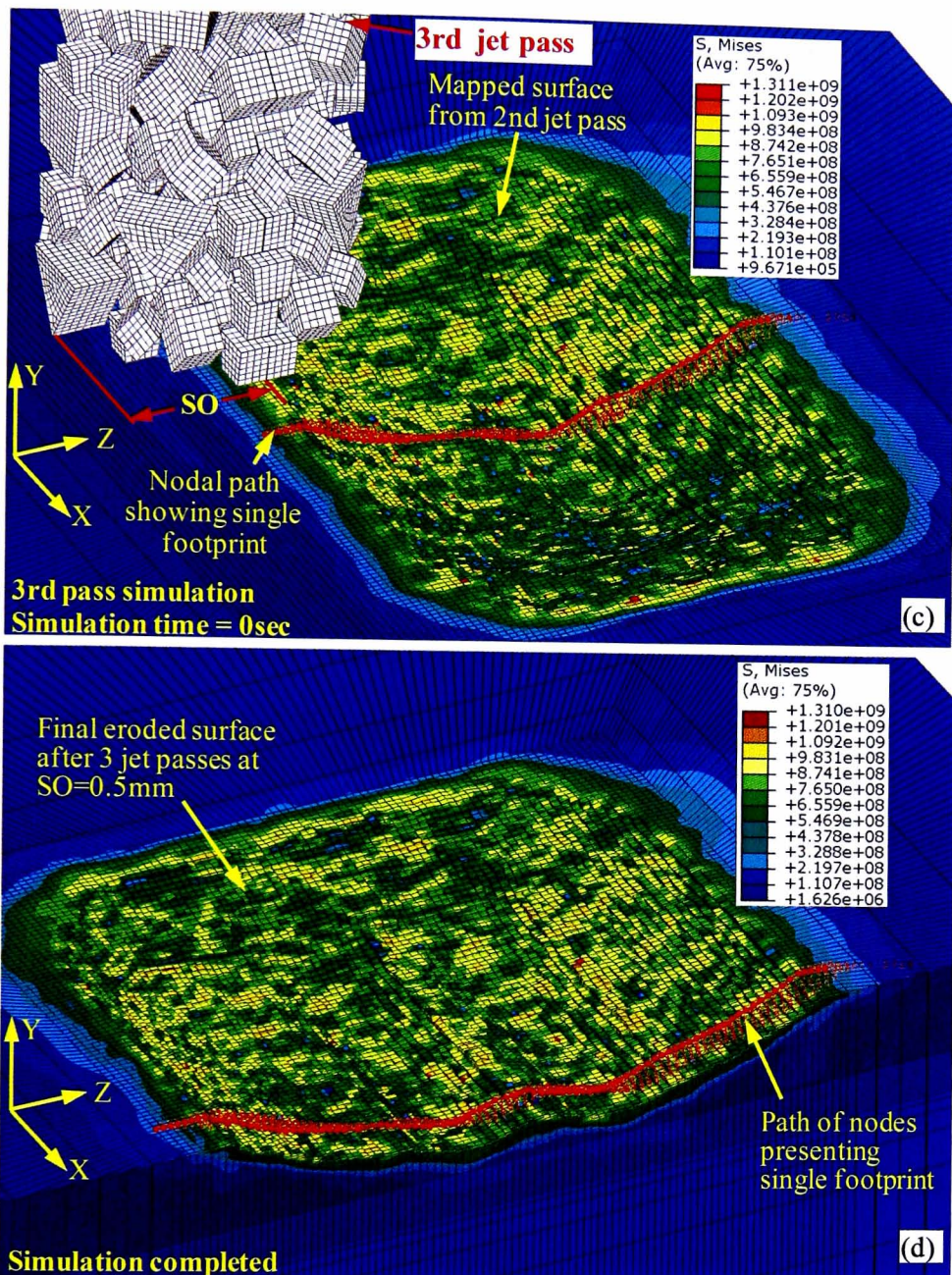


Figure 7-5: Explanation of the simulation process for three jet passes at $P = 207\text{MPa}$, $V_f = 1000\text{mm/min}$, $SO=0.5\text{mm}$. (a) First jet pass simulation; (b) second jet pass simulation; (c) third jet pass simulation; (d) cross-sectioned view of final target surface after three jet passes.

Figure 7-5: *Continued*

As mentioned in section 6.2.2, the spatial distribution of the abrasive particles within the jet plume was acquired from the work of Balz and Heiniger [122]. This distribution was based on the number of particles observed at various positions within the jet diameter. When the model was run for the overlapping jet passes based on this particles number based Gaussian distribution, the erosion behavior was

underestimated in the simulated footprints around the jet central axis for all the cases. These differences were minor and could not be spotted easily for the footprints generated as a result of single jet pass when compared with the experimental results. However, these variations became more noticeable after two and three passes of the jet. Figure 7-6 shows an example of the comparison of a simulated footprint with the corresponding experimental one for two jet passes at $SO=0.5\text{mm}$. It can be seen in Figure 7-6 that the simulated footprint agrees well with the experimental one away from the jet center as indicated by encircled region “a”. The main differences, i.e. lower depths (low erosion), are within a jet radius of 0.3mm . Zone “b” represents the less eroded region on the kerf during the first jet pass, whereas circle “c” shows the same location as region “b” around jet central axis during the second pass.

It can be seen that the disagreement between the simulated and experimental footprints increases in region “c”. This is due to the fact that during AWJ machining, the surfaces anomalies (e.g. craters/pits) once developed are further amplified during the successive passes of the jet [17]. Since it is known that the shape of the AWJ footprints depends on the kinetic energy distribution of the jet [18], [171]. Given that the velocity of the particles is almost constant across the jet [121], the shape of the footprint depends on the mass distribution of the abrasive particles around the jet central axis. This suggested that more mass was needed to be added to the layers of abrasive particles within the radius 0 to 0.3mm of the jet. It should be noted that this problem did not occur due to the material failure criterion, because otherwise a uniformly under- or over-erosion would be observed throughout the footprint. One of the reasons why the particles number based distribution model resulted in a deviation from the experimental results, was that the garnet abrasives mesh size used in ref [122] was 120, i.e. the average particle size 0.125mm , whereas in the current study

the garnet particles mesh size used was 80 with an average particle size of 0.180mm. This difference in abrasive mesh sizes affected the number and sizes of the abrasive particles travelling at various radii within the jet plume. This was the reason why more particles were required to be added in the as-is distribution from ref [122] inside the jet radius of 0.3mm.

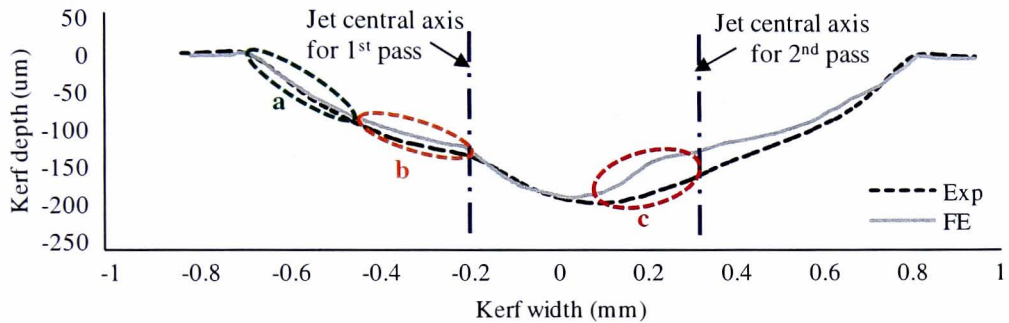


Figure 7-6: Preliminary comparison of FE and experimental (Exp) footprints at $P=276\text{MPa}$, $V_f=2000\text{mm/min}$, $SO=0.5\text{mm}$, $n=2$.

FE modelling provided the opportunity to present the mass distribution of the particles within the jet plume which is more accurate for modelling and studying the AWJ structure rather than a number-based spatial distribution of particles. Figure 7-7 presents the comparison of the mass distributions in the jet when the particles were arranged according to the number based spatial distribution in the model from the results of ref [122] and the improved particles mass distribution.

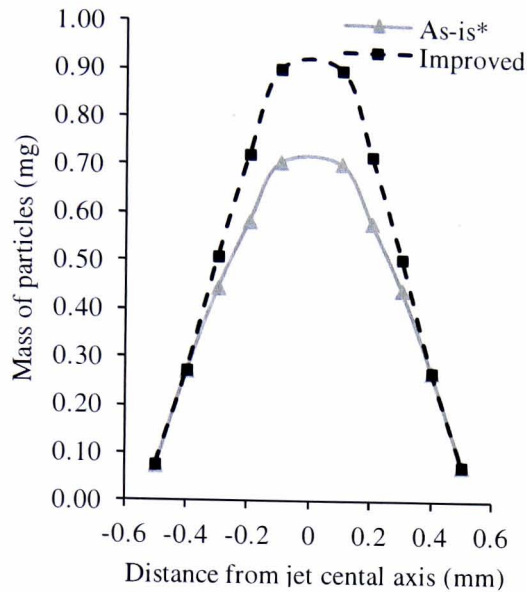
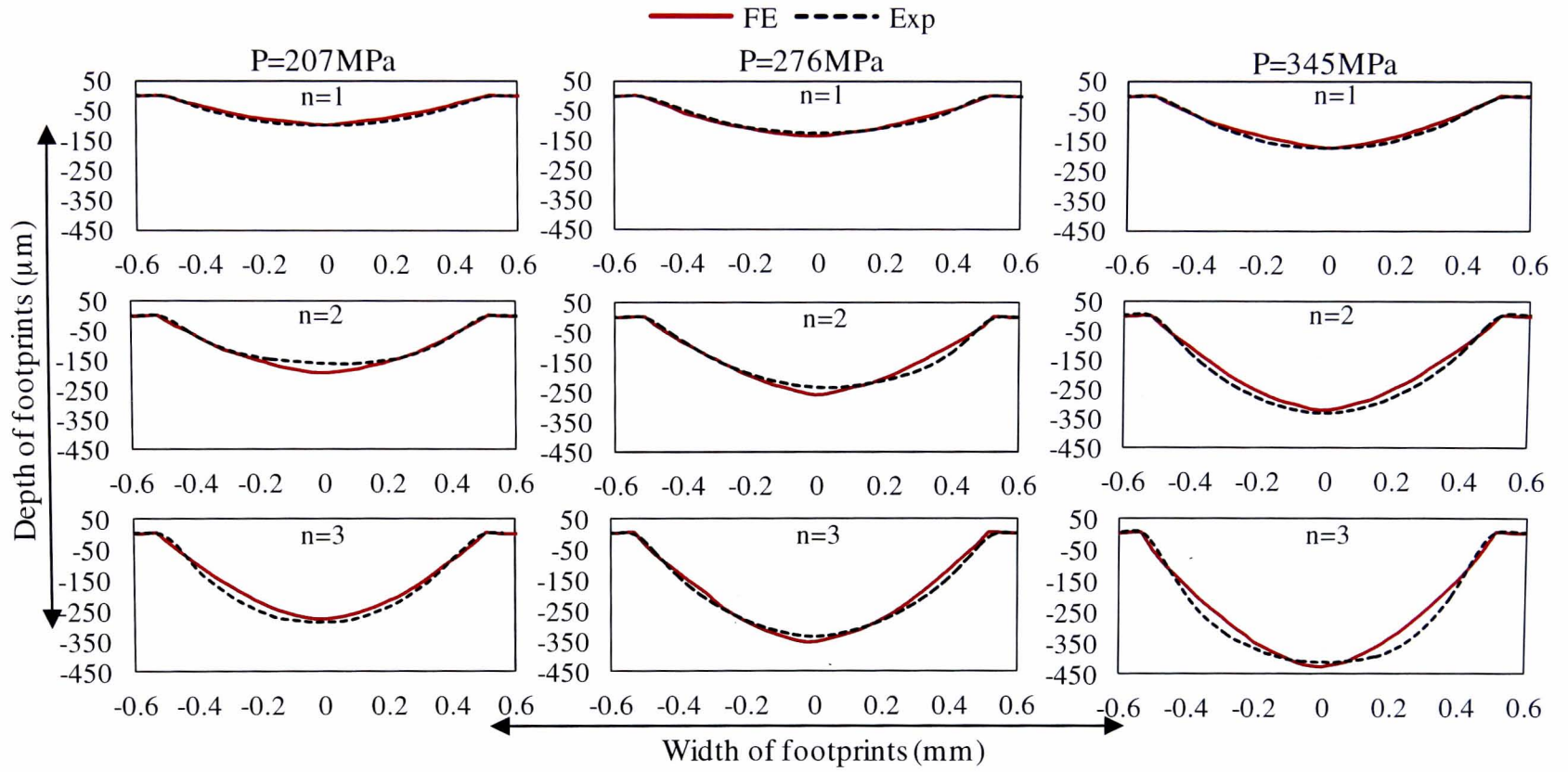


Figure 7-7: Comparison of mass distribution of particles in the jet plume. * As-is distribution is calculated when particles are arranged based on ref [122] number based spatial distribution.

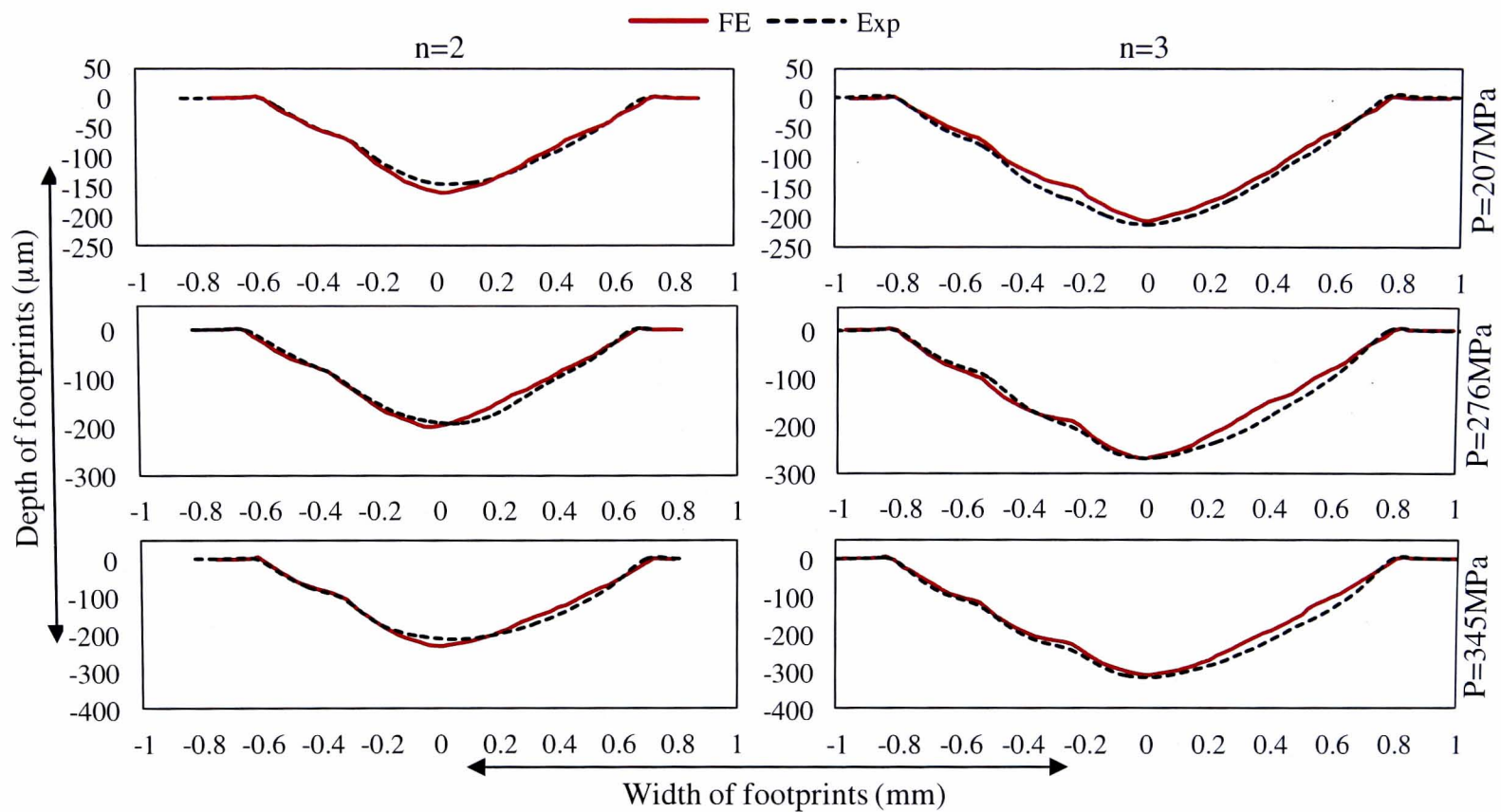
After improving the mass distribution of particles in the jet plume, the simulations were run at various parameters. Figure 7-8 shows an example of FE simulations results compared with the experimental results at given parameters. The simulated footprints now show a more realistic behavior when compared with the experimental data, i.e. the depths of some footprints match with the experimental ones, some show more depths, while some show lower depths. On the contrary, all the overlapped simulated footprints showed less depths compared to the experimental kerfs when the simulations were run based on the as-is (from ref [122]) particles distribution. For the ease of comparison among the results at various process parameters, the scale of the Y-axis on all the plots in the same row was kept equal. The simulated footprints were in good agreement with the experimental data both in terms of depth and shape of the profiles. The FE model correctly predicted the depth of the footprints at different pressures (P) and number of passes (n) of the jet with a maximum error of 15%.

Keeping the process variation in consideration, e.g. particles fragmentation and shapes etc, the simulation results are very encouraging.

(a)



(b)



(c)

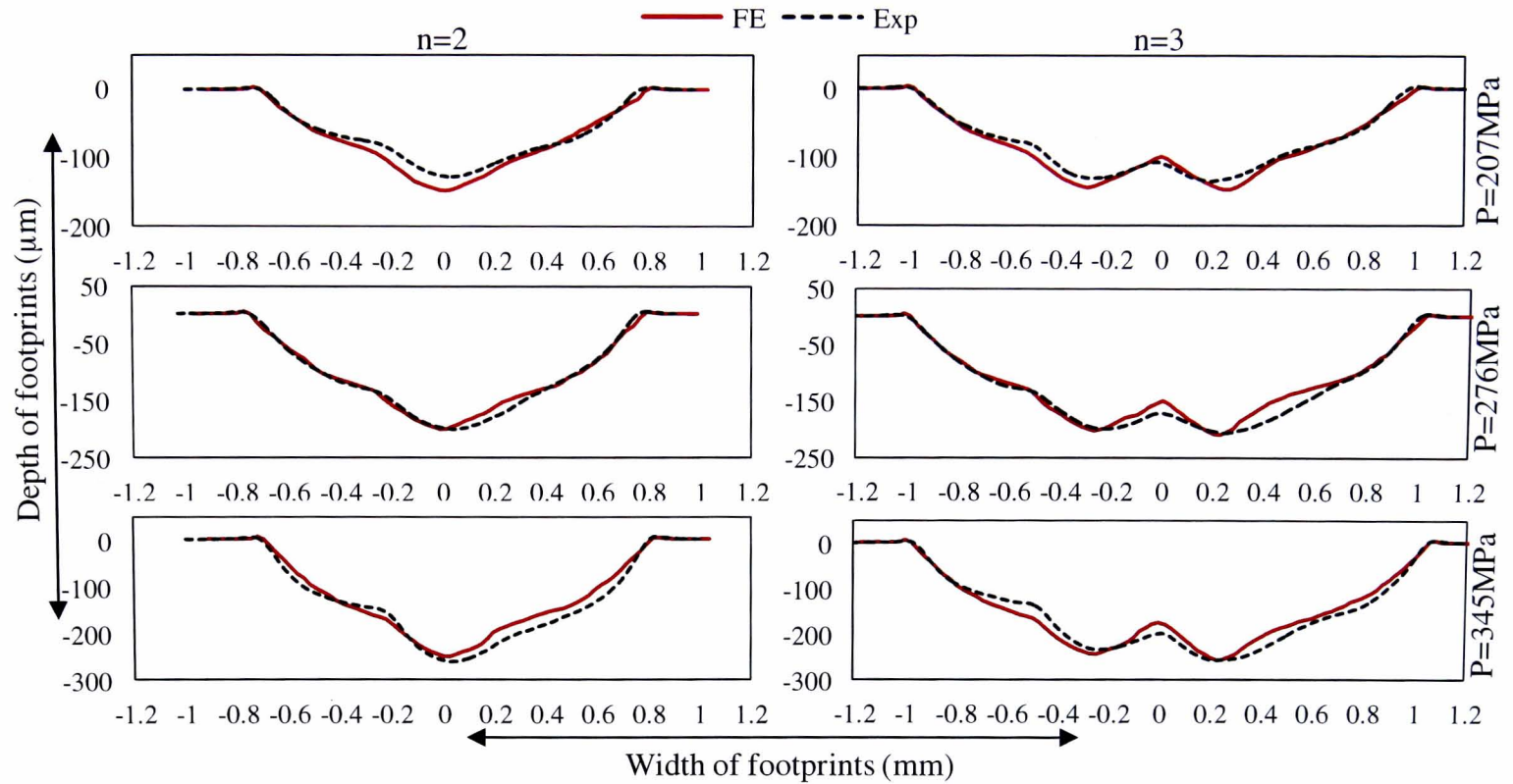


Figure 7-8: Comparison of simulated and experimental footprints at $V_f = 2000\text{mm/min}$ (a) $SO=0$ (b) $SO=0.3\text{mm}$ (c) $SO=0.5\text{mm}$.

Despite the good agreement with experimental data, there were some differences between the depths of the simulated and experimental footprints when it came to step-over distances of 0.3mm and 0.5mm. For example, in Figure 7-8, at $SO=0.5\text{mm}$ and $n=3$ for all the pressures, the midpoint ($x = 0$) of all the experimental footprints was deeper than the predicted ones. These differences were there due to the secondary erosion resulting from the reflected jet. Figure 7-9 presents three experimental footprints on top of each other for one, two and three passes of the jet as an example to explain this effect. The dotted circle “a” shows the difference between the eroded area for footprints for first and second jet pass. The profile of the footprint for two jet passes ($n=2$) shows more steepness i.e. more erosion compared to the footprint for one jet pass ($n=1$). This is due to the fact that when the AWJ impinged the target at point “c” during the second pass, the jet got reflected and hit the already eroded area “a” on the first footprint ($n=1$) and erode it further. Similarly, point “d” on the footprint after two jet passes underwent secondary erosion by the reflected jet during the third jet pass ($n=3$) and eventually settled at point “e”. The current FE model was unable to simulate the effect of the reflected jet because water was not included in the simulation. However, the effect of secondary erosion was not serious and the model predictions were still in good agreement with the experimental data.

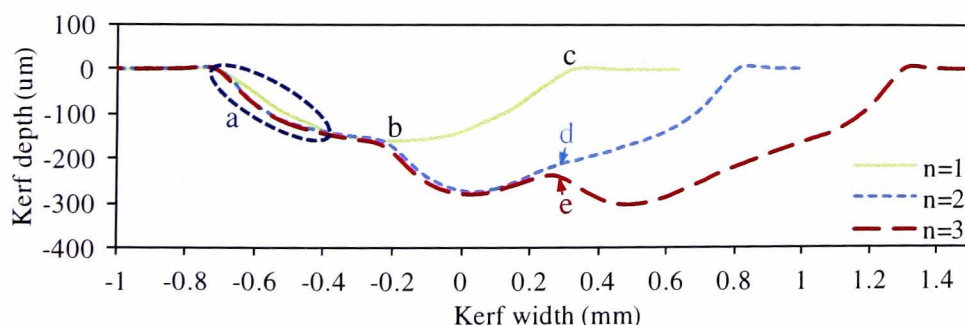


Figure 7-9: Effect of secondary (reflected) jet on the footprints; $P = 345\text{MPa}$, $V_f =$

2000mm/min, SO = 0.5mm

It can also be observed in Figure 7-9 that point “d” is deeper than point “b”. This is accounted for the facts that: (i) point “b” is created when the first jet pass impacts the flat (horizontal) target surface, whereas point “d” is generated on the kerf when the jet hits the surface of the target with a slope resulting in higher erosion rate compared to the former [60]; (ii) the region around point “c” has more tendency to erode as compared to the initial flat surface due to the stored residual stresses. Moreover, it can be noticed that the footprint after the second pass is not symmetric. This is attributed to the fact that when the second jet pass impinges the target with its central axis at point “c”, half of the jet on the left hand side impacts on the non-flat surface of an already eroded footprint, while the right half is incident on a flat surface. This results in a different erosion rate on both sides of jet central axis on the target, and hence generating an asymmetric profile.

As a result, it can be concluded that the overlapping footprints cannot be generated by simple linear summation of two or more single footprints at a given step-over distance. Instead it is a non-linear process where the effects of previously generated stresses and slopes of the eroded surfaces need to be taken into account. These effects were also captured by the FE model and the simulated footprints for non-zero step-over distances were not symmetric. This can easily be observed for example in the predicted footprints at SO=0.5 and $n = 2$ in Figure 7-8(c).

The FE model was validated further by considering the erosion rates generated during the simulations and the experiments. Figure 7-10 gives an example of the assessment of the erosion rates (ER) calculated from the FE model for three overlapping jet passes ($n=3$) and compared with the corresponding experimental values. The values of

ER presented in the graph are the average of erosion rates calculated during the three jet passes at each pressure.

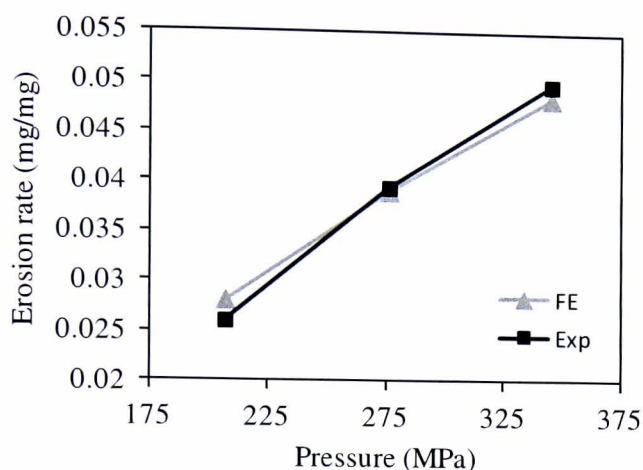


Figure 7-10: Comparison of FE simulated and experimental erosion rates at $V_f = 1000\text{mm/min}$, $SO = 0.3\text{mm}$, $n = 3$.

Once again, the good agreement between the FE and experimental erosion rates justifies the appropriateness of the assumption of not including the water in the current model. It proves that the erosion produced within the target by the water droplets in the AWJ plume is insignificant at the traverse speeds and pressures considered in the current study. Therefore, the current FE model provides an accurate and reliable method for predicting the overlapping milled footprints at various operating parameters, which is a first necessary step towards automating the AWJ milling process. Furthermore, the model can be used as a tool for studying the mass distribution of the abrasive particles in the AWJ plume which is crucial to understanding the process of kerf generation.

7.5 Conclusions

A new full scale 3D FE model for AWJ milling of overlapping footprints is

demonstrated in this chapter while considering the real life experimental conditions such as size distribution and sharp edged shape of abrasive particles, experimental impacting velocities, etc. The FE simulation results are presented and compared with the experimental data over a range of operating parameters such as water pressures, step-over distances and number of jet passes. The following main conclusions can be drawn from the current work.

- The FE model is able to predict the jet footprints and the erosion rates at various operating parameters, and the simulated results are in good agreement with the experimental data both qualitatively, i.e. with respect to shapes of footprints, and quantitatively, i.e. depths of the footprints (maximum errors < 15%) and magnitudes of the erosion rates (errors < 8%). The consistency between the predicted and experimental results confirms the validity of the FE model and the assumptions considered during the modelling process.
- The model enables the study of the interaction phenomena between the jet footprints when they are overlapped. This is in line with the observation that the overlapped footprints are not a linear summation of the single footprints; rather the effects of the slope of the eroded surfaces and the residual stresses stored in the target due to the earlier passes need to be taken into account.
- The FE model provides an opportunity to study and improve the mass distribution of abrasive particles within the jet plume which plays a significant role in the controlling the profiles of the overlapped footprints.
- A method is devised that can successfully include multiple passes of the jet in the FE model as sequential events to simulate the overlapping trenches without becoming extremely computationally expensive or not being able to run due to memory problems.

Although further challenges exist in the modelling of jet footprints, e.g. defining an automatic way of assembling the particles into the jet plume according to a Gaussian distribution, the proposed model enables accurate prediction of overlapping jet footprints and provides an opportunity for further enhancements of the models to be able to simulate the generation of 3D freeform surfaces as a result of an arbitrarily moving jet.

Chapter 8 Mathematical modelling of AWJ footprints

This chapter provides a detailed description of the mathematical modelling of the AWJ milled footprints at various nozzle tilt angles and jet path directions. The presented work is an extension of the work done by Axinte et al. [107] on the mathematical modelling of the AWJ milled footprints where the developed model was able to predict footprints at 90° incidence only. A procedure is provided to generate the test-pieces which can be used to generate the data for the calibration and validation of the mathematical model. A comparison of the predicted results from the model and the experiments is exhibited and discussed together with the plots of mean of residuals between the experimental and the predicted data. This is followed by an example of the application of the mathematical model and a brief comparison of the mathematical and FE modelling with conclusions.

8.1 Introduction

One of the reasons for undertaking mathematical modelling of AWJ milled footprints is that, in addition to the FE model for the AWJ milling, there is still a need for an analytical (mathematical) model that can be employed to predict the footprints in the real time to enable efficient control of the jet paths on CNC machines. Furthermore, a mathematical model is also required such that it can be used along with the CAM packages to generate CNC files for the surfaces to be milled. Although some analytical methods of predicting jet footprint profiles in abrasive waterjet technology have been proposed, these are limited to statistical and artificial intelligence approaches with their inherent disadvantages that they require a great deal of raw data for model construction [52], [134], [135]. In addition, most of these models are actually related to a larger jet penetration or a larger width variation of the cut, which

are not suitable for milling conditions. Another set of approaches reported for predicting footprint profiles are those based on geometric (mathematical) modelling [140], [141], [172]. However, these approaches are limited to predict footprints only in a masked or stationary target during air powder-blasted jets. Moreover, the execution times (about 16–150 min) were considered not fast enough to cater for the needs of actual CNC machining.

In order to address these issues, this chapter focuses on extending a previously reported model [107] a step further by making the model capable of predicting the AWJ milled footprints when the jet impinges the target surface at different nozzle tilt angles (θ) and follows trajectories (jet paths) of various directions (β) in the plane of the workpiece while travelling with variable traverse speeds (V_f), i.e. jet exposure times. The developed model is a generic mathematical model with the benefit of simplicity of having fewer variables for predicting maskless waterjetted footprints for arbitrarily moving jet-paths. The novelty of the proposed model is that the jet footprint can be predicted for a truly arbitrarily moving jet for a specific process or machine parameters referred to as fixed parameters in Figure 8-1, i.e. the target material and the jet energy parameters. Once the model is calibrated for a set of fixed parameters by using a shallow scanned footprint, it can be used to predict the footprints for various combinations of the variable parameters. For a new set of materials or machine configurations, only a single calibration will be required to predict footprint profiles at various tilt angles (θ), traverse speeds (V_f) and path directions (β). This footprint modelling approach is generally applicable and can effectively support the development of advanced jet path strategies to enable the controlled generation of complex workpiece geometries, i.e. freeform surface.

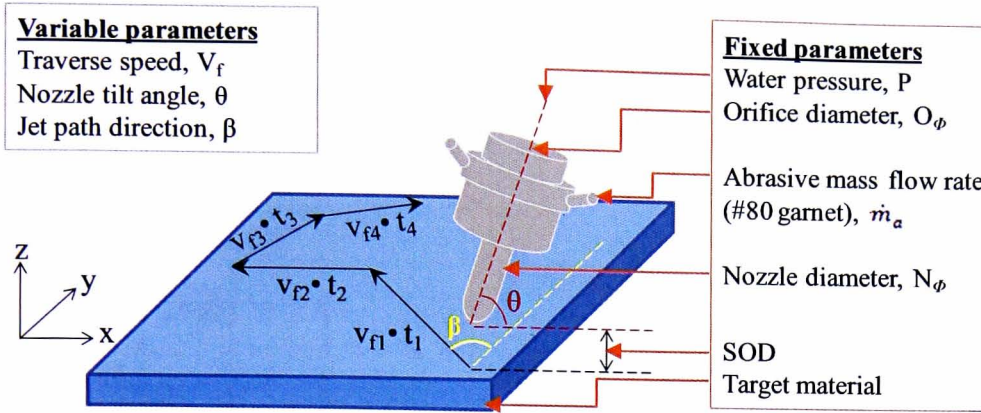


Figure 8-1: Variable and fixed parameters used in the footprint models for AWJ machining.

8.2 Footprint prediction model for an arbitrarily moving jet

The mathematical model for AWJ footprints reported by Axinte et al. [107] was cable of predicting footprints for a straight moving jet path at normal jet incidence only for the brittle materials. The present model is being developed further to cover the jet-path strategy for AWJ milling and takes into account the effect of the nozzle tilt angles (θ) and jet path directions (β) while moving at different traverse speeds (V_f).

8.2.1 Model Definitions

Consider a 3-dimensional Cartesian coordinate system with the Z-axis directed along the axis of the cylindrical jet, pointing towards the nozzle, and the Y-axis pointing in the direction in which the jet moves, i.e. along the jet traverse direction as shown in Figure 8-2(a). It was assumed that an abrasive waterjet jet, with radius a , impacts at an angle θ on a flat workpiece surface while moving with a constant traverse speed V_f ($v=v_f$) at an angle of β with the steepest descent line on the surface in the Y-direction as depicted in Figure 8-2(b). The jet footprint is a function $z = \bar{Z}(x, y, t)$, where x is the

distance from the jet central axis, y is the direction in which the jet moves and t is the jet dwell time, i.e. how fast or slow the jet moves over the workpiece surface.

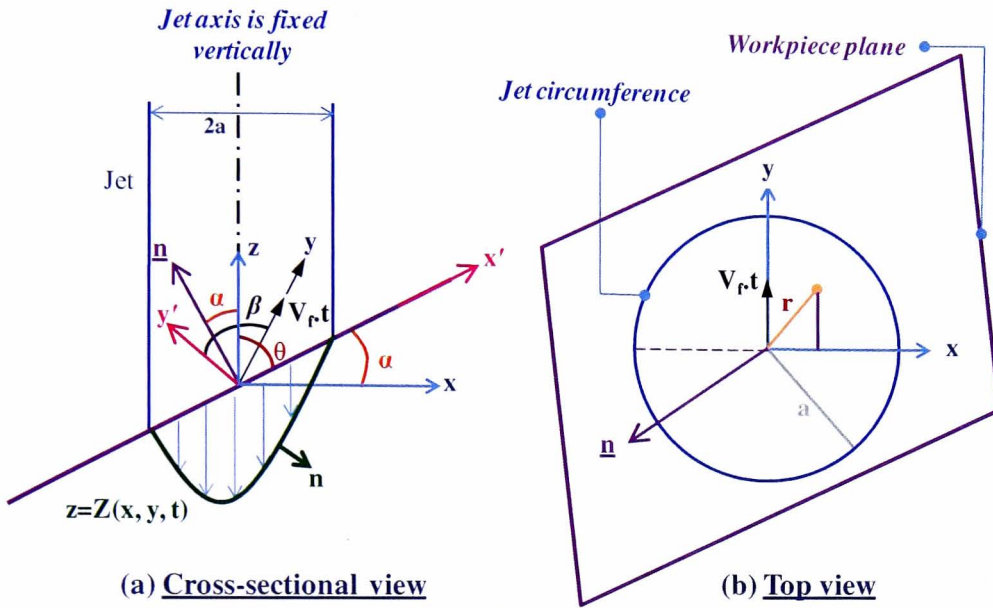


Figure 8-2: Schematic diagram of the jet footprint: (a) cross-sectional view and (b) top view.

Assume that the axis of the jet is at $x = 0$, $y = -a$ when $t = -a/V_f$, so that the jet impinges on the line of intersection of the surface and the plane $y=0$ when $-a < V_f t < a$.

The unit inward normal to the eroded (etched) surface ($z = \bar{Z}(x, y, t)$) is given as

$$n = \frac{\bar{Z}_x, \bar{Z}_y, -1}{\sqrt{1 + \bar{Z}_x^2 + \bar{Z}_y^2}}, \text{ where a subscript denotes a partial derivative (i.e. } \bar{Z}_x = \frac{\partial z}{\partial x},$$

$$\bar{Z}_y = \frac{\partial z}{\partial y}) \quad \text{Eq. 8.1}$$

Consider the unit normal vector $\underline{n} = \begin{bmatrix} n_x \\ n_y \\ n_z \end{bmatrix}$ to the initial plane surface to be milled. The

equation of the initial surface $\bar{Z}(x, y, 0)$ can be obtained by defining a plane ($\underline{n} \cdot (x, y, z) = 0$) by specifying a point and a normal vector to the plane as:

$$\bar{Z}(x, y, 0) = x \tan \alpha \cos \beta + y \tan \alpha \sin \beta \quad \text{Eq. 8.2}$$

If the surface is etched away at velocity $U(x, y, t)$ in the normal direction, then

$$\frac{\partial \bar{Z}}{\partial t} = U(x, y, t) \underline{n} \cdot \underline{e}_z = - \frac{U(x, y, t)}{\sqrt{1 + \bar{Z}_x^2 + \bar{Z}_y^2}} \quad \text{Eq. 8.3}$$

where \underline{e}_z is a unit vector along the z-axis

The model assumes that the etching rate of the surface depends on the component of the impact velocity ($V_{\text{imp}} = V$) of the particles in the jet normal to the free surface with power q (2.55 from experiments) of the impingement velocity in the direction of the inwards unit normal \underline{n} of the surface being etched ($\underline{V} \cdot \underline{n}$)^q [138], [169].

$$\frac{\partial \bar{Z}}{\partial t} = - \frac{C(\underline{V} \cdot \underline{n})^q}{\sqrt{1 + \bar{Z}_x^2 + \bar{Z}_y^2}}, \text{ where } C \text{ is a positive constant} \quad \text{Eq. 8.4}$$

$$\frac{\partial \bar{Z}}{\partial t} = - \frac{CV^q (-\underline{e}_z \cdot \underline{n})^q}{\sqrt{1 + \bar{Z}_x^2 + \bar{Z}_y^2}} = - \frac{CV^q}{\sqrt{1 + \bar{Z}_x^2 + \bar{Z}_y^2}^{q+1}} \quad \text{Eq. 8.5}$$

Knowing that the energy of the jet transmitted to the workpiece surface is a function of the radial position in the jet [122], [171]

$$r = \sqrt{x^2 + (y - vt)^2} \quad \text{Eq. 8.6}$$

and defining $E_0 E(r) \equiv CV^q$, where E_0 quantifies the typical etching rate, such that

$E(r)$ is a dimensionless function with a unit maximum value and let $k = q + 1$, this gives

$$\frac{\partial \bar{Z}}{\partial t} = -\frac{E_0 E(\sqrt{x^2 + (y - vt)^2})}{(1 + \bar{Z}_x^2 + \bar{Z}_y^2)^{\frac{k}{2}}} \quad \text{Eq. 8.7}$$

Now concentrate on the etched surface in the plane $y=0$ only i.e. $Z(x, y, t) = \bar{Z}(x, 0, t)$

$$\text{, when } -\sqrt{a^2 - x^2} < vt < \sqrt{a^2 - x^2} \quad \text{Eq. 8.8}$$

Since the jet moves with constant velocity V_f in the y -direction according to the jet path with an angle β , we have

$$\frac{\partial Z}{\partial y} = \tan \alpha \sin \beta - \frac{1}{v} \frac{\partial Z}{\partial t} \quad \text{Eq. 8.9}$$

Substituting Eq. 8.8 and Eq. 8.9 into Eq. 8.7, we get,

$$\frac{\partial \bar{Z}}{\partial t} = \begin{cases} \frac{E_0 E(x^2 + v^2 t^2)}{(1 + Z_x^2 + (\tan \alpha \sin \beta - \frac{1}{v} \frac{\partial Z}{\partial t})^2)^{\frac{k}{2}}} & \text{for } -\sqrt{a^2 - x^2} < vt < \sqrt{a^2 - x^2} \\ 0 & \text{for } -a < vt < -\sqrt{a^2 - x^2} \text{ and } \sqrt{a^2 - x^2} < vt < a \end{cases}$$

$$\text{Eq. 8.10}$$

to be solved subject to the initial condition in Eq. 8.2

$$\bar{Z}(x, 0, 0) = x \tan \alpha \cos \beta \quad \text{Eq. 8.11}$$

In order to be able to assess the relative sizes of the various terms in Eq. 8.10 & 8.11, the problem can be made dimensionless by defining the following dimensionless parameters:

$$(\hat{x}, \hat{y}, \hat{z}) = (x, y, z) / a; \quad \bar{Z} = a\hat{Z}; \quad t = \frac{a}{v_f} \hat{t}; \quad \varepsilon = E_0 / v_f; \quad \hat{E} = \bar{E}$$

The dimensionless model is given as:

$$\frac{\partial \hat{Z}}{\partial \hat{t}} = \begin{cases} \frac{-\varepsilon \hat{E} (\sqrt{\hat{x}^2 + \hat{t}^2})}{\left(1 + \left(\frac{\partial \hat{Z}}{\partial \hat{x}}\right)^2 + \left(\sin \beta \tan \alpha - \frac{\partial \hat{Z}}{\partial \hat{t}}\right)^2\right)^{\frac{k}{2}}} & \text{for } -\sqrt{1 - \hat{x}^2} \leq \hat{t} \leq \sqrt{1 - \hat{x}^2} \\ 0 & \text{for } -1 \leq \hat{t} \leq -\sqrt{1 - \hat{x}^2} \text{ and } \sqrt{1 - \hat{x}^2} \leq \hat{t} \leq 1 \end{cases}$$

Eq. 8.12

$$\text{and} \quad \hat{Z}(\hat{x}, 0, 0) = \hat{x} \tan \alpha \cos \beta \quad \text{Eq. 8.13}$$

Eq. 8.12 is a nonlinear partial differential equation, and there is no obvious analytical solution. However, if ε is small, i.e. the traverse speed is very high as compared to the rate of etching of the surface, the slope of the eroded surface is also small and the equation can be linearised. Furthermore, it can be assumed that:

$$\hat{Z} = \hat{x} \tan \alpha \cos \beta + \varepsilon \hat{Z}_0 \quad \text{Eq. 8.14}$$

i.e. adding a small change ($\varepsilon \hat{Z}_0$) as a result of the jet pass on the surface to its initial condition to determine the final state of

the surface (footprint $\hat{Z} = \hat{Z}_f(x)$). Differentiating Eq. 8.14 with respect to \hat{x} and \hat{t} and substituting the values in Eq. 8.12 gives:

$$\frac{\partial \hat{Z}_0}{\partial \hat{t}} = \begin{cases} \frac{-\hat{E} (\sqrt{\hat{x}^2 + \hat{t}^2})}{\left(1 + (\tan \alpha \cos \beta + \varepsilon \hat{Z}_{0x})^2 + (\sin \beta \tan \alpha - \varepsilon \hat{Z}_{0t})^2\right)^{\frac{k}{2}}} & \text{for } -\sqrt{1 - \hat{x}^2} < \hat{t} < \sqrt{1 - \hat{x}^2} \\ 0 & \text{for } -1 < \hat{t} < -\sqrt{1 - \hat{x}^2} \text{ and } \sqrt{1 - \hat{x}^2} < \hat{t} < 1 \end{cases}$$

Eq. 8.15

Now set $\varepsilon = 0$ to obtain the leading order problem

$$\frac{\partial \hat{Z}_0}{\partial \hat{t}} = -\frac{\hat{E}(\sqrt{\hat{x}^2 + \hat{t}^2})}{(1 + \tan^2 \alpha)^{\frac{k}{2}}} = -\cos^k \alpha \hat{E}(\sqrt{\hat{x}^2 + \hat{t}^2}) \text{ for } -\sqrt{1 - \hat{x}^2} < \hat{t} < \sqrt{1 - \hat{x}^2}$$

$$0 \quad \text{for} \quad -1 < \hat{t} < -\sqrt{1 - \hat{x}^2} \text{ and } \sqrt{1 - \hat{x}^2} < \hat{t} < 1 \quad \text{Eq. 8.16}$$

This linear equation can now be integrated to give the integral equation as

$$Z_f(x) = \hat{Z} = \hat{x} \tan \alpha \cos \beta - 2\varepsilon \cos^k \alpha \int_0^{\sqrt{1-x^2}} \hat{E}(\sqrt{\hat{x}^2 + \hat{t}^2}) dt \quad \text{Eq. 8.17}$$

$Z_f(x)$, i.e. the profile of the footprint, can be determined by scanning a shallow ($\varepsilon \ll 1$) experimentally milled trench, and the etching rate function $E(r)$ can be found if the integral equation can be inverted. After some manipulation, the inverted integral equation can be obtained as follows:

$$\varepsilon \cos^k \alpha \hat{E}(r) = \frac{1}{\pi} \left[\int_r^1 \frac{\hat{s} (\hat{Z}_f(\hat{s}) - \hat{Z}_f(\hat{r}))}{(\hat{s}^2 - \hat{r}^2)^{\frac{3}{2}}} d\hat{s} - \frac{\hat{Z}_f(\hat{r}) - \hat{r} \tan \alpha \cos \beta}{\sqrt{1 - \hat{r}^2}} \right] \quad \text{Eq. 8.18}$$

Once the etching function $E(r)$ is calibrated, it will be used in Eq. 8.17 to predict the footprints at other variable parameters as mentioned in Figure 8-1.

8.3 Generation of experimental data

As mentioned in the model operating conditions, the jet energy was set as constant during the trials; hence, the following operating parameters were considered fixed: $P=138\text{MPa}$, $\dot{m}_a = 0.04\text{kg/min}$, $\text{SOD} = 3\text{mm}$. The varying kinematic parameters were:

nozzle tilt angle θ (90° , 80° , 70°), jet path direction β (0 - 315°) and traverse speed V_f (1000 and 2000 mm/min).

With these constant and variable operating parameters, the experimental trials were conducted to generate the footprints used first for model calibration and then to check the prediction accuracy of the proposed model. For this purpose, special testpiece and part programs for the machining were designed which include various beta (β) angles -90° , -45° , 0° , 45° , 90° , 135° , 180° and -135° and were named a, b, c, d, e, f, g and h respectively. Figure 8-3(a) schematically illustrates the tilt angle and the jet path directions (β) in the experiments, and Figure 8-3(b) shows a typical test specimen after the jet passes. For each test the jet started inside the hole in the middle of the specimen (see Figure 8-3(b)) and was stationed for 3-4 seconds to obtain the steady abrasive flow within the jet. For each set of process parameters, two specimens were generated to ensure that the scanned footprints were good representations of the average response of the process. In this way, a significant number of jet footprints were generated as per the specifications in Table 3-6.

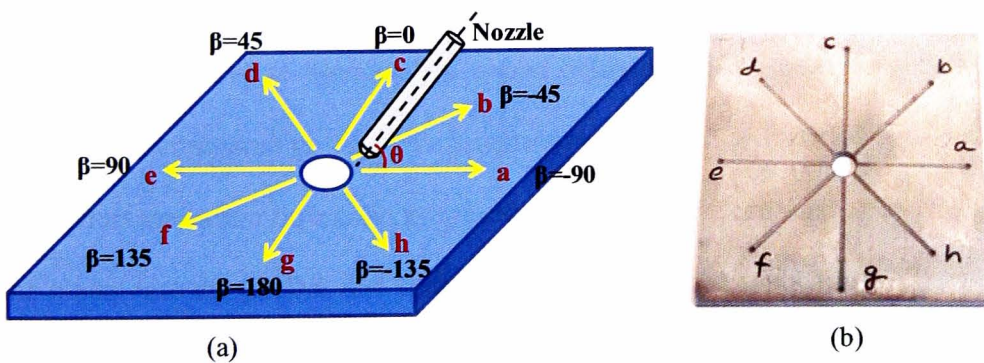


Figure 8-3: Test specimen designed for the model validation: (a) schematic illustration of the jet paths on the testpiece; (b) a testpiece after machining.

To summarize, the successive steps to predict the surface profiles of an arbitrarily-

moving jet path are as follows:

- Generate a shallow trench ($\varepsilon \ll 1$) ideally with depth of cut < 0.15 mm for 1mm wide trench as a candidate for calibrating the model with the jet energy parameters (such as pump pressure, abrasive mass flow, etc) set to constant at a tilt angle (e.g. $\theta=90^\circ$), path direction (e.g. $\beta= 0^\circ$) and a high jet speed (e.g. $V_f=2000$ mm/min);
- Using the coordinates of the scanned shallow trench, deduce the material specific etching rate function $E(r)$ from Eq. 8.18;
- Knowing the $E(r)$, Eq. 8.17 can be fully exploited and solved numerically when ε is not small i.e. for predicting relatively deeper trenches as well.

8.4 Results and discussion

The model presented in Section 8.2 was implemented in MATLAB 7.11 and the resulting predicted footprint profiles were compared to the experimental ones as presented in Figure 8-4. On a 2.6 GHz Quad-core Intel CPU with 4 GB of RAM, the execution times for the prediction of a single footprint at various levels of θ and β angles and jet traverse speeds (V_f), varied between 0.5–1.5 seconds which is 3–100 times faster compared to the other footprint models such as reported in [12, 13]. With such short execution times, the proposed prediction model makes it possible to embed the model into the CAD/CAM software for real industrial applications.

Since a linear theory i.e. $\varepsilon \ll 1$ was proposed for determining the etching rate function $E(r)$, a shallow footprint (mean surface profile) generated at a traverse speed of $V_f = 2000$ mm/min, $\theta = 90^\circ$, and $\beta = 0$ was used for the calibration of the model. Once the model was calibrated, i.e. the etching rate function for the specific material

and machine configuration was found, the model was run at various combinations of nozzle tilt angles (θ), jet path directions (β) and traverse speeds (V_f). Figure 8-4 shows examples of the comparison of the predicted and the experimental results when performing AWJ milling with variable kinematic parameters ($\theta=70^\circ, 90^\circ$; $\beta = -90^\circ, -45^\circ, 0^\circ, 45^\circ, 90^\circ, 135^\circ, 180^\circ, -135^\circ$; $V_f = 500, 1000$ mm/min) at constant energetic parameters of the jet ($P = 138\text{MPa}$; $\dot{m}_a = 0.04\text{kg/min}$; $\text{SOD} = 3\text{mm}$). It should be noted that jet impingement angles smaller than $\theta=70^\circ$ were not employed due to their impracticality in real AWJ milling operations owing to the potential hazards of the reflected jets.

(a)

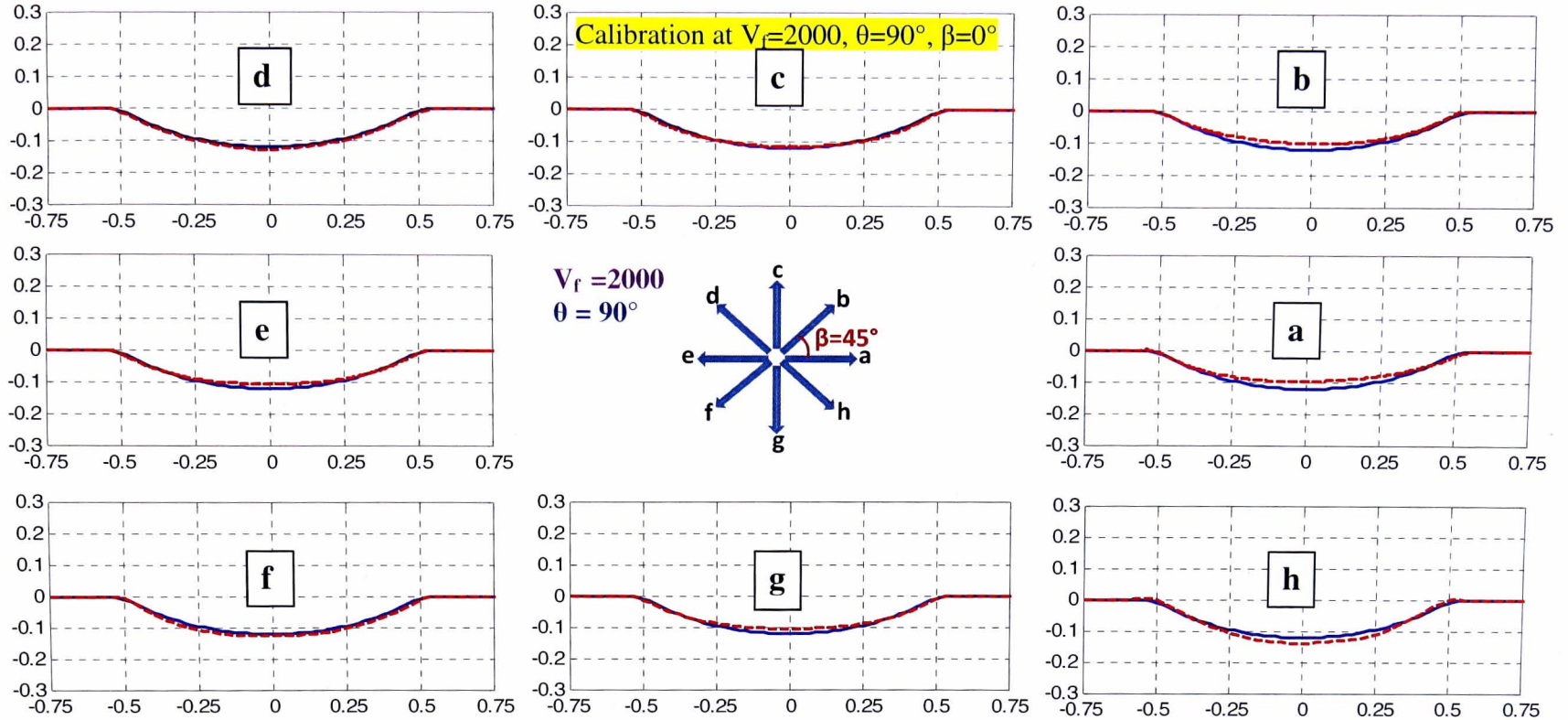


Figure 8-4: Examples of the model predicted footprint profiles (blue solid lines) against the experimental ones (red dotted lines) at indicated parameters:(a) $V_f=2000\text{mm/min}$ and $\theta=90^\circ$; (b) $V_f=2000\text{mm/min}$ and $\theta=70^\circ$; (c) $V_f=1000\text{mm/min}$ and $\theta=90^\circ$; (d) $V_f=1000\text{mm/min}$ and $\theta=70^\circ$. Jet impact direction is from right to left. (Note: the units for both the abscissa and the ordinate are “mm”).

(b)

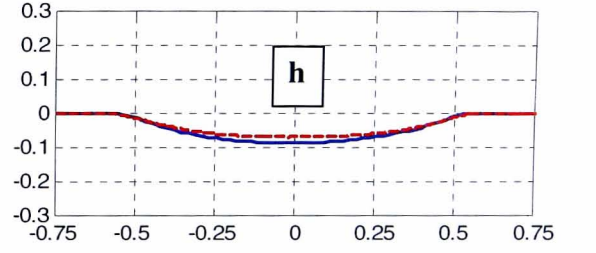
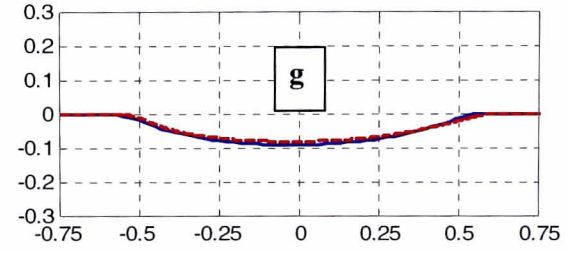
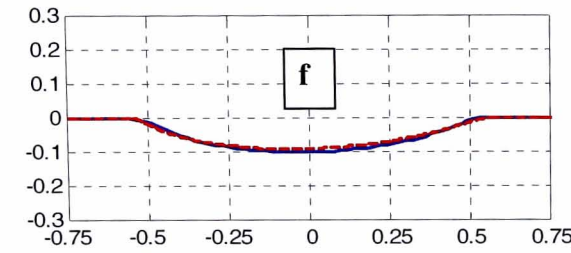
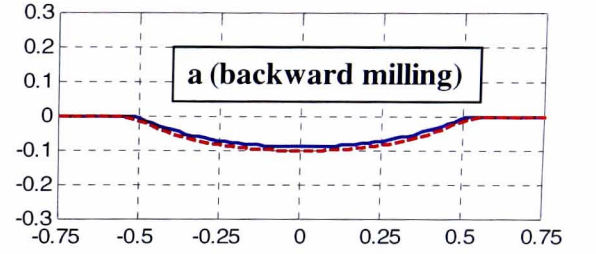
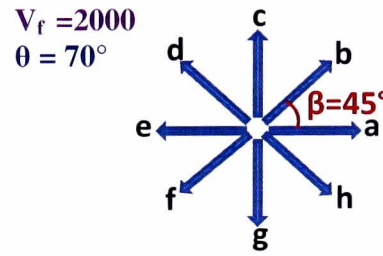
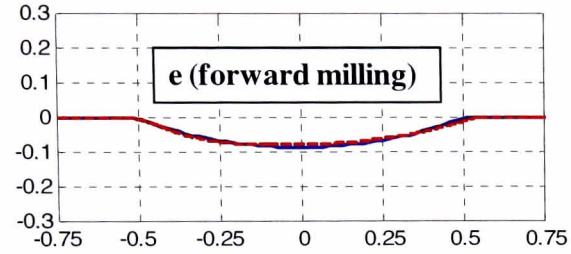
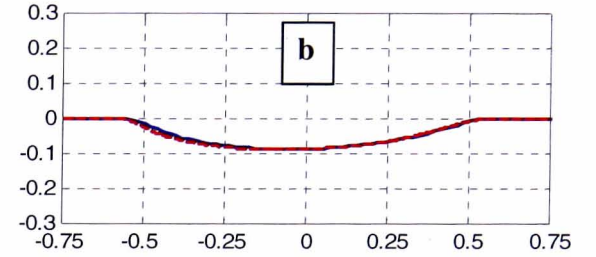
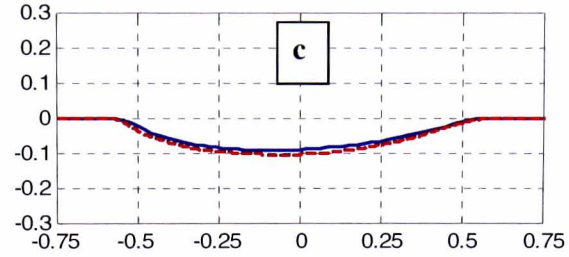
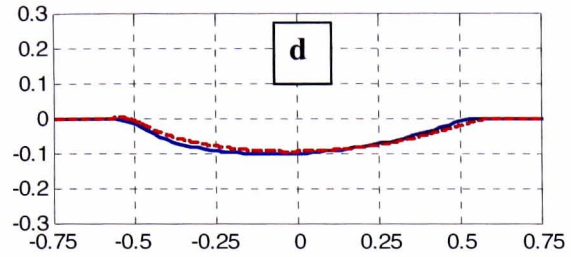


Figure 8-4: Continued

(c)

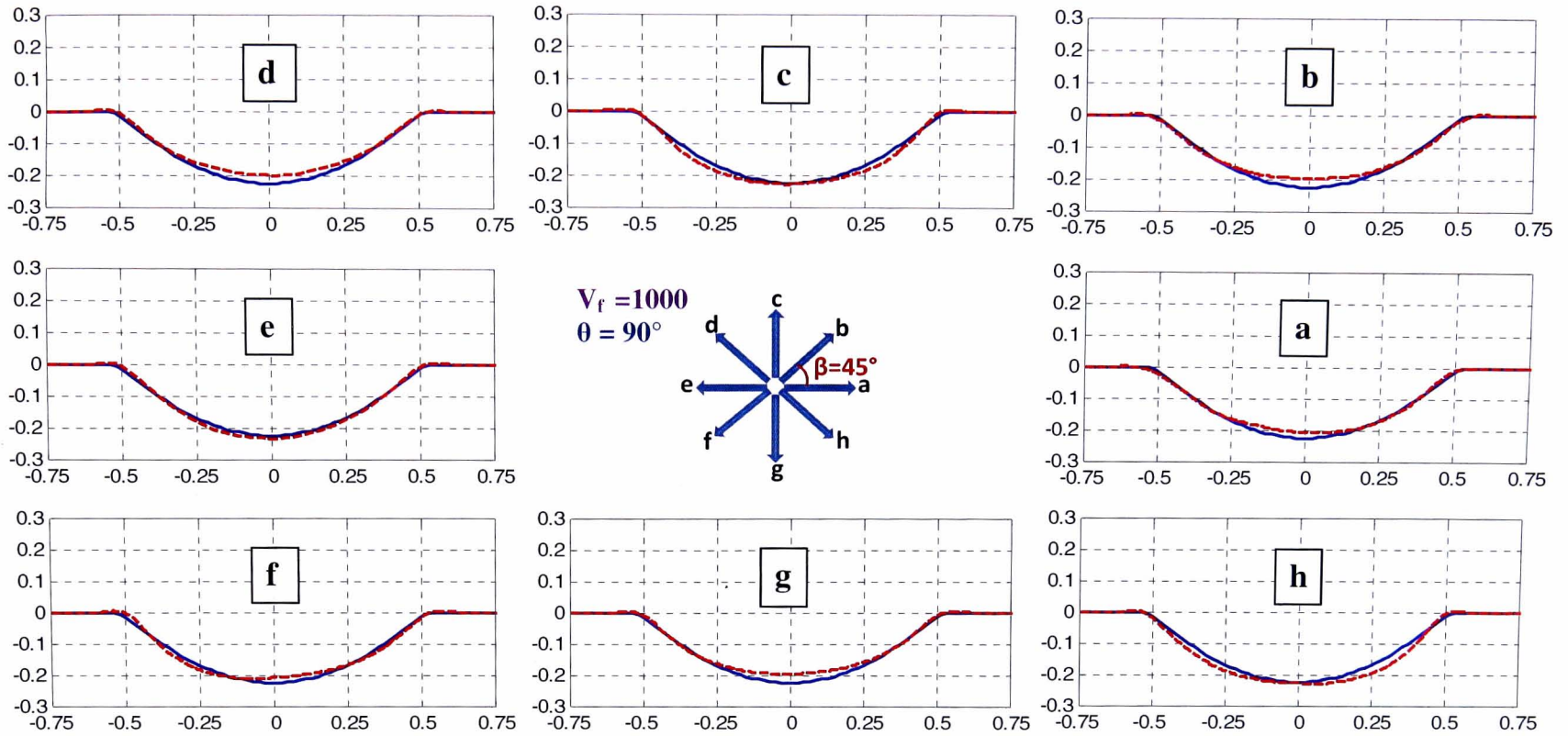


Figure 8-4: *Continued*

(d)

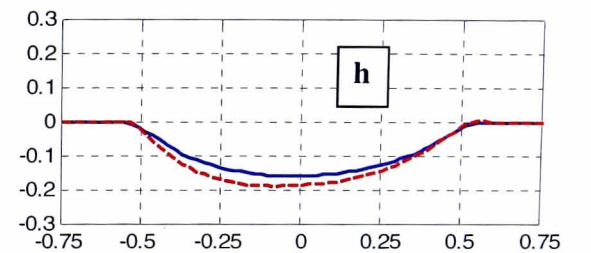
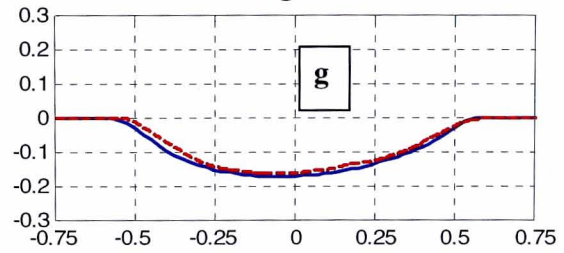
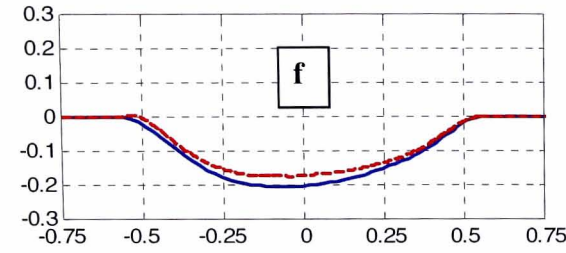
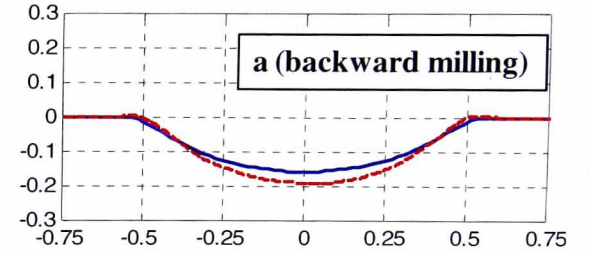
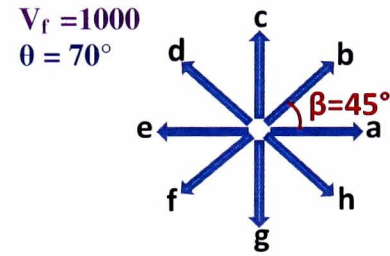
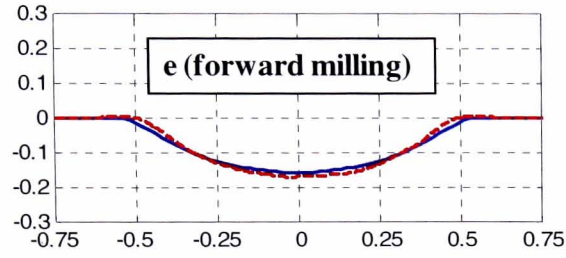
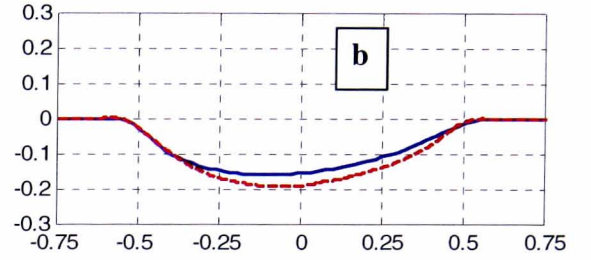
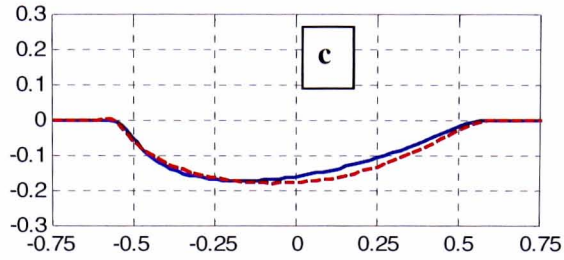
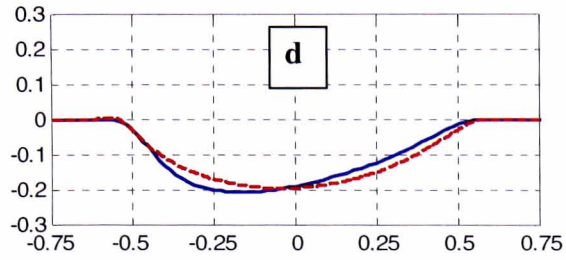


Figure 8-4: Continued

It can be seen in Figure 8-4 that once the calibration of the model is done at $V_f = 2000 \text{ mm/min}$, $\theta = 90^\circ$ and $\beta = 0^\circ$, the surface profiles of abrasive waterjet footprints can be predicted for arbitrarily-moving jet-paths. Observing the results presented in Figure 8-4 while taking into consideration the variations of the process, the predicted footprints are in a good agreement with the experimental ones in terms of their depth and geometry of the surface profiles. However, it can be noted that the prediction accuracy slightly decreases with the decrease of jet tilting angle and the traverse speed, e.g. in Figure 8-4(d). This is attributed to the facts that: (i) during the non-normal AWJ impact, the differences between the local slopes of the impacting particles and the nozzle tilt angle (θ) are higher as compared to the normal jet impingement [18]; (ii) with deeper footprints the secondary effects i.e. erosions made by jet reflections within the kerf become relatively more important.

As the errors between the real and predicted jet footprints are of non-constant distribution along their profiles, an indicator of the modelling accuracy can be provided by the residual plots (actual data – predicted data) of the two curves. In order to quantitatively evaluate the accuracy of the developed model, as shown in Figure 8-5, the mean of residuals (R_M) and root-mean-square of residuals (R_{RMS}) for the predicted depth and the actual (experimental) depth at different combinations of jet feed speeds ($V_f = 2000, 1000 \text{ mm/min}$), jet tilt angles ($\theta = 90^\circ, 70^\circ$) and milling paths ($\beta = a, b, c, d, e, f, g, h$) are considered. In this way, a better overview of the phenomena occurring during the machining process can be revealed. For example, the mean value of residuals (R_M) provides a quick overview of the variations in depth at different jet path directions (β) because of the process characteristics. On the other hand, the root-mean-square error combines the magnitudes of the errors in predicted footprints with respect to the experimental data and provides a measure of the predictive power of the

model. The R_{RMS} value is considered here instead of the standard deviation of the residuals as the latter considers the variation about the mean rather than about the theoretical zero (expected value).

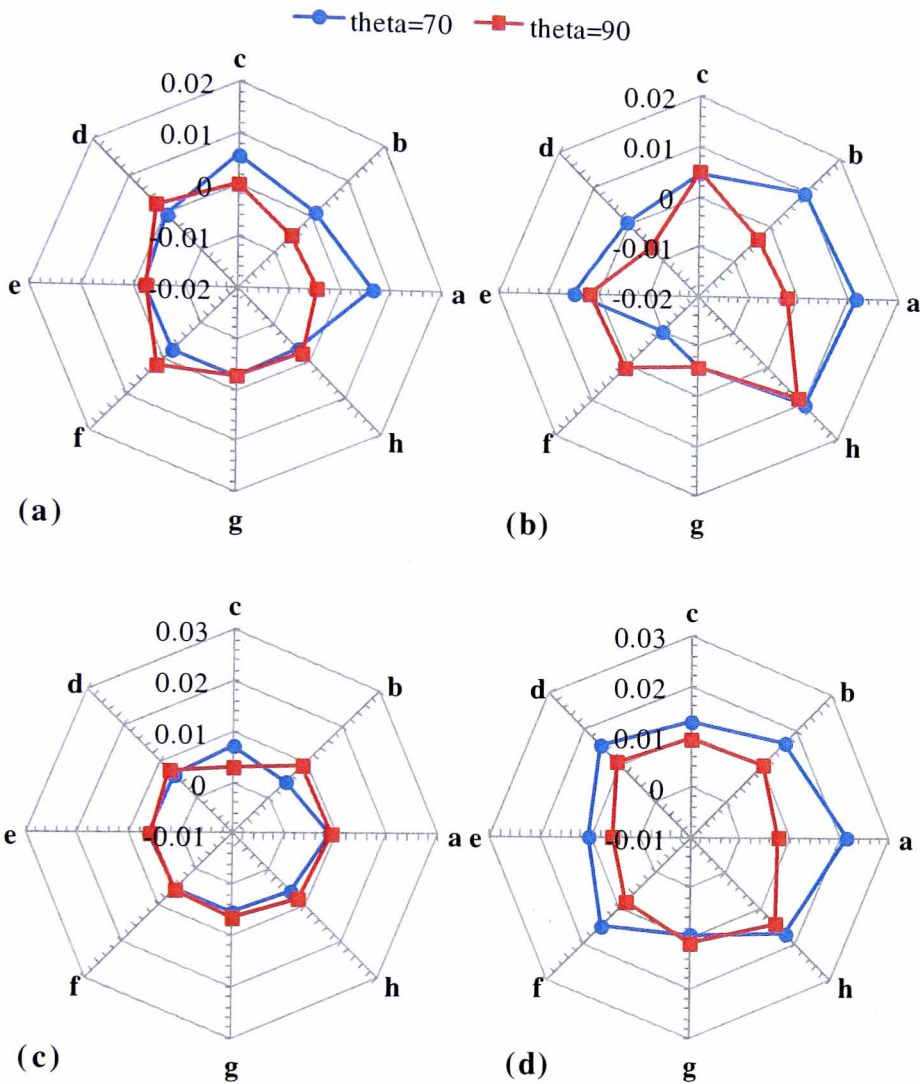


Figure 8-5: Mean of residuals, R_M at jet impingement angle $\theta = 70^\circ, 90^\circ$ when: (a) $V_f = 2000$ mm/min and (b) $V_f = 1000$ mm/min; root-mean-square error of residuals, R_{RMS} at $\theta = 70^\circ, 90^\circ$ when: (c) $V_f = 2000$ mm/min and (d) $V_f = 1000$ mm/min. [Note: the unit is in “mm”]

If the mean value of the residuals is larger than zero (+ve), it implies that the average penetration depth of the actual trench is larger than the predicted one. When

comparing the mean of residuals at different jet path directions (β) as shown in Figure 8-5(a), it can be noted that the variations among the different jet path directions (i.e. a, b, c, d, e, f, g, h) at normal jet impact (i.e. $\theta=90^\circ$) are small, but in the case of tilting AWJ impact (i.e. $\theta=70^\circ$) there is relatively more deviation in the depth of penetration. This also happens at a higher erosion penetration ($V_f=1000\text{mm/min}$) as well as shown in Figure 8-5 (b), but the variation among the jet path directions is relatively larger. When evaluating all the cases, the maximum range of the mean value of residuals is found to be less than $22\mu\text{m}$ ($< 13\%$) and the overall mean in any case is less than $4.5\mu\text{m}$ ($< 3\%$).

It can be noticed that higher differences are present between the jet path direction 'a' and 'e', which refer to forward and backward milling respectively, as mentioned in Figure 8-4 which only occurs when the jet is tilted. The residual mean (R_M) is closer to the positive side for the jet path direction 'a' (i.e. backward AWJ milling) and closer to the negative side for the forward milling i.e. path 'e'. This is due to the fact that when the jet is tilted relatively to the workpiece surface, the particles local impact angles are different between backward and forward milling. As illustrated in Figure 8-6, in the case of forward motion, due to the high local impact angles of the abrasive particles, there is more tendency for the particles to fracture and lose their momentums readily or embed into the workpiece surface and the overall abrasives erosion effect is less effective. That is why the crater morphology and higher percentage of grit embedment were found in relatively ductile material such as Ti-6Al-4V during the forward AWJ milling [24]. This can also explain the higher surface roughness of the AWJ milled surface found in the jet path direction 'a' (forward milling). In contrast, in the case of backward motion there is more likelihood that the grit particles impact the surface at lower impact angles. Hence, the 'cutting action' (as

shown in Figure 2-6 and Figure 2-10(b)) of the impacting particles on the cutting front wall is more significant and the overall abrasive erosion is more effective in the backward milling. In addition, because of the backward motion, the AWJ is 'channeled' along the generated trench which results in further grooving (scratching) of the trench. This results in further increasing the depth of the trench and lowering the surface roughness, e.g. for the same parameters, $R_a=4.19\mu\text{m}$ in backward milling; $R_a=5.38\mu\text{m}$ in forward milling.

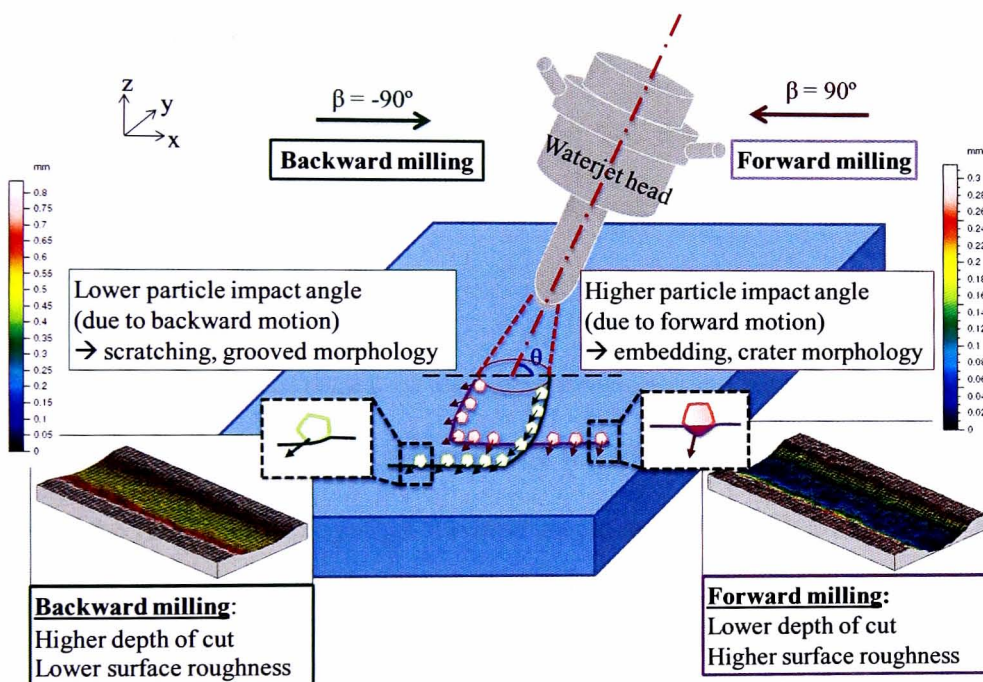


Figure 8-6: Illustration of different depth of cut and surface roughness in backward and forward milling resulting from different jet traverse directions.

Figure 8-5(c) and Figure 8-5(d) show R_{RMS} values based on the residuals at different combinations of jet traverse speeds ($V_f = 2000, 1000\text{mm/min}$), jet tilt angles ($\theta = 90^\circ, 70^\circ$) and arbitrarily-moving jet-paths ('a'- 'h'; $\Delta\beta=45^\circ$). The plots for the R_{RMS} error indicate that the model accuracy is slightly better at $\theta=90^\circ$ at both traverse speeds (V_f) as compared to $\theta=70^\circ$. The average R_{RMS} error at $\theta=90^\circ$ was found to be $7\mu\text{m} \pm 2\mu\text{m}$

(< 6%) and $11\mu\text{m} \pm 4\mu\text{m}$ (< 9%) for $\theta=70^\circ$ in the proposed model. It can be observed that, in general, for both the means of residuals (R_M) and R_{RMS} errors plots at $\theta = 70^\circ$, the errors tend to be larger on the right hand side of the plots at both traverse speeds, i.e. for the jet paths 'a', 'b' and 'h' while a random distribution of the errors could be seen at $\theta = 90^\circ$. This is due to the fact that all these paths (a, b, h) contain the jet channeling effect at $\theta = 70^\circ$ which results in comparatively deeper trenches, and conversely there is no backward milling effect at $\theta = 90^\circ$. Like the means of residuals (R_M), the largest R_{RMS} errors can be observed in jet paths 'a' where the effect of the jet channeling and grooving is maximum. This is also the reason that in order to determine the erosion rate function $E(r)$ in Eq. 8.18, the calibration trench was selected from those milled at normal jet incidence where no backward milling effect was present.

Despite the discussed issues of the jet channeling and secondary erosion by the reflected jet, the accuracy of the proposed model is quite good (max. error < 15%) within the range of employed jet traverse speeds which are often used in the practical AWJ milling applications [46].

8.5 Application of the mathematical model

It was mentioned in Chapter 1 that the current work has been undertaken as a part of the ConforM²Jet project in which one of the aims is to develop an automatic way to generate the G-Codes for the unmanned CNC machining of the desired parts. This task is accomplished by two partners, Tekniker Spain [174] and Zeeko Ltd, UK [175] by developing a CAD/CAM software where the key input for controlling the depth of the cut per AWJ pass is calculated from the current mathematical model. The software generates the CNC (G-codes) files that are run directly on the machine

without further manual editing. Figure 8-7 shows a logo of the ConforM²Jet project milled in a Ti-6Al-4V plate by using this software [40].



Figure 8-7: ConforM²-Jet logo milled in Ti-6Al-4V based on the traverse speeds computed by the developed mathematical model [40].

8.6 Comparison of the mathematical and FE modelling

Both the FE and mathematical modelling approaches have their own distinct advantages and some limitations as well. A brief comparison of the FE and mathematical models is discussed below.

Figure 8-8 shows an example of comparison of the footprint predicted by the FE and mathematical model with the experimental ones for a single set of energy parameters i.e. at $P=138\text{MPa}$, $\dot{m}_a=0.04\text{kg/min}$.

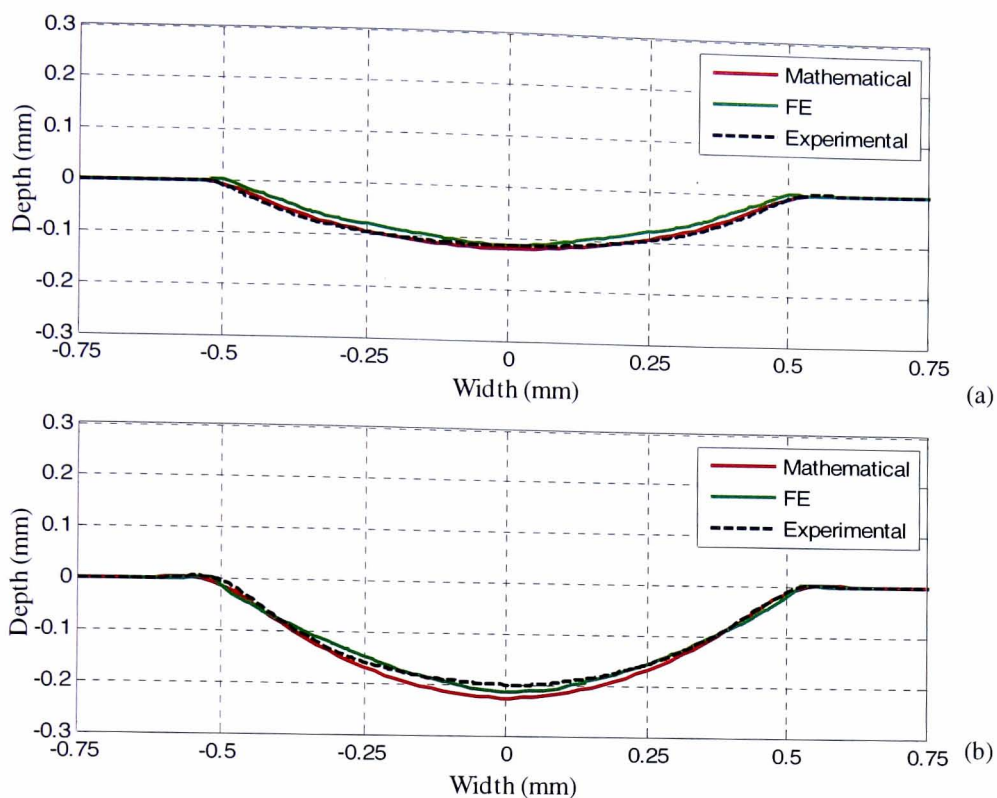


Figure 8-8: Comparison of footprint prediction from FE and mathematical models at $P=138\text{MPa}$, $\dot{m}_a=0.04\text{kg/min}$: (a) $V_f=2000\text{mm/min}$; (b) $V_f=1000\text{mm/min}$.

It can be seen from Figure 8-8 that both the FE and the mathematical models can equally be used for the accurate prediction of the AWJ milled footprints. However, the mathematical model is fast and can be used for real time simulations and can be embedded in CAD/CAM softwares for industrial applications, whereas the longer computational times involved in the FE model prevent it from being directly used in real time machining.

On the other hand, the mathematical model needs to be calibrated and it can predict the footprints as long as the jet energy parameters (water pressure, abrasive mass flow rate) remain constant. In contrast, the FE model, once validated, can predict the jet footprints for other combinations of the jet energy parameters as well. This capability

of the FE model can also be utilized to generate the shallow footprints for calibrating the mathematical model at various jet energy parameters, hence replacing the need for the experimentation. Figure 8-9 shows an example of a scenario where a shallow footprint generated by the FE model has been utilized to calibrate the analytical model and after calibration, footprints are simulated further for variable parameters (e.g. traverse speeds).

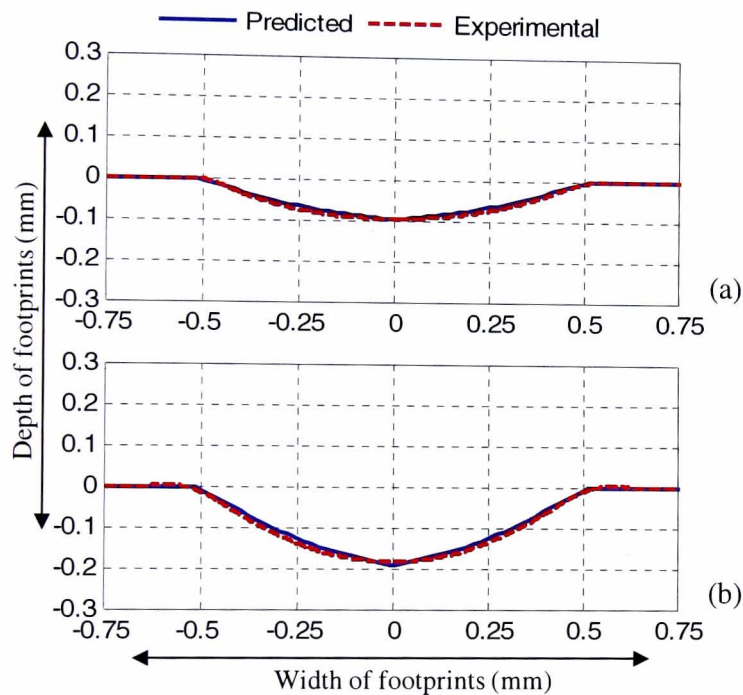


Figure 8-9: Footprints predicted by the mathematical model after being calibrated from the data generated by the FE model at $P=207\text{MPa}$, $\dot{m}_a=0.02\text{kg/min}$: (a) $V_f=2000\text{mm/min}$; (b) $V_f=1000\text{mm/min}$.

The FE model can be employed to obtain an insight into the AWJ process such as studying the jet plume structure, the behaviour of the overlapping footprints, the effect of the abrasive particles shapes and sizes, stresses generated in the target material, etc. Moreover, along with the 2D footprint, the 3D view of the milled trenches can also be extracted from the FE model, whereas the mathematical model cannot be used for

these purposes.

8.7 Conclusions

This chapter presents a modelling approach to predict the footprint of an unrestrained (i.e. no surface masking) high velocity abrasive waterjet impact upon a target surface. The model is capable of taking into consideration different jet impingement angles (θ) while the jet paths (β) within the target surface are of truly arbitrary directions. To account for new working conditions (e.g. jet energetic parameters – water pressure, abrasive mass flow – and workpiece material) the model needs a single shallow jet footprint generated at a high value of jet feed speed from where the erosion rate function is obtained. Once this is found, the footprint of the arbitrary-moving jet at any feed speed can be obtained with a high degree of accuracy. The modelling approach is powerful since it is computationally inexpensive.

When comparing the experimental results with the predictions over the entire 2D footprint profile, small values of root-mean-square errors of the residuals (R_{RMS}) between 6% and 9% have been found at $\theta=90^\circ$ and $\theta=70^\circ$ respectively. The errors were mostly contributed from the deviations in depth of penetration arising due to the jet channeling effect and secondary erosion from the reflected jet. The mathematical model yielded accurate footprints even when it was calibrated by a simulated footprint from the FE model.

The proposed model is general in its approach as it can be applicable to other energy beam (dwell time dependant) material removal processes such as pulsed laser ablation and focus ion beam. For all these processes, only the kinematics of the continuous/discontinuous beam movements have to be incorporated into the model

while the material response to the process can be evaluated via the calibration procedure to enable prediction of the geometry of the resulting processed trenches.

Although further challenges in the modelling of the jet footprint exist (e.g. modelling of overlapping between individual trenches and inclusion of dynamics of the machine acceleration/deceleration), the proposed model is regarded as an enabling step for the development of jet path strategies for the generation of complex geometry surfaces by controlled-depth abrasive waterjet milling where the jet plume follows multi-axis movements while its footprint needs to be controlled/predicted at any time.

Chapter 9 Final Conclusions and Future work

9.1 Conclusions

The overall aim behind the work presented in this thesis as described in Chapter 1 was to develop reliable models to predict the abrasive waterjet milled footprints and enhance the process understanding. The objectives of the study have been fully achieved as presented in this thesis. Two modelling approaches; finite element (FE) modelling and mathematical modelling have been presented in this work. The developed models can accurately simulate the AWJ milling process and have been validated with a substantial amount of experimental data.

A comprehensive literature review of AWJ machining was first conducted in Chapter 2 in order to fully understand this technology, and it was recognized that abrasive water jet machining is one of the most promising environmental friendly non-conventional machining processes that has the capability to machine difficult-to-cut materials (e.g. Ti-6Al-4V). However, it was realized from the state-of-the-art in the modelling of the AWJ machining that although some models exist for simulating eroded footprints, they were limited either in terms of their relevance to AWJ machining conditions or the modelling approaches selected. The majority of the reported models were not capable of predicting footprints as a result of AWJ milling, which is one of the essential prerequisites to be able to employ AWJ machining for controlled depth cutting applications. It was further established from the literature survey (Chapter 2) that valuable studies have been reported regarding the analytical modelling of eroded footprints during attrition based processes (e.g. powder blasting). However, from the standpoint of FE modelling, the majority of the reported models were limited to a single or a few rigid multiple particles impact. This is the reason that

more focus was given in the current study to develop FE based models for AWJ milling (Chapter 4 to Chapter 7) where a significant room for improvement was present and an existing analytical model was used as a base for further mathematical modelling work (Chapter 8).

The development and the validation of the FE models progressed in logical stages starting from the basic event of the footprint generation process leading to higher levels as: (i) single particle impact modelling during AWJ machining (Chapter 4); (ii) multiple particles impact modelling during AWJ machining (Chapter 5); (iii) single AWJ pass modelling (Chapter 6); and (iv) modelling of overlapping AWJ passes (Chapter 7). At each stage, the models were validated by a significant amount of experimental results conducted within this research.

The main original contributions of this thesis are summarized as follows.

9.1.1 FE modelling

- In contrast to previous studies reported for the FE modelling of AWJ machining, the present study takes into account more real life conditions of the AWJ such as: (i) utilizing the high velocity of the impacting particle (up to 581m/s) obtained from the experimental data; (ii) modelling the abrasive particles as elastic with a tensile failure criteria rather than considering them as rigid during the impact. This was based on a large majority of published literature which state that the brittle particles fracture upon impact at relatively much lower impact velocities than those encountered in AWJ machining; (iii) keeping in view the critical importance of inertial effects during the impact problem, the FE model takes into account the size distribution of the abrasive particles after the fragmentation from the

focussing nozzle rather than the usual approach of assuming one single size for all the particles; and (iv) considering the significant effect of the shape of the particle during the impact, the garnet particles were modelled in three different shapes with sharp edges (triangular, rhombic and trapezoidal), contrary to the commonly reported approach of considering them spherical shaped.

- It was demonstrated that in order to validate the single particle AWJ FE model, garnet abrasive particles should not be employed due to the issues of their fragmentation and irregular shapes; rather particles with regular shapes and sizes (such as steel shots) should be used. A procedure was established to successfully obtain clear and well defined single particle indentations from steel shots during the AWJ impingement over the Ti-6Al-4V target surface. These indentations could easily be distinguished from the craters produced by the water droplets, unlike the case when garnet particles are employed as abrasives. The depth and width of the profiles of the indentations generated by the FE model were in close agreement (average error $\leq 13\%$) with the scanned profiles of the experimentally generated indentations by steel shots (Chapter 4).
- A method was devised that incorporated the abrasive particles of various sizes in the FE model in the same proportions as reported after fragmentation through the focusing nozzle. Thus, the FE model attempted to consider the total mass of each size of the impacting particles in the proportions as close to the reality as possible. The predicted velocity exponent, n (2.25) for Ti-6Al-4V was in close agreement with the experimentally determined velocity exponent 2.55 (Chapter 5).
- A procedure was established to include the effects of the mass flow rate of the abrasive particles and the exposure time, i.e. the traverse speed in the FE model in such a manner that the model can be run for the same amount of the mass of

abrasive particles impacting per unit length of the target as in the experiments, without becoming computationally expensive. Furthermore, the abrasive particles were arranged in layers in the jet plume to form a Gaussian spatial distribution which was an essential parameter for controlling the shape of the footprints. The model also provided further understanding of the AWJ process by uncovering the fact that the spatial distribution of the abrasive particles in the jet plume is not affected by the changing the water pump pressure. The simulated single jet footprints from the FE model were consistent (maximum errors $\leq 10\%$) with the experimental results (Chapter 6).

- The FE model was extended to allow including the multiple passes of the jet in the model to simulate the overlapping trenches without becoming extremely computationally expensive or not being able to run due to memory problems. The simulation of the interaction process between the jet footprints revealed that the footprints overlapping was not a linear summation of the single footprints; rather the slope of the eroded surfaces and the residual stresses stored in the target due to earlier jet passes affect the overlapping phenomenon. The overlapping footprints predicted by the FE model at various operating parameters were in good agreement with the experimental data both qualitatively, i.e. with respect to shapes of footprints, and quantitatively, i.e. depths of the footprints (maximum errors $< 15\%$) (Chapter 7).

The consistency between the simulated and the experimental results throughout the FE modelling confirms the validity of the modelling procedure and the appropriateness of the assumptions considered during the modelling process.

9.1.2 Mathematical modelling

A generic mathematical model was developed to predict AWJ milled footprints while taking into consideration the jet impingement angles (θ) and the arbitrary jet paths (β) within the target surface. The model, being computationally inexpensive, is powerful and can be used for real time predictions of traverse speeds for controlling the depth of the cuts during CNC machining. The model only needs one shallow footprint to calibrate itself for a set of given fixed parameters (e.g. water pressure, abrasive mass flow and workpiece material) to determine the erosion rate function. Once this is found, the footprint of an arbitrary-moving jet at any traverse speed can be obtained with a high degree of accuracy. The model can also be calibrated by using the shallow footprints generated by the FE model. The predicted footprints from the model were in good agreement with the experimentally generated footprints with $R_{RMS} < 9\%$. The causes of the errors were mostly related to the effects of jet channeling and reflections within the eroded trench (Chapter 8).

9.2 Future work

From the research carried out and reported in this thesis, various possible future avenues of research, derived from this work, are suggested as follows.

- Garnet is one of the most commonly employed abrasives during the AWJ machining. However, very limited work is reported in the literature regarding experimental determination of the properties of garnet at conditions occurring during abrasive waterjetting. Future work can focus on quantifying how much abrasion is caused on garnet particles during entrainment process and carefully designing experiments to calculate the fracture velocity of the garnet particles for

the sizes generated after fragmentation through the nozzle. This knowledge will be of high importance for calculating the failure stresses in the garnet particles and will introduce more accuracy in the FE models.

- In the presented FE modelling work, the tasks of generating the particles mix, i.e. selecting the sizes of the abrasive particles in required proportions (Chapter 5) and the assignment of different shapes to these sizes, were manually accomplished within ABAQUS. In order to make this process simpler and be readily applicable to different abrasive mesh (sieve) sizes (e.g. 80, 100, 230 etc) and shapes of abrasive particles used during the experiments, an algorithm should be developed that can take the input of required sizes of the particles to be generated and then randomly transform those sizes into different selected shapes with the necessary proportion of each size. This means that the abrasive particles with different shapes following the sizes distribution after fragmentation can be achieved automatically.

Similarly, the garnet particles were manually assembled in the FE model to form a Gaussian spatial distribution within the jet plume diameter. A program may be developed that can automatically arrange the abrasive particles in any given jet diameter according to a required spatial arrangement of the particles. By incorporating these two previous mentioned features in the FE model, the model can readily be used for both macro and micro AWJ machining setups which differ in terms of applied particles and jet sizes.

- At the moment, when the surfaces are milled by using the AWJ milling approach, relatively deeper depths are produced near the walls or edges of the surface. This happens due to the confinement of the jet plume due to the presence of the edges/walls next to the area being milled. A comprehensive investigation is

required to study this effect and transform it into mathematical or empirical relations, and combine them into the analytical model developed within the current study. This should be done in such a way that the new formulation should be able to extract the required information to offset the deeper depth of cuts around the edges of the milled surface from a single shallow footprint, in order that the simplicity of the mathematical model will still be maintained, i.e. being able to be calibrated from a single footprint.

References

- [1] “Air Force ManTech Sustainable Aerospace Manufacturing Initiative,” ManTech International Corporation, 2011.
- [2] M. Finley, “Composites make for greener aircraft engines,” *Reinforced Plastics*, vol. 52, no. 1, pp. 24–26, 2008.
- [3] E. O. Ezugwu and J. Bonney, “Effect of high-pressure coolant supply when machining nickel-base, Inconel 718, alloy with coated carbide tools,” *Journal of Materials Processing Technology*, vol. 153–154, pp. 1045–1050, Nov. 2004.
- [4] E. O. Ezugwu, “Key improvements in the machining of difficult-to-cut aerospace superalloys,” *International Journal of Machine Tools and Manufacture*, vol. 45, no. 12–13, pp. 1353–1367, Oct. 2005.
- [5] A. Molinari, C. Musquar, and G. Sutter, “Adiabatic shear banding in high speed machining of Ti – 6Al – 4V : experiments and modeling,” *International Journal of Plasticity*, vol. 18, pp. 443–459, 2002.
- [6] D. Dudzinski, a Devillez, a Moufki, D. Larrouquère, V. Zerrouki, and J. Vigneau, “A review of developments towards dry and high speed machining of Inconel 718 alloy,” *International Journal of Machine Tools and Manufacture*, vol. 44, no. 4, pp. 439–456, Mar. 2004.
- [7] G. A. Ibrahim and C. H. C. Haron, “The effect of dry machining on surface integrity of titanium alloy Ti-6Al-4V ELI,” *Journal of Applied Sciences*, vol. 9, no. 1, pp. 121–127, 2009.
- [8] E. O. Ezugwu, J. Bonney, R. B. Da Silva, and O. Çakir, “Surface integrity of finished turned Ti-6Al-4V alloy with PCD tools using conventional and high pressure coolant supplies,” *International Journal of Machine Tools and Manufacture*, vol. 47, no. 6, pp. 884–891, May 2007.
- [9] Y. Su, N. He, L. Li, and X. L. Li, “An experimental investigation of effects of cooling/lubrication conditions on tool wear in high-speed end milling of Ti-6Al-4V,” *Wear*, vol. 261, no. 7–8, pp. 760–766, Oct. 2006.
- [10] A. Hasçalık and U. Çaydaş, “Electrical discharge machining of titanium alloy (Ti-6Al-4V),” *Applied Surface Science*, vol. 253, no. 22, pp. 9007–9016, Sep. 2007.
- [11] D. P. Adlera, W. W.-S. Hii, D. J. Michaleka, and J. W. Sutherlanda, “Examining the role of cutting fluids in machining and efforts to address associated environmental/health concerns,” *Machining Science and Technology: An International Journal*, vol. 10, no. 1, pp. 23–58, 2006.
- [12] A. W. Momber and R. Kovacevic, *Principles of abrasive water jet machining*. New York: Springer, New York, 1998.

- [13] a. . Osman, T. Mabrouki, B. Théry, and D. Buisine, "Experimental analysis of high-speed air–water jet flow in an abrasive water jet mixing tube," *Flow Measurement and Instrumentation*, vol. 15, no. 1, pp. 37–48, Mar. 2004.
- [14] "Water cutting machine." [Online]. Available: http://waterjet-cutting.blogspot.co.uk/2011/10/waterjet-machining.html?utm_source=BP_recent. [Accessed: 20-Jun-2012].
- [15] "Conform-Jet Project." [Online]. Available: <http://simplesensors.co.uk/2012/03/conform-jet-project/>. [Accessed: 20-Jun-2012].
- [16] M. K. Babu and O. V. K. Chetty, "A study on recycling of abrasives in abrasive water jet machining," *Wear*, vol. 254, no. 7–8, pp. 763–773, Apr. 2003.
- [17] M. C. Kong, D. Axinte, and W. Voice, "Challenges in using waterjet machining of NiTi shape memory alloys: An analysis of controlled-depth milling," *Journal of Materials Processing Technology*, vol. 211, no. 6, pp. 959–971, Jun. 2011.
- [18] D. S. S. Srinivasu, D. a. Axinte, P. H. H. Shipway, and J. Folkes, "Influence of kinematic operating parameters on kerf geometry in abrasive waterjet machining of silicon carbide ceramics," *International Journal of Machine Tools and Manufacture*, vol. 49, no. 14, pp. 1077–1088, Nov. 2009.
- [19] S. Zhang, Y. Wu, and Y. Wang, "A Review on Abrasive Waterjet and Wire Electrical Discharge Machining," *Mechanical Engineering*, vol. 65106122, pp. 178–185, 2011.
- [20] J. J. R. Jegaraj and N. R. Babu, "A strategy for efficient and quality cutting of materials with abrasive waterjets considering the variation in orifice and focusing nozzle diameter," *International Journal of Machine Tools and Manufacture*, vol. 45, no. 12–13, pp. 1443–1450, Oct. 2005.
- [21] M. G. Mostofa, K. Y. Kil, and A. J. Hwan, "Computational fluid analysis of abrasive waterjet cutting head," *Journal of Mechanical Science and Technology*, vol. 24, no. 1, pp. 249–252, Mar. 2010.
- [22] R. Kovacevic, R. Mohan, and H. Beardsley, "Monitoring of Thermal Energy Distribution in Abrasive Waterjet Cutting Using Infrared Thermography," *ASME, Journal of Manufacturing Science and Engineering*, vol. 118, pp. 555–563, 1996.
- [23] M. M. Ohand, A. I. Ansari, and M. Hashish, "Thermal Energy Distribution in the Workpiece During Cutting with an Abrasive Waterjet," *ASME, Journal of Engineering for Industry*, vol. 114, pp. 67–73, 1992.
- [24] G. Fowler, P. Shipway, and I. Pashby, "A technical note on grit embedment following abrasive water-jet milling of a titanium alloy," *Journal of Materials*

- Processing Technology*, vol. 159, no. 3, pp. 356–368, Apr. 2005.
- [25] P. Shipway, G. Fowler, and I. Pashby, “Characteristics of the surface of a titanium alloy following milling with abrasive waterjets,” *Wear*, vol. 258, no. 1–4, pp. 123–132, Jan. 2005.
- [26] M. C. Kong, “Response of special purpose aerospace materials to abrasive waterjet machining,” University of Nottingham, UK, 2010.
- [27] M. C. Kong, D. Srinivasu, D. Axinte, W. Voice, J. McGourlay, and B. Hon, “On geometrical accuracy and integrity of surfaces in multi-mode abrasive waterjet machining of NiTi shape memory alloys,” *CIRP Annals Manufacturing Technology (in Press)*, 2013.
- [28] F. . Chen and E. Siores, “The effect of cutting jet variation on striation formation in abrasive water jet cutting,” *International Journal of Machine Tools and Manufacture*, vol. 41, no. 10, pp. 1479–1486, Aug. 2001.
- [29] M. C. C. Kong, D. Axinte, and W. Voice, “Aspects of material removal mechanism in plain waterjet milling on gamma titanium aluminide,” *Journal of Materials Processing Technology*, vol. 210, no. 3, pp. 573–584, Feb. 2010.
- [30] P. Gudimetla, J. Wang, and W. Wong, “Kerf formation analysis in the abrasive waterjet cutting of industrial ceramics,” *Journal of Materials Processing Technology*, vol. 128, pp. 123–129, 2002.
- [31] D. A. Axinte, D. S. Srinivasu, M. C. Kong, and P. W. Butler-Smith, “Abrasive waterjet cutting of polycrystalline diamond: A preliminary investigation,” *International Journal of Machine Tools and Manufacture*, vol. 49, no. 10, pp. 797–803, Aug. 2009.
- [32] D. Arola and M. Ramulu, “A study of kerf characteristics in abrasive waterjet machining of graphite/epoxy composite,” *Journal of engineering materials and technology*, vol. 118, no. 2, pp. 256–265, 1996.
- [33] J. Wang, “Abrasive Waterjet Machining of Polymer Matrix Composites – Cutting Performance , Erosive Process and Predictive Models,” *International Journal*, pp. 757–768, 1999.
- [34] D. a. A. Axinte, J. P. P. Stepanian, M. C. C. Kong, and J. Mcgourlay, “Abrasive waterjet turning—An efficient method to profile and dress grinding wheels,” *International Journal of Machine Tools and Manufacture*, vol. 49, no. 3–4, pp. 351–356, Mar. 2009.
- [35] BHR, “Abrasive water-jet cutting and cleaning,” 2011. [Online]. Available: http://www.bhrgroup.com/abrasive_water-jet_cutting_and_cleaning.aspx. [Accessed: 11-Jun-2012].
- [36] ThomasNet, “Robot is equipped for water jet cutting applications.” [Online]. Available: <http://news.thomasnet.com/fullstory/Robot-is-equipped-for-water-jet-cutting-applications-14984>. [Accessed: 11-Jun-2012].

- [37] “Composite machining solutions for aerospace.” Flow Inc, Flow Inc, 2009.
- [38] “Waterjet Cutting Machines: A Global Strategic Business,” Global Industry Analysts Inc, 2010.
- [39] M. C. Kong, “Trends in the use of waterjet machining,” Exp003-270707RPv02, University of Nottingham, 2007.
- [40] “Conform2Jet.” [Online]. Available: <http://conformjet.eu/>. [Accessed: 11-Jun-2012].
- [41] K. L. Pang, T. Nguyen, J. M. Fan, and J. Wang, “Modelling of the micro-channelling process on glasses using an abrasive slurry jet,” *International Journal of Machine Tools and Manufacture*, vol. 53, no. 1, pp. 118–126, Feb. 2012.
- [42] M. K. Kulekci, “Processes and apparatus developments in industrial waterjet applications,” *International Journal of Machine Tools and Manufacture*, vol. 42, no. 12, pp. 1297–1306, 2002.
- [43] G. A. Mort, “Results of abrasive water jet market survey,” in *Proc. of 8th American Water Jet Conference*, 1995.
- [44] G. M. Evans, G. J. Jameson, and C. D. Rielly, “Free jet expansion and gas entrainment characteristics of a plunging liquid jet,” *Experimental Thermal and Fluid Science*, vol. 12, no. 2, pp. 142–149, 1996.
- [45] M. Nanduri, D. G. Taggart, and T. J. Kim, “The effects of system and geometric parameters on abrasive water jet nozzle wear,” *International Journal of Machine Tools and Manufacture*, vol. 42, no. 5, pp. 615–623, Apr. 2002.
- [46] M. Hashish, “Controlled-Depth Milling of Isogrid Structures With AWJs,” *Journal of Manufacturing Science and Engineering*, vol. 120, no. 1, pp. 21–27, 1998.
- [47] A. M. Hoogstrate and C. A. Luttervelt, “Opportunities in Abrasive Water-Jet Machining,” *Annals of the CIRP*, vol. 46, no. 2, pp. 697–714, 1997.
- [48] S. Paul, a. . Hoogstrate, C. . van Luttervelt, and H. J. . Kals, “An experimental investigation of rectangular pocket milling with abrasive water jet,” *Journal of Materials Processing Technology*, vol. 73, no. 1–3, pp. 179–188, Jan. 1998.
- [49] M. Hashish, “Milling with abrasivewater jets: A preliminary investigation,” in *Proc. 4th US Water Jet Conference*, 1984, pp. 1–10.
- [50] K. M. C. Ojmertz, “A study on abrasive water jet milling,” PhD Thesis, Chalmers University of Technology, Gotenborg, Sweden, 1997.
- [51] M. Hashish, “AWJ Milling of Gamma Titanium Aluminide,” *Journal of Manufacturing Science and Engineering*, vol. 132, no. 4, 2010.
- [52] C. Öjmerts and N. Amini, “Discrete approach to the abrasive waterjet milling process,” in *12th International Conference on Jet Cutting Technology*, 1994,

- pp. 425–434.
- [53] T. Mabrouki, “Numerical simulation and experimental study of the interaction between a pure high-velocity waterjet and targets: contribution to investigate the decoating process,” *Wear*, vol. 239, no. 2, pp. 260–273, Apr. 2000.
- [54] T. Mabrouki and K. Raissi, “Stripping process modelling: interaction between a moving waterjet and coated target,” *International Journal of Machine Tools and Manufacture*, vol. 42, no. 11, pp. 1247–1258, Sep. 2002.
- [55] M. C. Kong, D. Axinte, and W. Voice, “An innovative method to perform maskless plain waterjet milling for pocket generation: a case study in Ti-based superalloys,” *International Journal of Machine Tools and Manufacture*, vol. 51, no. 7–8, pp. 642–648, Jul. 2011.
- [56] M. Hashish, “Comparative evaluation of abrasive liquid jet machining systems,” *Journal of Engineering for Industry*, vol. 115, no. 1, pp. 44–50, 1993.
- [57] M. Hashish, “Abrasive-fluid jet machinery systems: entrainment versus direct pumping,” in *Proceedings of 10th International Symposium on Jet cutting technology*, 1990, pp. 99–113.
- [58] M. J. Bunce and T. R. Fewell, “Portable cutting applications,” in *18th International Conference on Water Jetting*, 2006.
- [59] Y. Iwai, T. Honda, H. Yamada, T. Matsubara, M. Larsson, and S. Hogmark, “Evaluation of wear resistance of thin hard coatings by a new solid particle impact test,” *Wear*, vol. 251, no. 1–12, pp. 861–867, Oct. 2001.
- [60] I. Finnie, “Erosion of surfaces by solid particles,” *Wear*, vol. 3, no. 87–103, pp. 87–103, 1960.
- [61] I. Finnie and D. H. McFadden, “On the velocity dependence of the erosion of ductile metals by solid particles at low angles of incidence,” *Wear*, vol. 48, pp. 181–190, 1978.
- [62] J. Bitter, “A study of erosion phenomena, part 1,” *Wear*, vol. 6, pp. 161–190, 1963.
- [63] J. G. A. Bitter, “A study of erosion phenomena, part 2,” *Wear*, vol. 6, pp. 161–190, 1963.
- [64] I. M. Hutchings, “Mechanism of the erosion of metals by solid particles,” in *ASTM STP 664, Erosion: Prevention and Useful Applications (3rd edn.)*, ASTM, 1979, pp. 59–75.
- [65] I. M. Hutchings and R. E. Winter, “Particle erosion of ductile metals: a mechanism of material removal,” *Wear*, vol. 27, pp. 121–128, 1974.
- [66] K. E. Webb and K. P. Rajurkar, “Surface characterization of inconel cut by abrasive water jet,” in *CSME Mechanical Engng. Forum*, 1990.

- [67] D. Arola and M. Ramulu, "Abrasive waterjet machining of titanium alloy," in *8th Amer. Water Jet Conf, Water Jet Techn. Ass.*, 1995, pp. 389–408.
- [68] J. Zeng and T. J. Kim, "Development of an abrasive waterjet kerf cutting model for brittle materials," in *Proceedings of 11th International Conference Jet Cutting Technology*, 1992, pp. 483–501.
- [69] G. T. Camacho and M. Ortizt, "COMPUTATIONAL MODELLING OF IMPACT DAMAGE IN BRITTLE MATERIALS," vol. 33, no. 2, pp. 2899–2938, 1996.
- [70] A. G. Evans, W. E. Gulden, and M. Rosenblatt, "Impact damage in ceramics," *Fracture mechanics of ceramics*, vol. 3, pp. 303–330, 1978.
- [71] G. L. Sheldon and I. Finnie, "The Mechanism of Material Removal in the Erosive Cutting of Brittle Materials," *Journal of Engineering for Industry*, vol. 88, no. 4, p. 393, 1966.
- [72] J. Zeng and T. J. Kim, "An erosion model of polycrystalline ceramics in abrasive waterjet cutting," *Wear*, vol. 193, no. 2, pp. 207–217, May 1996.
- [73] C. S. Yust and R. S. Crouse, "Melting at particle impact sites during erosion of ceramics," *Wear*, vol. 51, pp. 193–196, 1978.
- [74] A. G. Evans and D. B. Marshall, "Wear mechanisms in ceramics," *Fundamentals of friction and wear of material*, Ed. by Rigney, D. A. ASME., p. 439, 1981.
- [75] M. Hashish, "A Modeling Study of Metal Cutting with Abrasive-Waterjets," *ASME Transactions - Journal of Engineering Materials and Technology*, vol. 106, pp. 88–100, 1984.
- [76] M. Hashish, "Visualization of the abrasive-waterjet cutting process," *Experimental Mechanics*, vol. 28, no. 2, pp. 159–169, Jun. 1988.
- [77] A. Akkurt, M. K. Kulekci, U. Seker, and F. Ercan, "Effect of feed rate on surface roughness in abrasive waterjet cutting applications," *Journal of Materials Processing Technology*, vol. 147, no. 3, pp. 389–396, Apr. 2004.
- [78] M. Hashish, "On the modeling of abrasive-waterjet cutting," in *The International Symposium on Jet Cutting Technology*, 1984, pp. 249–265.
- [79] D. Arola and M. Ramulu, "Material removal in abrasive waterjet machining of metals Surface integrity and texture," *Wear*, vol. 210, pp. 50–58, 1997.
- [80] A. Hascalik, U. Caydas, and H. Gurun, "Effect of traverse speed on abrasive waterjet machining of Ti–6Al–4V alloy," *Materials & Design*, vol. 28, no. 6, pp. 1953–1957, 2007.
- [81] M. C. Kong and D. Axinte, "Response of titanium aluminide alloy to abrasive waterjet cutting: geometrical accuracy and surface integrity issues versus process parameters," *Proceedings of the Institution of Mechanical Engineers*,

- Part B: Journal of Engineering Manufacture*, vol. 223, no. 1, pp. 019–042, Jan. 2009.
- [82] M. Hashish, “Characteristics of Surfaces Machined with Abrasive-Waterjets,” *Journal of Engineering Materials and Technology*, vol. 113, pp. 354–362, 1991.
- [83] S. S. Wu and T. J. Kim, “An application study of plain waterjet process for coating removal,” in *8th US Water Jet Conference*, 1995, pp. 779–792.
- [84] M. Mazurkiewics, Z. Sebastian, and G. Galecki, “Analysis of the mechanism of interaction between high-pressure water jet and the material being cut,” in *4th International Symposium on Jet Cutting Technology*, 1978, pp. 31–36.
- [85] A. W. Momber and R. Kovacevic, “Fracture of brittle multiphase materials by high energy water jets,” *Journal of materials science*, vol. 31, no. 4, pp. 1081–1085, 1996.
- [86] A. W. Momber and R. Kovacevic, “Statistical character of the failure of multiphase materials due to high pressure water jet impingement,” *International Journal of Fracture*, vol. 71, no. 1, pp. 1–14, 1995.
- [87] Y. X. Feng, C. Z. Huang, J. Wang, R. G. Hou, and X. Y. Lu, “An Experimental Study on Milling Al₂O₃ Ceramics with Abrasive Waterjet,” *Key Engineering Materials*, vol. 339, pp. 500–504, 2007.
- [88] A. A. El-Domiatty, M. A. Shabara, A. A. Abdel-Rahman, and A. K. Al-Sabeeh, “On the modelling of abrasive waterjet cutting,” *International Journal of Advanced Manufacturing Technology*, vol. 12, no. 4, pp. 255–265, 1996.
- [89] M. Hashish, “Pressure effects in abrasive-waterjet(AWJ) machining,” *Journal of engineering materials and technology*, vol. 111, pp. 221–228, 1989.
- [90] a. W. Momber and R. Kovacevic, “Test parameter analysis in abrasive water jet cutting of rocklike materials,” *International Journal of Rock Mechanics and Mining Sciences*, vol. 34, no. 1, pp. 17–25, Jan. 1997.
- [91] R. Kovacevic, “Monitoring the depth of abrasive water jet penetration,” *International Journal of Machine tools & Manufacture*, vol. 32, no. 5, pp. 725–736, 1992.
- [92] L. Chen, E. Siores, and W. C. K. Wong, “Kerf characteristics in abrasive waterjet cutting of ceramic materials,” *International Journal of Machine Tools and Manufacture*, vol. 36, no. 11, pp. 1201–1206, 1996.
- [93] G. Fowler, P. Shipway, and I. Pashby, “Abrasive water-jet controlled depth milling of Ti6Al4V alloy - an investigation of the role of jet-workpiece traverse speed and abrasive grit size on the characteristics of the milled material,” *Journal of Materials Processing Technology*, vol. 161, no. 3, pp. 407–414, Apr. 2005.
- [94] N. . S. Guo, H. Louis, G. Meier, and J. Ohlsen, “Recycling Capacity of

- Abrasives in Abrasive Water Jet Cutting,” in *Jet Cutting Technology*, 1992, pp. 503–523.
- [95] G. Fowler, I. R. R. Pashby, and P. H. H. Shipway, “The effect of particle hardness and shape when abrasive water jet milling titanium alloy Ti6Al4V,” *Wear*, vol. 266, no. 7–8, pp. 613–620, Mar. 2009.
- [96] I. M. Hutchings, “Ductile-brittle transitions and wear maps for the erosion and abrasion of brittle materials,” *Materials Science*, vol. 25, no. 1A, pp. 212–221, 1992.
- [97] Z. Feng and a. Ball, “The erosion of four materials using seven erodents — towards an understanding,” *Wear*, vol. 233–235, pp. 674–684, Dec. 1999.
- [98] K. A. Schwetz, L. S. Sigl, J. Greim, and H. Knoch, “Wear of boron carbide ceramics by abrasive waterjets,” *Wear*, vol. 181–183, pp. 148–155, 1995.
- [99] U. Himmelreich and W. Riess, “Laser-velocimetry investigations of the flow in abrasive water jets with varying cutting head geometry,” in *6th American Water Jet Conference*, 1991, pp. 305–313.
- [100] R. Kovacevic, “Rehabilitation of concrete pavements assisted with abrasive waterjets,” in *11th International Conference on Jet Cutting Technology*, 1992, pp. 425–442.
- [101] M. Hashish, “Optimization factors in abrasive-waterjet machining,” *ASME Journal of Engineering for Industry*, vol. 113, pp. 29–37, 1991.
- [102] M. Nanduri, D. G. Taggart, and T. J. Kim, “Cutting efficiency of abrasive waterjet nozzles,” in *10th American Waterjet Conference*, 1999, pp. 217–232.
- [103] M. Hashish, “Aspects of abrasive-waterjet (AWJ) performance optimization,” in *Eighth International Symposium on Jet Cutting Technology*, 1986, pp. 297–308.
- [104] M. Ramulu and D. Arola, “Influence of abrasive waterjet cutting conditions on the surface quality of graphite/epoxy laminates,” *International Journal of Machine Tools and Manufacture*, vol. 34, no. 3, pp. 295–313, 1994.
- [105] K. M. C. Ojmertz, “Abrasive water jet milling: an experimental investigation,” in *Proceedings of the Seventh US Water Jet Conference, Water Jet Technical Association, St. Louis*, 1993, pp. 777–791.
- [106] J. Wang, *Abrasive Waterjet Machining of Engineering Materials*. Trans Tech Publications Ltd, 2003.
- [107] D. a. A. Axinte, D. S. S. Srinivasu, J. Billingham, and M. Cooper, “Geometrical modelling of abrasive waterjet footprints: A study for 90° jet impact angle,” *CIRP Annals - Manufacturing Technology*, vol. 59, no. 1, pp. 341–346, 2010.
- [108] K. Shimizu, T. Noguchi, H. Seitoh, M. Okada, and Y. Matsubara, “FEM

- analysis of erosive wear,” *Wear*, vol. 250, pp. 779–784, 2001.
- [109] K. Shimizu, T. Noguchi, H. Seitoh, and E. Muranaka, “FEM analysis of the dependency on impact angle during erosive wear,” *Wear*, vol. 233–235, pp. 157–159, 1999.
- [110] M. Takaffoli and M. Papini, “Finite element analysis of single impacts of angular particles on ductile targets,” *Wear*, vol. 267, no. 1–4, pp. 144–151, Jun. 2009.
- [111] G. R. Johnson and W. H. Cook, “A constitutive model and data for metals subjected to large strains, high strain rates and high temperatures,” in *Proceedings of the 7th International Symposium on Ballistics*, 1983, pp. 541–547.
- [112] M. S. Eltobgy, E. Ng, and M. A. Elbestawi, “Finite element modeling of erosive wear, Int,” *J. Mach. Tool. Manuf.*, vol. 45, pp. 1337–1346, 2005.
- [113] G. R. Johnson and W. H. Cook, “fracture characteristics of three metals subjected to various strains, strain rates, temperatures and pressures,” *Engineering Fracture Mechanics*, vol. 21, no. 1, pp. 31–48, 1985.
- [114] D. Griffin, A. Daadbin, and S. Datta, “The development of a three-dimensional finite element model for solid particle erosion on an alumina scale/MA956 substrate,” *Wear*, vol. 256, no. 9–10, pp. 900–906, May 2004.
- [115] Y. Wang and Z. Yang, “Finite element model of erosive wear on ductile and brittle materials,” *Wear*, vol. 265, no. 5–6, pp. 871–878, Aug. 2008.
- [116] A. I. Hassan and J. Kosmol, “Dynamic elastic–plastic analysis of 3D deformation in abrasive waterjet machining,” *Journal of Materials Processing Technology*, vol. 113, no. 1–3, pp. 337–341, Jun. 2001.
- [117] P. Gudimetla and P. K. D. V. Yarlagadda, “Finite element analysis of the interaction between an AWJ particle and a polycrystalline alumina ceramic,” *Manufacturing Engineering*, vol. 23, no. 1, 2007.
- [118] “SIMULIA Inc. ABAQUS 6.9-1 Documentation.” 2009.
- [119] M. Junkar, B. Jurisevic, M. Fajdiga, and M. Grah, “Finite element analysis of single-particle impact in abrasive water jet machining,” *International Journal of Impact Engineering*, vol. 32, no. 7, pp. 1095–1112, Jul. 2006.
- [120] X. Claude, A. Merlen, B. Theyry, and O. Gatti, “Abrasive waterjet velocity measurements,” in *Proceedings from the 14th International Conference on Jet Cutting Technology*, 1998, pp. 235–251.
- [121] P. Roth, H. Looser, K. C. Heiniger, and S. Buhler, “Determination of abrasive particle velocity using laser-induced fluorescence and particle tracking methods in abrasive water jets,” in *WJTA American Waterjet Conference*, 2005.
- [122] R. Balz and K. C. Heiniger, “Determination of spatial velocity distributions of

- abrasive particles in abrasive water jets using laser-induced fluorescence under real conditions,” in *WJTA-IMCA Conference and Expo*, 2011.
- [123] K. Maniadaki, A. Antoniadis, and N. Bilalis, “Effect of impact angle and velocity in crater circularity in abrasive water jet machining by means of multi-particle impact simulation Kyriaki Maniadaki Aristomenis Antoniadis * and Nicholas Bilalis,” *Int. J. Machining and Machinability of Materials*, vol. 10, no. 1/2, pp. 34–47, 2011.
- [124] N. Kumar and M. Shukla, “Finite element analysis of multi-particle impact on erosion in abrasive water jet machining of titanium alloy,” *Journal of Computational and Applied Mathematics*, vol. 236, no. 18, pp. 4600–4610, Dec. 2012.
- [125] P. Shipway, “Erosion of particles under impact and compression loading,” PhD thesis, University of Cambridge, 1994.
- [126] A. D. Salman, C. A. Biggs, J. Fu, I. Angyal, M. Szabó, and M. J. Hounslow, “An experimental investigation of particle fragmentation using single particle impact studies,” *Powder Technology*, vol. 128, no. 1, pp. 36–46, Dec. 2002.
- [127] T. Z. Blazynski, *Materials at high strain rates*. New York: Elsevier, New York, 1987.
- [128] Q. Chen and D. Y. Li, “Computer simulation of solid particle erosion,” *Wear*, vol. 254, no. 3–4, pp. 203–210, Feb. 2003.
- [129] G. Wenjun, W. Jianming, and G. Na, “Numerical simulation for abrasive water jet machining based on ALE algorithm,” *The International Journal of Advanced Manufacturing Technology*, pp. 247–253, Jul. 2010.
- [130] I. M. Hutchings, “Mechanisms of wear in powder technology: a review,” *Powder Technology*, vol. 76, no. 1, pp. 3–13, 1993.
- [131] W. Jianming, G. Na, and G. Wenjun, “Abrasive waterjet machining simulation by SPH method,” *The International Journal of Advanced Manufacturing Technology*, vol. 50, no. 1–4, pp. 227–234, Jan. 2010.
- [132] A. W. Momber and R. Kovacevic, “An energy balance of high-speed abrasive water jet erosion,” *Proceedings of the Institution of Mechanical Engineers, Part J: Journal of Engineering Tribology*, vol. 213, no. 6, pp. 463–472, Jan. 1999.
- [133] M. Hashish, “Modified model for erosion,” in *Seventh International Conference on Erosion by Liquid and Solid Impact, Cambridge, England*, 1987, pp. 461–480.
- [134] R. Kovacevic and M. Fang, “Modeling of the influence of the abrasive waterjet cutting parameters on the depth of cut based on fuzzy rules,” *International Journal of Machine Tools and Manufacture*, vol. 34, no. 1, pp. 55–72, 1994.
- [135] A. Carrascal and A. Alberdi, “Evolutionary Industrial Physical Model

- Generation,” in in *Hybrid Artificial Intelligence Systems*, M. G. Romay, E. Corchado, and M. T. G. Sebastian, Eds. Springer Berlin Heidelberg, 2010, pp. 327–334.
- [136] A. Lebar and M. Junkar, “Simulation of abrasive waterjet machining based on unit event features,” *Proceedings of the Institution of Mechanical Engineers, Part B: Journal of Engineering Manufacture*, vol. 217, pp. 699–703, 2003.
- [137] H. Orbanic and M. Junkar, “Simulation of abrasive water jet cutting process: Part 2. Cellular automata approach,” *Modelling and Simulation in Materials Science and Engineering*, vol. 12, no. 6, pp. 1171–1184, Nov. 2004.
- [138] P. Slikkerveer and F. H. Veld, “Model for patterned erosion,” *Wear*, vol. 233–235, no. 1–2, pp. 377–386, Dec. 1999.
- [139] J. H. M. T. T. Boonkkamp and J. K. M. Jansen, “An analytical solution for mechanical etching of glass by powder,” *Journal of Engineering Mathematics*, pp. 385–399, 2002.
- [140] H. Getu, A. Ghobeity, J. Spelt, and M. Papini, “Abrasive jet micromachining of acrylic and polycarbonate polymers at oblique angles of attack,” *Wear*, vol. 265, no. 5–6, pp. 888–901, Aug. 2008.
- [141] a. Ghobeity, M. Papini, and J. K. Spelt, “Abrasive jet micro-machining of planar areas and transitional slopes in glass using target oscillation,” *Journal of Materials Processing Technology*, vol. 209, no. 11, pp. 5123–5132, Jun. 2009.
- [142] T. Burzynski and M. Papini, “Level set methods for the modelling of surface evolution in the abrasive jet micromachining of features used in MEMS and microfluidic devices,” *Journal of Micromechanics and Microengineering*, vol. 20, no. 8, p. 085004, Aug. 2010.
- [143] M. Meo and R. Vignjevic, “Finite element analysis of residual stress induced by shot peening process,” *Advances in Engineering Software*, vol. 34, no. 9, pp. 569–575, Sep. 2003.
- [144] K.-H. Grote and E. K. Antonsson, Eds., *Handbook of Mechanical Engineering, Volume 10*. Springer, 2009.
- [145] I. M. Hutchings, “Strain rate effects in microparticle impact,” *J. Phys. D: Appl. Phys.*, vol. 10, pp. 179–184, Jan. 1977.
- [146] L. Schwer, “Optional Strain-Rate Forms for the Johnson Cook Constitutive Model and the Role of the Parameter Epsilon ϵ_0 ,” in *6th European LS-DYNA Users’ Conference*, 2007.
- [147] D. R. Lesuer and F. Report, “Experimental Investigations of Material Models for Ti-6Al-4V Titanium and 2024-T3 Aluminum,” *U.S. Department of Transportation/Federal Aviation Administration, DTFA03-97-Z-90007*, no. September, 2000.

- [148] G. Fowler, P. Shipway, and I. Pashby, "Abrasive water-jet controlled depth milling of Ti6Al4V alloy - an investigation of the role of jet-workpiece traverse speed and abrasive grit size on the characteristics of the milled material," *Journal of Materials Processing Technology*, vol. 161, no. 3, pp. 407–414, Apr. 2005.
- [149] J. D. Cinnamon, A. N. Palazotto, N. S. Brar, Z. Kennan, and D. Bajaj, "Johnson-Cook Strength Model Constants for VascoMax 300 and 1080 Steels," in *Proceedings of the 14th American physical society (APS) topical conference on shock compression of condensed matter*, 2005, pp. 709–712.
- [150] M. R. Karim and M. S. H. Fatt, "Impact of the Boeing 767 Aircraft into the World Trade Center," *Journal of Engineering Mechanics*, vol. 131, no. 10, pp. 1066–1072, 2005.
- [151] M. Niinomi, "Mechanical properties of biomedical titanium alloys," *Materials Science and Engineering: A*, vol. 243, no. 1–2, pp. 231–236, Mar. 1998.
- [152] "Steel properties." [Online]. Available: http://www.efunda.com/materials/alloys/carbon_steels/show_carbon.cfm?ID=AISI_1080&prop=all&Page_Title=AISI_1080. [Accessed: 10-May-2011].
- [153] "Titanium Alloy properties." [Online]. Available: http://www.efunda.com/materials/alloys/titanium/show_titanium.cfm?ID=T18_AB&show_prop=all&Page_Title=Ti-6Al-4V. [Accessed: 10-May-2011].
- [154] N. Nagy, M. Mohamed, and J. C. Boot, "Nonlinear numerical modelling for the effects of surface explosions on buried reinforced concrete structures," vol. 2, no. 1, pp. 1–18, 2010.
- [155] S. Bagherifard, R. Ghelichi, and M. Guagliano, "A numerical model of severe shot peening (SSP) to predict the generation of a nanostructured surface layer of material," *Surface and Coatings Technology*, vol. 204, no. 24, pp. 4081–4090, Sep. 2010.
- [156] M. Zimmermann, V. Schulze, H. U. Baron, and D. Löhe, "A Novel 3D Finite Element Simulation Model for the Prediction of the Residual Stress State after Shot Peening," *Simulation*, pp. 1–6.
- [157] J. W. Nam, J.-H. J. Kim, S. B. Kim, N. H. Yi, and K. J. Byun, "A study on mesh size dependency of finite element blast structural analysis induced by non-uniform pressure distribution from high explosive blast wave," *KSCE Journal of Civil Engineering*, vol. 12, no. 4, pp. 259–265, Jul. 2008.
- [158] M. Klemenz, V. Schulze, I. Rohr, and D. Löhe, "Application of the FEM for the prediction of the surface layer characteristics after shot peening," *Journal of Materials Processing Technology*, vol. 209, no. 8, pp. 4093–4102, Apr. 2009.
- [159] F. Boud, C. Carpenter, J. Folkes, and P. H. H. Shipway, "Abrasive waterjet cutting of a titanium alloy: The influence of abrasive morphology and

- mechanical properties on workpiece grit embedment and cut quality,” *Journal of Materials Processing Technology*, vol. 210, no. 15, pp. 2197–2205, Nov. 2010.
- [160] P. H. Shipway and I. M. Hutchings, “Attrition of brittle spheres by fracture impact loading under compression and,” *Powder Technology*, vol. 76, pp. 23–30, 1993.
- [161] P. H. Shipway, “Erosive wear of brittle materials and its laboratory simulation,” PhD Thesis, Cambridge, 1992.
- [162] P. H. Shipway and I. M. Hutchings, “Fracture of brittle spheres under compression and impact loading II. Results for lead-glass and sapphire spheres,” *Philosophical Magazine A*, vol. 67, no. 6, pp. 1405–1421, 1993.
- [163] J. C. E. Anderson, I. S. Chocron, and A. E. Nicholls, “Damage modeling for Taylor impact simulations,” *Journal De Physique IV (Proceedings)*, vol. 134, pp. 331–337, 2006.
- [164] M. Buyuk, S. Kan, and M. J. Loikkanen, “Explicit Finite-Element Analysis of 2024-T3/T351 Aluminum Material under Impact Loading for Airplane Engine Containment and Fragment Shielding,” *Journal of Aerospace Engineering*, vol. 22, no. 3, p. 287, 2009.
- [165] C. Lim, V. P. W. Shim, and Y. H. Ng, “Finite-element modeling of the ballistic impact of fabric armor,” *International Journal of Impact Engineering*, vol. 28, no. 1, pp. 13–31, Jan. 2003.
- [166] H. Billon, “A Model for Ballistic Impact on Soft Armour,” *DSTO Aeronautical and Maritime Research Laboratory, Melbourne*, 1998.
- [167] P. A. Pincosy and M. J. Murphy, “Calculated concrete target damage by multiple rod impact and penetration,” in *23rd international symposium on ballistics, Tarragona, Spain*, 2007.
- [168] G. Desale, B. Gandhi, and S. Jain, “Effect of erodent properties on erosion wear of ductile type materials,” *Wear*, vol. 261, no. 7–8, pp. 914–921, Oct. 2006.
- [169] B. a. Lindsley and a. R. Marder, “The effect of velocity on the solid particle erosion rate of alloys,” *Wear*, vol. 225–229, pp. 510–516, Apr. 1999.
- [170] S. Yerramareddy and S. Bahadur, “Effect of operational variables, microstructure and mechanical properties on the erosion of Ti-6Al-4V,” *Wear*, vol. 142, no. 2, pp. 253–263, 1991.
- [171] A. Henning and E. Westkamper, “Modelling of wear mechanisms at the abrasive waterjet cutting front,” in *WJTA American Waterjet Conference, Houston, Texas, USA*, 2003.
- [172] P. Slikkerveer, “Erosion and damage by sharp particles,” *Wear*, vol. 217, no. 2, pp. 237–250, May 1998.

- [173] T. Burzynski and M. Papini, "A level set methodology for predicting the surface evolution of inclined masked micro-channels resulting from abrasive jet micro-machining at oblique incidence," *International Journal of Machine Tools and Manufacture*, vol. 51, no. 7–8, pp. 628–641, Jul. 2011.
- [174] "Tekniker." [Online]. Available: <http://www.tekniker.es/es/>. [Accessed: 04-Jul-2012].
- [175] "ZEEKO, Ltd." [Online]. Available: <http://www.zeeko.co.uk/site/tiki-index.php?page=HomePagePublic>. [Accessed: 04-Jul-2012].